UCLA
UCLA Electronic Theses and Dissertations

Title

Tissue Characterization in Reperfused Myocardial Infarction with Cardiac Magnetic Resonance Imaging

Permalink

https://escholarship.org/uc/item/4m9179nm

Author

Zhang, Xinheng

Publication Date

2024

Peer reviewed|Thesis/dissertation

eScholarship.org Powered by the California Digital Library
University of California

UNIVERSITY OF CALIFORNIA

Los Angeles

Tissue Characterization in Reperfused Myocardial Infarction with Cardiac Magnetic Resonance Imaging

A dissertation submitted in partial satisfaction of the

requirements for the degree Doctor of Philosophy

in Bioengineering

by

Xinheng Zhang

2024

@ Copyright by

Xinheng Zhang

2024

ABSTRACT OF THE DISSERTATION

Tissue Characterization in Reperfused Myocardial Infarction

with Cardiac Magnetic Resonance Imaging

by

Xinheng Zhang

Doctor of Philosophy in Bioengineering

University of California, Los Angeles, 2024

Professor Rohan Dharmakumar, Co-Chair

Professor Debiao Li, Co-Chair

Cardiovascular disease (CAD) is still the most prevalent disease although there are extensive improvements in mortality and healthcare. More patients who received initial treatment for heart failure suffer greatly from reperfusion injury, resulting in myocardial infarction (MI). Hemorrhagic MI is proven to be the severest form of MI, and there is the calling for comprehensively characterize MI for patient's long-term survival and quality of life.

Cardiac magnetic resonance (CMR) imaging has been developed as first-line imaging modality for tissue characterization: fibrosis, edema, microvascular obstruction (MVO), intramyocardial hemorrhage (IMH) and its residual iron, and fat deposition. Those substrates are independent predictors of major adverse cardiac events (MACE) and manifests as different severity of MIs. Thus, being able to characterize MVO, IMH, MVO and its fat deposition is of

great significance. Current practice of MI characterization continues to demand strong needs and technical challenges. Three needs were identified: a fast-imaging protocol to identifying MI, non-contrast technique to characterize multiple substrates underlying MI, and overlooked influence of spatial resolution on IMH detection.

First, the lengthy CMR protocol in multiple tissue characterization may have impeded its implementation. A fast, comprehensive acquisition to characterize MI, MVO, IMH, cardiac function is on demand. In Chapter 2, we developed a free-breathing, non-ECG gating 3D T1, T2* imaging approach based on low-rank tensor (LRT) framework to shorten the imaging protocol of the same conventional acquisition by factor of 3-4. This framework also overcomes critical image artifacts from undesirable cardiac and respiratory motion and provides additional information in MVO characterization.

Second, native T1 mapping has been extensively studied to provide diagnostic values in identifying acute and chronic MIs by characterizing edema or fibrotic tissue with elevated their T1 values. However, we realized that the co-existence of fibrosis, IMH and/or its induced fat deposition are causing inhomogeneity of T1 values within MI. Instead of treating them as confounding factors, in Chapter 3, we demonstrated native T1 heterogeneity within MIs as a new look for MI characterization and theorized it as a potential application for MI patient risk stratification. Specifically, we probed the heterogeneity of MIs in T1 mapping using entropy analysis, known as T1 entropy. We have shown that T1 entropy is capable of distinguishing MI from remote myocardium in both acute and chronic MI. We found T1 entropy is strongly associated with fat fraction and R2* (iron content) in the high fat fraction and high R2* group. The results were also validated in patient studies. In conclusion, T1 entropy is a promising

predictor for heterogeneity of MI, and it is a reliable biomarker for analysis of severity of chronic MI.

Third, the current imaging protocol in T2* mapping for IMH and iron remnants detection is derived from iron overload from thalassemia. However, for iron deposits from chronic MI with wall thinning (< 6 mm), the long-overlooked influence of spatial resolution may play a significant role in its detection. The primary goal of Chapter 4 in this dissertation is to address the limitations by investigating the influence of spatial infarction on T2* mapping in the competing effect of partial volume and SNR with simulation phantoms, ex-vivo heart scans and in-vivo scans in detecting iron residuals from thinned myocardial wall. We found that the spatial resolution can be optimized given SNR greater than 10. However, the current in-vivo CMR protocol may be limited in detecting thinned narrowed iron band (< 1 mm) due to insufficient SNR level.

In general, this dissertation contributed MI tissue characterization with CMR by addressing the spatial, temporal, and contrast challenges. It paves the way for MRI to characterize MI for prognosis and therapeutic care of patients with the capability to characterize severe form of MI such as IMH. These challenges have been addressed in this dissertation.

In future work, our developed fully ungated free-breathing 3D LRT T1, T2* will be investigated for patients for MI characterization. And we will further specialize the technique due to its advantages in MVO characterization for delayed enhancement. The T1 entropy will be validated in post-contrast T1 mapping. We would also employ the free-breathing nature of LRT framework to improve the SNR profile for iron remnants detection in T2* mapping.

The dissertation of Xinheng Zhang is approved.

Michael Albert Thomas

Holden H. Wu

Rohan Dharmakumar, Committee Co-chair

Debiao Li, Committee Co-chair

University of California, Los Angeles

2024

Dedicated to my parents Jianmin Zhang and Qin Guo, my brother, the ones I love, and my friends who supported me throughout my graduate studies.

TABLE OF CONTENTS

ABSTRACT OF THE DISSERTATION ..... **ii**

LIST OF FIGURES ..... **xiv**

LIST OF TABLES ..... **xxviii**

LIST OF ABBREVIATIONS ..... **xxix**

ACKNOWLEDGEMENTS ..... **xxxiv**

VITA ..... **xxxvii**

CHAPTER 1: INTRODUCTION **1**

1.1 Significance of Cardiovascular Disease 1

1.2 Myocardial Infarction (MI) 1

1.2.1 Therapy for MI and Reperfusion Injury 2

1.2.2 Classification of Reperfused MI 2

1.2.3 Microvascular Injury in Reperfused MI 3

1.3 Pathophysiology of Reperfusion Injury and Temporal Progression of MI 5

1.3.1 Acute Phase (First Few Hours to Days Post Reperfusion) 6

1.3.2 Sub-Acute Phase (Days to Weeks) 7

1.3.3 Chronic Phase (Months to Years) 7

1.4 Existing Methods for MI Detection and Characterization of MI 8

1.4.1 Invasive techniques 8

1.4.2 Non-invasive techniques 9

1.4.3 Cardiac MR 10

1.4.3.1 Gadolinium-enhanced CMR 10
1.4.3.2 Native T1 mapping 12
1.4.3.3 T2 CMR 14
1.4.3.4 T2* CMR 15
1.4.3.5 Other techniques 15
1.5 Characterization of MI with CMR 16
1.5.1 Fibrosis/necrosis 18
1.5.2 Microvascular Injury 19
1.5.2.1 Microvascular obstruction (MVO) 19
1.5.2.2 IMH and iron deposits 20
1.5.3 Fat Deposition 21
1.5.4 Edema 23
1.6 Needs and Challenges in CMR for Characterizing MI 24
1.6.1 Need for Fast, Comprehensive MI Characterization to Facilitate Patient Management 24
1.6.1.1 Low-rank Tensor Framework 25
1.6.2 Need for Cardiac Outcome Stratification for MI Patients with Non-Contrast Techniques 28
1.6.3 Need for Optimizing Spatial Resolution and Signal-to-Noise Ratio (SNR) of T2* Mapping in Detection of Iron Deposits in MI 30
1.7 Key Objectives of the Dissertation 32
1.7.1 Aim 1: To develop, test, and validate a 15-min protocol comprising of free-breathing, non-ECG gating, motion resolved whole LV 3D acquisition using LRT-based

reconstruction to characterize MIs with cardiac function, MI size, MVO size and IMH size. 33

1.7.2 Aim 2: To characterize the MI severity using heterogeneity analysis on native T1 mapping in chronic MI patients. 33

1.7.3 Aim 3: To address the limitation of identification of residual iron deposition from IMH in chronic MI and provide guidance for improving the accuracy of iron detection. ... 34

CHAPTER 2: FAST, COMPREHENSIVE 3D FREE-BREATHING, NON-ECG GATING LOW-RANK TENSOR BASED CMR CHARACTERIZATION OF MYOCARDIAL INFARCTION 35

2.1 Introduction 35

2.2 Methods 37

2.2.1 Sequence Diagram 37

2.2.2 Low-rank tensor imaging model 38

2.2.3 Image reconstruction 40

2.2.4 Animal studies 41

2.2.5 CMR Acquisition 42

2.2.6 Image analysis 43

2.2.7 Histology validation 44

2.2.8 Statistical analysis 45

2.3 Results 45

2.3.1 Comparison of LVEF between proposed and conventional method 47

2.3.2 Comparison of MI size and MI transmurality between proposed and conventional method 50

2.3.3 Comparison of IMH and MVO size characterized by proposed and conventional method 51
2.3.4 Representative images from the two methods and histological validation 53
2.3.5 Characterization of Early MVO and Late MVO between proposed and conventional methods 55
2.4 Discussion 57
2.5 Conclusion 59
CHAPTER 3: NATIVE T1 ENTROPY FOR RISK STRATIFICATION IN MYOCARDIAL INFARCTION 61
3.1 Introduction 61
3.2 Methods 64
3.2.1 Simulation Study 64
3.2.2 Phantom Study 65
3.2.3 Animal Study: Preparation and Study Design 65
3.2.4 Patient Study 66
3.2.5 MRI protocols 67
3.2.5.1 Ex-vivo Phantom MRI 67
3.2.5.2 CMR in canine study 68
3.2.5.3 CMR in patient study 69
3.2.6 Image Processing 69
3.2.6.1 Myocardium mask ROI identification 69
3.2.6.2 Fat-water Separation 69

3.2.6.3 Heterogeneity analysis on T1 map 70
3.2.7 Statistical Analysis 70
3.3 Results 71
3.3.1 Simulation Results from T1 MOLLI on Fat Fraction 71
3.3.2 T1 MOLLI Response Validation in Fat Phantom 72
3.3.3 T1 Entropy, Fat Fraction and R2* In The Canine Model At All Time Points 74
3.3.4 T1 Entropy Categorized Based on R2* and Fat Fraction within MI in The Canine Model 79
3.3.5 T1 Entropy Validation in Patient Data 86
3.4 Discussion 91
3.5 Conclusion 94
CHAPTER 4: INFLUENCE OF SPATIAL RESOLUTION AND SNR IN T2* MAPPING FOR DETECTION OF IRON DEPOSITS IN CHRONIC MI 95
4.1 Introduction 95
4.2 Methods 97
4.2.1 Numerical Simulations 97
4.2.1.1 Ventricular Modeling 97
4.2.1.2 Imaging Simulation 99
4.2.2 Animal Studies 101
4.2.3 CMR Acquisitions 102
4.2.3.1 Ex-vivo Acquisition 102
4.2.3.2 In-vivo Acquisition 103

4.2.4 Image Analysis 104
4.2.5 Sample Preparation & Validation Studies 107
4.2.6 Statistical Analysis 108
4.3 Results 109
4.3.1 Numerical Simulations – SNR vs Spatial Resolution 109
4.3.2 Results from animal studies 113
4.3.2.1 IMH transmurality and width in Chronic MI 113
4.3.2.2 Definition of Spatial Resolution Reference Standard for Detection of Iron Deposition 114
4.3.2.3 Effect of Partial Volume Artifact 115
4.3.2.4 Effect of In-Plane vs. Through-Plane Resolution 117
4.3.2.5 Effect of Spatial Extent of Iron Distribution 119
4.3.2.6 Limitation of Detection of Iron Deposition From CNR Analysis 119
4.3.2.7 Histology and Mass Spectrometry Based Validation for Detecting Iron within Chronic MI 120
4.3.2.8 Limitation of detection in *In-vivo* CMR 122
4.4 Discussion 124
4.5 Study Limitations 130
CHAPTER 5: SUMMARY AND FUTURE DIRECTIONS 132
5.1 Summary 132
5.2 Future Directions 134
5.2.1 Validation on Proposed LRT T1, T2* Patients with IMH 135

5.2.2 Further Development of LRT T1, T2* Imaging Method 135

5.2.3 Post-contrast T1 entropy vs Pre-contrast T1 entropy 135

5.2.4 Improvement of spatial resolution on T2* CMR 137

REFERENCES 138

LIST OF FIGURES

Figure 1.1 Summary of CCS Classification of Stages of Acute Reperfused Myocardial Infarction Based on Tissue Injury. MACE increased for 2-4-fold in CCS stage III and CCS stage IV, when microvascular injury is present. Adopted from [38]. 4

Figure 1.2 An overarching model of how hemorrhagic infarction promotes chronic heart failure via fat deposition. Following MI, compensatory remodeling promotes the partial recovery of LV function in the early weeks following the index event. Hemorrhagic MI promotes the formation of fat deposition and functional losses, which define CHF. While non-hemorrhagic MIs stabilizes the infarct zone leading to stable functional remodeling in the chronic phase of MI. Adopted from [45]. 5

Figure 1.3 MOLLI pulse sequence scheme. Vertical bars represent image acquisition. Dashed lines represent undisturbed signal recovery. For T1 value calculation, the images were regrouped into one data set according to their effective T1. Adopted from [122]. 13

Figure 1.4 Illustration of MI, characterized by fibrotic tissue, fat and iron deposition and its development over time. A) The severest form of hemorrhagic MI is shown as relatively homogeneous region on LGE image, but the underlying substrates may be missed. **B)** Temporal evolution of key substrates (Edema [181], MVO [44], Fibrosis [21,182], Iron deposits [44] and Fat deposits [45,183]) within MI. 17

Figure 1.5 Typical appearance of T1 maps in healthy subjects and in subjects with myocardial disease. Arrows denote relative change in respective T1 maps. Adopted from [143] and [245]. 29

Figure 2.1 Imaging protocol with LRT pulse sequence diagram. Inversion recovery (IR) pulses are applied at constant intervals by mGRE readouts. Following each IR preparation

module, RF pulse flip angles are 5° for 192 segments. The training auxiliary data are interleaved with imaging data every eight segments. Protocol 1: Pre-contrast acquisition (CINE and mGRE) followed by contrast injection and LRT sequence acquisition and conventional LGE acquisition. Protocol 2: The same pre-contrast and LGE protocol, but with early enhancement and late enhancement acquisition after Gd injection.....38

Figure 2.2 Representative images reconstructed with proposed LRT methods for 3D coverage, respiratory and cardiac dimension. A) A short-axis image sliced in two planes (Blue: 4-chamber view; Red: 2-chamber view) and two sliced views are shown on the right side. **B)** 4 respiratory phases are shown with planes at the tip of the liver highlighted with cyan dashed lines. **C)** 8 representative cardiac phases from end-diastole (cardiac phase 1) to systole (cardiac phase 8). Notably, blood pool contours for cardiac phases 1 and 8 are highlighted. 46

Figure 2.3 Representative images with proposed LRT method in contrast dimensions. A) T2* dimension with 6 TEs goes from 1.47 to 11.42 ms incrementally; **B)** T1 recovery dimension from segment (Seg) 1 to segment 192, with Seg #1, 11, 14, 21, 31, 41, 61, 81, 101, 121, 141, 181 shown as representative magnetization recovery on myocardium. **C)** Gd dynamic dimension from section 1 to section 15. Notably, each section is recovered from data in about 1 min, and the curve on the left illustrates MVO size decrease over time. The dashed lines on the left represent corresponding time points to the right. 47

Figure 2.4 Representative image for Conventional (Conv.) CINE and Proposed LRT CINE (short-axis view) and ejection fraction comparison. End-diastole and end-systole cardiac phases are compared between conventional and the proposed approaches with three representative slices at base, mid-ventricle and apex of the hearts. Both **A)** acute and **B)** chronic of the same subject are shown above. The endocardium and epicardium contours were manually

draw in each slice for both approaches with matched slice location**. C)** linear regression analyses comparing LVEF between conventional and LRT approaches, fitted equation and R^2 are shown in each plot. **D)** Bland-Altman analyses comparing agreement between the two approaches, RPC is shown in each plot. From left to right are all data points (both red and blue), only acute data points (red) and chronic data points (blue). 49

Figure 2.5 Capability of MI characterization between proposed LRT and Conv. approaches. A) linear regression analyses comparing MI size between Conv. and LRT approaches, fitted equation and R^2 are shown in each plot. On right: Bland-Altman analyses comparing agreement between the two approaches, RPC is shown in each plot. From top to bottom are all data points, only acute data points (red) and chronic data points (blue). **B)** Linear regression and Bland-Altman comparing MI transmurality between two approaches with the same lay-out. 51

Figure 2.6 Intramyocardial hemorrhage (IMH) and MVO comparison between the proposed LRT and Conv. approaches. A) On left: linear regression analyses comparing hemorrhage size between Conv. and LRT approaches, fitted equation and R^2 are shown in each plot. On right: Bland-Altman analyses comparing agreement between the two approaches, RPC is shown in each plot. From top to bottom are all data points, only acute data points (red) and chronic data points (blue). **B)** Linear regression and Bland-Altman comparing MVO size between two approaches on acute time point. Only acute time point was shown because no MVO was found in chronic phase. 52

Figure 2.7 Representative cases of T2*w and LGE between conventional CMR and proposed LRT approaches. A) The subject was scanned on both acute and chronic time points. T2* weighted images (TE=11.43 ms) and LGE images were compared between LRT and 2D

Conv. method with slice matched. Epicardium (green), endocardium (red) and MI region (blue) contours were drawn. Hemorrhage were pointed out by red triangular arrows, MVO were pointed with yellow arrows and off-resonance artifact were pointed with cyan arrows. **B)** The sliced heart tissue and its histology: Masson's Trichrome and Prussian Blue are shown at 10-magnification (10×). An infarcted region and one remote region were drawn in the 10× image and specifically shown in 40-magnification (40×) next to it.....54

Figure 2.8 Representative images of MVO at 2 min (Early) and 13 min (Late) enhancement and after 15 min (LGE) and statistical analysis between the proposed and conventional methods. A) are MVO size progression for LRT and 2D Conv. CMR approaches. **B)** are representative images at early, late, and after late enhancement between LRT and Conv. Unprocessed image is shown on left while processed image on right, with endocardium (red), epicardium (green), MI (blue) and MVO (cyan) contours. **C)** Bar plot of MVO size in LRT and Conv. with each data point progression from early enhancement to late enhancement. **D)** On left: linear regression analyses comparing MVO size between Conv. and LRT approaches, fitted equation and R^2 are shown in each plot. On right: Bland-Altman analyses comparing agreement between the two approaches, RPC is shown in each plot. From top to bottom are at early enhancement time point (light gray) and late enhancement time point (dark gray).....56

Figure 3.1 Illustration of chronic MI severity based on substrates and increase of native T1 heterogeneity as chronic MI become severer. 62

Figure 3.2 Study Details - canine subjects and human patient. A) Illustration of canine subjects undergoing reperfusion injury. Subjects that have at least one chronic scan in Month 6 were included in this study (N = 14). 9 out of 14 subjects underwent 6-month scan, 11 out of 14 subjects underwent 1-year scan, and 9 out of 14 subjects underwent 1.5-year scan. **B)** 26 patient

data were analyzed due to loss of follow-up scans (n = 24), unmet image quality (n = 5) and missing native T1 mapping and T2* images from 70 prospectively recruited patients. 67

Figure 3.3 Simulation results to illustrate native T1 MOLLI response to mixture of water and fat. A) bSSFP off-resonance response for myocardium (blue) and fat (red) illustrating that the polarized signal at on-resonance (0 Hz) for typical MOLLI protocol with TR = 2.40 ms and FA = 35°. **B)** Inversion recovery measurements (circles) for out-of-phase water and fat mixtures at various fat fractions (0 – 100 %, with 10% increments) and 3-parameter mono-exponential fits (blue) using MOLLI protocol. Estimated T1 values are displayed on top of each plot. **C)** Estimated T1 of fat water mixtures vs FF for inversion recovery using MOLLI protocol. 72

Figure 3.4 The make of the fat phantom and its validation in two T1 sequences. A) Illustration of fat phantom from left to right: 0%, 2.5%, 5%, 10%, 20%, 30%, 40% and 100% fat fraction, notably 100% fat fraction is made of soybean oil completely. **B)** Comparison of T1 values of from MOLLI scheme and IRSE at each fat fraction. The fitted maps are shown in **C)** and **D)**. 73

Figure 3.5 Time evolution of T1 entropy, fat fraction and R2* of MI and Remote myocardium. Bar plot of **A)** T1 entropy, **C)** FF, **E)** R2* and at Day 7, Week 8, Month 6 and Year 1+ (denoted as D7, W8, M6 and Y1+ respectively). Red columns are values in MI while blue columns are remote myocardium. All the columns are presented as mean values (column) plus standard deviations (whiskers). Line charts of **B)** T1 entropy, **D)** FF, **F)** R2* within MI from Day 7 to Year 1+. ns denotes P > 0.05, * P < 0.05, ** P < 0.01 and *** P < 0.001. 77

Figure 3.6 Linear regressions at 4 different timepoints on R2* vs fat fraction, FF vs T1 entropy, R2* vs T1 entropy in MI respectively. A) Scatter plots of relationship between R2* and fat fraction with linear regression, the fitted equations are shown in each plot with coefficient

of determination and t-test results showing if the fitted slope is significantly different from 0. The results show strong correlation of fat fraction and iron deposition is shown in chronic MI. **B)** Scatter plots of relationship between fat fraction and T1 entropy, the correlation is established over time. **C)** Also scatter plots of relationship between R2* and T1 entropy is shown. Linear regression result shows that R2* is also a determinant factor of T1 entropy in MI.....79

Figure 3.7 Linear regressions of fat fraction and R2* for timepoints > 6 months can be divided into 3 sub-groups. A) Linear regression of FF vs. R2* are shown and categorized into 3 groups. Group 1: high fat fraction, high R2* group (R2* > 35 ms^{-1}, FF > 4%, red circle, N = 46), Group 2: low fat fraction, high R2* group (R2* > 35 ms^{-1}, FF < 4%, blue square, N = 27) and Group 3: low fat fraction and low R2* (R2* < 35 ms^{-1}, FF < 4%, red purple triangle, N = 13). Equation of linear regression is shown on top of the plot. The curves of linear regression fitting are shown only if the fitted slope is significantly different from 0 ($P<0.05$). Linear regression plots are shown in each group for R2* and fat fraction, fat fraction and T1 entropy, and R2* and T1 entropy respectively for 3 sub-groups in **B)**, **C)** and **D)**.....82

Figure 3.8 T1 entropy comparison in chronic MI (> 6 months) from three categories. Bar plot of T1 entropy in three categorized groups based on fat fraction and R2*. MI is encoded in red, and remote myocardium is encoded in blue. ns denotes $P > 0.05$ and *** $P < 0.001$. 82

Figure 3.9 Representative cases for three subjects in each category depending on its fat fraction and R2* in MI region. One representative case for each zone is shown. On left: Scatter plot of R2* vs FF for each subject is shown at each time points, with arrows pointing from acute to sub-chronic to chronic phase. On right: Each subject contains native T1 map, histogram of T1 values within MI region, FF map, R2* map and LGE images at acute, sub-chronic and chronic phases. For T1 maps, the myocardium is overlapped with a purple mask, with delineation of

black contours denoting MI masks. Within MI masks, a color map was applied from -500 ms to +500 ms variation from T1 values of average remote myocardium. For T1 histogram, 20 bins were applied from T1 from 750 ms to 1750 ms, smoothed density plots are shown above the histogram. The dash lines show mean T1 values of the ROI and T1 entropy values are displayed on top of each plot. Both FF map and R2* maps are shown overlapping with myocardium masks in dark blue, with orange contoured MI region. And similarly, within MI region, color maps of fat fraction and R2* are shown respectively. LGE images for each subject with corresponding slices are shown with epicardium contours in green, endocardium in red, and MI in black. 84

Figure 3.10 Histology validation of 3 Representative Subjects. Masson's Trichrome, Prussian Blue for three subjects: **A)** High fat fraction is shown as large nodules within fibrotic stains, blue spots were observed in Prussian blue staining with co-localization with fat nodules. **B)** Blue iron spots were found in Prussian blue staining while no high fat fraction area is seen**. C)** Small fibrotic region was found in Trichrome staining while no notable fat nodules or iron deposits were found in the infarcted region. Small rectangular arrows pointing to the 10× view images are magnified on the right with one remote region and one MI for each. Iron deposition is highlighted with triangular arrows.....85

Figure 3.11 Time evolution of T1 entropy, fat fraction and R2* comparing between MI and remote myocardium in Day 7 (D7) and Month 6 (M6) respectively. Bar plot of **A)** T1 entropy, **C)** FF, **E)** R2* and at Day 7 and Month 6 (denoted as D7 and M6 respectively). Red bar denotes as MI while blue bar denotes as remote myocardium. All the columns are presented as mean values (column) plus standard deviations (whiskers). Line charts of **B)** T1 entropy, **D)** fat fraction (FF) and **F)** R2* within MI at D7 and M6 are shown on the left column. ns denotes $P > 0.05$, and *** denotes $P < 0.001$.....88

Figure 3.12 Linear regression between T1 entropy, fat fraction (FF) and R2* within MI region respectively at Month 6. Scatter plots of relationship between **A)** R2* and FF, **B)** FF and T1 entropy and **C)** R2* and T1 entropy within MI region with linear regression, and the fitted equations are shown in each plot with coefficient of determination and t-test results showing if the fitted slope is significantly different from 0. The results show strong correlation of fat fraction and iron deposition is shown in chronic MI. 89

Figure 3.13 Categorization due to fat fraction (FF) and R2* on patient data. A) Linear regression of FF vs. R2* are shown and categorized into 3 groups same as canine data. Group 1: high FF, high R2* group (red circle, N = 15), Group 2: low FF, high R2* group (blue square, N = 17) and Group 3: low FF and low R2* (red purple triangle, N = 48). **B)** Scatter plot of R2* and fat fraction, fat fraction and T1 entropy, and R2* and T1 entropy respectively with linear regression is shown for Group 1. C) Bar plot of T1 entropy for each categorized group. T-test results are shown for each T1 entropy within MI among the three groups. *** denotes $P < 0.001$ and * denotes $P < 0.05$.....90

Figure 3.14 Representative images of two patients for hemorrhagic MI (hMI) and non-hemorrhagic MI (non-hMI). The subject of hMI is from Group 1 while non-hMI from Group 3. Each subject contains Native T1 map, histogram of T1 values within MI region, fat fraction map, R2* map and LGE images at Day 7 (acute) and Month 6 (chronic). For T1 maps, the myocardium overlapped with a purple mask, with delineation of black contours denoting MI masks. Within MI masks, a color map was applied from -500 ms to +500 ms variation from T1 values of average remote myocardium. For T1 histogram, 20 bins were applied from T1 from 6000 ms to 1600 ms, smoothed density plots are shown above the histogram. The dash lines show mean T1 values of the ROI and T1 entropy values are displayed on top of each plot. Both

FF map and R2* maps are shown overlapping with myocardium masks in dark blue, with orange contoured MI region. Similarly, within the MI region, color maps of fat fraction and R2* are shown respectively. Heart-lung interface artifact from T2*w images were delineated in both maps as while crosses. LGE images for each subject with corresponding slices are shown with epicardium contours in green, endocardium in red, and MI in dark red. The extent of MI is also pointed out by white arrows. 91

Figure 4.1 Side view and top view of the simulated ellipsoid for LV myocardium. The LV was simulated based on the ellipsoid modeling [347], **A)** where $am = 5.0$ cm, $am = 4.0$ cm, $bm = 4.0$ cm, $bO = 2.4$ cm, the heart was truncated in long-axis dimension, where k = 0.6. **B)** In the short-axis view, the ellipsoid was truncated with the second quadrant. The iron-rich (iron+) band is simulated with parameters $bi1 = 1.2bO$ and $bi2 = 1.2bO + 0.025(bm - bO)$, such that the iron+ band is 1.0 mm wide at subendocardium. 98

Figure 4.2 Numerical Phantom Simulation of iron deposits in the heart as T2* maps in various spatial resolution. A) Tissue canvas with $0.04 \times 0.04 \times 0.5$ mm^3 of matrix size $1024 \times 1024 \times 48$, the images are shown in T2* weighting. Three slices were imaged as basal, mid-ventricle and apical locations of the LV myocardium. Imaging voxels were simulated in a sliding window fashion. Here the sliding windows are $0.4 \times 0.4 \times 2$ mm^3 and $2.0 \times 2.0 \times 6$ mm^3 for illustration. **B)** Illustration of five, T2*-weighted (T2*w) images were simulated with TE1 to TE5 = 2.55, 5.80, 9.90, 15.56, 21.22 ms. This set of TEs was also used in ex-vivo imaging parameters (see Table 4.1). **C)** Illustration of different noise level adding to the weighted images, averaged to different resolution windows, and then fitted to T2* map. SNR analysis and ROC analysis were then computed to probe the image quality and capability of iron-rich (iron+) region detection. 101

Figure 4.3 Image processing workflow to analyze detection capability of Ex-vivo and In-vivo T2* maps acquired with assigned spatial resolution. Ex-vivo Reference Standard Image Processing: The T2* map of spatial resolution 0.3×0.3×2 mm^3 with 16 averages was chosen as reference standard. Subsequently, contours (epi- and endo-cardium, MI, remote myocardium) were drawn and binary masks were created. The myocardium was then evenly divided into 50 segments and applied to MI mask. Iron deposits from hemorrhage (iron+) were identified within MI region using Mean-2SD method, converted to a segmental percentage of iron+. The mean iron+ transmurality, the width of the iron+ were then computed. Finally, the array of iron+ percentage was converted to binary array at 1% cutoff for as reference standard in ROC analysis. The rest of ex-vivo group: The contours drawn from the reference standard were scaled accordingly to the remaining T2* images and binary ROI masks were generated. Similarly, each image was divided evenly into 50 segments for analysis, iron+ array with percentage was similarly generated as predictor group for ROC analysis as continuous variables. In-vivo group: The ROIs (epi- and endo-cardium, remote) were drawn from in-vivo T2* maps and iron+ masks were identified by Mean-2SD method. The iron+ volume normalized by total LV myocardium volume (represented as percentage of iron+ in the myocardium) for both in-vivo and reference standard (RS) is computed (as V(Invivo) and V(RS) respectively), and the bias of the volume percentage between in-vivo and ex-vivo Reference Standard was then computed as an indicator for the accuracy of iron+ detection for in-vivo data. 106

Figure 4.4 Representative T2* map images in various spatial resolution at 3 noise levels at basal, mid-ventricle and apex of simulated LV. A) Scatter plot of SNR with error bars at 3 noise levels with varying voxel size. SNR = 5 (from Rose Criterion), SNR = 10 (“acceptable”) and SNR = 40 (“excellent”) is plotted. Notably, Y-axis is log-scaled to make noise level 3

proportional in the plot. **B)** Representative T2* maps at resolution 0.4×0.4×2, 0.4×0.4×8, 2.0×2.0×2 and 2.0×2.0×8 mm^3 from these the noise levels at basal, mid-ventricle and apical location with SNR in below to illustrate visibility of iron+ band from the influence of spatial resolution on SNR and partial volume effect.....110

Figure 4.5 AUC of ROC curves as capability of iron+ detection from the simulated phantom at 3 noise levels and 3 locations. Three sketched simulated myocardium with iron deposits are illustrated on the left for each row (Base, Mid-ventricle and Apex). Nine scatter plots were shown: in horizontal direction from noise level 1 to 3, while in vertical direction from base to apex. In each scatter plots shows voxel size vs. AUC from ROC curves, where through-plane thickness 2, 4, 6, 8 mm is encoded in circle, square, diamond and triangle respectively. Optimal voxel size range is identified by a red circle encompassing the data points for its spatial resolution using 95% of maximum AUC (AUC_{max}) as cutoff (shown in dotted line in y-axis). The cutoff values are displayed in each plot as well.....112

Figure 4.6 Iron+ widths and transmurality. Panel A: two representative cases are shown, one with extensive iron deposition (Swine 2) and the other with significantly lower iron deposition (Swine 1). B) and C) show the distribution of transmurality and iron+ width across all subjects studied, including the two representative cases highlighted. 113

Figure 4.7 Goodness of fitting and SNR analysis T2* maps as indicators for image quality. A) Scatter plot with error bars in determination of correlation for imaging acquisition in all three groups ($0.3 \times 0.3 \times 2$ mm^3 Ex-vivo 16 Avgs, Ex-vivo CMR and In-vivo groups) is shown for goodness of fitting. Y-axis is log-scaled. ns indicates no significant difference ($P > 0.05$). * ($P < 0.05$), ** ($P < 0.01$), *** ($P < 0.001$) comparing to $R^2 = 0.99$, # ($P < 0.05$), ## ($P < 0.01$), ### ($P <$

0.001) comparing to $R^2 = 0.9$. **B)** Scatter plot with error bars showing SNR of T2* maps as function of voxel size in the same groups as A). 115

Figure 4.8 ROC analysis with AUC in iron deposits detection accuracy for ex-vivo subjects to demonstrate partial volume effect. Two examples **A)** Swine 1 and **B)** Swine 2 of One reference standard and 3 ex-vivo acquisitions with 16 averages of T2* map: Left to right are 0.3×0.3×2, 1.6×1.6×2, 1.6×1.6×6 and 2.1×2.1×8 mm^3. The iron+ region is pointed out by triangle arrows. **C)** ROC curves and AUC at each spatial resolution is shown for Ex-vivo 16 Avgs group. Two-way ANOVA analysis of in-plane resolution and through-plane resolution showed significant difference respectively. AUC is shown on each of the ROC curve with its background color coded from 0.5 to 1.0. **D)** A scatter plot of different through-plane resolution (2, 4, 6, 8 mm) is encoded with different shapes (circle, square, diamond and triangle).....116

Figure 4.9 ROC analysis with AUC in iron deposits detection accuracy for Ex-vivo CMR subjects. Two examples **A)** Swine 1 and **B)** Swine 2 of one 0.3×0.3×2 mm^3 from Ex-vivo 16 Avgs group and 3 Ex-vivo CMR acquisitions of T2* map: Left to right are 1.6×1.6×2, 1.6×1.6×6 and 2.1×2.1×8 mm^3. Iron+ is pointed out by triangle arrows. **C)** ROC curves and AUC at each spatial resolution is shown for Ex-vivo CMR group. Two-way ANOVA analysis of in-plane resolution and through-plane resolution for is shown. AUC is shown on each of the ROC curve with its background color coded from 0.5 to 1.0. **D)** Optimal voxel size range for Ex-vivo CMR group is identified by a circle encompassing the data points for its spatial resolution: 1.6×1.6×2 and 1.3×1.3×4 mm^3 using 95% AUC as a cutoff, forth AUC ranging from 0.8 to 0.82. Different through-plane resolution (2, 4, 6, 8 mm) is encoded with different shapes (circle, square, diamond and triangle). E) Scatterplot of mean AUC vs iron+ width. A trend of higher

AUC with higher iron+ width is observed (Y = 0.50X + 0.16, R^2=0.84, P<0.001). As highlighted AUC for Swine 1 is 0.56 while AUC for Swine 2 is 0.85. 118

Figure 4.10 Effect of Spatial Resolution on CNR and Iron+ Detection. Representative images magnified around MI region in the two subjects are shown in **A)** and **B)**. Reference standard 0.3×0.3×2 mm^3 from Ex-vivo 16 Avgs group and 3 Ex-vivo CMR acquisitions: Left to right are 1.6×1.6×2, 1.6×1.6×6 and 2.1×2.1×8 mm^3. Iron+ region was identified by Mean-2SD method and down-sampled to the rest of the three sets of spatial resolution overlaid with cyan masks. For Ex-vivo CMR group, each iron-positive region from IMH was identified by Mean-2SD method overlaid with magenta masks. **C)** and **D)** are scatter plots of voxel size and number of subjects with CNR > 2 and CNR > 1 respectively. All ex-vivo scans are displayed on the plots, in both Ex-vivo 16 Avgs (Blue) and Ex-vivo CMR (Red) groups.....120

Figure 4.11 Histology Validation of Representative Subjects. A) and **D)** H&E and **B)** and **E)** Trichrome staining show infarct, fibrosis and nonviable myocytes, with low transmurality/width for Swine 1 and relatively high transmurality/width for Swine 2 (same as in Figure 4.9). Prussian blue staining of Swine 1 **C)** shows relatively low abundance inside the infarct, while Swine 2 **F)** shows abundant iron accumulation. Small rectangular arrows pointing to the 10× view images are magnified on the right with one remote region and one MI for each. Iron deposition is highlighted with triangular arrows. **G)** Bar plot of iron concentration in remote myocardium vs. MI zone. ** denotes in paired t-test P < 0.01. **H)** Linear regression of hemorrhage width vs the ratio of c(Fe) in MI vs c(Fe) in remote, showed good correlation (Y = 0.65X + 0.64, R^2 = 0.87). 122

Figure 4.12 Iron Deposits Detection for in-vivo Subjects. A) Scatter plot of Normalized Iron volume bias vs. Iron+ width is shown. A trend of larger Iron+ band with lower bias is observed.

Three representative examples with B) 10 subjects were divided into two groups by hemorrhage width: Low Iron (n=5) and High Iron (n=5). F-test was done to compare the variance (P=0.05) between two groups. C) Three representative examples with over-estimated of iron+ region in Swine 1, low-bias estimation of Swine 2 and under-estimation of iron+ region in Swine 3 (in this case, the iron+ is completely undetected) are shown. 123

Figure 4.13 SNR analysis on simulated and CMR acquired T2* maps on remote myocardium. Scatter plot with error bars of square root of voxel size vs SNR of the remote myocardium on T2* maps (Simulation: circle, Ex-vivo CMR: square, and In-vivo: triangle) is shown. Linear regression was performed to the simulation and ex-vivo dataset. The slope of the linear regression for simulation noise level 1, 2, and Ex-vivo CMR are 1.43, 4.08 and 5.24 respectively. 129

Figure 5.1 Entropy analysis on post-contrast T1 maps. A) Representative images of pre-contrast and post-contrast T1 maps. Processed MI masks is shown as ± 500 ms of mean value within the MI region. T1 histograms are shown in the same range (1400 ms) for both pre- and post-contrast images, with pre-contrast 400 ms to 1800 ms, while post-contrast 100 ms to 1500 ms. B) Scatter plot to compare Pre-contrast T1 entropy and post-contrast T1 entropy. Two representative subjects were highlighted as red data points. And linear regression shows moderate correlation between two entropies determined with pre- and post-contrast T1 maps ($R^2 = 0.45$, $P < 0.001$). C) Strong correlation of R2* and FF is shown in this subset of the chronic data ($R^2 = 0.78$, $P < 0.001$). D) and E) shows relationship of R2* vs T1 entropy, and FF vs T1 entropy in both pre- and post-contrast T1 maps. Notably, pre-contrast is shown in blue square while post-contrast is shown in red circle. 136

LIST OF TABLES

Table 1.1 List of experimental techniques in MI characterization and its clinical studies. 16

Table 1.2 Summary of Imaging Resolutions from Previous Studies. 31

Table 2.1 Imaging Parameters 42

Table 3.1 Key parameters of our imaging protocol compared to previous simulation. 65

Table 3.2 Descriptive T1 values on volume-based analysis at all time points. Mean, Standard Deviation (SD), 1st percentile and 99th percentile for MI and remote myocardium is displayed. The lowest 1st percentile and highest 99th percentile are highlighted in red for both MI and remote myocardium. 74

Table 3.3 Characteristics of Patient Study Cohort 87

Table 4.1 Imaging Parameters. **A)** Ex-vivo scan parameters for Ex-vivo 16 Avgs group, Ex-vivo CMR group and In-vivo group respectively. **B)** In-plane resolution between Ex-vivo 16 Avgs group (0.3×0.3 mm^2 - 2.1×2.1 mm^2), Ex-vivo CMR group (0.8×0.8 - 2.1×2.1 mm^2) and In-vivo group (1.6×1.6 mm^2). 103

LIST OF ABBREVIATIONS

^{1}H	Hydrogen nuclei
2D/3D	Two/Three Dimensional
AAR	Area At Risk
ADC	Apparent Diffusion Coefficient
AHA	American Heart Association
ANOVA	ANalysis Of Variance
AUC	Area Under the Curve
bSSFP	balanced Steady-State Free Precession
BW	BandWidth
CAD	Coronary Arteries Diseases
CEST	Chemical Exchange Saturation Transfer
CCS	Canadian Cardiovascular Society
CrCEST	Creatine CEST
CT	Computed Tomography
CCT	Cardiac Computed Tomography
CHD	Chronic heart disease
CMR	Cardiac Magnetic Resonance imaging
CNR	Contrast-to-Noise Ratio
CV	Coefficient of Variation
CVF	Collagen Volume Fraction
dDCE	delayed-phase Dynamic Contrast-Enhanced

ECG	ElectroCardioGraphy
ECV	ExtraCellular Volume
EDV	End Diastolic Volume
EF	Ejection Fraction
EGE	Early Gadolinium Enhancement
EMT	Elastin Masson's Trichrome
EMVO	Early MicroVascular Obstruction
ESV	End Systolic Volume
FA	Flip Angle
FLASH	Fast Low Angle SHot
FOV	Field Of View
FF	Fat Fraction
FWHM	Full-Width at Half Maximum
GBCA	Gadolinium-Based Contrast Agent
Gd	Gadolinium
GRAPPA	GeneRalized Auto-calibrating Partially Parallel Imaging
GRE	GRadient-Echo
H&E	Hematoxylin and Eosin
HEART	History, Electrocardiography, Age, Risk factors, Troponin
HR	Heart Rate
IACUC	Institutional Animal Care and Use Committee
ICA	Independent Component Analysis
ICP-MS	Inductively Coupled Plasma – Mass Spectrometry

IDEAL	Iterative Decomposition with Echo Asymmetry and Least squares estimation
IMH	IntraMyocardial Hemorrhage
IR	Inversion Recovery
IRB	Institutional Review Board
IRSE	Inversion Recovery Spin Echo
ISO	International Organization for Standardization
LAD	Left Anterior Descending coronary artery
LMVO	Late MicroVascular Obstruction
LVEF	Left Ventricle Ejection Fraction
LGE	Late Gadolinium Enhancement
LIE	Late Iodine Enhancement
LL	Look-Locker
LRT	Low-Rank Tensor
LV	Left Ventricle
mGRE	Multi-Gradient-Echo
MACE	Major Adverse Cardiovascular Events
MI	Myocardial Infarction
MOLLI	Modified Look-Locker Inversion recovery
MR	Magnetic Resonance
MRI	Magnetic Resonance Imaging
MRTA	Magnetic Resonance Texture Analysis
MT	Magnetization Transfer
MVO	Microvascular Obstruction

PA	Propagation Angle
PCI	Percutaneous Coronary Intervention
PDFF	Proton Density Fat Fraction
PET	Positron Emission Tomography
ppm	parts per million
PSIR	Phase-Sensitive-Inversion-Recovery
R_2*	Rate of decay of transverse magnetization in the presence of static magnetic field inhomogeneities
RF	Radio-Frequency
RBCs	Red Blood Cells
ROC	Receiver Operating Characteristic
ROI	Region Of Interest
RPC	ReProducibility Coefficient
RV	Right Ventricle
SASHA	Saturation Recovery Single Shot Acquisition
SCD	Sudden Cardiac Death
SD	Standard Deviation
SNR	Signal-to-Noise Ratio
STEMI	ST-Elevated Myocardial Infarction
SPECT	Single Photon Emission Computed Tomography
SSFP	Steady-State Free Precession
SVD	Singular Value Decomposition
T_1	Longitudinal or spin-lattice relaxation time constant

T_1w	T_1-weighted
T_2	Transverse or spin-spin relaxation time constant
T_2w	T_2-weighted
T_2*	Transverse or spin-spin relaxation time constant in the presence of static magnetic field inhomogeneities
TE	Echo Time
TI	Inversion Time
TIMI	Thrombolysis in Myocardial Infarction
TR	Repetition Time
TTC	TriphenylTetrazolium Chloride
UTE	Ultrashort TE
VAs	Ventricular Arrhythmias
YLDs	Years of healthy life Lost to Disabilities

ACKNOWLEDGEMENTS

I would like to express my gratitude to my supervisor Dr. Rohan Dharmakumar. I'm grateful that he directed me into wide spectrum of MRI. His emphasis on the impact of research has always been a guideline for me to evolve unrealistic ideas into clinical applications. He has provided me with endless research resources to my research and encourages me when I'm facing challenges. This journey with Dr. Dharmakumar has inspired me tremendously and equipped me with solid tools for tackling fundamental questions. I would also like to extend my gratitude to my committee co-chair Dr. Debiao Li, committee members Dr. Holden Wu and Dr. Albert Thomas, and ex-members Dr. Peng Hu and Dr. Behzad Sharif for their advice and guidance in my qualifying exam and for this dissertation.

I'm also deeply thankful for Dr. Hsin-Jung Yang for his mentorship, collaboration and support for my research projects. My graduate colleagues, Xinming Guan, Eric Johnson and Yuheng Huang for their friendship, and sharing thoughts, brainstorming, and generous help on my projects. In addition, I would like to thank people who went along from Biomedical Imaging Research Institute (BIRI) at Cedars Sinai Medical Center to Krannert Cardiovascular Institute, Dr. Richard Tang, Dr. Behzad Sharif, Dr. Khalid Youssef and Ghazal Yoosefian, who have been supporting me in research, or life, or both along my whole PhD journey. I would express my appreciation to the entire group in BIRI where I met a lot of talents. Special thanks to all the members in contributing to a productive research environment including but not limited to Drs. Debiao Li, Ivan Cokic, Anthony G. Christodoulou, Zhaoyang Fan, Yibin Xie and Hui Han, the support research staff Laura Smith, Ed Gill and Irene Lee from imaging core, visiting scholars Drs. Guan Wang, Ting Liu and Yinyin Chen, and my fellow graduate students and friends Nan Wang, Sen Ma, Yuhua Chen, Pei Han, Tianle Cao, Zhehao Hu, Chaowei Wu. I would also

express my gratitude to the group in Krannert, supporting me overcome the challenges in transitioning institutions and setting up the lab during difficult COVID times including but not limited to faculties (Drs. Shing Fai Chan, Keyur Vora, Zhenhui Chen, Gabriel Groionu) for exchanging insightful thoughts in my research, supporting research staff Glen A. Schmeisser in providing high quality pathohistologic slides with countless iterations to my customization, administrators Amy L. Carlile, Garrett W. Hunter, Linda Altmeyer and Michele Diann Schlegelmilch for taking care of extra administrative works in time of transitioning and communicating with my home school.

My sincere thanks also go to the Siemens support team (Dr. Xiaoming Bi and Dr. Fei Han) for helping me in pulse sequence developments. I would also like to thank my collaborators from Lawson Health Research Institute (Dr. Frank S. Prato, Jane Sykes, John Butler, Heather Biernaski), University of Wisconsin, Madison (Dr. Scott B. Reeder and Dr. Diego Hernando), University of Edinburgh (Dr. Sotirios Tsaftaris, Haochuan Jiang, Agisilaos Chartsias) and University of Oxford (Dr. Mayooran Shanmuganathan and Qiang Zhang).

I would like to express appreciation to my boyfriend Zhiyang Wang, who supported my decision to pursue my self-development for PhD and continued supporting me by giving me time and space in doing research, encouraging me though all the ups and downs in life. I also would like to extend my thanks to Peiwei Chen for numerous study sessions in exchange of thoughts in research and life, and all my friends I made during my PhD journey including but not limited to Leo Yang, Shizheng Zhang, Suisui Wang, Terry Kirts and my old friends including but not limited to Yanjie Yang, Chenxing Sun, Xiaoxuan Lin, Gang Liu, who made my PhD life more colorful and I wish to keep our friendship for the rest of our lives.

My deepest gratitude goes to my parents Jianmin Zhang and Qin Guo for their unconditional love and support to me. They are my believers and always leave me spaces to explore the possibilities of my life. I wasn't always the advocate of my father when I was younger, but in a hindsight, I started to resonate with him and truly appreciate the unparallel love he has for me. I would like to thank my mother for her tenacity in supporting the family through difficult times. My thanks also extend to my brother Xinrui Zhang, for how much he has grown up and starts to hold responsibility to the family.

VITA

Education:

- M.S., Biomedical Imaging, University of California, San Francisco (2016)
- B.M., Basic Medical Sciences, Zhejiang University, China (2015)

Journal Publications:

- **Xinheng Zhang**, Hsin-Jung Yang, Xingmin Guan, Rohan Dharmakumar. A Novel Approach in Chronic Myocardial Infarction Characterization: The Heterogeneity in Native T1 Mapping. (In Preparation)
- **Xinheng Zhang**, Hsin-Jung Yang, Xingmin Guan, Behzad Sharif, Anthony Christodoulou, Debiao Li, Rohan Dharmakumar. Moton-resolved, non-ECG gated, Free-breathing 3D Low-rank Tensor Based Reconstruction for Hemorrhagic Myocardial Infarction Characterization. (In Submission)
- **Xinheng Zhang**, Hsin-Jung Yang, Rohan Dharmakumar. Influence of Spatial Resolution on T2*-based Detection of Intramyocardial Hemorrhage. J Cardiovasc Magn Reson. (In Review)
- Khalid Youssef, **Xinheng Zhang**, Ghazal Yoosefian, Yinyin Chen, Shing Chan, Hsin-Jung Yang, Keyur Vora, Andrew Howarth, Andreas Kumar, Behzad Sharif, and Rohan Dharmakumar. Enabling Reliable Visual Detection of Chronic Myocardial Infarction with Native T1-based CMR Using Data-Driven Native Contrast Mapping. Radiology: Cardiothoracic Imaging. 2024; 6(4)
- Yuheng Huang, Xingmin Guan, **Xinheng Zhang**, Ghazal Yoosefian, Hao Ho, LiTing Huang, Hsinyao Lin, Greg Anthony, Hsu-Lei, Lee, Xiaoming Bi, Fei Han, Shing Fai Chan, Keyur Vora, Behzad Sharif, Debiao Li, Hui Han, Anthony Christodoulou, Rohan Dharmakumar, Hsin-Jung Yang. Myocardial iron imaging in HMI with free-breathing, ungated whole heart, high-dynamic-range cardiac quantitative susceptibility mapping (HDR-QSM). Radiology: Cardiothoracic Imaging. (In Press)
- Xingmin Guan, Hsin-Jung Yang, **Xinheng Zhang**, Richard Tang, Anthony G Christodoulou, Debiao Li, Rohan Dharmakumar. Fully ungated, free-breathing 3D high-resolution T2* mapping for imaging intramyocardial hemorrhage. (In Review)
- Xingmin Guan, **Xinheng Zhang**, Hsin-Jung Yang, Rohan Dharmakumar. On the loss of image contrast in double-inversion-recovery prepared T2* MRI of Intramyocardial hemorrhage. Magn Reson Imaging. 2023 Nov 21: 125-132.
- Xingmin Guan, Hsin-Jung Yang, **Xinheng Zhang**, Nan Wang, Hui Han, Richard Tang, Zhehao Hu, Khalid Yousef, Keyur Vora, Anthony G Christodoulou, Debiao Li, Behzad Sharif, Rohan Dharmakumar. Fully Ungated, Free-Breathing, Off_Resonance Reduced, High-Resolution, Whole-Heart Myocardial T2* Mapping at 3T within 5 Minutes. Magn Res Med. 2024;1–15
- Yinyin Chen, Hang Jin, Xingming Guan, Hsin-Jung Yang, **Xinheng Zhang**, Zhenhui Chen, Shing Fai Chan, Dhirendra Singh, Nithya Jambunathan, Khalid Yousef, Vora Keyur, Gabi

Gruionu, Glen Schmeisser, Richard Tang, Mengsu Zeng, Rohan Dharmakumar. Detecting Hemorrhagic Myocardial Infarction with 3T CMR: Insights into Spatial Manifestation, Time-dependence and Optimal Acquisitions. JACC Cardiovasc. Imaging.

- Antje Bischof, Nico Papinutto, Anisha Keshavan, Anand Rajesh, Gina Kirkish, **Xinheng Zhang**, Jacob M. Mallott, Carlo Asteggiano, Simone Sacco, Tristan J Gundel, Chao Zhao, Adam Santaniello, Alyssa H. Zhu, Jeremy Juwono, Carolyn J. Bevan, Riley M. Bove, Elizabeth Crabtree, Jeffrey M. Gelfand, Douglas S. Goodin, Jennifer S. Graves, Ari J. Green, Jorge R. Oksenberg, Emmanuelle Waubant, Michael R. Wilson, Scott S. Zamvil, University of California, San Francisco MS-EPIC Team, Bruce A. C. Cree, Stephen L. Hauser, Roland G. Henry. Spinal Cord Atrophy Predicts Progressive Disease in Relapsing Multiple Sclerosis. Annals of Neurology. 2022; 91:268-281
- Xingmin Guan, Yinyin Chen, Hsin-Jung Yang, **Xinheng Zhang**, Daoyuan Ren, Jane Sykes, John Butler, Hui Han, Mengsu Zeng, Frank S Prato, Rohan Dharmakumar. Assessment of intramyocardial hemorrhage with dark-blood T2* weighted cardiovascular magnetic resonance. J Cardiovasc Magn Reson (2021) 23:88
- Qiang Zhang, Matthew K Burrage, Mayooran Shanmuganathan, Ricardo A Gonzales, Elena Lukaschuk, Katharine E Thomas, Rebecca Mills, Joana Leal Pelado, Chrysovalantou Nikolaidou, Iulia A Popescu, Yung P Lee, **Xinheng Zhang**, Rohan Dharmakumar, Saul G Myerson, Oliver Rider, Oxford Acute Myocardial Infarction (OxAMI) Study, Keith M Channon, Stefan Neubauer, Stefan K Piechnik, Vanessa M Ferreira. Artificial Intelligence for Contrast-Free MRI: Scar Assessment in Myocardial Infarction Using Deep Learning–Based Virtual Native Enhancement. Circulation. (2022) 146:1492-1503

Selected Conference Publications:

- **Xinheng Zhang**, Hsin-Jung Yang, Xingmin Guan, Behzad Sharif, Antony Christodoulou, Debiao Li, Rohan Dharmakumar. Motion-Resolved, Non-ECG gated, Free-Breathing 3D Low-Rank Tensor Based Reconstruction for Hemorrhagic Myocardial Infarction Characterization. SCMR 2023.
- **Xinheng Zhang**, Hsin-Jung Yang, Rohan Dharmakumar. Influence of Spatial Resolution in T2* maps of Intramyocardial Hemorrhage. ISMRM 2022.
- **Xinheng Zhang**, Hsin-Jung Yang, Richard Yang, Rohan Dharmakumar. Magnetization Transfer Contribution to Balanced SSFP Imaging Contrast in Chronic Myocardial Infarction. ISMRM 2020.
- **Xinheng Zhang**, Hsin-Jung Yang, Guan Wang, Ivan Cokic, Qi Yang, Sotirios A Tsaftaris, Rohan Dharmakumar. Automatic Detection of Myocardial Scar in Native T1 Maps at 3T from Patients with Prior Myocardial Infarction. SCMR 2019.
- Lin Hua Jiang, Mao Ye, Wei Yang, Justin Ainscough, Alicia Sedo, **Xinheng Zhang**, Xiangnan Zhang, Zhong Chen, Xiao-Ming Li, David Beech, Asipu Sivaprasadarao, Jianhong Luo, Xupang Xu, and Xin Li. TRPM2 channel deficiency prevents delayed cytosolic Zn2+ accumulation and after transient global ischemia. Cell Death & Disease. 2014 Nov 27;5:e1541. doi: 10.1038 /cddis.2014.494.

CHAPTER 1: INTRODUCTION

1.1 Significance of Cardiovascular Disease

Cardiovascular disease (CVD) is the leading cause of morbidity and mortality in the world, accounting for 19.9 million deaths a year [1]. In the United States, 127.9 million adults are reported to have some form of CVD, and the total cost of treating CVD was astonishingly over $422 billion. CVD has accounted for 930 thousand deaths in the United States per year, amounting to one death every 34 seconds.

Coronary heart disease (CHD), also known as coronary artery disease (CAD) is the leading cause of deaths (40.3%) within CVD, causing 375,476 deaths per year in the United States. Someone will have a myocardial infarction (MI) approximately every 40 seconds. Due to current advances in diagnosing, treating and managing CHD patients, from 2011 to 2021, the annual death rate attributable to CHD has declined 15%. However, the actual number of deaths still increased 0.05%, and Years of healthy life Lost to Disabilities (YLDs) witnessed 0.7% increase [2]. It remains as one of the largest problems in the field of healthcare for chronic CHD patients for their long-term survival and quality of life.

1.2 Myocardial Infarction (MI)

CAD emanates from narrowing of coronary artery. If this is accompanied by sudden obstructions for a prolonged period, it can result in irreversible changes such as myocardial cell death and necrosis [3]. Myocardial Infarction (MI), colloquially known as heart attack, is caused by significant or complete impedance of blood flow and oxygen from coronary artery that supplies to the myocardium [4]. Myocardial infarction may be “silent” and go undetected, or it could be a catastrophic event leading to hemodynamic deterioration and sudden death [5].

1.2.1 Therapy for MI and Reperfusion Injury

Timely reperfusion of MI related artery by thrombolytics or percutaneous coronary intervention (PCI) can significantly reduce morbidity and mortality in patient suffering from ST-elevation myocardial infarction (STEMI) [6–12]. Despite enormous progress in its diagnostics and therapy, MI is still one of the leading causes of death for over 50 years. In acute atherothrombotic MI (type 1 MI), cardiomyocyte necrosis evolves as a wavefront within an area at risk. Early reperfusion treatments emerged as life-saving therapy, the wavefront of necrosis and saving salvageable myocardium, reducing final infarct size, diminishing risk of HF, arrhythmia, and death [13–15]. However, the process of restoring blood flow to the ischemic myocardium can induce ischemia-reperfusion (I-R) injury [16], which can accentuate the injury and contribute to MACE.

1.2.2 Classification of Reperfused MI

Many scores and classifications have evolved for acute MI to help with patient care and research: STEMI vs non-STEMI, the Thrombolysis in Myocardial Infarction (TIMI) risk score, the History, Electrocardiography (ECG), Age, Risk factors, Troponin (HEART) score, and the Killip classification. Unlike those well-established classifications and scores relying on clinical parameters, the new consensus from the Canadian Cardiovascular Society Classification (CCS) incorporates tissue-level changes and exploits the predictive power of tissue damage, enabling development of future tissue-directed therapies [17]. From the CCS consensus, four stages of progressively worsening myocardial tissue injury are identified: 1) aborted MI (no/minimal myocardial necrosis); 2) MI with significant cardiomyocyte necrosis but without microvascular injury; 3) cardiomyocyte necrosis and microvascular dysfunction leading to microvascular obstruction (MVO, the “no-reflow” phenomenon within the infarct zone); and 4) cardiomyocyte and microvascular necrosis leading to reperfusion hemorrhage. Each stage reflects the

progression of tissue pathology of myocardial ischemia and reperfusion injury from the previous stage. Clinical studies have shown that as an injury progresses, myocardial remodeling worsens, and adverse clinical outcomes increases. Notably, microvascular injury is of particular importance, with the most severe form (hemorrhagic MI) leading to MI expansion and risk of mechanical complications, potentially facilitating risk stratification in MI patients, and laying the foundation for development of novel, injury stage-specific and tissue pathology-based therapies for MI.

1.2.3 Microvascular Injury in Reperfused MI

Myocardial necrosis is not the only form of tissue damage that contributes to acute MI. Studies have been concluded that myocardial edema occurs concomitantly and can precede myocardial necrosis [18]. Microvascular injury can also be observed and result in MVO [19] and intramyocardial hemorrhage (IMH) [20–22]. MVO and IMH are closely associated with ischemic reperfusion injury. MVO leads to decreased or fully impaired microvascular blood flow despite revascularized culprit epicardial coronary artery [16, 20, 21]. This can possibly further result in IMH, featuring erythrocytes extravasation through severely damaged endothelial walls into the interstitial space [20, 22].

Both MVO and IMH are independent predictors of major adverse cardiac events (MACE) [26–31]. The presence of MVO has been a powerful predictor of functional recovery, left ventricle (LV) remodeling and chronic heart failure (CHF) [32–35]. While IMH has emerged as an important predictor of adverse long-term outcomes in patients treated with reperfusion therapy for MI [22,36–39]. Based on CCS classification of acute atherothrombotic MI, stage III and stage IV of MI (severest) are defined as MI with significant cardiomyocyte necrosis, MVO and IMH due to mass extravasation and gross microvascular injury [22,40], suggesting that

hemorrhagic MI is the most damaging form of setting of revascularized acute MI. The incidence of MI patients with microvascular injury present is shown to be 2-4 times the MACE rate of those without microvascular injury (Figure 1.1).

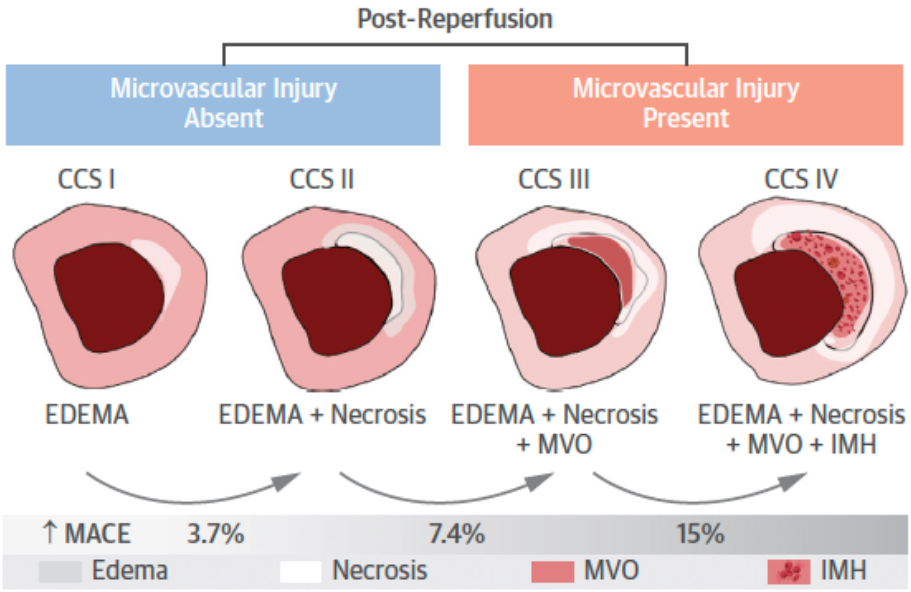


Figure 1.1 Summary of CCS Classification of Stages of Acute Reperfused Myocardial Infarction Based on Tissue Injury. MACE increased for 2-4-fold in CCS stage III and CCS stage IV, when microvascular injury is present. Adopted from [38].

For MI patients who underwent PCI, MVO occurred in about 50% of cases [41], while IMH occurred in 25% - 40% of patients. A large meta-analysis reported an incidence of 39% of MI patients with IMH [26,27,42,43]. In acute MI, IMH is a mediator of inflammation, directly contributing to myocardial and microvascular damage. Another feature of IMH is that iron within the MI zone peaks during the subacute phase of MI and remains elevated for nearly a decade [44,45]. Such deposits facilitate the perpetual recruitment of macrophages for months and years during the chronic phase of MI [44,46].

Specifically, IMH results in ferric iron crystals within MI tissue, triggering a sustained pro-inflammatory response, and contributes to adverse remodeling and a unique inflammatory

pathway toward HF [46,47]. It has also been proposed as a mechanism for generation of ventricular arrhythmias (VAs) [48,49]. As hemorrhagic MI evolves, fatty degeneration of cardiac tissue driven by macrophage activation, lipid peroxidation, foam cell formation and ceroid production is observed [45]. Fatty metaplasia of infarcted scars has been identified as a driver of increased VAs risk [50]. The next section addresses the pathophysiology of MI from acute toward chronic phase.

1.3 Pathophysiology of Reperfusion Injury and Temporal Progression of MI

Prompt restoration of culprit coronary artery (lasting hours to days: Figure 1.2) has been a major advance in patient treatment and has reduced immediate death from acute MI with partial recovery of LV function during the sub-acute phase of MI (lasting days to weeks: Figure 1.2). However, adverse remodeling of the LV of the heart in the chronic phase of MI (lasting months to years: Figure 1.2) often results in HF, which increases mortality.

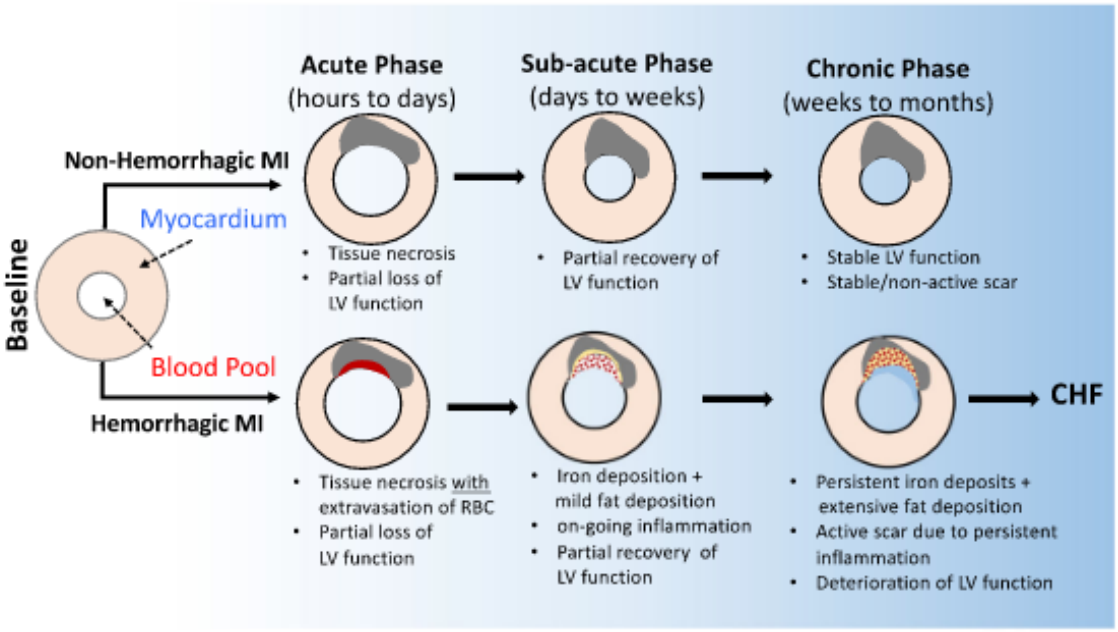


Figure 1.2 An overarching model of how hemorrhagic infarction promotes chronic heart failure via fat deposition. Following MI, compensatory remodeling promotes the partial recovery of LV function in the early weeks following the index event. Hemorrhagic MI promotes the formation of fat deposition and

functional losses, which define CHF. While non-hemorrhagic MIs stabilizes the infarct zone leading to stable functional remodeling in the chronic phase of MI. Adopted from [45].

Evidence indicates that hemorrhagic MIs lead to chronic iron deposition and perpetuate for months and years to come [44,46]. Current evidence also suggests that the macrophages recruited to the site of iron-rich MI take up the iron and are polarized into a pro-inflammatory phenotype. And the iron-laden macrophages can transform into foam cells when they oxidize lipids encountered in their vicinity to form ceroids (lipo-pigments) within the cells [51,52]. Further, in the chronic phase of MI, fat deposition within the infarction zone is a common finding [53,54] and is known to significantly impair cardiac energetics, cardiac function [55,56], and adverse outcomes including CHF in post-MI patients [57].

1.3.1 Acute Phase (First Few Hours to Days Post Reperfusion)

While recanalization of the occluded coronary artery is broadly known to reduce the morbidity and mortality of the patients suffering from STEMI [6–12], the success of reperfusion is often diminished by a persistent post-procedural reduction of tissue perfusion at a microvascular level [19,58]. The sudden restoration of blood flow can lead to microvascular injury, which results in the obstruction of myocardial microcirculation (MVO). This injury can further lead to the rupture of weakened vessels within the necrotic tissue, causing blood to leak into the myocardial tissue (IMH). The area of hemorrhage is characterized by the presence of red blood cells (RBCs) outside of blood vessels, within the interstitial spaces of the necrotic myocardium. This can lead to an increase in local pressure and further damage to the surrounding myocardial tissue.

When blood components leak outside of the vascular compartment, an inflammatory reaction is initiated, drawing neutrophils and macrophages to the injury site. These cells begin to

phagocytose the RBCs and debris, a critical process in resolving the hemorrhage. However, this process may also intensify tissue damage by contributing to edema during the acute phase of a MI. As RBCs break down, hemoglobin is released and undergoes oxidation, which oxidizes to oxyhemoglobin, and eventually to methemoglobin. This conversion contains unique properties that can be detected by magnetic resonance imaging (MRI) [59]. The acute phase of MI is also characterized by the loss of myocytes and the extracellular connective tissue matrix [60,61]. Inflammatory cells invade the infarcted myocardium, which is essential for removing necrotic debris and facilitating wound healing [61].

1.3.2 Sub-Acute Phase (Days to Weeks)

The continued breakdown of hemoglobin leads to the formation of hemosiderin, a storage form of iron, which engages the ingestion of macrophages [37,59,62]. Hemosiderin can persist in the tissue for weeks to months and is detectable on MRI as a signal of hemorrhagic remnants. Alongside the clearing of the hemorrhage, myofibroblasts migrate to the area, laying down collagen fibers that begin the process of collagen network reconstruction [60]. This scar tissue replaces the necrotic myocardium and is less elastic and contractile than the original tissue, affecting the overall function of the heart.

1.3.3 Chronic Phase (Months to Years)

Over time, the scar tissue further matures, leading to changes in the structure and geometry of the heart, known as LV remodeling. This remodeling is characterized by LV chamber enlargement and significant reduction in LV ejection fraction (LVEF), which can potentially lead to HF. The presence of hemosiderin (iron) and the structural changes associated with scar formation can lead to chronic complications, including arrhythmias, due to the disruption of the normal myocardial conduction pathways, and HF, as the cardiac function is compromised. Iron deposition in

myocardium in the form of ferritin and hemosiderin promotes the recruitment of unpolarized macrophages and oxidizes the lipids in its vicinity; the oxidized lipid and iron are taken up by the macrophages, which promote their polarization into a pro-inflammatory state and transform into foam-cells. The foam cells produce ceroids and destabilize the lysosomes and drive foam cell apoptosis, the remnants of which participate in fat deposition, with the released iron recycled to enter the pathway, perpetuating to continually support inflammation and growth of the fat depot [45,51,52]. Fat deposition within the infarction zone is a common finding as studies have shown it is evident at week 8, and substantially increased between week 8 and month 6 [55,57,63]. 84% of chronic MI patients was found with some mature fat tissue [55]. The fat deposition is known to significantly impair cardiac energetics, function and adverse outcomes including CHF in post-MI patients [64,65].

1.4 Existing Methods for MI Detection and Characterization of MI

1.4.1 Invasive techniques

Current invasive techniques such as endomyocardial biopsies can provide a qualitative and quantitative assessment of tissue components such as myocardial fibrosis, iron deposition, fat infiltration etc. For instance, tissue biopsies enable qualitative macroscopic assessment of myocardial fibrosis after Elastin Masson's Trichrome (EMT) staining [66] and quantitative absolute assessment of the collagen volume fraction (CVF) in tissue samples by quantitative morphometry with picrosirius red that specifically stains fibrillar collagen under polarized light [67–69]. Although this technique offers an absolute quantification of fibrosis in myocardial samples [70], it presents three clear disadvantages: 1) it necessitates invasive biopsy procedures; 2) the accuracy of biopsy is limited by sampling error in the case of localizing fibrosis [71,72]; 3) and it is not possible to ascertain fibrotic involvement across the entire LV.

1.4.2 Non-invasive techniques

There are several non-invasive imaging approaches that can detect and characterize infarcted myocardium, including echocardiography, single photon emission computed tomography (SPECT), positron emission tomography (PET), Computed Tomography (CT) and MRI. Echocardiography is an imaging technique that uses ultrasound to examine the heart. It is widely used to rapidly acquire measurements of LV mass and monitor systolic and diastolic function [73,74]. Given the relation between hypertrophy, dysfunction, and fibrosis, echocardiography has been extended to the assessment of fibrosis in patients. However, the accuracy and the reproducibility of this technique is limited [75,76]. SPECT is a nuclear medicine tomographic imaging technique that uses gamma rays to generate signal. It is widely used for detecting perfusion changes of myocardium to diagnose ischemic heart diseases. Similarly, PET is another nuclear medicine tomographic imaging technique that is based on gamma rays emitted from annihilation between positron and electron. It is the gold standard for cardiac viability assessment [77–79]. However, both SPECT and PET are limited by low spatial resolution, which results in poor sensitivity for detecting subendocardial MI [80]. Cardiac CT (CCT) has emerged as a useful modality in patients as low-intermediate pre-test probability of CAD [81]. CCT can detect MI with accurate visualization of infarct size by late iodine enhancement (LIE) techniques in animal model [82,83] and humans [84] with relatively good accuracy [84–86]. However, its relatively low image contrast limits it from detecting small infarctions [87].

MRI is a non-invasive imaging technology that uses strong magnetic field, radio waves, and field gradients to generate detailed images of the organs and tissues within the body. Clinical MRI relies on the magnetic properties of hydrogen nuclei (^{1}H) mostly in water molecules, which are abundant in the human body. Unlike echocardiography, MRI is not limited by acoustic window. It also offers significantly higher spatial and temporal resolution than nuclear medicine

modalities [88]. Additionally, MRI does not use ionizing radiation, which is major advantage over other imaging modalities such as CT or nuclear medicine [89]. More importantly, MRI offers better myocardial tissue characterization over other imaging modalities for quantifying the infarct extent, hemorrhage, iron deposits, MVO, fat deposition, among others [88]. In summary, MRI offers several advantages: detailed tissue characterization, lack of radiation, and comprehensive functional and anatomical assessment capabilities, making it superior choice for the characterization of MI. Given these advantages, we will employ MRI throughout this dissertation to develop myocardial tissue characterization in the setting of MI.

1.4.3 Cardiac MR

Cardiac MRI (CMR) is a noninvasive, tomographic, non-ionizing technique widely used numerous forms of cardiovascular disease, including MI [90–93]. CMR provides comprehensive assessment of myocardial anatomy and function with unparalleled levels of accuracy and reproducibility. It has been gold standard as a non-invasive method that allows comprehensive assessment of MI. For examining tissue damage associated with MI the following CMR techniques for characterizing various components of MI:

1.4.3.1 Gadolinium-enhanced CMR

Late Gadolinium Enhancement (LGE) imaging typically involves the acquisition of inversion-recovery based T1-weighted (T1w) images during the passage of an intravenously administered Gadolinium (Gd)-based contrast agent (GBCA) within the tissue of interest [94]. The delayed enhancement region is assessed based on large relative signal intensity differences between hyper-enhanced (focally scarred myocardium) and low signal intensity region (normal myocardium). To achieve this normal myocardium is to an inversion time to “null” the normal

myocardial signal so as to appear dark in the final image relative to the bright signal of the infarcted myocardium.

LGE has become a first-line non-invasive exam for the etiologic assessment of new onset myocardial dysfunction [95–97]. It provides prognostic information (transumural extent of MI, MI size etc.) that could be used to define more appropriate therapeutic strategies for various cardiac conditions including ischemic and non-ischemic cardiomyopathies, hypertrophic cardiomyopathy, and cardiac amyloidosis [98–106]. LGE has been widely validated in determining MI from acute to chronic phase with high accuracy and reproducibility [98,107–112].

Other than the concerns over long-term effect of GBCA deposition in the brain and other organs, and its contraindications in patients with moderate-to-severe renal dysfunction, studies have shown that LGE is capable of identifying replacement fibrosis and gray zone (a mixture of viable myocytes and collagen strands in myocardium) [103,113–115], in chronic MI subjects. The late enhancement is caused by modifications of the contrast distribution space as well as wash-in and wash-out kinetics of the contrast into interstitial space or extra-cellular matrix. Thus, measuring late enhancement regions are a reflection of the size of the extracellular matrix, which is usually depicted as myocardial fibrosis, but it may also expand due to other pathological conditions, such as edema, inflammation or fat deposition [116]. Therefore, those characteristic tissue substrates from identifying hyper-enhanced region may be omitted using LGE.

1.4.3.2 Native T1 mapping

T1 relaxation is the process by which the net magnetization (M_z) returns to its initial maximum value (M_0) along the magnetic field (B_0). This process is commonly modelled as a simple exponential with T1 as a first-order time constant:

$$M_z = M_0 \left(1 - e^{-\frac{t}{T1}}\right) \tag{1.1}$$

Native T1 mapping can be a substitute LGE, which enables direct myocardial signal quantification. Studies have shown that it is as sensitive and specific as LGE in identifying LGE in acute MI, based on the substantially different T1 values between MI and remote myocardium, both in large animal models and patients [117–121]. The most widely used T1 mapping sequence is the Modified Look-Locker Inversion-recovery (MOLLI) sequence [119,122–125]. The MOLLI sequence is comprised of three successive ECG-triggered Look-Locker (LL) experiments with each of them with 3, 3, and 5 single-shot balanced Steady-State Free Precession (bSSFP) readouts respectively (Figure 1.3) [122]. T1 values are thus fitted by a three-parameter nonlinear curve fitting:

$$y = A - B \exp\left(-\frac{t}{T1^*}\right), \tag{1.2}$$

where y denotes signal intensity, and T1* corresponds to the apparent, modified T1 in an LL experiment. T1 is calculated from the resulting parameters T1*, A, and B by applying the LL correction [122]:

$$T1 = T1^* \left(\left(\frac{B}{A}\right) - 1\right), \tag{1.3}$$

In MOLLI acquisition, a single-slice T1 map can be obtained in high-resolution in a single breath-hold (< 20s).

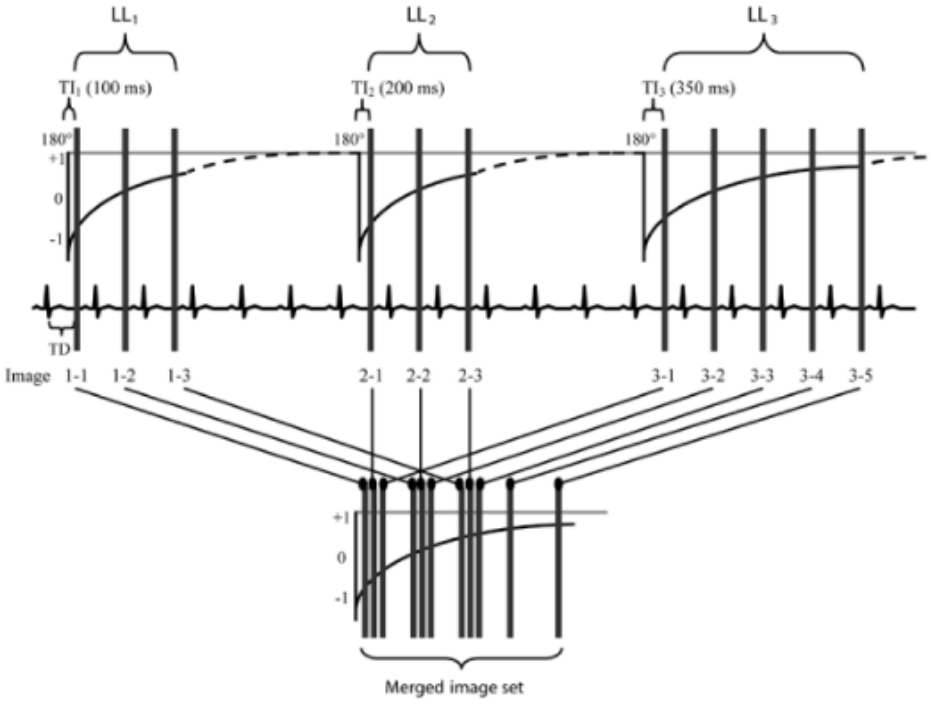


Figure 1.3 MOLLI pulse sequence scheme. Vertical bars represent image acquisition. Dashed lines represent undisturbed signal recovery. For T1 value calculation, the images were regrouped into one data set according to their effective T1. Adopted from [122].

There is substantial evidence for native T1 mapping techniques to diagnose and prognosticate acute and chronic MI [126–130]. In a recent study of 30 patients with acute ST-elevation MI and chronic MI respectively, native T1 mapping was able to differentiate between viable and non-viable myocardium in patients with chronic MI with a sensitivity and specificity of 88% and 88% respectively [131]. For acute MI, the T1 mapping technique has shown to offer comparably good diagnostic performance due to existence of edema [132]. For chronic MI, this technique demonstrates a complex response to different types of tissue substrates, which I will elucidate in the later section.

1.4.3.3 T2 CMR

T2 relaxation is the process by which the transverse components of magnetization (M_{xy}) decays in the transverse plane following excitation. It is considered to follow first order kinetics, resulting in a simple exponential decay with the time constant T2 [133]:

$$M_{xy} = M_0 e^{-\frac{t}{T2}}, \tag{1.4}$$

where M_0 is the equilibrium magnetization (normally considered as 1), and t is echo time.

T2 CMR imaging is commonly used to assess myocardial inflammation and edema, which is prevalent in acute MI. These source images can be acquired by a Turbo-Spin-Echo (TSE) sequence with varying echo time [134], a bSSFP or spoiled GRE sequence with an initial T2 preparation module [135–138], or a sequence scheme combines spin echo excitation with GRE readout [139–141], or a pulse sequence combining TSE with short-inversion-time (STIR) and blood signal nulling [142].

T2 mapping is generally performed by pixel-wise exponential fitting of T2 decay curve of a series of T2w images at different echo times (TEs):

$$y = Ke^{-\frac{TE}{T2}}, \tag{1.5}$$

Where y represents signal intensity and K is a fitting constant. By characterizing tissue on the basis of T2, reliance on subjective assessments of signal intensity can be eliminated. Both T1 and T2 CMR have been shown to be sensitive to multiple MI substrates, e.g. edema, fibrosis, and iron deposition. T2 mapping has been proven to be the first-line technique in edema characterization and quantification of acute MI [143]. Although T2 CMR has inferior sensitivity in the iron-rich region or hemorrhage compared to T2*-based techniques, T2 mapping is second

to T2*-based techniques of characterizing iron given its robustness against off-resonance artifacts [144–146].

1.4.3.4 T2* CMR

T2* relaxation is the represents the free-induction decay that can be measured using GRadient-Echo (GRE) sequences. It is common practice to define:

$$\frac{1}{T2^*} = \frac{1}{T2} + \gamma \Delta B_i, \tag{1.6}$$

where $\gamma \Delta B_i$ is the relaxation rate contributing to field inhomogeneities (ΔB_i) across a voxel but this is strictly only valid when the field inhomogeneity is Lorentzian. In CMR, myocardial T2* is measured using a 2D breath-held, ECG-triggered, segmented multi-gradient-echo (mGRE) sequence with images acquired at diastole. Similar to T2 mapping, the T2* mapping can be derived by fitting signal intensities at different TEs to a mono-exponential equation:

$$y = Ke^{-\frac{TE}{T2^*}}, \tag{1.7}$$

where y represents signal intensity, K is a fitting constant, T2* is the region of interest transverse relaxation time. T2* imaging has been validated to show its clinical utility in myocardial iron overload measurement [147–151] due to its paramagnetic nature. Similarly, IMH and its remnants are also found to be iron-rich from the deposition of hemoglobin and its metabolites [152], T2* CMR is also a preferred method for identifying and characterizing iron deposition from IMH [153–155].

1.4.3.5 Other techniques

Other emerging CMR techniques include the following: T1ρ [156–159], ultrashort TE (UTE) [160], Chemical Exchange Saturation Transfer (CEST) [161,162], diffusion [163–165] and

magnetization transfer (MT) [166–170] in MI tissue characterization has been investigated but clinical utility are under investigation. Table 1.1 summarizes the status of these methods.

Table 1.1 List of experimental techniques in MI characterization and its clinical studies.

CMR Techniques	Tissue Characterization	Clinical Status
T1rho	Depends mainly on macromolecular interactions in the tissue	One healthy volunteer study (n=10) [171] and One patient study with chronic MI (n=21) [172]
UTE	Short T2* of large molecules	A patient demonstration [173]
CEST	Myocardial viability: metabolic component creatine CEST (CrCEST); Biochemical information	One patient study (n = 16) [174]; One patient study in idiopathic inflammatory myopathy (n = 26) [175]
Diffusion	Apparent diffusion coefficient (ADC), requires minimal amount of fibrosis (20%) [176]	One patient study (n = 12) [177]; One study with 5 patients, introducing propagation angle (PA) [178]
MT	Interaction between bulk water protons and protons contained in macromolecules	One patient study (n = 5) [179]; One study with healthy volunteer [180]

1.5 Characterization of MI with CMR

Identifying the pathological characteristics of acute and chronic MIs is crucial for assessing the risk of MI patients developing serious cardiac outcomes, such as HF and sudden cardiac death (SCD). T1, T2, T2* pre-/post-contrast CMR now permit the routine spatial visualization of

quantitative changes in myocardium based on changes in tissue specific parameters. There is growing evidence that that hemorrhagic MI would induce multiple substrates on the heart from edema/inflammation, fibrosis/necrosis, MVO, IMH, fat deposition etc. (illustrated in Figure 1.4A), and they are independent predictors for adverse cardiac outcomes. These substrates composition changes over time after the initial onset of MI, which is summarized in Figure 1.4B. To have comprehensive tissue characterization, CMR is playing a pivotal role but it needs further development to image different substrate compositions according to the time after MI.

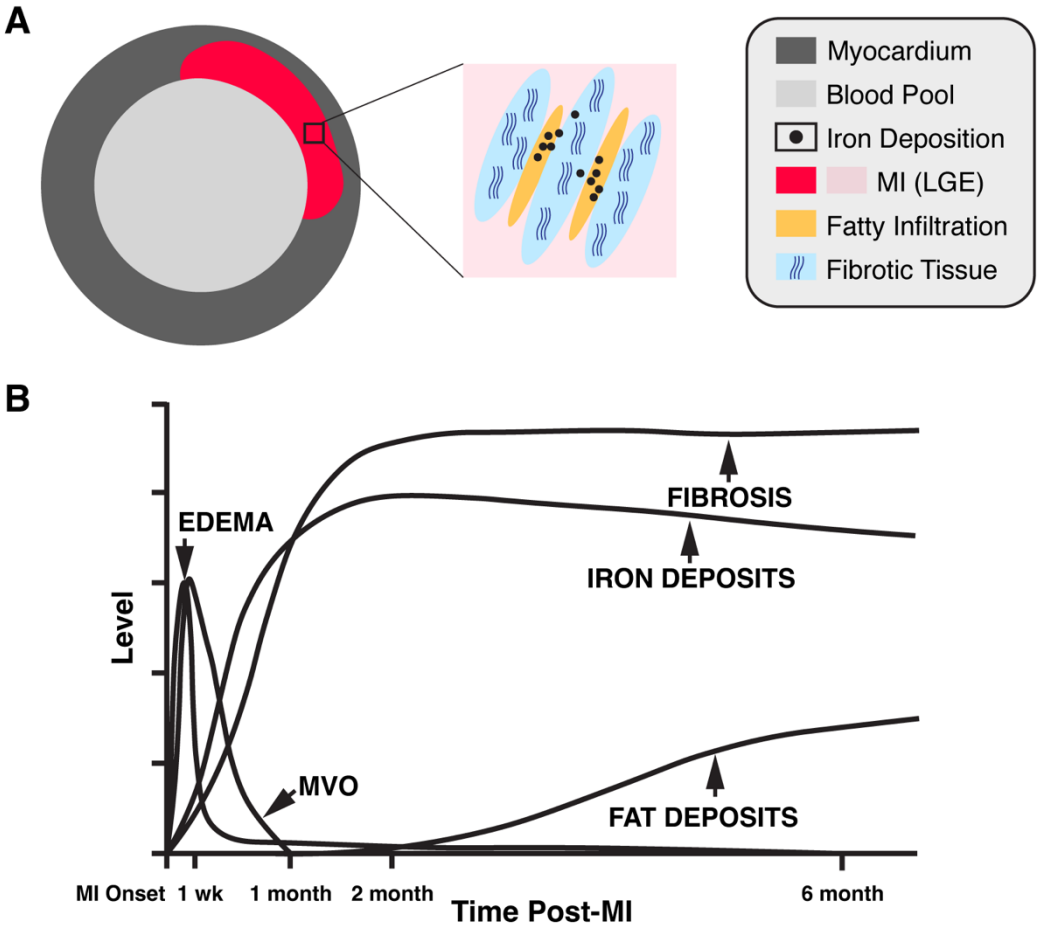


Figure 1.4 Illustration of MI, characterized by fibrotic tissue, fat and iron deposition and its development over time. **A)** The severest form of hemorrhagic MI is shown as relatively homogeneous region on LGE image, but the underlying substrates may be missed. **B)** Temporal evolution of key substrates (Edema *[181]*, MVO *[44]*, Fibrosis *[21,182]*, Iron deposits *[44]* and Fat deposits *[45,183]*) within MI.

1.5.1 Fibrosis/necrosis

The extent of fibrosis is often validated on 2,3,5-Triphenyltetrazolium chloride (TTC) staining or histological staining (e.g. EMT), which is invasive and not feasible in the clinical setting. On CMR, LGE imaging is used for quantifying infarct size in both acute and chronic MIs. However, the hyper-enhanced region identified in LGE as a hyper-intense region reflective of tissue necrosis in acute MI can consist of edema/inflammation or hemorrhage and fibrosis, iron, and fat deposition in chronic MI.

Following intravenous injection of Gadolinium, the contrast agent circulates through the capillaries in the myocardium, and it disperses into the interstitial space, achieving a dynamic equilibrium that enables the measurement of the extracellular volume (ECV). ECV mapping is determined by obtaining pre- and post-contrast T1 maps before (native T1 map) and after contrast media administration [143]. ECV agrees well with final infarct size revealed by LGE [184]. Although ECV mapping may address certain limitations inherent in late gadolinium enhancement (LGE) imaging, it is still influenced by the same factors that affect the measurement of MI size. Moreover, the detail with which ECV mapping can depict structures, or its spatial resolution, is naturally lower compared to that of LGE CMR [185].

Native T1 mapping has been applied to a number of cardiac conditions in both diffuse myocardial fibrosis [186–193] and replacement myocardial fibrosis [117,194]. Most studies found a significant increase in myocardial T1 values in cardiac diseases as compared with that in health control subjects. However, the magnitude of this increase was much lower than that found in myocardial edema, or amyloidosis and there was large overlap between diseased and normal groups. Moreover, whether the state-of-the-art MOLLI T1 mapping technique accurately reflects

replacement fibrosis in chronic MI characterization in the presence of fatty metaplasia remains to be further studied [195].

1.5.2 Microvascular Injury

1.5.2.1 Microvascular obstruction (MVO)

While the intracoronary injection of Thioflavin-S dye can clearly delineate MVO in excised hearts [19], it is impractical in the clinical setting. In CMR, MVO appears as a dark center within the brighter region of an infarct on LGE scans. This pattern occurs because the contrast agent does not penetrate the center of the infarct. T1 mapping could identify regions with lower T1 values encircled by areas with higher T1 values within the damaged tissue [196–198]. The decreased T1 values in MVO are likely due to the extravasation of iron-containing erythrocytes and myocardial hemorrhage in MVO [196,198,199].

Early Gadolinium Enhancement (EGE) and LGE techniques are being increasingly used to detect MVO [14,33,200–207]. MVO is detected as hypointense core within hyperintense infarcted territories at approximately 2-5 minutes following contrast administration on EGE images, while persistent or late MVOs are observed in LGE images at approximately 10-15 minutes following contrast administration. Studies have shown that MVO can be more accurately characterized by LGE, and is a stronger prognostic marker for MACE than MVO characterized by EGE [29]. Moreover, a steep contrast agent wash-out dynamics has made EGE imaging a more difficult to perform than LGE. On the other hand, EGE outperforms LGE in its sensitivity in small MVO measurement. This indicates that late MVO reflects a more severe form of microvascular injury, while early MVO may be more sensitive in depicting regions with reduced residual blood flow [43].

1.5.2.2 IMH and iron deposits

IMH is considered a severe form of MVO and follows MVO development in the infarct core [25,208,209] with a tendency to expand for several hours after PCI. Deoxyhemoglobin has paramagnetic effects that enable myocardial iron accumulation to be detected using T1, T2 and T2* CMR [145,152]. IMH is visually defined as a hypointense area in the center of a hyperintense zone within MIs.

As discussed in the previous section, T2*-based CMR is the most sensitive method for imaging IMH. However, given that the current T2* technique uses relatively low spatial resolution, its sensitivity to off-resonance artifacts, particularly in the lateral wall, as well as the strong influence of motion and blood flow, T2* CMR image quality can be suboptimal. Both T2*-weighted (T2*w) imaging and T2* can identify iron deposition with CMR, but quantitative T2* mapping is more preferred as it provides highly accurate and reproducible information with respect to iron content quantification. To quantify IMH volume, two different cut-offs are widely used: Mean minus two times standard deviation (Mean-2SD) and T2* <20 ms on T2* mapping [152,210]. T2* < 20 ms methods were initially adopted for iron-overloading conditions such as thalassemia and hemochromatosis but they have been shown to be less robust over different field strengths and noise level [146,211]. Recent studies have shown that Mean-2SD method is better choice for quantifying IMH at 3T [153].

An alternative to T2* imaging that has been extensively investigated is T2 imaging, as T2 images can be sensitive to IMH. Although T2 images often provide better image quality than T2* images, their sensitivity in the acute phase to IMH is compromised by the presence of edema [212]. However, T2 mapping can still be the alternative for IMH detection and characterization when T2* images are strongly deteriorated [213]. Because T1 is sensitive to the

degradation products of hemorrhage, some studies have also investigated the capacity to image hemorrhage with T1 CMR. These studies have shown that the opposite effects IMH and edema impose on T1. Thus, the sensitivity for detecting hemorrhage based on T1 after MI is often compromised [214].

1.5.3 Fat Deposition

Even though the mechanism of development of adipose tissue within myocardial infarctions is not thoroughly studied, fat infiltration within myocardial infarctions is a well-established phenomenon [215–219]. Studies have shown that nearly 80% of myocardial scars associated with chronic ischemic heart disease show fatty replacement [55,63,220]. The presence of intramyocardial fat has been identified as a substrate for arrhythmias that drive SCD [50,221–223] due to its lower electrical conductivity. The hydrogen nuclei (^{1}H) protons in long chain triglycerides of fat are shielded by a dense electron cloud, which are more effective than ^{1}H protons of water due to its highly electronegative oxygen atom pulling away the protective electron clouds. As a result, ^{1}H protons in fat are subjected to a slightly weaker local magnetic field compared to those in water, leading to a lower resonate frequency than nearby ^{1}H protons in water at about 3.3 parts per million (ppm) [224]. At 1.5T, this corresponds to an absolute frequency shift of approximately 210 Hz; and 420 Hz at 3.0T at body temperature [225–228]. There has been a variety of methods developed to isolate the undesirable influence of fat by suppressing fat signal or by quantifying fat fraction by separating fat signal based the chemical shift effect in MR imaging [219,229–233].

More specifically, to quantify fat signals, a class of approaches exploiting phase differences due to chemical shifts between water and fat signals were developed to separate fat from water signals. The Dixon imaging, a popular method in this category, was first introduced in 1984 and

utilized across a wide array of applications for water and fat signal correction [219]. In the 2-point Dixon method, two images are acquired at different TEs: one when water and fat signals are aligned in the same direction on the transverse plane (in-phase), and another when they point in opposite directions (out-of-phase). By adding or subtracting these in-phase and out-of-phase images, separate images of water and fat can be produced. This method was advanced by adding a third echo time [234,235] for B_0 inhomogeneity correction. Three-point Dixon approaches are now extensively employed for water and fat signal correction in numerous applications [236–240].

A more advanced multi-point iterative decomposition of water and fat algorithm called Iterative Decomposition with Echo Asymmetry and Least squares estimation (IDEAL) was described more recently and has been used extensively as a robust method [232,241]. The robustness of the method is established by the use of several arbitrary echoes from GRE readout for the iterative separation of water and fat signals by least squares estimation. Unlike other methods that consider fat signals as a single spectral peak, the IDEAL algorithm improves accuracy by accounting for the multiple spectral peaks present in fat signals [242]. Additionally, this multi-echo technique based on chemical-shift algorithm can also simultaneously evaluate the amount of iron by estimating T2* decay within the voxel [243].

The bSSFP readout was normally thought to be robust to off-resonance within a certain range. However, it introduces a characteristic frequency response featuring periodic nulls and pass bands. In bSSFP imaging, fat in adjunct pass bands will experience bulk phase offsets that change the expected constructive and destructive interference between fat and water components [244]. For example, the widely used native T1 mapping with bSSFP readout was shown to be subject to artifactual bias when there is a mixture of water and fat in the myocardium [245]. The

T1 bias will be additive or subtractive depending on whether the center frequency corresponds to the myocardium and fat being in-phase or out-of-phase, respectively. Instead of suppressing fat signal, some studies try to utilize the such property in bSSFP signal to improve fat and water decomposition [244]. The aspect of utilizing bSSFP signal in fat characterization is still under investigation.

1.5.4 Edema

In addition to microvascular injury resulting in plasma leakage into the interstitum, edema develops as a consequence of inflammatory responses in areas of acute MI. The post-MI edema formation assessed by both ex-vivo and in-vivo [246,247], has been shown to correlate with acute myocardial injury [13,248–253]. CMR offers the possibility of identifying areas of increased myocardial free water content or edema [139,143,246,254]. Nevertheless, there might be other factors affecting the edema-related post-MI CMR signal, such as changes in water fractions (protein-bound vs. free) [255] or the paramagnetic effect of hemoglobin denaturation in the presence of tissue hemorrhage [212]. CMR sequences for edema imaging are mostly based on T2 or T1.

Hyperintense zones on T2w CMR images are indicative of myocardial edema. By allowing the detection of edema post-acute ischemic injury [256], T2w CMR might help its discrimination from chronic MI [250,257]. Quantitative T2 mapping techniques overcome several limitations of T2w imaging and provides voxel-based tissue characterization which results in more accurate evaluation of myocardial edema [135]. T2 mapping has been validated against pathology for myocardial water content quantification in experimental MI models [135,139]. A comparative study employing 4 different edema measurements/sequences showed higher intra-observer and

inter-observer agreement and greater test-retest reproducibility in the quantification of edema using T2 mapping [258].

Longer T1 value is seen in water content/edema in T1 CMR as well [259–261]. Myocardial injury due to MI or inflammation increases water content, lengthening local T1 relaxation times [143]. Similarly, non-contrast T1-weighted MRI has been shown to be capable of quantifying the edema ex vivo [262] and detecting regions of edema of acute MI in vivo [56]. Quantitative T1 mapping is exploited to delineate the extent of edema, which agrees well with other measures [263–265].

1.6 Needs and Challenges in CMR for Characterizing MI

There are multiple challenges in CMR with respect to MI characterization. These challenges originate from the need for CMR to provide high quality images (high signal-to-noise ratio, SNR and spatial resolution) in the shortest possible time (faster acquisitions) to gather critical details (multiple key substrates) with sufficient accuracy while ensuring patient comfort. Each of these elements requires specific technological and methodological advancements to overcome inherent limitations and improve capabilities of CMR for MI patient management, cardiac outcome risk stratification and diagnosis.

1.6.1 Need for Fast, Comprehensive MI Characterization to Facilitate Patient Management

In conventional MRI acquisitions, redundant data is often acquired multiple times to overcome the limitations of motion. For example, in CMR, the heart beats in a regular pattern and the shape of the heart does not change much over time, while this information is captured in every k-space readout. Given this redundancy, current techniques aim to use the acquisition scheme more

efficiently so that MR signals can be acquired within shorter acquisition time, without compromising image quality.

Current CMR protocol possesses multiple limitations in MI characterization:

1) High demand for patients' breath-holding, which is difficult for patients with impaired cardiac function. Failure to perform breath-holding can lead to corrupted image quality and thus further impair the robustness in diagnosis or treatment plan in the clinical setting;
2) A lengthy CMR protocol results in logistical challenges for patients and clinical practitioners. Shorter acquisitions can increase imaging throughput, resulting in greater efficiency;
3) Artifacts could be introduced by irregular heartbeats and unsuccessful breathe-holdings between acquisitions in conventional 2D CMR protocol, lowering image quality; and
4) Conventionally, multiple 2D short-axis single-slice multi-contrast images need to be acquired for MI characterization (Cardiac function, necrosis/fibrosis, iron deposition, MVO etc.). However, this will result in extra work in image registration which can be difficult to perform a more slice-aligned and pixel-match analysis between different contrast.

1.6.1.1 Low-rank Tensor Framework

A low-rank tensor (LRT) reconstruction framework [266–271], which shows significant flexibility and promise for advancing free-breathing, non-ECG-gated, CMR for MI characterization, has been recently introduced. The LRT framework [267] leverages the relationship between the shape of the heart and its motion patterns over time within a

multidimensional framework. By doing this, it efficiently minimizes redundant information, enabling the continuous motion-resolved, free-breathing, 3D cardiac images without ECG synchronization.

In this framework, a cardiovascular image can be represented as a multidimensional function $I(\boldsymbol{x}, t_1, t_2, \dots, t_N)$ of spatial location $\boldsymbol{x}$ and N time dimensions $t_1, t_2, \dots, t_N$. Each time dimension in CMR typically corresponds to cardiac motion, respiratory motion, T1, T2, T2* relaxation etc. The image I can be represented in discretized form as an (N+1)-way tensor (or multidimensional array) $\boldsymbol{A}$ consisting of elements $A_{jkm\dots q} = I(x_j, t_{1,k}, t_{2,m}, \dots, t_{N,q})$, where the first tensor dimension indexes the set of J voxel locations $\{x_j\}_{j=1}^{J}$ and every remaining tensor dimension indexes one of the time dimensions. With Tucker form [272] of the LRT decomposition, $\boldsymbol{A}$ can be decomposed into the product of a core tensor $\boldsymbol{G}$ and $N+1$ factor matrices:

$$\boldsymbol{A}_{(1)} = \boldsymbol{U}_x \boldsymbol{G}_{(1)} \left(\boldsymbol{U}_{t_N} \otimes \boldsymbol{U}_{t_{N-1}} \otimes \dots \otimes \boldsymbol{U}_{t_1}\right)^T, \tag{1.8}$$

where the $\otimes$ operator denotes the Kronecker product. The subscript (n) (Equation 1.8) denotes mode-n unfolding of the tensor into a matrix. The factor matrix $\boldsymbol{U}_{\boldsymbol{x}} \in \mathbb{C}^{\mathbf{J}\times\mathbf{L}}$ contains L spatial basis functions each of which comprises J voxels. Each factor matrix U_{t_i} contains L_i basis functions for the ith time dimension t_i. $\mathbf{G} \in \mathbb{C}^{\mathrm{L}\times\mathrm{L}_1\times\dots\times\mathrm{L}_\mathrm{N}}$ is the coefficient dominating the interaction between factor matrices. The low-rankness of $\boldsymbol{A}$ confirms that the number of basis functions is smaller than its original elements ($L \ll J$) for each factor matrix, which reduces the total elements of the core tensor and factor matrices from $JK \cdots Q$ to $LJ + L_1K + \cdots + L_NQ + LL_1 \cdots L_N$. The acquired multi-channel signal $\boldsymbol{d}$ from tensor $\boldsymbol{A}$ can be expressed as $\boldsymbol{d} = \Omega\left(\boldsymbol{FSA}_{(1)}\right)$, where $\boldsymbol{S}$ is the multi-channel coil sensitivity maps, $\boldsymbol{F}$ is the Fourier encoding operator, and $\boldsymbol{\Omega}$ is the under-sampling pattern. The image tensor $\boldsymbol{A}$ can then be reconstructed by LRT completion [273]:

$$\widehat{\boldsymbol{A}} = arg\min_{A} \left|\left|\boldsymbol{d} - \Omega\left(\boldsymbol{FSA}_{(1)}\right)\right|\right|_2^2 + \lambda \sum_{n=1}^{N+1} \left|\left|\boldsymbol{A}_{(n)}\right|\right|_* + R(A), \tag{1.9}$$

where λ is the rank regularization factor, $\left|\left|\cdot\right|\right|_*$ denotes the nuclear norm (accounting for low-rank-ness), and $R(\cdot)$ is an optional additional regularization function that can be employed to enforce complementary image properties such as transform sparsity.

Nonetheless, direct reconstruction of $\boldsymbol{A}$ remains impractical due to the considerable computational costs. In the LRT framework [267], $\boldsymbol{A}$ can be reconstructed in factored form using an explicit tensor subspace constraint:

$$\widehat{\boldsymbol{U}}_{\boldsymbol{x}} = arg\min_{\boldsymbol{U_x}} \left|\left|\boldsymbol{d} - \Omega\left(\boldsymbol{\phi} \times \boldsymbol{FSU}_p\right)\right|\right|_2^2 + R(\boldsymbol{U_x}), \tag{1.10}$$

where $\boldsymbol{\phi}$ is constructed from the temporal factor matrices as $\boldsymbol{\phi} = \boldsymbol{G}\left(\boldsymbol{U}_{t_N} \otimes \boldsymbol{U}_{t_{N-1}} \otimes \cdots \otimes \boldsymbol{U}_{t_1}\right)^T$. Since $\boldsymbol{\phi}$ doesn't contain spatial information, it can be reconstructed from a frequently sampled subset of data (the 'subspace training data') acquired at the center of k-space to resolve temporal dimensions. The training tensor $\boldsymbol{D}_{tr}$ can still be undersampled since training data acquisition cannot typically cover every combination of motion states and contrast states. Therefore, we apply a small-scale LRT completion algorithm by solving the following optimization problem:

$$\widehat{\boldsymbol{D}}_{tr} = \arg\min_{\boldsymbol{D}_{tr}} \left|\left|\boldsymbol{d}_{tr} - \Omega_{tr}(\boldsymbol{D}_{tr})\right|\right|_2^2 + \lambda \sum_{n=1}^{N+1} ||\boldsymbol{D}_{tr,(n)}||_* + R(\boldsymbol{D}_{tr}), \tag{1.11}$$

Once the tensor is completed, matrix $\boldsymbol{\phi}$ can be extracted from $\boldsymbol{D}_{tr}$ by higher-order singular value decomposition (SVD) [274]. With the determined temporal basis function $\boldsymbol{\phi}$, and recovered spatial basis function from Equation 1.10, the reconstructed image tensor $\boldsymbol{A}$ is computed by $\boldsymbol{A}_{(1)} = \boldsymbol{U_x}\boldsymbol{\phi}$**.** The efficacy of the LRT framework for resolving motion has been proven in many cardiovascular MR imaging applications, as detailed in several key studies [266–271,275–277]. However, this framework needs to be further developed to facilitate MI characterization to answer essential questions for MI patients. In Chapter 2, we incorporated the LRT framework to

overcome principal technical challenges for MI characterization. To this end, we developed a motion-resolved free-breathing non-ECG-gated 3D cardiac MR imaging technique using the LRT framework to characterize MI through rigorous validation using animal studies.

1.6.2 Need for Cardiac Outcome Stratification for MI Patients with Non-Contrast Techniques

As previously outlined, native T1 mapping can yield diagnostic values for identifying acute and chronic MIs. Evidence accumulates from previous studies that T1 values are elevated in acute MI because of extensive existence of edema and necrosis/fibrosis within the MI region and it remains to be elevated toward chronic MIs compared to the remote myocardium due to mildly elevation of fibrotic tissue. However, consensus now has been reached that MI is more than just fibrosis and edema. Previous studies found that IMH and its iron remnants also coexist within MIs, where the drop of T1 value are always thought to be its characteristics. And studies now point to IMH as not a bystander but of significant promoter of consequential pathophysiology of reperfused MIs. A key example of this is that fat infiltration, a long-term consequence of hemorrhagic MI, is now realized as a substrate for life-threatening arrythmias in chronic MI patients.

The study by Kellman et al. [245] showed out that the current native T1 mapping using bSSFP readouts also have fat information encoded, with non-monotonic T1 response to fat fraction. More broadly native T1 mapping is sensitive to fibrosis, edema, necrosis, hemorrhage/iron and fat deposition, making complex response of T1 values in MI characterization (Figure 1.5). This has made traditional visual inspection and obtained averaged intensity levels in native T1 maps not align. For example, patchy depositions of iron and fat in chronic MI may have normal mean T1 value within MI region but it is one of the most severe forms of MI that could result in multi-

fold MACE. This has made tissue characterization in MI a challenging problem for the cases where the diagnosis, risk stratification are most needed to adjust the treatment plan accordingly.

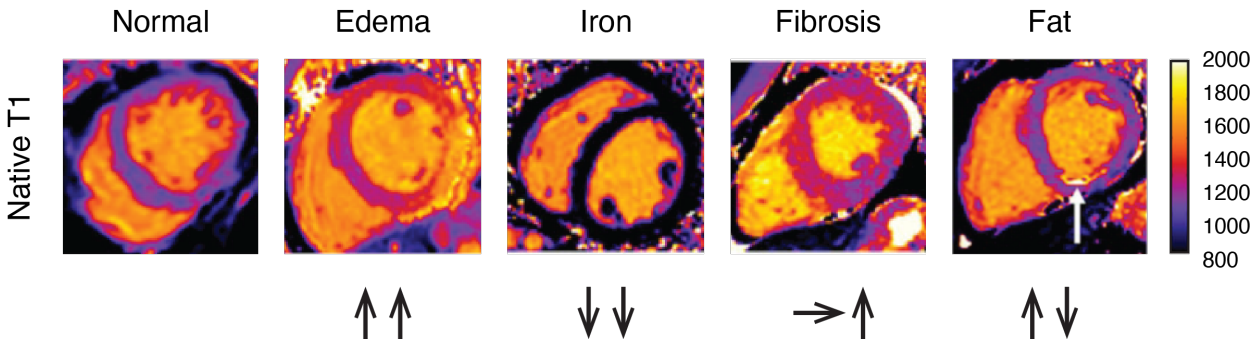


Figure 1.5 Typical appearance of T1 maps in healthy subjects and in subjects with myocardial disease. Arrows denote relative change in respective T1 maps. Adopted from [143] and [245].

The heterogeneity of T1 within myocardium poses a problem regarding the way to investigate the T1 map with only average values of T1 may miss some deterministic aspect in MI characterization. Studies in the field of radiomics aim to extract texture features reflecting MI characteristics in various CMR techniques such as CINE, LGE and T1 mapping. This has been studied in clinically to establish diagnosis [278], determine age of infarct [279,280] and risk stratification [281–285].

Specifically, for native T1 maps, Ma et al. [282] combined texture information and T1 values to provide higher diagnostic accuracy for MVO, and with texture information it provides incremental value in the prediction of LV longitudinal systolic myocardial contractility at six months; Antiochos et al. [286] used entropy as a measure of LV myocardial tissue heterogeneity in patients with VAs and found additional value in risk stratification in patients with absence of myocardial scar or with non-sustained VAs. While these studies attempt to exploit the utility of native T1 mapping to provide additional information, the underlying changes with respect to the

characteristics of myocardial tissue is not studied, which undermines the reason why acquiring additional information is critical. Moreover, by discovering its mechanism, we would be able to use native T1 mapping alone as a multi-substrate characterizer without other CMR acquisition. In chapter 3, we demonstrated native T1 heterogeneity within MIs as a new form of contrast with its underlying mechanism and for MI characterization, as well as the tool for mapping post MI risk for MACE.

1.6.3 Need for Optimizing Spatial Resolution and Signal-to-Noise Ratio (SNR) of T2* Mapping in Detection of Iron Deposits in MI

As is mentioned the previous section, T2* CMR is the preferred method for detecting global and regional alterations in iron content in the heart. However, current T2* CMR acquisitions are typically optimized for global myocardial iron deposition conditions (e.g. thalassemia) but not for iron deposition that take place within chronic MI territory, which is substantially different in the makeup of iron compared to global iron overloading conditions. The focal lesions of iron deposition may impose high demand for spatial resolution and SNR for its detection.

It has been shown in pathological studies that the complete scarred myocardium of chronic infarcts is commonly associated with substantial myocardial thinning to <6 mm [287].

A multi-center large cohort (n=1043) patient study has shown about 20% prevalence of myocardial wall thinning in patients with CAD referred to CMR more than 2 weeks [288]. 82% of the subjects with thin myocardial walls were found to have severely scarred within the MI region. In these situations, being able to detect iron deposition is essential but its challenge is not clearly identified or studied. On the other hand, having the capability for detecting thin iron-rich region in small infarcts has become important as it is now clear that hemorrhagic MI is considered as the most severest form of MI [14] and persistent iron would continuously induce inflammation and fat deposition [45,46]. Therefore, the detection and characterization of iron

deposition from IMH provides capability of stratifying risks of MI patients, facilitating the treatment plan and its prognosis.

Spatial resolution has been playing an important role in diagnosis of focal lesions [289,290] such as IMH. However, it is not thoroughly studied for the broadly used 2D cardiac T2* imaging for IMH characterization in MI. There is large variety of spatial resolution being used in previous clinical/preclinical CMR studies (Table 1.2).

Table 1.2 Summary of Imaging Resolutions from Previous Studies.

Manuscript	**Spatial resolution (mm^3)**	**Species**	**Time after reperfusion**
Ghugre et al. [291]	1.9x1.9x5	Swine	6 weeks
Moon et al. [292]	0.9x0.9x4	Swine	8 weeks
Cokic et al. [293]	1.3x1.3x6	Canine	16 weeks
Kali et al. [211]	1.4x1.4x6	Canine	8 weeks
Guan et al. [154]	1.1x1.1x6	Canine	6 months
	1.6x1.6x8	Human	6 months
Bulluck et al. [294]	Not reported	Human	5-7 months
Carberry et al. [155]	2.6x1.6x8	Human	6 months
Carrick et al. [181]	2.6x1.6x8	Human	7 months
Kali et al. [46]	1.3x1.3x8	Human	6 months
Reinstadler et al. [30]	1.6x1.6x8	Human	12 months

However, under scenarios of thinned LV wall (< 6 mm), there will be only few pixels across the wall from epicardium to endocardium for practical MR imaging protocols, leaving the current protocols in spatial resolution under question. In MRI, spatial resolution is a key determinant of SNR. The significance of spatial resolution for IMH detection from T2* CMR stems from the

need to balance spatial resolution and SNR, since SNR is proportional to the voxel size, if other parameters are kept constant [295]:

$$SNR \propto \frac{\Delta x \Delta y \Delta z \sqrt{N_{acq} N_x N_y N_z}}{\sqrt{BW_{read}}}, \quad (1.12)$$

where Δx, Δy, and Δz are voxel size in frequency encoding, in-plane phase encoding and slice-encoding directions respectively. N_{acq} represents number of acquisitions. N_x, N_y, and N_z are number of samples in frequency encoding, in-plane phase encoding and through-plane phase encoding directions respectively; and BW_{read} represents readout bandwidth.

Thus, spatial resolution is critical as coarser imaging resolution offers greater SNR, it also introduces partial volume effects that will diminish the sensitivity for detecting highly localized IMH lesions. Conversely, although the higher spatial resolution is desirable for detecting small IMH lesions, it also comes with a price of lower SNR and longer scan time (breath-hold time), compromising accuracy for detection of localized accumulation of iron in MIs. This challenged is amplified for MIs with thinned LV walls. Therefore, there is a pressing need for understanding the limitation of IMH detection with respect to the current widely used 2D T2* CMR protocols. To address this issue, we studied the influence of spatial resolution and SNR on T2* maps on detection of iron deposits in MIs in Chapter 4.

1.7 Key Objectives of the Dissertation

The overall goal of this dissertation is to improve capabilities of CMR and develop MRI novel techniques to characterize MI tissue to improve clinically important readouts. To achieve this, we aim to propose to investigate specific approaches that can yield greater insight into MI based CMR techniques with a focus on spatial resolution, time-efficient acquisitions, and multi-contrast readouts. First, a novel technique is developed using LRT framework with 3D free-

breathing, non-ECG-gating to characterize MIs in determining its severity within 15 mins. Then a new form of native T1 mapping contrast in MI substrate characterization is studied with heterogeneity analysis. At last, we will identify the influence of spatial resolution in T2* CMR technique for detection of iron deposits in MI.

1.7.1 Aim 1: To develop, test, and validate a 15-min protocol comprising of free-breathing, non-ECG gating, motion resolved whole LV 3D acquisition using LRT-based reconstruction to characterize MIs with cardiac function, MI size, MVO size and IMH size.

Chapter 2 focuses on developing a novel technique based on LRT framework to accelerate acquisition and to facilitate a more accurate analysis. This technique was tested in canine subjects in acute MI and chronic MI to characterize cardiac function, MI size, MVO size and IMH size with the proposed MR sequence within 15 min. The proposed method was compared with conventional 2D methods acquired with the same through-plane coverage with CINE, LGE, EGE and T2*-weighted images, where possible CMR findings were validated with histopathological staining. Additional information that is not usually acquired with the conventional methods and shortened acquisition time was demonstrated for the proposed method.

1.7.2 Aim 2: To characterize the MI severity using heterogeneity analysis on native T1 mapping in chronic MI patients.

Chapter 3 proposes an entropy analysis as a radiomic biomarker for stratifying chronic MI based on heterogeneity of T1. First, we validated potential source of heterogeneity of T1 values with our own imaging parameters from various fat fraction using Bloch simulation and in an ex-vivo fat phantom. Secondly, entropy in MI model was studied over timepoints from acute phase to chronic phase, with correlation to processed fat fraction map and R2* map (in relation to iron).

Representative tissues were also validated using histopathology. Subsequently we illustrate MI substrates based on the entropy from native T1 map. Similarly, the entropy analysis on T1 maps was also studied in MI patients.

1.7.3 Aim 3: To address the limitation of identification of residual iron deposition from IMH in chronic MI and provide guidance for improving the accuracy of iron detection.

Chapter 4 discussed the effect of spatial resolution and SNR on detection of chronic hemorrhagic MI. A numerical simulation of a 3D heart with a thinned IMH was performed to illustrate the theoretical underpinnings behind the influence of spatial resolution. To isolate the artifacts from motions and off-resonance in in-vivo scans, ex-vivo scans on swine were studied with the goal of identifying the detection accuracy at various spatial resolutions in the presence of wall thinning in chronic MIs. We then tested the detection capability in a regular setting of T2* mapping in vivo with the same subjects to demonstrate the limitation of detection with the constraint of spatial resolution and SNR.

CHAPTER 2: FAST, COMPREHENSIVE 3D FREE-BREATHING, NON-ECG GATING LOW-RANK TENSOR BASED CMR CHARACTERIZATION OF MYOCARDIAL INFARCTION

2.1 Introduction

Patients with STEMI is in significant decline in mortality due to advancements in clinical therapies. The extent of MI is a main determinant of post-MI mortality, including HF [26,296]. About 50% patients with STEMI experience an incomplete restoration of blood flow to the heart tissue, despite successful opening of the blocked artery through primary PCI, which is mainly caused by ischemia-reperfusion injury [297,298]. The primary causes of the injury are from erythrocyte extravasation, and further leads to the occurrence of microvascular injury: MVO and/or IMH. As discussed in Chapter 1, the most severe form of MIs [17] results in MVO and IMH, both of which are independently associated with extensive myocardial damages and associated with MACE [298]. We showed in Figure 1.1 that MVO has been proven to add incremental prognostic values over edema and necrosis (CCS Stage III), while IMH provides additional prognostic information over established CMR prognosis markers including cardiac function, MI size and MVO (CCS Stage IV) [17,29,49]. Thus, prompt detection and characterization of cardiac function, MI, MVO, and IMH are essential for improving patient survival and prevention of long-term complications.

LGE has been the current gold standard for identifying MIs [112,299–301] for patient diagnosis, characterization and treatment monitoring [104,302–306]. The technique is based on the IR prepared sequence with bSSFP or Fast Low Angle Shot (FLASH) readout, where it typically involves the acquisition of sequential T1-weighted images during the passage of an intravenous

Gadolinium (Gd) injection. Detecting and accurate assessment of the infarcted region such as determining MI's location, size and transmurality has expanded prognostic role of LGE [307]. For example, LGE is shown to predict contractility recovery after coronary revascularization in MI with LV dysfunction by determining the transmural extent of LGE [98]. On CMR (CMR provides the most comprehensive assessment of MVO), MVO is revealed as a hypointense core within the hyperintense infarct zone within the area of delayed gadolinium enhanced imaging [308–310]. The imaging feature is explained by failure of the contrast agent to penetrate within the infarct core. MVO as assessed by CMR is defined as "early" or "late" in reference to the timing of imaging relative to gadolinium administration. Early MVO is identified as a hypointense region in the core of the infarct on T1-weighted images obtained 2 to 5 min after contrast administration [311]. The duration of the absence of gadolinium wash-in can persist for over 10 min [312], depending on the severity of MVO. This leads to a consistent area of hypo-enhancement within the core of the infarct on conventional LGE images, which is termed as late MVO. For IMH characterization, T2* CMR imaging has been proven to be the preferred method to non-invasively depict IMH despite some existing disadvantages (e.g. off-resonance artefacts) [31,38,146,210,313]. However, these conventional CMR methods must be used with breath-holding and ECG triggering to minimize respiratory and cardiac motion effects. Moreover, these acquisitions are conventionally two-dimensional, and separate acquisitions are needed for imaging parameters, resulting in potential misaligned images and are compromised by variable breath-holding patterns. Furthermore, the prolonged wait-time during breath-holds, and additional wait time for the contrast agent to wash out in the myocardium is a major bottleneck for the length CMR protocol, hindering a broader clinical adoption. The CMR society has put extensive effort to tailor the CMR exams to be done within 30 min to answer essential questions for the patients. However, this protocol missed IMH characterization, is more demanding for

patient to breath-hold because they suggested only 20 second intervals between scans, and highly depends on experienced technologist to quickly navigate and adjust the scans.

Free-breathing, non-ECG gated CMR technique has been achieved using the MR multitasking framework [266,267,275,276,314], which models the underlying image as a low-rank tensor and acquires training data to identify and resolve cardiac and respiratory motion. These studies have showed flexibility and promises. However, this framework has yet been optimized for comprehensive MI characterization (with information of MVO and MI, along with cardiac function) with full heart coverage although early work has been reported [267]. In this study, we developed a free-breathing, non-ECG gating, motion-resolved whole LV 3D acquisition using low-rank tensor-based reconstruction to integrate multiple quantitative measurements to characterize cardiac function and severity of MI (MI size and transmurality, MVO size and IMH size) after Gd injection within 15 min.

2.2 Methods

2.2.1 Sequence Diagram

Our LRT technique uses a continuous randomized Gaussian-distributed 3D Cartesian k-space pattern to avoid synchronization between sampling and periodic motion (Figure 2.1). The acquisition cycles through a fixed IR module, with FLASH excitations for data readout filling the entire recovery period between preparation pulses. Two interleaved data sets are collected during the continuous acquisition: The training auxiliary data ($\boldsymbol{d_{tr}}$) are frequently collected at the k-space center line to provide temporal information, and the imaging data ($\boldsymbol{d_{img}}$) are randomly collected with a 3D Gaussian sampling with Cartesian trajectory to provide spatial information.

Each readout consisted of 6 multi-gradient echoes, and they are used for both training and imaging data. The sequence lasts for 14 min and 20 sec.

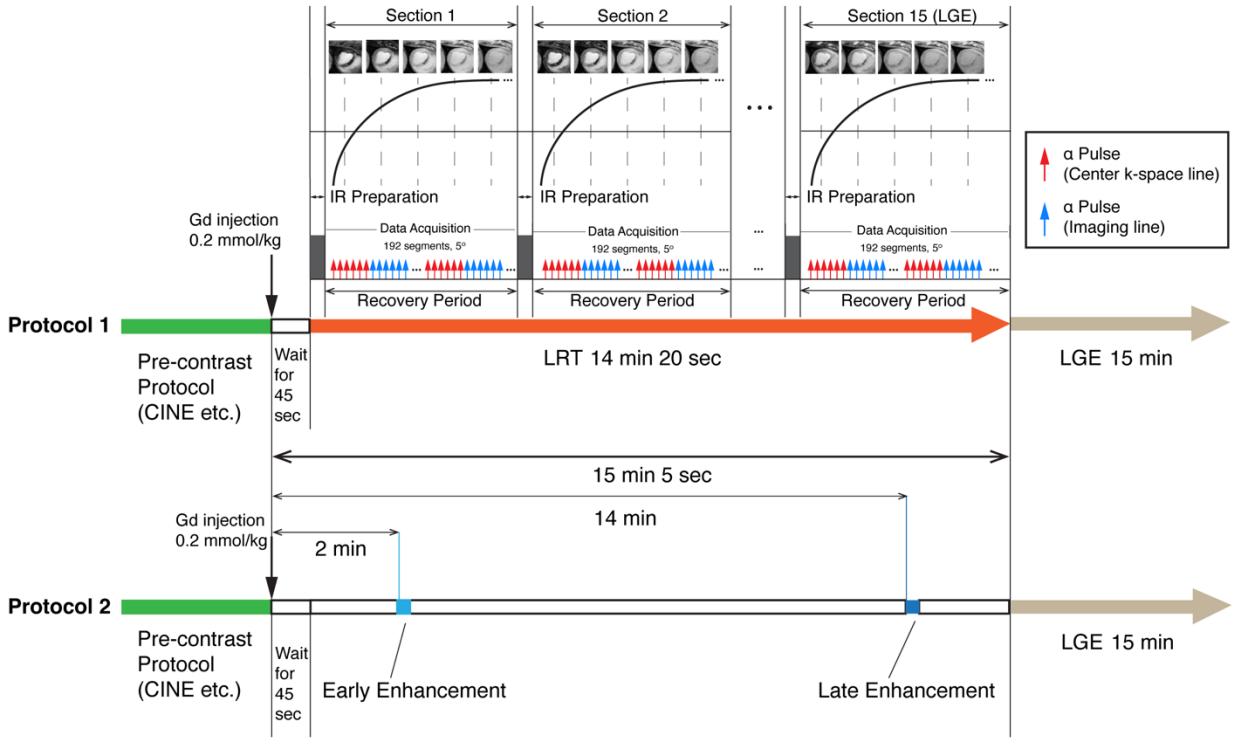


Figure 2.1 Imaging protocol with LRT pulse sequence diagram. Inversion recovery (IR) pulses are applied at constant intervals by mGRE readouts. Following each IR preparation module, RF pulse flip angles are 5° for 192 segments. The training auxiliary data are interleaved with imaging data every eight segments. Protocol 1: Pre-contrast acquisition (CINE and mGRE) followed by contrast injection and LRT sequence acquisition and conventional LGE acquisition. Protocol 2: The same pre-contrast and LGE protocol, but with early enhancement and late enhancement acquisition after Gd injection.

2.2.2 Low-rank tensor imaging model

In Chapter 1, we detailed the LRT framework and how it can be used to model CMR images as a multi-dimensional tensor. In this chapter specifically, we will employ the LRT framework to model the underlying image as a 6-dimensional image $x(\boldsymbol{r}, T_c, T_r, T_t, T_I, T_E)$ with two spatial dimensions indexed by $\boldsymbol{r} = [x, y, z]$, and five temporal dimensions describing cardiac motion, respiratory motion, temporal dynamics along Gd enhancement, T_1 recovery, and T_2^* decay

indexed by T_c, T_r, T_t, T_I, T_E respectively. By taking advantage of the spatial-temporal correlations, the image can be factorized as:

$$x(\boldsymbol{r}, T_c, T_r, T_t, T_{t1}, T_{te}) = \sum_{l=1}^{L} u_l(r)\ \phi_l(T_c, T_r, T_t, T_{t1}, T_{te}), \tag{2.1}$$

$$\phi_l(T_c, T_r, T_t, T_{t1}, T_{te}) = \sum_{j=1}^{J}\sum_{k=1}^{K}\sum_{m=1}^{M}\sum_{n=1}^{N}\sum_{p=1}^{P} g_{ljkmnp}\, c_j(T_c) r_k(T_r) t_m(T_t) w_n(T_{t1}) q_p(T_{te}), \tag{2.2}$$

where $\{u_l(\boldsymbol{r})\}_{l=1}^{L}$ represent spatial coefficients and $\phi_l(T_c, T_r, T_t, T_{t1}, T_{te})_{l=1}^{L}$ represent temporal functions that can be further decomposed into a core tensor G with elements g_{ljkmnp} and individual bases for each temporal dimension: $\{c_j(T_c)\}_{j=1}^{J}$, $\{r_k(T_r)\}_{k=1}^{K}$, $\{t_m(T_t)\}_{m=1}^{M}$, $\{w_n(T_{t1})\}_{n=1}^{N}$, $\{q_p(T_{t2})\}_{p=1}^{P}$. The combination of Equations 2.1 and 2.2 suggests that a discretized image tensor X with elements $x_{ijkmnp} = x(\boldsymbol{r}_i, T_{c,j}, T_{r,k}, T_{t,m}, T_{t1,n}, T_{te,p})$ can be decomposed in Tucker form as follows:

$$X = G \times U_X \times U_C \times U_R \times U_T \times U_{T1} \times U_{TE}, \tag{2.3}$$

where the columns of $U_X, U_C, U_R, U_{T1}, U_{TE}$, and U_T contain the basis functions for each corresponding dimension.

As presented in Chapter 1, the core tensor, and temporal bases are often extracted from the training data. We individually decompose each tensor x_p to reduce computational expenses, the subset of the image tensor X at the p^{th} echo, as follows:

$$X_p = \hat{G} \times U_p \times U_C \times U_R \times U_T \times U_{T1}, \tag{2.4}$$

Where $\hat{G}$ is an updated core tensor without T2* dimension, and U_p are the spatial coefficients for the p^{th} echo. All echoes share the motion and T1 relaxation bases, as changes in motion bases and T1 relaxation bases are negligible on the time scale between echoes.

2.2.3 Image reconstruction

This work adopts a strategy for image reconstruction with LRT framework from previously published methods [267,275]. Specifically, the 6-way low-rank image tensor was reconstructed with the following steps:

(1) Reconstructs "real-time" images using explicit low-rank matrix imaging with only one time dimension representing elapsed time and is similar to ϕ_l in Equation 2.1. A modified independent component analysis (ICA) algorithm is used to automatically place the corresponding images into 4 respiratory bin and 24 cardiac bins. Respiratory motion is identified first, and respiratory bins assigned at each iteration are low-pass-filtered with 40 Hz cutoff frequency. Then cardiac bins are band-pass-filtered with range of 40-130 Hz (a range for possible heart rates). And temporal dynamics is evenly divided into 15 sections, each section is about 57 seconds.

(2) Predetermine the temporal basis functions in $\boldsymbol{U}_{T1}$. According to the Bloch equation, a dictionary of feasible IR GRE signal curves is generated using the sequence parameters with a range of T_1 and B_1 inhomogeneity values. The dictionary consists of 21 T_1 values logarithmically spaced from 100 to 3000 ms, 10 flip angles equally spaced between 0.5° to 5°, and 6 inversion efficiency factor equally spaced between -1 (perfect inversion) and -0.5. Basis functions in $\boldsymbol{U}_{T1}$ are extracted from SVD of the dictionary.

(3) The training tensor $\boldsymbol{D}_{tr}$ can still be undersampled as training data acquisition cannot typically cover every combination of cardiac phase, respiratory phase, T1 and temporal dynamics dimensions. We apply a small-scale, low-rank tensor completion algorithm by solving the following optimization problem:

$$\widehat{\boldsymbol{D}}_{tr} = \arg \min_{\substack{D_{tr}, s.t. \\ \boldsymbol{D_{tr,(4)}} \in range(\boldsymbol{U_{T1}})}} \left|\left|\boldsymbol{d}_{tr} - \Omega_{tr}(\boldsymbol{D}_{tr})\right|\right|_2^2 + \lambda \sum_{i=1}^{4} ||\boldsymbol{D}_{tr,(i)}||_* + R(\boldsymbol{D}_{tr}), \qquad (2.5)$$

where $\boldsymbol{d}_{tr}$ is the collected training data; $\Omega_{tr}(\cdot)$ is the sampling operator for the training data set; $\boldsymbol{D}_{tr,(i)}$ is the mode-i unfolding of the complete training tensor; $||\cdot||_*$ denotes the matrix nuclear norm and λ weights the nuclear norm penalties and $R(\cdot)$ is a temporal regularizer.

(4) Extract temporal basis functions along the cardiac phase, respiratory motion, temporal dynamics and T1 recovery dimensions, namely, columns in U_C, U_R, U_T and U_{T1} respectively, as well as the core tensor $\hat{G}$ from the high-order SVD of the completed training tensor $\boldsymbol{D}_{tr}$

(5) Solve the spatial coefficients $\boldsymbol{U}$ echo-by-echo:

$$\widehat{U}_p = arg\min_{U_p} \left|\left|\boldsymbol{d}_{img,p} - \Omega\left(\hat{\phi} \times FSU_p\right)\right|\right|_2^2 + R\left(U_p\right) \tag{2.6}$$

For known temporal factor tensor $\hat{\phi} = \hat{G} \times U_C \times U_R \times U_T \times U_{T1}$, where $\boldsymbol{d}_{img,p}$ are the imaging data at the p^{th} echo, and $R(\cdot)$ is a wavelet sparsity regularizer. The reconstructed image tensor for the p^{th} echo is then given by the product $\hat{X}_p = \hat{\phi} \times \widehat{U}_p$.

2.2.4 Animal studies

The proposed fully ungated, free-breathing, 3D T1, T2* approach was tested in canine models. The protocol approved by the Institutional Animal Care and Use Committee (IACUC), canine (n = 12), were recruited and imaged in a whole-body 3.0 T MRI system (Verio, Siemens Healthcare). MI was created using left anterolateral thoracotomy, namely, 3 hours left anterior descending coronary artery (LAD) occlusion followed by reperfusion [49]. The animals underwent CMR scans at day 6 and day 8 (acute) and 8 weeks (chronic) post-MI. Prior to MRI scans, all animals were intubated and anesthetized with isoflurane (1-1.5%/volume).

2.2.5 CMR Acquisition

Conventional 2D breath-hold ECG-gated, short-axis pre-contrast bSSFP CINE, mGRE T2* images, and LGE of the whole LV were acquired. The proposed fully ungated, whole heart, 3D data were acquired with spatial resolution and slice location matched to the conventional 2D acquisitions 45 seconds after Gd injection (Figure 2.1, Protocol 1). Particularly, for acute MVO comparison, in acute phase (day 6 or day 8) single-slice early Gd enhancement and late Gd enhancement were acquired 2 min and 13 min after Gd injection, respectively (Figure 2.1, Protocol 2). Details on imaging parameters with the proposed and conventional approaches are summarized in **Table 2.1**.

Table 2.1 Imaging Parameters

	Proposed LRT	**T2* mGRE**	**CINE**	**EGE/LGE**
Purpose	Cardiac function, hemorrhage, MI and MVO	Hemorrhage	Cardiac function	MI and MVO
Field of View (FOV) (mm)	270 x 270	270 x 270	270 x 185	270 x 270
Matrix size	192 x 192	192 x 192	192 x 132	192 x 192
Resolution (mm^3)	1.4 x 1.4 x 6			
Partial Fourier	/	6/8		
GRAPPA	/	R = 2		
Inversion time (ms)	10	/		According to nulling time
TE (ms)	1.47, 3.38, 5.39, 7.4, 9.41, 11.42	1.47, 3.38, 5.39, 7.4, 9.41, 11.42, 13.43, 15.44	1.34	2.07
Bandwidth (Hz/pixel)	1185	1185	930	285
TR (ms)	13.2	17.32	2.68	4.14
Flip angle (°)	5	20	50	20
Acquisition time	14 min 20 sec	11 sec	15 sec	17 sec

2.2.6 Image analysis

All reconstructions were performed using MATLAB 2019a (MathWorks, Natick, Massachusetts) on a Windows workstation with a 2.30-GHz dual 24-core Intel Xeon processor and 256 GB RAM, which took about 1.5 h for each echo. The reconstructed images were then converted to DICOM-format and were analyzed quantitatively altogether with conventional 2D images using cvi42 version 5.13.9 (Circle Cardiovascular Imaging Inc. Calgary, Canada).

To validate the accuracy of proposed LRT method in quantifying cardiac function, extent of MI, MVO and hemorrhage (corresponds to microvascular injury), LVEF (corresponds to cardiac function), MI size and MI transmurality (corresponds to extent of MI), MVO and hemorrhage size (corresponds to MVO and hemorrhage) were measured at end-expiration, end-diastole phase from proposed methods and compared with the conventional reference images in both acute and chronic timepoint, if not stated otherwise. Specifically, for LVEF measurement, proposed LRT in end-expiration phase, late enhancement and the 41st T1 recovery segment (slightly after remote myocardium nulling point to maximize contrast between blood pool and remote myocardium while keeps myocardium still visible) was chosen for comparison. The endocardium was manually contoured in each slice for both images, and the end-diastole and end-systole phase were identified. LVEF was then calculated for each method using the following equation:

$$LVEF = \frac{LVEDV - LVESV}{LVEDV} \times 100\%, \tag{2.7}$$

where LVEDV and LVESV represents end-diastolic and end-systolic LV volume respectively.

For MI size and MI transmurality measurement, the proposed approach with nulled remote myocardium chosen for comparison. Similarly, endo- and epi-cardium were drawn and remote

myocardium ROI was then drawn to identify MI region with Mean+5SD method for each slice from base to apex. MI transmurality was computed with 50-chord analysis and then mean transmurality was calculated by averaging the infarct transmurality across all the chords that have >1% MI extent [118]. For hemorrhage size measurement, proposed LRT at late enhancement with the last segment (segment # 192) in T1 recovery was identified, and both were at TE = 11.43 ms. Endo-, epi-cardium and remote ROI were drawn and Mean-2SD method were applied to hemorrhage identification, for each slice acquired.

For MVO size measurement, only acute timepoints were analyzed because MVO resolves, because no MVO was found at chronic timepoint. Proposed LRT in end-expiration, end-diastole with nulled remote myocardium, at section 2, section 13 and section 15 for comparison with conventional early enhancement, pseudo-late enhancement and LGE. Endo- and epi-cardium were drawn and MVO were carefully identified. Volumetric MVO size was compared between proposed LRT at session 15 and LGE right after the proposed acquisition (Figure 2.1), while single slice MVO size was compared between proposed LRT at section 2 and section 13 to early enhancement and pseudo-late enhancement at different date (Day 6 vs. Day 8), due to its sensitive time window for the conventional acquisition.

2.2.7 Histology validation

One excised heart (euthanized after week 8 scan) was sliced along the short axis at 2-3 mm thickness. The slice matched to CMR based on fiducial landmarks (MI/hemorrhage appearance, papillary muscles, trabecular and RV insertion point geometry) was identified. It was then sectioned contiguously with 5 μm thickness and stained with EMT (for fibrosis) and Prussian Blue (for iron deposits). Tissue fiducial markers were used to correlate MR images with

histology and imaged at both 10-fold and 40-fold magnification (ECLIPSE Ni-E microscope, Nikon, Tokyo, Japan).

2.2.8 Statistical analysis

All analyses were performed using Prism 9.2.0 (GraphPad, San Diego, California) and MATLAB. Descriptive statistics were calculated for all variables as mean ± standard deviation. The normality of the data was assessed using the Shapiro-Wilk test, and the homogeneity of variances was evaluated using Levene's test. Paired t-test was used to test the difference between mean MI size, MI transmurality, MVO size, and hemorrhage size from two imaging approaches. Linear regression was performed between the proposed LRT method and the conventional method. Regression coefficients were calculated, and the goodness of fitting of the model was assessed using the R-squared values. Bland-Altman analysis was performed to determine bias in measurement and the reproducibility coefficient (RPC) was computed between the two imaging approaches. The significance was set at $p < 0.05$.

2.3 Results

The scan time to acquire each 2D short-axis breath-held ECG-gated cardiac CINE, T2* and LGE images was 1 min per slice, which includes recovery between breath-holds with 12 - 14 slices in total (6 mm each). To have full coverage of LV, with 15 min wait time during Gd injection, the total scan time for the conventional methods is 52 - 57 min. For the proposed LRT data acquisition, a total of 14 partitions were acquired for 3D covering the LV. And total acquisition time for the proposed approach was under 15 minutes. The under-sampling rate of the LRT data relative to a full tensor was approximately 12%.

The proposed LRT imaging was performed successfully on all subjects. It allows the visualization of anatomy, functional information and multiple imaging contrasts (Figure 2.2 and Figure 2.3). Representative slices of one short-axis view, 2-chamber view and 4-chamber view are shown to illustrate the 3D coverage of the heart (Figure 2.2A). The reconstructed tensors were able to resolve respiratory and cardiac motion with great image quality (Figure 2.2B & C). Figure 2.3 shows presentative slices on short axis view at end-diastole, end-expiration with T2* weighting, T1 weighting and Gd wash-out dynamic dimensions, each of which shows the contrast evolution over one period.

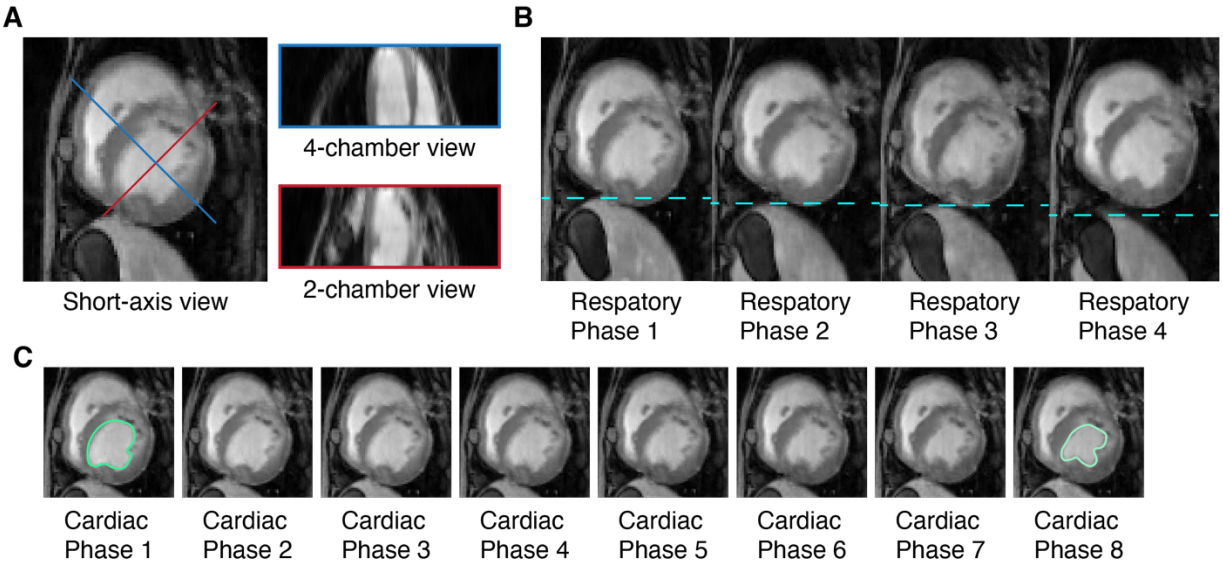


Figure 2.2 Representative images reconstructed with proposed LRT methods for 3D coverage, respiratory and cardiac dimension. **A)** A short-axis image sliced in two planes (Blue: 4-chamber view; Red: 2-chamber view) and two sliced views are shown on the right side. **B)** 4 respiratory phases are shown with planes at the tip of the liver highlighted with cyan dashed lines. **C)** 8 representative cardiac phases from end-diastole (cardiac phase 1) to systole (cardiac phase 8). Notably, blood pool contours for cardiac phases 1 and 8 are highlighted.

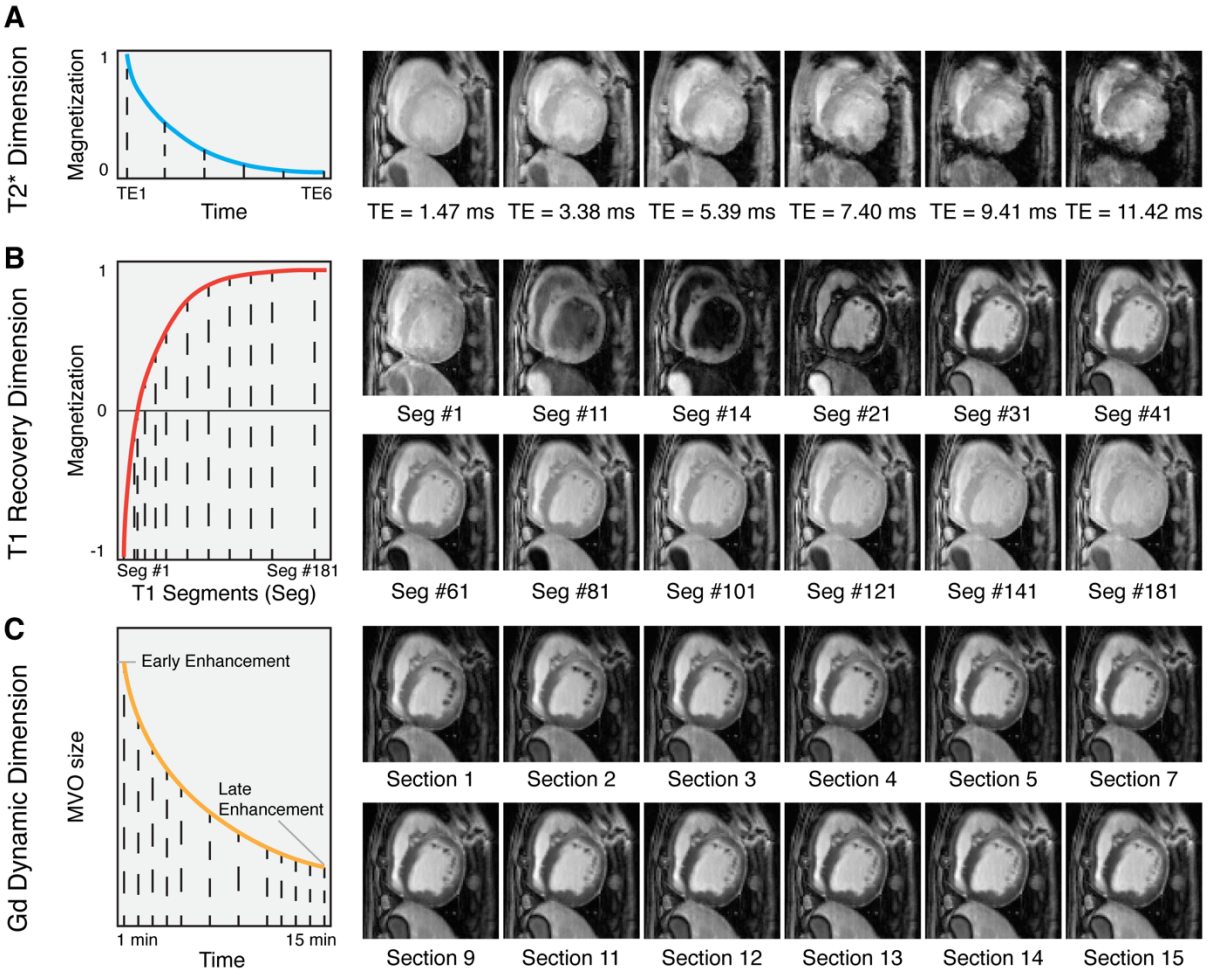


Figure 2.3 Representative images with proposed LRT method in contrast dimensions. **A)** T2* dimension with 6 TEs goes from 1.47 to 11.42 ms incrementally; **B)** T1 recovery dimension from segment (Seg) 1 to segment 192, with Seg #1, 11, 14, 21, 31, 41, 61, 81, 101, 121, 141, 181 shown as representative magnetization recovery on myocardium. **C)** Gd dynamic dimension from section 1 to section 15. Notably, each section is recovered from data in about 1 min, and the curve on the left illustrates MVO size decrease over time. The dashed lines on the left represent corresponding time points to the right.

2.3.1 Comparison of LVEF between proposed and conventional method

Representative slices of short-axis view at end-diastole and end-systole end-expiration phase in three representative slice locations in one subject is shown in Figure 2.4A&B. Comparing between the proposed and the conventional methods, the proposed LRT method can show comparable cardiac function state with 2D CINE, with enhanced MI region. For quantitative

analysis, there are no differences in LVEF measured using conventional 2D CMR and the proposed 3D methods (Figure 2.4). LVEF in all timepoints, acute and chronic for Proposed LRT vs. Conventional (Conv.) methods are 31.28 ± 5.42 % vs. 34.34 ± 3.89 % (P = 0.54), 31.72 ± 4.91 % vs. 34.14 ± 3.81 % (P = 0.35) and 30.84 ± 5.66 % vs. 34.54 ± 3.72 % (P = 0.32) respectively (Figure 2.4C). Linear regression including conventional and proposed approaches showed excellent correlation (slope = 0.93, 0.92, 0.99, R^2 = 0.96, 0.97, 0.93, P<0.001) and Bland-Altman analysis results showed excellent agreement and minimal bias (RPCs are: -0.19 ± 2.1 %, -0.03 ± 1.9 %, -0.4 ± 2.1 % respectively, Figure 2.4D)).

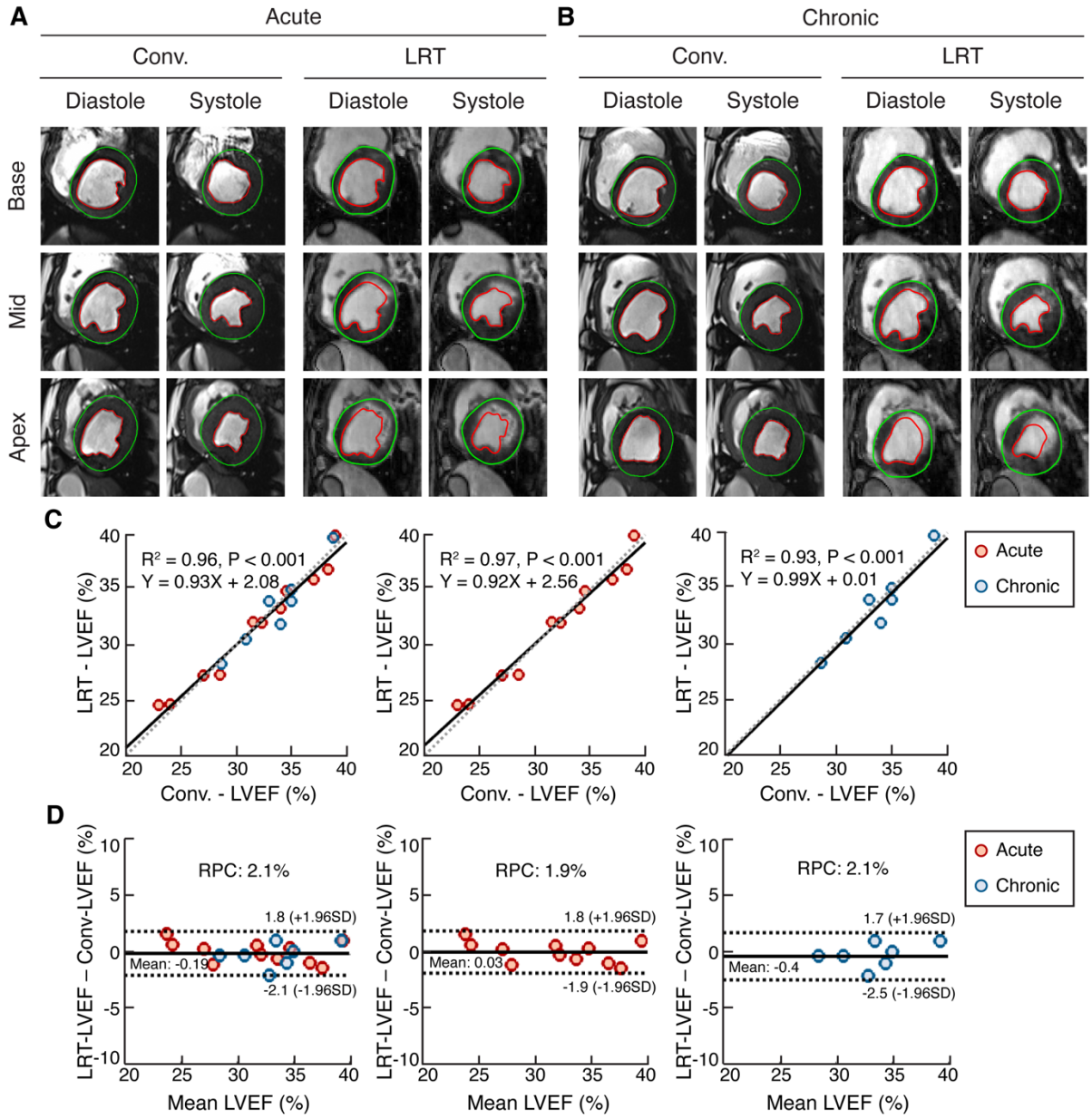


Figure 2.4 Representative image for Conventional (Conv.) CINE and Proposed LRT CINE (short-axis view) and ejection fraction comparison. End-diastole and end-systole cardiac phases are compared between conventional and the proposed approaches with three representative slices at base, mid-ventricle and apex of the hearts. Both **A)** acute and **B)** chronic of the same subject are shown above. The endocardium and epicardium contours were manually draw in each slice for both approaches with matched slice location**. C)** linear regression analyses comparing LVEF between conventional and LRT approaches, fitted equation and R^2 are shown in each plot. **D)** Bland-Altman analyses comparing agreement between the two approaches, RPC is shown in each plot. From left to right are all data points (both red and blue), only acute data points (red) and chronic data points (blue).

2.3.2 Comparison of MI size and MI transmurality between proposed and conventional method

MI size, MI transmurality were then analyzed to validate the capability of the proposed LRT method in MI characterization. MI size in all timepoints, acute and chronic for LRT vs. Conv. are 16.30 ± 8.93 % vs. 16.17 ± 8.23 % (P = 0.57), 21.58 ± 9.35 % vs. 21.00 ± 8.57 % (P = 0.26) and 11.02 ± 2.74 % vs. 11.35 ± 2.92 % (P = 0.47) respectively. MI transmurality in all timepoints, acute and chronic for LRT vs. Conv. are 58.41 ± 10.07 % vs. 56.97 ± 9.76 % (P = 0.13), 60.30 ± 10.95 % vs. 59.80 ± 10.79 % (P = 0.71) and 55.89 ± 8.74 % vs. 53.19 ± 7.08 % (P = 0.05) respectively. No difference in MI size and MI transmurality were found between the conventional 2D and proposed 3D methods (Figure 2.5). Linear regression of MI size including conventional and proposed approaches showed excellent correlation (Figure 2.5A, slope = 1.07, 1.07, 0.85, R^2 = 0.97, 0.97, 0.81, P<0.001), and for MI transmurality (Figure 2.5B, slope = 0.94, 0.92, 1.14, R^2 = 0.83, 0.83, 0.86, P<0.001). Bland-Altman analysis results showed excellent agreement and minimal bias for MI size (Figure 2.5A, RPCs are -0.01 ± 1.6 %, -0.59 ± 3.3 %, -0.32 ± 2.5 % respectively) and MI transmurality (Figure 2.5B, RPCs are -0.13 ± 8.3 %, -0.50 ± 9.1 %, -2.7 ± 6.8 % respectively).

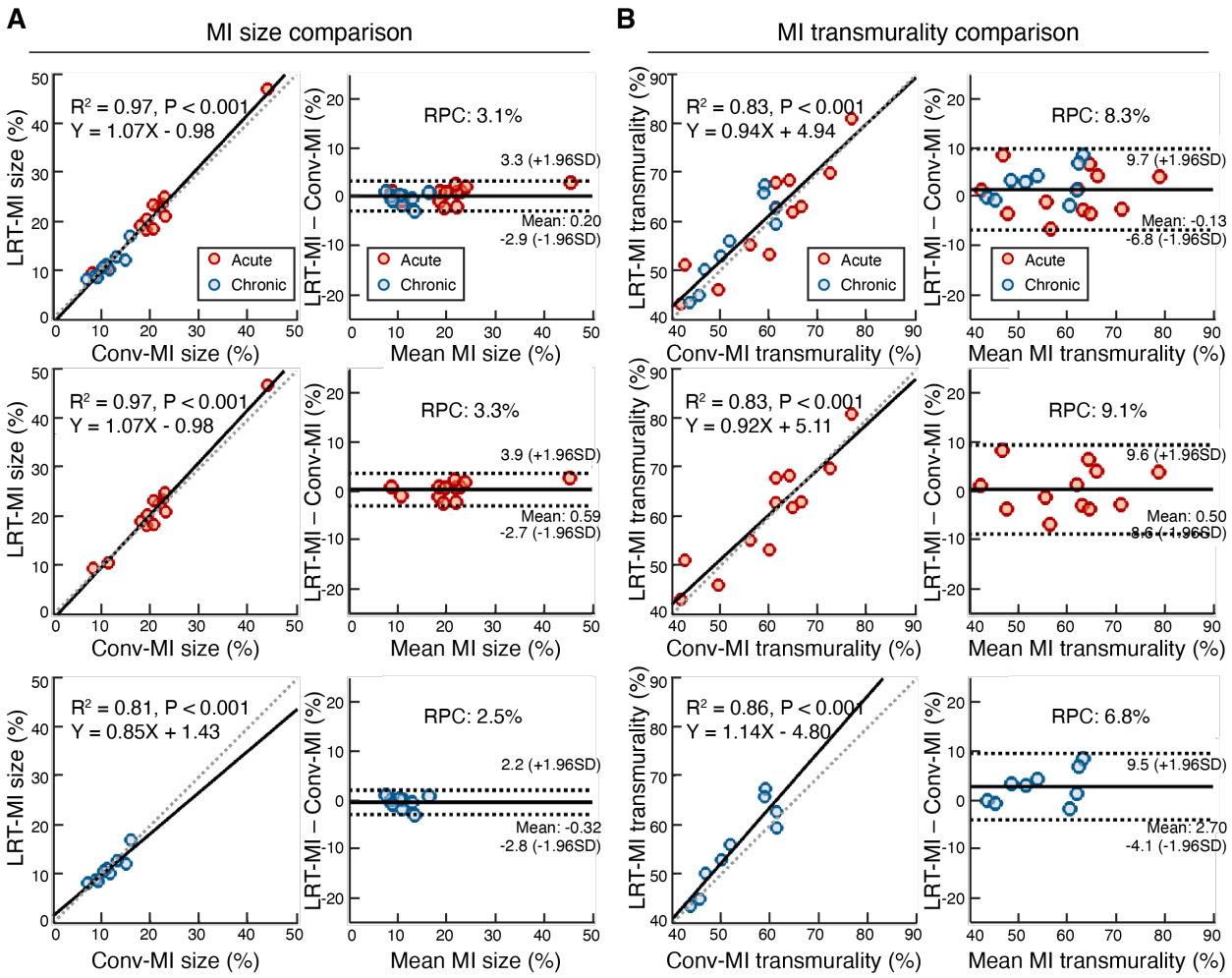


Figure 2.5 Capability of MI characterization between proposed LRT and Conv. approaches. **A)** linear regression analyses comparing MI size between Conv. and LRT approaches, fitted equation and R^2 are shown in each plot. On right: Bland-Altman analyses comparing agreement between the two approaches, RPC is shown in each plot. From top to bottom are all data points, only acute data points (red) and chronic data points (blue). **B)** Linear regression and Bland-Altman comparing MI transmurality between two approaches with the same lay-out.

2.3.3 Comparison of IMH and MVO size characterized by proposed and conventional method

To test the ability of MI characterization, the hemorrhage (IMH) and MVO size were analyzed (Figure 2.6) on the proposed reconstructed and conventional T2*w images and late enhancement images respectively. Hemorrhage size in all timepoints, acute and chronic for LRT vs. Conv. are 4.57 ± 3.30 % vs. 4.57 ± 3.31 % (P = 0.98), 6.60 ± 3.04 % vs. 6.73 ± 2.88 % (P = 0.67) and 2.54

± 2.16 % vs. 2.11 ± 4.57 % (P = 0.41) respectively. No measures showed significant differences between the two approaches. MVO size in acute time point for LRT vs. Conv. were 6.94 ± 5.42 % vs. 6.11 ± 4.93 % (P = 0.17) respectively. Linear regression of IMH size including conventional and proposed approaches showed excellent correlation (Figure 2.6A, slope = 0.97, 1.00, 1.00, R^2 =0.95, 0.90, 0.95, P<0.001) and for MVO size (Figure 2.6B, slope = 0.97, R^2 = 0.91, P<0.001). Bland-Altman analysis results showed excellent agreement and minimal bias (Figure 2.6A, RPCs are -0.01 ± 1.5 %, -0.16 ± 1.8 %, -0.14 ± 0.98 %, respectively) and MVO size (Figure 2.6B, 0.83 ± 3.3 %). Significant correlation was found in hemorrhage size for both acute and chronic phase. Good correlation and agreement in MVO size was found in acute phase.

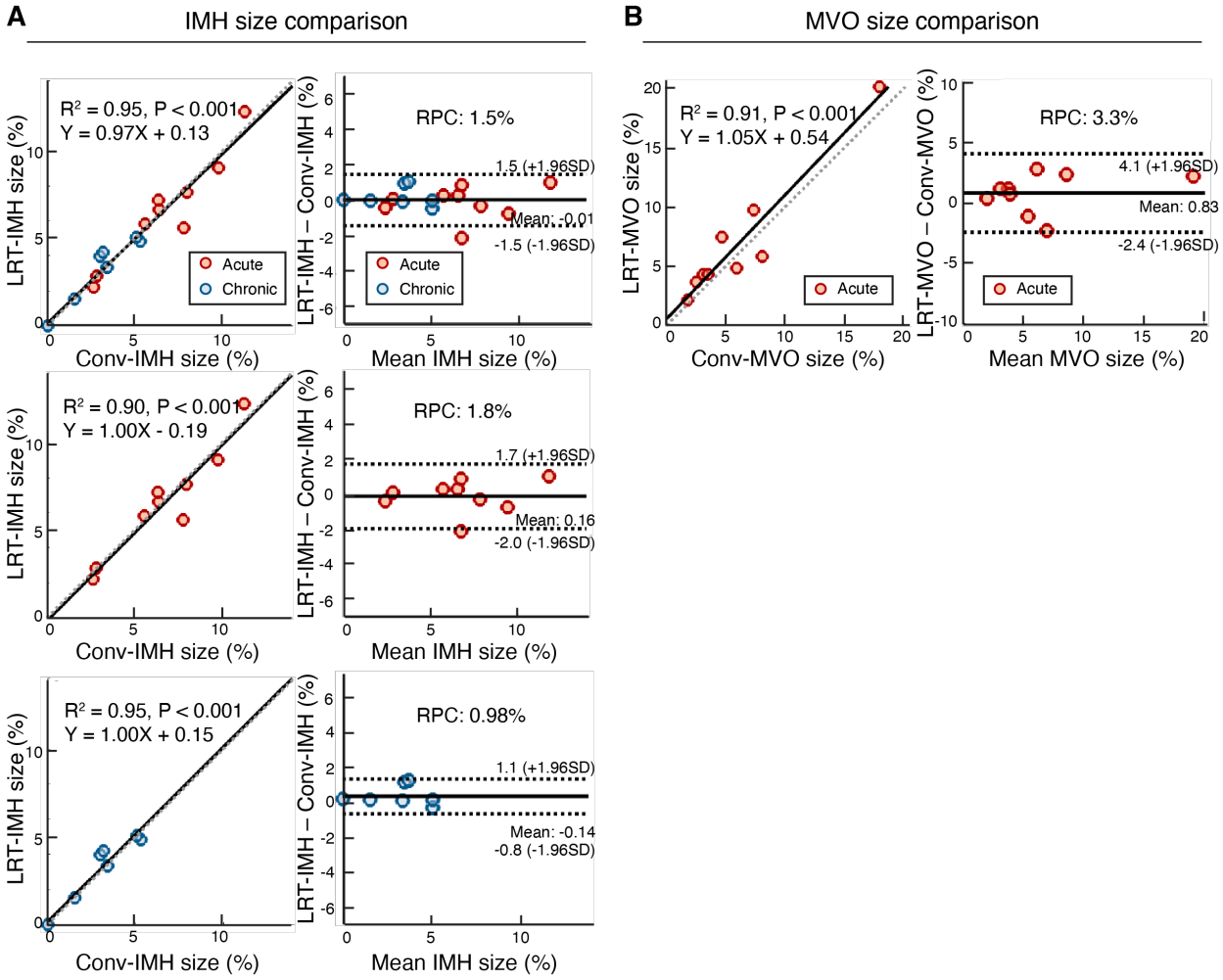


Figure 2.6 Intramyocardial hemorrhage (IMH) and MVO comparison between the proposed LRT and Conv. approaches. **A)** On left: linear regression analyses comparing hemorrhage size between Conv. and

LRT approaches, fitted equation and R^2 are shown in each plot. On right: Bland-Altman analyses comparing agreement between the two approaches, RPC is shown in each plot. From top to bottom are all data points, only acute data points (red) and chronic data points (blue). **B)** Linear regression and Bland-Altman comparing MVO size between two approaches on acute time point. Only acute time point was shown because no MVO was found in chronic phase.

2.3.4 Representative images from the two methods and histological validation

An illustration of T2* weighted and LGE images for proposed 3D LRT approach and 2D CMR approach with histological validation in chronic time point is shown in Figure 2.7. Good agreement between two approaches is shown in Figure 2.7A. Notably, the proposed LRT method showed higher resistance to off-resonance artifact than 2D conventional method. EMT staining and Prussian Blue staining show colocalization of MI and IMH in the chronic subject (Figure 2.7B).

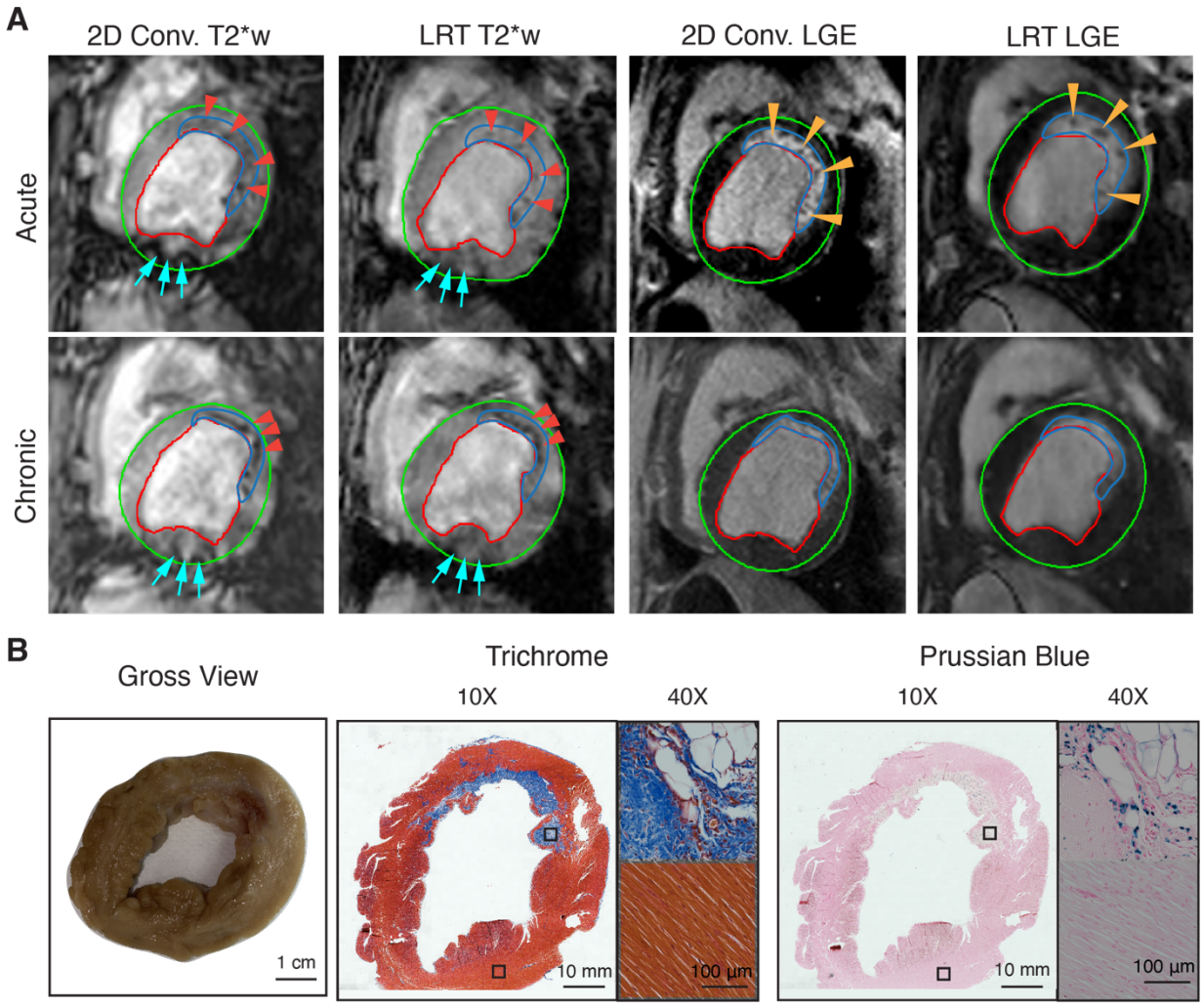


Figure 2.7 Representative cases of T2*w and LGE between conventional CMR and proposed LRT approaches. **A)** The subject was scanned on both acute and chronic time points. T2* weighted images (TE=11.43 ms) and LGE images were compared between LRT and 2D Conv. method with slice matched. Epicardium (green), endocardium (red) and MI region (blue) contours were drawn. Hemorrhage were pointed out by red triangular arrows, MVO were pointed with yellow arrows and off-resonance artifact were pointed with cyan arrows. **B)** The sliced heart tissue and its histology: Masson's Trichrome and Prussian Blue are shown at 10-magnification (10×). An infarcted region and one remote region were drawn in the 10× image and specifically shown in 40-magnification (40×) next to it.

2.3.5 Characterization of Early MVO and Late MVO between proposed and conventional methods

One example of MVO size progression within 20 min after Gd injection is shown in Figure 2.8A, where the proposed and conventional approaches with representative images shown at 2 min (Early), 13 min (Late) and ≥15 min (LGE) after contrast agent injection (Figure 2.8B). Good agreement is found between the proposed and conventional methods at early and late enhancement (Figure 2.8A).

Due to the misalignment in time between the 15th section of proposed LRT method (approximate 15 min after Gd injection) and 2D conventional LGE (about 20 min after Gd injection) we quantitatively compare the early and late enhancement between the two approaches. No significant difference was found in MVO size in early and late enhancement respectively between LRT and 2D CMR approach (Figure 2.8C). Decrease MVO size over time from both methods was observable ($P < 0.001$). Linear regression of IMH size between conventional and proposed approaches showed strong correlation (slope = 0.83, 0.98, $R^2 = 0.85$, 0.98 respectively, $P<0.001$) in both early and late enhancement (Figure 2.8D). Excellent agreement was found from Bland-Altman analysis (RPCs: 0.82 ± 7.4%, 0.37 ± 2.4%) for both early and late enhancement.

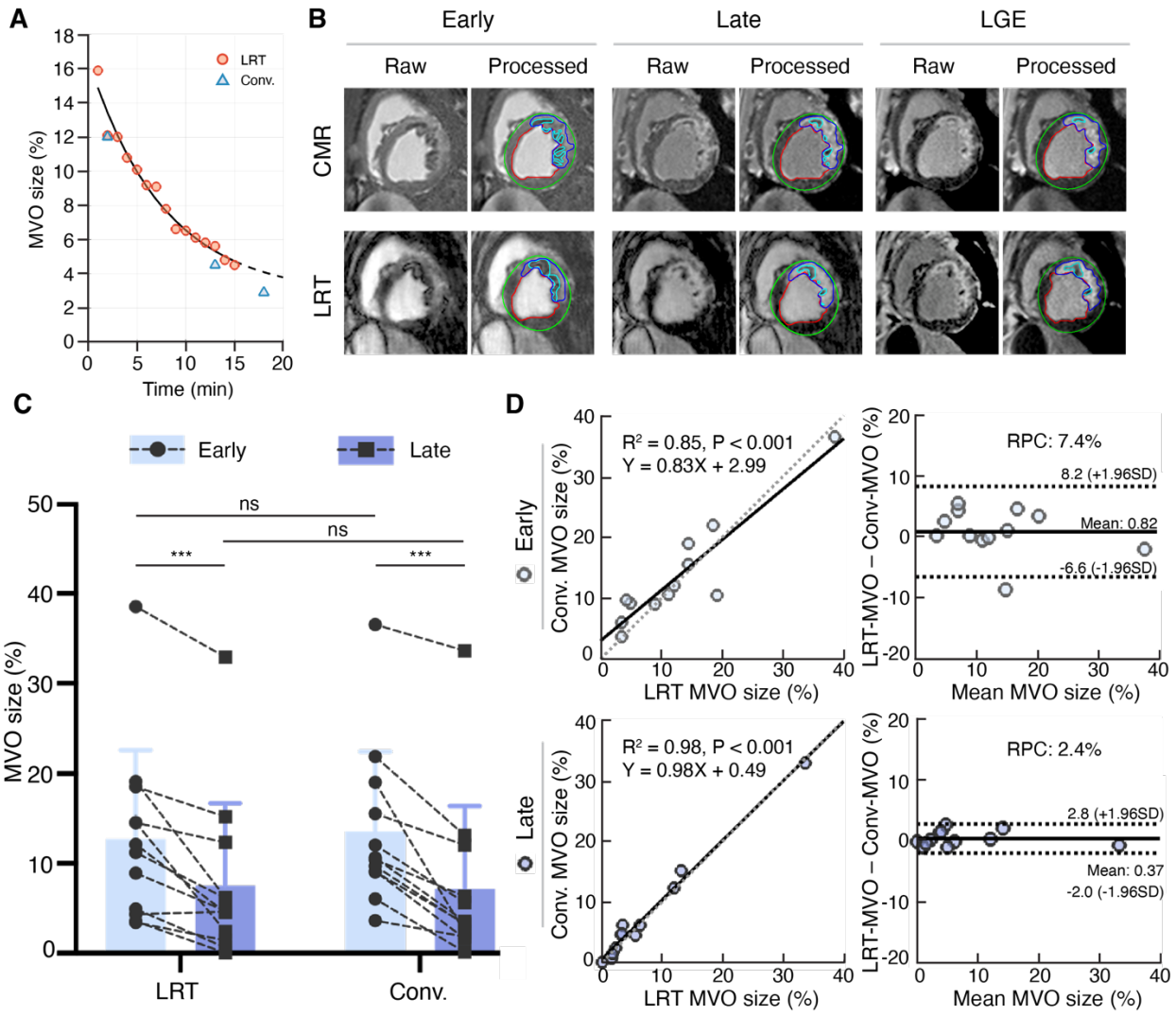


Figure 2.8 Representative images of MVO at 2 min (Early) and 13 min (Late) enhancement and after 15 min (LGE) and statistical analysis between the proposed and conventional methods. **A)** are MVO size progression for LRT and 2D Conv. CMR approaches. **B)** are representative images at early, late, and after late enhancement between LRT and Conv. Unprocessed image is shown on left while processed image on right, with endocardium (red), epicardium (green), MI (blue) and MVO (cyan) contours. **C)** Bar plot of MVO size in LRT and Conv. with each data point progression from early enhancement to late enhancement. **D)** On left: linear regression analyses comparing MVO size between Conv. and LRT approaches, fitted equation and R^2 are shown in each plot. On right: Bland-Altman analyses comparing agreement between the two approaches, RPC is shown in each plot. From top to bottom are at early enhancement time point (light gray) and late enhancement time point (dark gray).

2.4 Discussion

Although conventional Gd enhancement imaging has been widely used in the clinical implementation of MI/MVO characterization, T2* imaging for hemorrhage extent characterization and CINE imaging for cardiac function characterization, its slow imaging speed and complex clinical workflow can be challenging in the clinical environment. To our knowledge, this is the first study provide a comprehensive tissue characterization to optimize clinical scan time and simplify imaging workflow to further facilitate utility of CMR in subjects with MI. In this study, we developed a free-breathing, non-ECG-gated technique to build up a workflow in cardiac function, MI, MVO and IMH characterization with approximately 1/3 to 1/4 time of conventional workflow. We demonstrated that the proposed LRT approach provided comparable capability in LVEF, MI size, MI transmurality, MVO size and IMH size to 2D conventional method, with resolved cardiac and respiratory motion artifact in both acute (6-8 days after MI) and chronic (8 week) MI in a canine ischemic heart disease model, with which reducing the total scan time from about 55 min to less than 15 min.

To meet the clinical needs and address the drawbacks of conventional CMR, in this work, our proposed LRT approach enables comprehensive MI characterization after contrast injection for patient risk stratification. Notable features/advances our proposed approach brings forth are:

1) The proposed LRT method provides multiple co-registered images with different weightings in a single 14.3 min acquisition, focused on MI tissue characterization (including IMH and MVO). An IR preparation module was adopted to maximize the contrast between the remote myocardium and infarcted myocardium and can be retrospectively identified with optimal nulled remote myocardium to maximize MI contrast. It is worth mentioning that with the IR module with mGRE readout, the proposed LRT method may hold the potential for joint

T1/T2* mapping. The co-registered images also allow for pixel level analysis on various contrasts which facilitates further analysis.

2) By adopting a continuous 2D Gaussian sampling scheme, proposed LRT eliminates the need for ECG triggering, respiratory navigators, or breath-holds. This greatly improves the acquisition efficiency and reduces the complexity of imaging workflow, and in the meantime, avoids unreliability or discomfort induced by those external motion compensation methods. Moreover, by reconstructing the 6-dimensional imaging tensor along the cardiac motion dimension, the proposed LRT imaging tensor can provide cardiac phase-resolved cine images for functional imaging (i.e. LVEF quantification), which serves as an important clinical value for certain types of cardiovascular diseases.

3) It is common for conventional 2D T2*w image to have off-resonance artifact at inferior wall (heart-lung interface) present [315–317]. This issue is much more improved in the proposed LRT method because the continuous acquisition does not require breath holds or ECG gating, and the self-navigated retrospective gating allows for the retrospectively selection of a cardiac and respiratory state, mitigating off-resonance and motion artifacts [318].

4) Standard cardiac early enhancement acquisitions are performed at 1-3 min after Gd injection. Given the time-sensitive nature, only a few slices can be acquired within the time window. Although early MVO has been proven to be more sensitive [319,320], late MVO is by far a more preferred method because its stronger relationship between MVO size and MACE and LV remodeling [202,321,322], which may be attributed to late MVO is more stabilized contrast to facilitate a more robust MVO characterization. With the proposed LRT approach, 3D volumetric MVO can be characterized in a much more segmented contrast dynamics from early enhancement to late enhancement, enabling more sophisticated analyses. Besides, for both early and late enhancement T1-weighted acquisitions, inversion time needs to be determined

beforehand. However, the proposed LRT method will only need to be determined retrospectively, which also optimizing the imaging workflow.

The slight deviation of MVO size can be attributable to imperfect slice matching and potential imaging artifact acquisition from conventional 2D single-shot acquisition.
In conventional CMR, 2D single slice early MVO imaging was acquired within 10-15 s. However, in the proposed LRT imaging, each section takes about 57 s. The slight discrepancy in early MVO size (Figure 2.8B) can be due time course of MVO change is more drastically at first few minutes.

Despite the achievement of simultaneous characterization of MI, MVO, IMH and LVEF using the fully ungated, free-breathing 3D imaging within 15 min, some aspects of the method can still be improved. First, IMH characterization was compared between conventional pre-contrast T2* and post-contrast LRT T2* imaging. It is also true that there are mild T2/T2* shortening effects of low doses of gadolinium [323]. However, in our study, no significant difference was found in IMH characterization. In our study design, we compared single-slice MVO characterization in early and late enhancement between two methods two days apart (Day 6 and Day 8). This may introduce some level of mismatch in slice location due to two separate localizers during scans. In addition, the current study has only been validated in animals with LAD infarctions. Additional studies are needed to validate the method, particularly in IMH patients in a clinical setting among the spectrum of MI patients.

2.5 Conclusion

A fully ungated, free-breathing 3D T1, T2* weighted imaging approach based on the low-rank tensor formulation has been successfully developed. It shortens the whole CMR protocol by a

factor of 4 and overcomes critical image artifacts from undesirable cardiac and respiratory motion. The proposed approach is expected to facilitate patients in post-contrast MI characterization and risk stratification.

CHAPTER 3: NATIVE T1 ENTROPY FOR RISK STRATIFICATION IN MYOCARDIAL INFARCTION

3.1 Introduction

As described in Chapter 1, MI from sudden obstruction of coronary artery affects ~1 million people in the US per year [324]. Despite the major advance in the diagnosis and treatment on cardiovascular diseases, the incidence of post-MI CHF has increased in recent studies [324,325]. Recently, a growing appreciation underlying the development of CHF in the post-MI settings is that there are large varieties of tissue characteristics between MIs, whether acute or chronic. The fibrotic tissue is widely validated as a signature tissue substrate within MI starts from several days after MI. IMH plays a pivotal role in evolving substrates in the MI tissue, as its presence is the hallmark injury the most severe form of tissue injury post MI, CCS stage 4 MI [17]. IMH expands the injury following extravasation of red blood cells into the necrotic tissue, culminates in the deposition of ferric iron crystals within MI tissue, and leads to fatty degeneration of cardiac tissue driven by macrophage activation, lipid peroxidation, foam cell formation, and ceroid production toward chronic MI remodeling. IMH has also been identified as a key predictor of MACE including HF, VAs, myocardial rupture etc. Therefore, there is a need to characterize substrates within MI to facilitate improved understanding of the pathophysiology of the MI and disease progression. With such information, optimal diagnosis, treatment plan with a more differentiated, tissue injury stage-specific therapies and improved prognostics can be developed and tested.

MRI is a powerful non-invasive imaging tool used to assess MI. The gold standard CMR method, namely LGE, for MI assessment currently depends on detecting large relative signal

intensity differences between hyper-enhanced, focally scarred myocardium and normal myocardium with low signal intensity. However, studies have shown that LGE identified MI has its limitations in characterizing its physical substrate and MI is more than just a region with homogeneous replacement fibrosis, or as defined previously, gray zone (a mixture of viable myocytes and collagen strands) in myocardium, in both acute and chronic MI subjects.

Several non-contrast parametric mapping techniques in CMR imaging are capable of characterizing the substrates of MI. Of these, native T1 mapping is one the most established methods in chronic MI. However, T1 mapping can be sensitive to multiple tissue substrates such as fibrosis, iron deposition and fat deposition. And to our knowledge, these substrates play significant role in MACE of MI patients independently. As is summarized in CCS consensus and, these three substrates manifest as different severity of MI from least severe as fibrosis, to coexistence of fibrosis and iron, then to coexistence of fibrosis, iron and fat as the severest form of MI (chronic). On native T1 mapping, T1 is slightly elevated for fibrosis, lowered for iron deposition and there is complex T1 response to fat depending on the fat fraction (Figure 3.1). In a severest form of MI, the traditional averaging intensity levels is unlikely to capture its heterogeneity in the region.

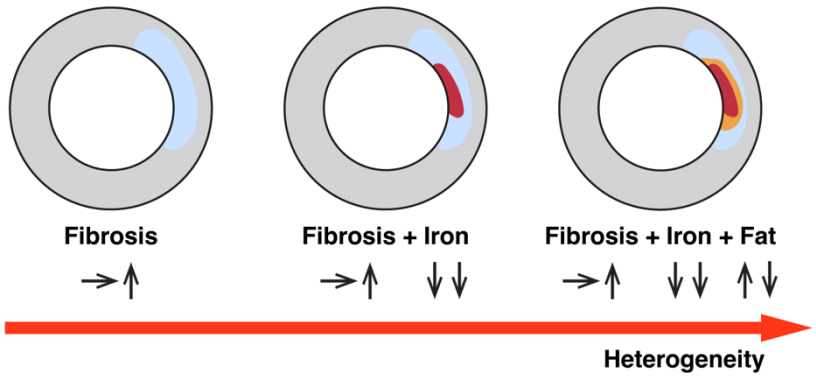


Figure 3.1 Illustration of chronic MI severity based on substrates and increase of native T1 heterogeneity as chronic MI become severer.

Thus, due to the concerns over such traditional signal intensity averaging of images unable to recognize subtle differences and detect invisible signal changes [326,327], magnetic resonance texture analysis (MRTA), which belongs to radiomics, includes extensive technologies modeling the spatial distribution of pixel grayscale based on the latent texture. Studies have shown that MRTA in MI has the potential to strengthen the diagnostic and prognostic value of imaging [278,326,328–331]. Recently, there have been several novel approaches to measure new imaging markers from native T1 maps which may provide diagnostic or prognostic values. T1 mapping tissue heterogeneity on the whole LV myocardium has been found to provide improved risk stratification and prognostic values. There have been several studies for texture analysis on MI based on its heterogeneous nature in the MI region, most of which are based on LGE images [332], which showed promising prognostic values for patients with ventricular arrythmia. There is one study which showed that combination of texture analysis and T1 mapping values could provide high diagnostic accuracy for transmurality and MVO [282]. Despite these findings, the underlying mechanism of native T1 heterogeneity on its MI physical substrate is not well studied.

To study the heterogeneity of T1 mapping within the MI region, we investigated how strongly affected of MI region with substrates such as fibrosis, iron and fat deposition due to different severity of MI corresponds to different native T1 heterogeneities. In this chapter, we employed entropy as indicator of heterogeneity on native T1 maps to study its potential in MI characterization for cardiac risk stratification. We hypothesized that based on what is known about MI, there is substantial heterogeneity of native T1 within the MI region due to the colocalization of replacement fibrosis, iron deposition and fatty metaplasia at different stage of MI severity. In this way, by characterizing the infarction, T1 heterogeneity can be a potential biomarker for probing severity of MI, facilitating disease stratification for surviving MI patients.

3.2 Methods

3.2.1 Simulation Study

Native T1 MOLLI response to fat fraction was theoretically validated by Kellman et al. [245] on 1.5T system in theory, with specific patient cases at 1.5T and 3T. Since there are some key differences in imaging parameters from our MOLLI protocol at 3T imaging system, we conducted the Bloch simulation on our own native T1 mapping parameters. Balanced SSFP readout was simulated to illustrate signal polarity of water and fat. We used the MOLLI imaging scheme with some key differences (Table 3.1): the TR for bSSFP readout was 2.40 ms, FA was 35^{o} and MOLLI used 5 pulses with linear ramp flip angle to catalyze toward steady state. The actual number of phase encoding was 60 with center at line 30. MOLLI used a tan/tanh adiabatic inversion with 10.24 ms duration, a minimum TI of 100 ms, and TI increment of 80 ms, and the MOLLI acquisition used a 3(3)5 protocol employed by Siemens 3T system. The simulation was performed using a heart rate of 60 bpm. Then the magnetization for varying combinations of water and fat based on was simulated based on Bloch simulation. T1 measurements was estimated with PSIR 3-parameter curve fitting (Equation 1.2) with recovered signal polarity and the conventional LL correction (Equation 1.3).

MT effect was not simulated in the calculation of myocardial signal, therefore a myocardial T1 assumed a nominal value of T1 = 1000 ms and T2 = 45 ms in the calculations. Fat was modeled by a single spectral component at -420 Hz (3T) with T1 = 400 and T2 = 100 ms [243]. The fat fraction was defined as $FF = F/(W + F)$, where W and F are the water and fat signal amplitudes respectively.

Magnetization signal recovery curves were plotted as the magnitude of the transverse magnetization (M_{xy}) using the phase of the fully recovered image at FF = 0% at longest TI as

positive. After the 3-parameter non-linear curve fitting, the curves and fits were shown to illustrate the mismatch between the bi-exponential model of combined water/fat and the fitted mono-exponential model. The estimated values of T1 versus FF are indicated for each plot and resembled in an individual plot to show the relationship between T1 and FF.

Table 3.1 Key parameters of our imaging protocol compared to previous simulation.

	Kellman et al.	**Our Protocol**
TR (ms)	2.65	2.40
Flip angle (°)	35	35
catalyzation	5 linear ramp-up	5 linear ramp-up
# of Phase Encode	63	60
Center line of k space	27	30
MOLLI scheme	5(3)3	3(3)5

3.2.2 Phantom Study

To validate the T1 response to various fat fraction, we constructed a stable fat-water phantom comprised of eight 15mL vials with varying fat volume percentages (0, 2.5, 5, 10, 20, 30, 40, 100%) by emulsifying method. Eight corresponding volumes of soybean oil were dispensed into vials. 43 mM sodium dodecyl sulfate (surfactant) and 43 mM sodium chloride were dissolved in distilled, deionized water at room temperature. 3.75 mM sodium azide was added to suppress microbial growth. Agar (2.0% w/v) was added over heat until it melted. More details are described in [333].

3.2.3 Animal Study: Preparation and Study Design

27 canines were studied according to the protocol approved by IACUC. 3 hours occlusion of LAD followed by reperfusion was conducted in order to create ischemic reperfusion injury.

CMR scans were performed in Day 5 to Day 7 (acute), Week 8 (sub-chronic), Month 6, Year 1+ (includes Year 1 and Year 1.5) after MI. 14 subjects include at least one chronic scan (Month 6, Year 1 or Year 1.5) were recruited for this study. Of those, number of 6-month, 1-year and 1.5-year scans were 9, 11 and 9 respectively (Figure 3.2A).

3.2.4 Patient Study

Patient studies were approved by the Institutional Review Board (IRB) and all patients provided written informed consent prior to enrollment. Seventy MI patients were prospectively enrolled between August 2017 and October 2018. The primary inclusion criteria were STEMI subjects who have undergone primary PCI and were not contraindicated for CMR; primary exclusion criteria were previous MI, arrhythmia, renal insufficiency, metallic prosthetic implant, and claustrophobia. 46 out of 70 patients underwent two CMR scans on 5-7 days post PCI and 6 months follow-up. Due to its image quality and whether the full image protocol was run, 26 patients were included for the analysis in the end (Figure 3.2B).

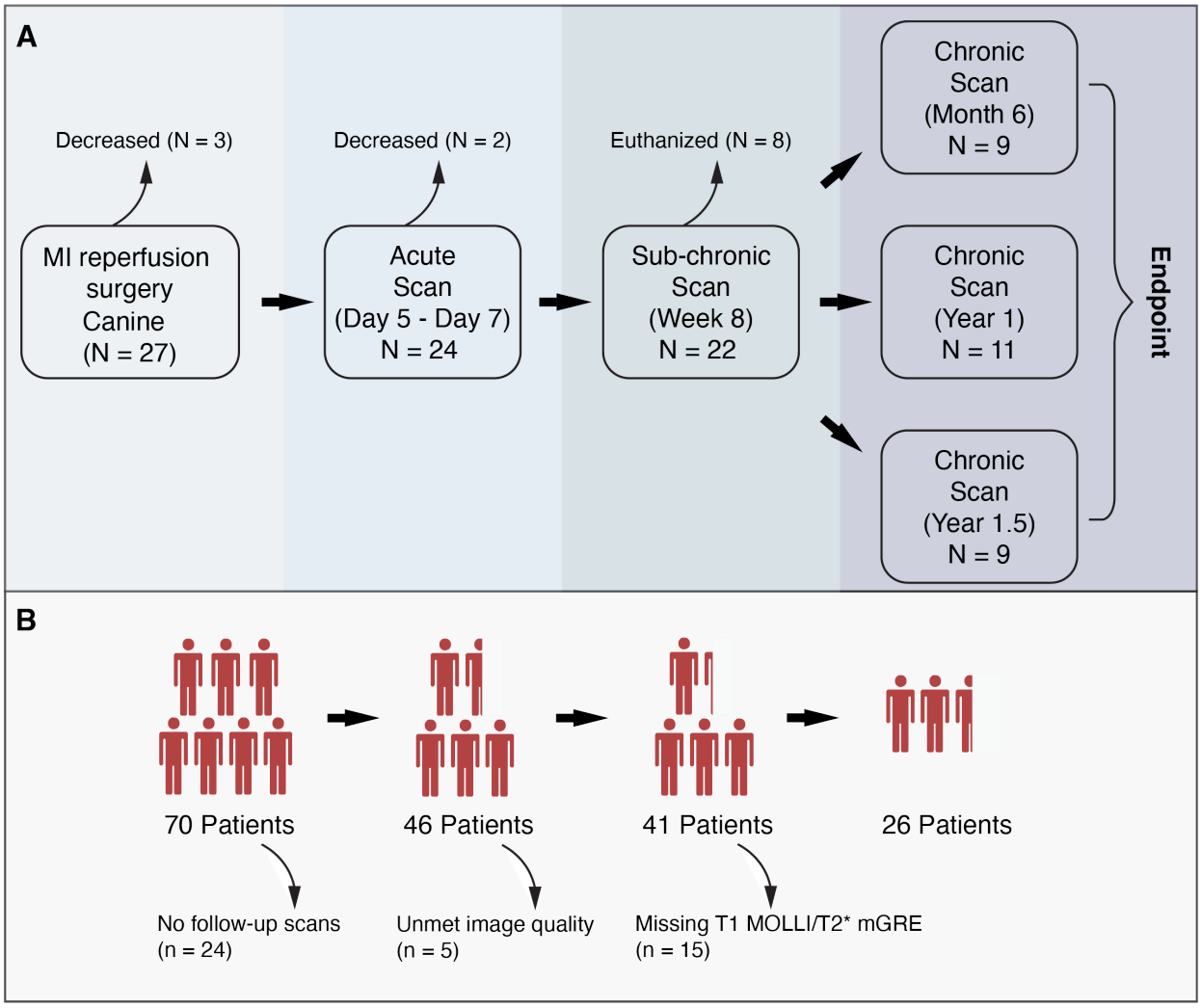


Figure 3.2 Study Details - canine subjects and human patient. **A)** Illustration of canine subjects undergoing reperfusion injury. Subjects that have at least one chronic scan in Month 6 were included in this study (N = 14). 9 out of 14 subjects underwent 6-month scan, 11 out of 14 subjects underwent 1-year scan, and 9 out of 14 subjects underwent 1.5-year scan. **B)** 26 patient data were analyzed due to loss of follow-up scans (n = 24), unmet image quality (n = 5) and missing native T1 mapping and T2* images from 70 prospectively recruited patients.

3.2.5 MRI protocols

3.2.5.1 Ex-vivo Phantom MRI

The fat phantom was scanned in a 3.0T MRI system (MAGNETOM Biograph scanner, Siemens Healthcare, Erlangen, Germany). Native T1 maps were acquired using MOLLI sequence (8 inversion times with 3+5 images) and IR Spin Echo (IRSE) sequences on the phantom in a cross-

sectional view. In order to be able to run MOLLI sequence in ex-vivo phantom, ECG triggering was simulated on the console for 60 bpm. Imaging parameters run for MOLLI are: TIs = 100, 180, 1100, 1800, 2100, 2180, 3100, 4100 ms, flip angle = 35°, TE = 1.10 ms, TR = 287.36 ms and bandwidth = 1078 Hz/pixel. IRSE were acquired with TIs = 50, 210, 350, 500, 1000, 1500, 2400, 3000 ms, TE = 8.00 ms, TR = 8000 ms, bandwidth = 789 Hz/pixel. Both images were acquired on cross-sectional direction of the vials at $1.4 \times 1.4 \times 6$ mm^3 voxel size with matched slice location. T1 MOLLI maps were generated on the console, while the IRSE T1 maps were created offline in MATLAB.

3.2.5.2 CMR in canine study

CMR scans at 4 distinct timepoints post MI were studied: 5 – 7 days (denoted as 1 week), 8 week, 6 months and $\geqslant$ 1 year post MI. Canine studies were performed in a 3.0T MRI system (MAGNETOM Biograph scanner, Siemens Healthcare, Erlangen, Germany). T1, T2* mapping and LGE covering the entire LV (with no slice gap) were performed, respectively. Native T1 maps were acquired using MOLLI sequence (8 inversion times with 3+5 images). Minimum inversion time = 120 ms, flip angle = 35^o, and bandwidth = 1185 Hz/pixel. T2* maps were constructed from mGRE images acquired using the following imaging parameters: TR = 81.9 ms, 8 echoes with TEs = 1.39 to 9.79 ms with ΔTE = 1.20 ms, flip angle = 12^o, and bandwidth = 1185 Hz/pixel. LGE images were acquired using segmented PSIR reconstruction (TR/TE = 656/2.05 ms, TI = 340 ms, flip angle = 20^o, and bandwidth = 285 Hz/pixel). All T1, T2* and LGE images were slice and resolution matched and were acquired with spatial resolution $1.6 \times 1.6 \times 6$ mm^3.

3.2.5.3 CMR in patient study

Human studies were performed in a 3.0T MRI system (Vero, Siemens Healthcare, Erlangen, Germany). Native T1 maps were acquired using MOLLI sequence (8 inversion times with 3+5 images). Minimum TI = 120 ms, flip angle = 35°, and bandwidth = 1085 Hz/pixel. T2* maps were constructed from multi-gradient-echo images acquired using the following imaging parameters: TR = 650 ms, 8 echoes with TEs = 2.15 to 15.73 ms with ΔTE = 1.94 ms, flip angle = 18°, bandwidth = 815 Hz/pixel. LGE images were acquired using segmented PSIR reconstruction (TR/TE = 122/3.22 ms, flip angle = 25°, and bandwidth = 140 Hz/pixel, optimal inversion time was chosen accordingly to null remote myocardium). All T1, T2* and LGE images were resolution matched and were acquired in the short-axis orientation at spatial resolution $1.4 \times 1.4 \times 6$ mm^3.

3.2.6 Image Processing

3.2.6.1 Myocardium mask ROI identification

All image contours were delineated using cvi42 software (Circle Cardiovascular Imaging Inc. Calgary, Canada). Epi- and endo-cardium, and remote myocardial contours were manually drawn on LGE images and all quantitative maps with careful exclusion of any blood pool signal. MIs were identified by semi-automated Mean+5SD method on LGE images. Similarly, those contours were copied to the T1 and T2* quantitative maps with visual adjustment according to the change of anatomy during scans.

3.2.6.2 Fat-water Separation

Fat fraction (FF) map and R2* maps were generated using an already validated algorithm: advanced multi-echo iterative decomposition of water and fat (previously described as IDEAL algorithm) [232,241]. And ROIs drawn from T2* maps were applied to FF and R2* maps to

calculate the mean fat fraction and R2* in MI and remote region respectively. Level of fat and iron deposition were measured within the infarcted region.

3.2.6.3 Heterogeneity analysis on T1 map

Histogram of ROIs (MI and remote myocardium) in native T1 maps was computed. The 1st and 99th percentile (sorted from minimum to maximum) were identified per subject on canine T1 maps at all time points. In this way, it was possible to remove the outliers from artifacts and a full range of T1 from the dataset were assessed. The histogram was then applied with 20 bins, and entropy analysis was performed according to the equation:

$$Entropy = -\sum_{i=1}^{n} p_i \log_2 p_i \,, \tag{3.1}$$

where n is number of bins from histogram, p_i contains the normalized histogram counts.

3.2.7 Statistical Analysis

Statistical analyses were performed on Prism 10 (GraphPad Software, La Jolla, USA) and IBM SPSS Statistics (version 29.0, IBM Corporation, Armonk, USA). Data normality was tested using Shapiro-Wilk test. The paired t-test or Wilcoxon signed-rank test was conducted based on data normality to compare the entropy score of ROIs on native T1 maps (denoted as T1 entropy), fat fraction and R2* values between MI and remote myocardium. The unpaired t-test or Wilcoxon signed-rank test was used to compare those three metrics of the same ROIs across different timepoints. Simple linear regression was used to estimate the correlation between T1 entropy and fat fraction, T1 entropy and R2*, and fat fraction and R2*. R-square was measured to determine goodness of fitting. $P < 0.05$ was set to statistical significance for all analyses.

3.3 Results

3.3.1 Simulation Results from T1 MOLLI on Fat Fraction

The alternating polarity of bands between water (myocardium) and fat using bSSFP readout is shown in Figure 3.3A. The opposite polarity of the off-resonance response of fat when the myocardium is on-resonance illustrates that the apparent signal measured during recovery can be combined as the difference rather than sum of the individual components. The magnetization of recovery signal is plotted for water/fat mixtures (from 0% FF: water only to 100% FF: fat only) at varying FF for MOLLI acquisition scheme (Figure 3.3B). Notably, the estimated T1 values of fat water combination varies substantially with FF. The circles represent the measurements times of our MOLLI protocol, and the blue lines are curve fits for estimating T1 based on a mono-exponential model for a single species. The estimate of T1 vs FF due to the mismatch from a mono-exponential are plotted (Figure 3.3C) with mixtures of myocardium and fat. T1 elevation is approximately linear with FF in the range of low FF (< 20%). For FF in the range of 30-50%, the recovery signal model is in drastically poor fit, where the estimated T1 can be undefined in this range.

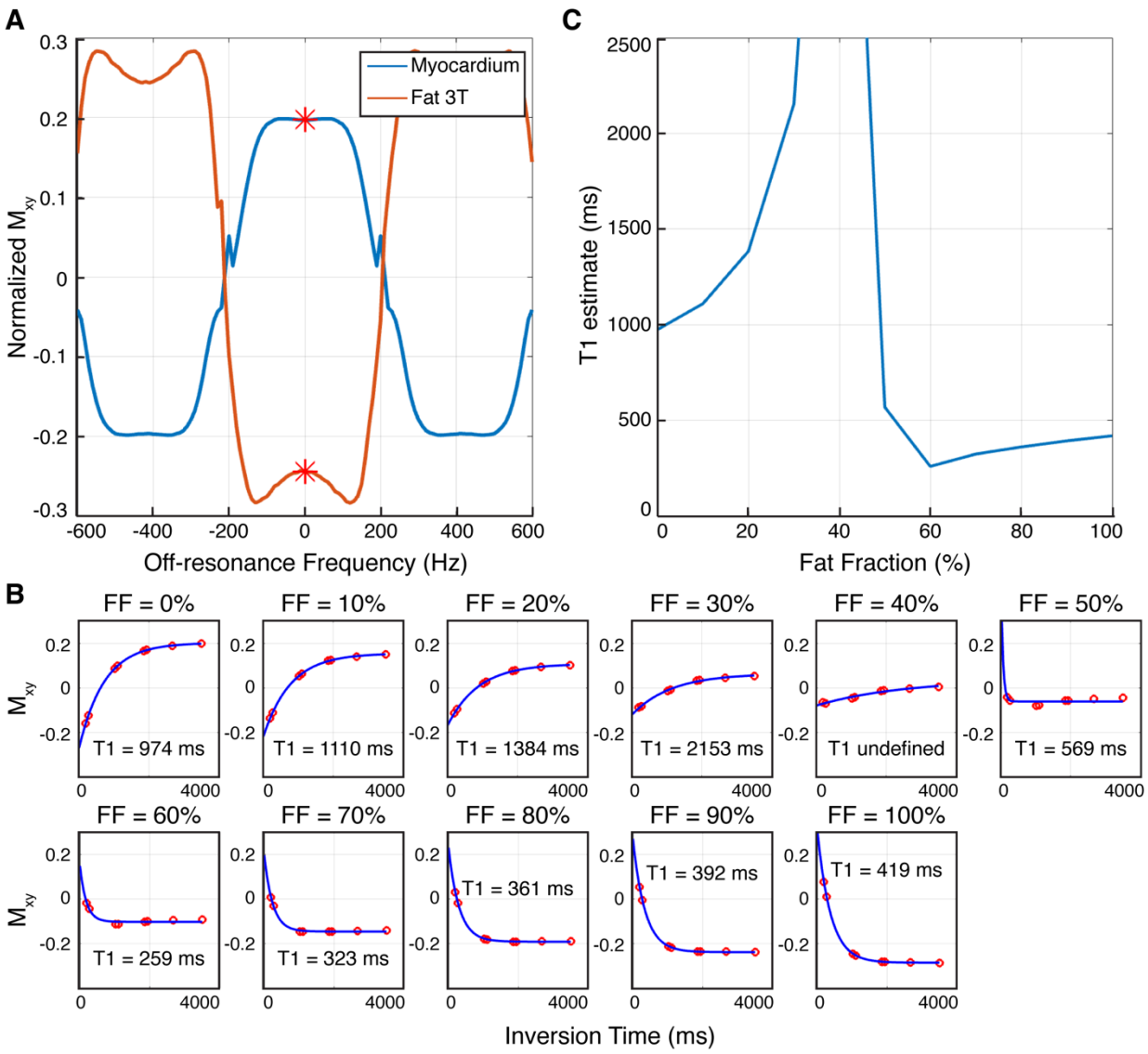


Figure 3.3 Simulation results to illustrate native T1 MOLLI response to mixture of water and fat. **A)** bSSFP off-resonance response for myocardium (blue) and fat (red) illustrating that the polarized signal at on-resonance (0 Hz) for typical MOLLI protocol with TR = 2.40 ms and FA = 35°. **B)** Inversion recovery measurements (circles) for out-of-phase water and fat mixtures at various fat fractions (0 – 100 %, with 10% increments) and 3-parameter mono-exponential fits (blue) using MOLLI protocol. Estimated T1 values are displayed on top of each plot. **C)** Estimated T1 of fat water mixtures vs FF for inversion recovery using MOLLI protocol.

3.3.2 T1 MOLLI Response Validation in Fat Phantom

The fat phantom made with 0, 2.5, 5, 10, 20, 30, 40, 100% fat fraction was shown in Figure 3.4A and its T1 maps from MOLLI and IRSE are shown in Figure 3.4C and Figure 3.4D. T1 values

from each fat fraction fitted by IRSE sequence shows decrease of T1 values as fat fraction increases. However, in T1 MOLLI maps, T1 value increased as fat fraction increases in low fat fraction (<20%). This effect peaked at 20% fat fraction and then decreased as fat fraction increased. The T1 response in MOLLI sequence was in line with the T1 response from the analytical simulation. Notably, the T1 value in 30% and 40% fat fraction showed high variability, which can also be explained our simulation due to the fitted T1 value can be extremely poor or even undefined so that the T1 value can be either high or low. In general, the phantom results align well with our results from simulation. Both results lay foundation for the high T1 heterogeneity for fat deposited MIs.

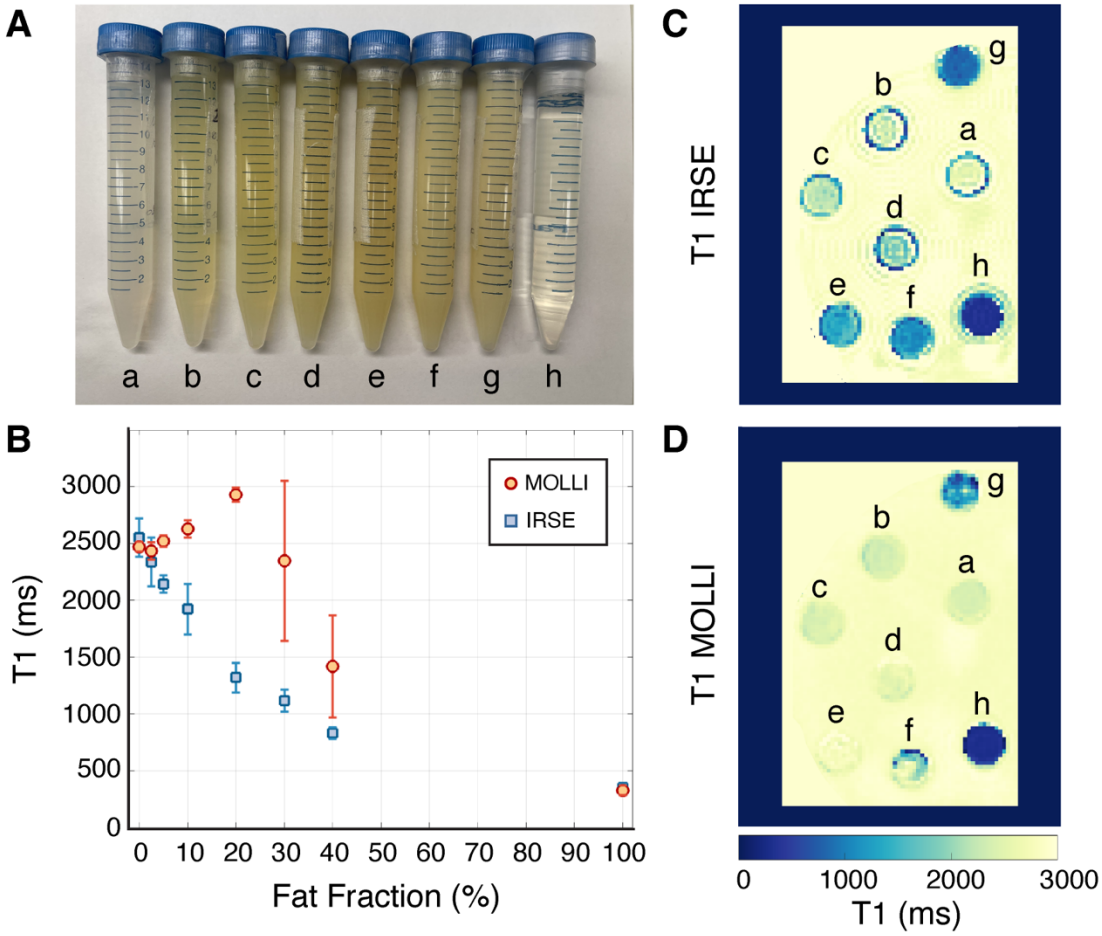


Figure 3.4 The make of the fat phantom and its validation in two T1 sequences. **A)** Illustration of fat phantom from left to right: 0%, 2.5%, 5%, 10%, 20%, 30%, 40% and 100% fat fraction, notably 100% fat

fraction is made of soybean oil completely. **B)** Comparison of T1 values of from MOLLI scheme and IRSE at each fat fraction. The fitted maps are shown in **C)** and **D)**.

3.3.3 T1 Entropy, Fat Fraction and R2* In The Canine Model At All Time Points

The mean, SD, 1 percentile and 99 percentiles of T1 values within MI and remote myocardium are shown in Table 3.2. The 1st percentile and 99th percentile of T1 values for MI and remote myocardium are 772 ms (subject 1, Year 1.5) and 1723 ms (Subject 8, Day 7), and 951 ms (Subject 7, Year 1.5) and 1475 (Subject 14, Day 7) ms respectively. To enable a wide range of T1 values for entropy analysis, T1 range was set from 750 ms to 1750 ms with 20 bins. Thus, each bin contained a range of 50 ms T1 value.

Table 3.2 Descriptive T1 values on volume-based analysis at all time points. Mean, Standard Deviation (SD), 1st percentile and 99th percentile for MI and remote myocardium is displayed. The lowest 1st percentile and highest 99th percentile are highlighted in red for both MI and remote myocardium.

Subject	Time points	MI				Remote			
		Mean	SD	1%	99%	Mean	SD	1%	99%
1	Day 7	1385	106	1107	1659	1168	24	1096	1220
	Week 8	1149	101	874	1344	1197	32	1113	1275
	Month 6	1227	120	893	1562	1177	26	1117	1244
	Year 1	1241	156	823	1680	1139	32	1078	1201
	Year 1.5	1247	164	**772**	1654	1150	33	1082	1219
2	Week 8	1273	94	1016	1482	1163	48	1050	1270
	Year 1	1311	117	1036	1596	1145	44	1044	1275
	Year 1.5	1245	105	981	1543	1161	44	1080	1309
3	Day 7	1376	94	1114	1586	1163	48	1065	1265
	Week 8	1156	76	984	1349	1161	33	1095	1232
	Year 1	1175	102	979	1482	1160	51	1042	1291
	Year 1.5	1156	82	953	1327	1168	45	1076	1303
4	Day 7	1353	99	1139	1551	1126	47	996	1237
	Week 8	1192	73	1066	1393	1117	27	1055	1191
	Year 1	1352	137	1096	1698	1167	48	1043	1277
	Year 1.5	1138	56	953	1327	1084	43	1076	1303
5	Day 7	1345	66	1183	1507	1204	37	1101	1286
	Week 8	1298	63	1177	1428	1224	40	1046	1342
	Month 6	1225	62	1109	1416	1153	37	1090	1246
	Year 1	1238	98	1091	1596	1123	46	1015	1286

6	Day 7	1364	96	1088	1616	1211	31	1141	1276
	Week 8	1307	63	1177	1478	1222	36	1156	1336
	Month 6	1323	78	1180	1493	1177	28	1108	1232
	Year 1	1259	96	999	1490	1158	24	1095	1214
7	Day 7	1387	78	1172	1532	1149	29	1075	1197
	Week 8	1157	98	930	1406	1139	42	1034	1235
	Month 6	1202	129	878	1529	1166	29	1100	1231
	Year 1	1194	168	798	1623	1155	37	1073	1238
	Year 1.5	1197	148	809	1543	1102	49	**951**	1279
8	Day 7	1368	108	1169	**1723**	1186	51	1087	1329
	Week 8	1280	75	1138	1490	1167	21	1118	1214
	Month 6	1290	103	1101	1581	1153	28	1090	1217
9	Day 7	1388	84	1172	1547	1160	27	1110	1247
	Week 8	1185	48	1072	1314	1161	34	1106	1276
	Month 6	1197	57	1065	1382	1180	30	1100	1237
	Year 1.5	1221	67	1063	1389	1162	38	1062	1264
10	Day 7	1399	90	1193	1649	1172	36	1085	1235
	Week 8	1162	94	878	1350	1174	32	1114	1273
	Year 1	1146	100	891	1384	1154	47	1054	1262
	Year 1.5	1176	113	795	1412	1145	41	1046	1242
11	Day 7	1389	72	1234	1603	1179	42	1085	1301
	Week 8	1223	88	977	1424	1181	30	1118	1264
	Month 6	1215	161	792	1615	1176	32	1116	1254
12	Day 7	1389	87	1200	1610	1183	37	1106	1293
	Week 8	1287	87	1100	1532	1209	33	1145	1329
	Month 6	1370	94	1175	1592	1280	61	1190	1404
	Year 1	1277	140	942	1560	1199	37	1135	1333
	Year 1.5	1313	146	994	1647	1174	51	1029	1282
13	Day 7	1388	104	1168	1625	1169	38	1094	1241
	Week 8	1147	94	905	1347	1198	33	1127	1285
	Year 1	1144	117	827	1386	1191	55	1051	1336
	Year 1.5	1149	105	859	1331	1208	35	1144	1298
14	Day 7	1458	70	1283	1598	1238	71	1124	**1475**
	Week 8	1240	79	1129	1453	1161	38	1066	1242
	Month 6	1184	90	1038	1507	1157	39	1080	1244
	Year 1	1181	49	1107	1315	1193	35	1104	1244

As is shown in Figure 3.5A, T1 entropy within MI at all timepoints were significantly higher than that in remote myocardium (Day 7: 2.55 ± 0.31 vs 1.28 ± 0.43, Week 8: 2.45 ± 0.37 vs 1.23 ± 0.34, Month 6: 2.65 ± 0.57 vs 1.22 ± 0.36 and Year 1+: 2.87 ± 0.49 vs 1.51 ± 0.40, $P < 0.001$ for all comparisons). Over time, T1 entropy was significantly increased in MI at Year 1+

comparing to its earlier time points (Figure 3.5B, Day 7: $P < 0.001$, Week 8: $P < 0.001$). Fat fraction of MI in Day 7 and Week 8 were both at the same level as remote myocardium ($2.44 \pm 0.98\%$ vs $1.94 \pm 1.15\%$, $P > 0.05$ and $2.58 \pm 1.36\%$ vs 2.12 vs 1.52%, $P > 0.05$ respectively) while fat fraction of MI in both chronic time points (Month 6 and Year 1+) were significantly higher (Figure 3.5C, $4.92 \pm 2.95\%$ vs $2.39 \pm 1.36\%$, $P < 0.001$ and $5.98 \pm 3.93\%$ vs 1.83 vs 1.72%, $P < 0.001$ respectively). Comparing within MI regions, Fat fraction in both chronic time points (Month 6 and Year 1+) were significantly higher than Day 7 and Week 8 (Figure 3.5D, $P < 0.001$), which indicates fat deposition over time courses of MI remodeling from acute ischemic myocardium diseases. R2* of MI at Week 8, Month 6 and Year 1+ were significantly higher than that of remote myocardium (Figure 3.5E, Week 8: 53.81 ± 15.70 ms^{-1} vs 35.82 ± 13.14 ms^{-1}, $P < 0.001$, Month 6: 51.15 ± 18.03 ms^{-1} vs 38.30 ± 6.86 ms^{-1}, $P < 0.01$, Year 1+: 45.34 ± 9.87 ms^{-1} vs 31.69 ± 6.96 ms^{-1}, $P < 0.001$). In MI region, R2* in Day 7 was not significantly different from Year 1+. However, it was significantly elevated in Week 8 and Month 6 (Figure 3.5F).

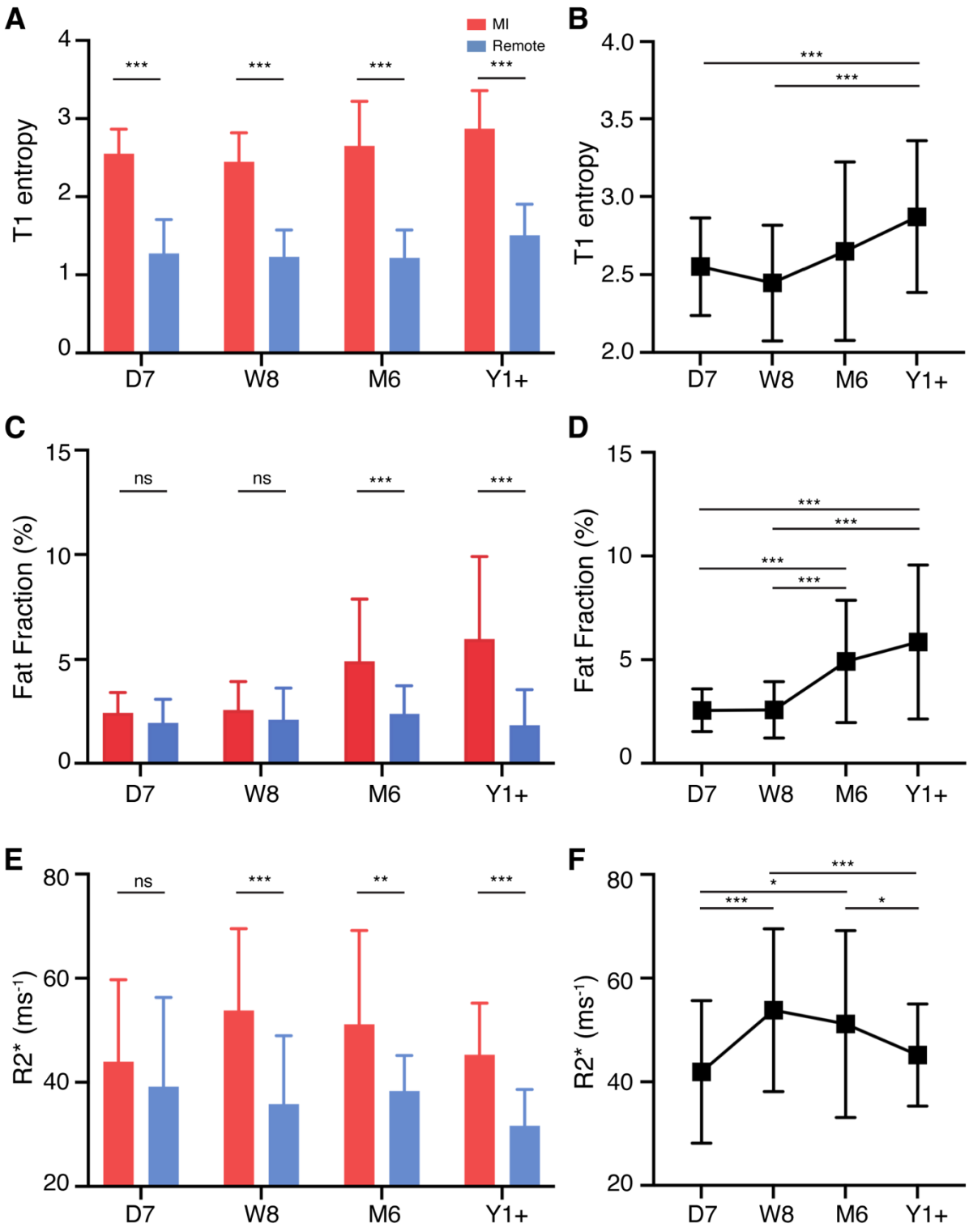


Figure 3.5 Time evolution of T1 entropy, fat fraction and R2* of MI and Remote myocardium. Bar plot of **A)** T1 entropy, **C)** FF, **E)** R2* and at Day 7, Week 8, Month 6 and Year 1+ (denoted as D7, W8, M6 and Y1+ respectively). Red columns are values in MI while blue columns are remote myocardium. All the columns are presented as mean values (column) plus standard deviations (whiskers). Line charts of **B)** T1 entropy, **D)** FF, **F)** R2* within MI from Day 7 to Year 1+. ns denotes $P > 0.05$, * $P < 0.05$, ** $P < 0.01$ and *** $P < 0.001$.

The relationship between R2* and fat fraction at all four timepoints is shown in Figure 3.6A. The stronger relationship between those two is further established over time as R^2 goes from 0.25 and 0.20 in acute to sub-chronic phase to 0.53 and 0.55 in Month 6 and Year 1+ (chronic), as well as higher slopes from Day 7 and Week 8 (0.042 and 0.039 respectively) to Month 6 and Year 1+ (0.14 and 0.28 respectively), which indicates that iron deposition in acute phase of MI may introduce fat metaplasia in chronic phases.

As for T1 entropy, the correlation from fat fraction is slowly established from no correlation in Day 7 ($R^2 = 0.013$, $P > 0.05$) to weak correlation in Week 8 ($R^2 = 0.093$, $P < 0.05$) to stronger correlation in Month 6 ($R^2 = 0.31$, $P < 0.01$) and Year 1+ ($R^2 = 0.45$, $P < 0.001$), showing that fat deposition in chronic MI strongly contributes to heterogeneity of T1 in MI region (Figure 3.6B). The correlation of T1 entropy and R2* is similarly established from acute (Day 7, $R^2 = 0.0049$, $P > 0.05$) to Week 8 ($R^2 = 0.20$, $P < 0.01$), Month 6 and Year 1+ ($R^2 = 0.47$, $P < 0.001$ and $R^2 = 0.42$, $P < 0.001$ respectively), also indicating that iron deposition is strongly contributing to T1 entropy (Figure 3.6C).

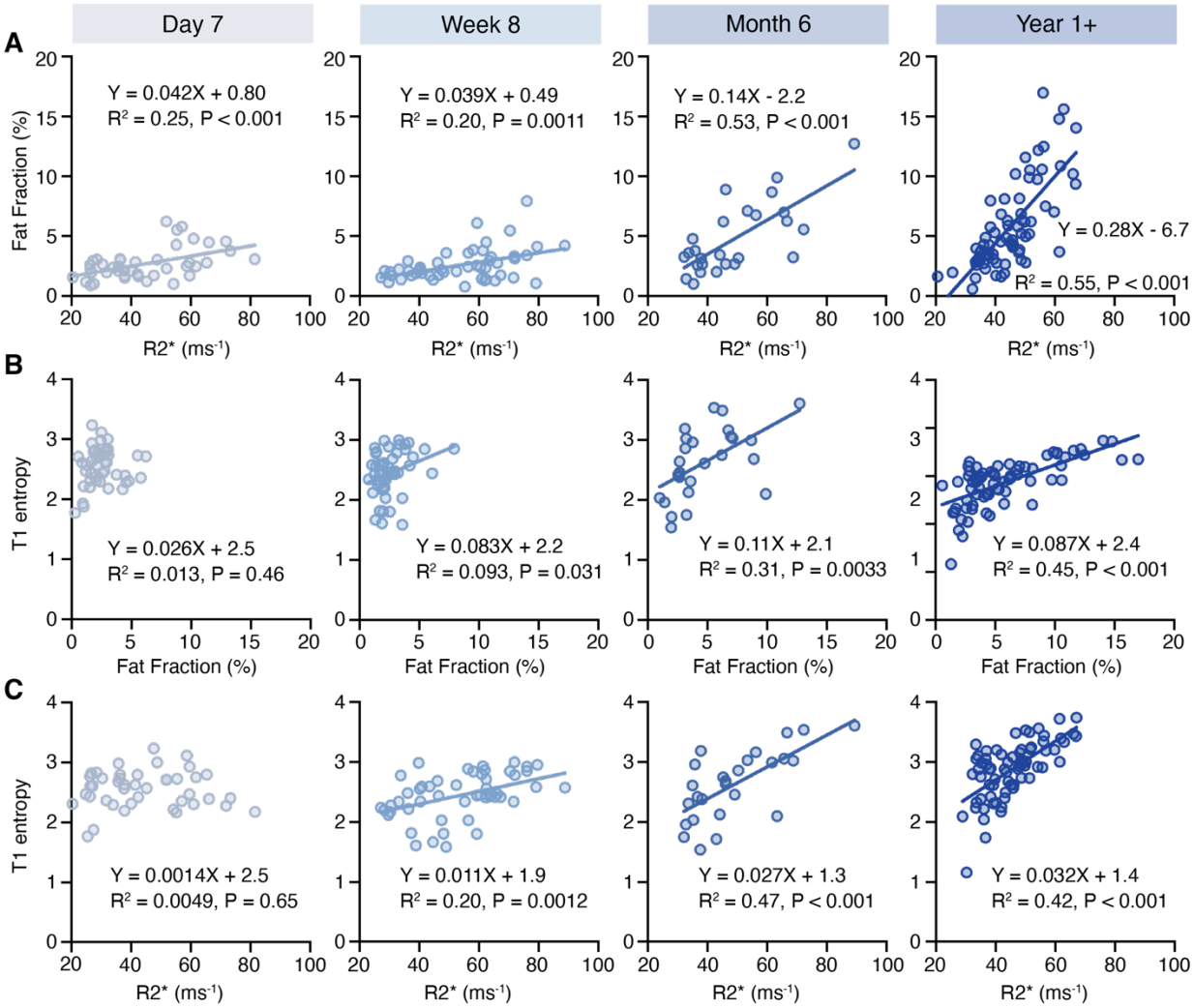


Figure 3.6 Linear regressions at 4 different timepoints on R2* vs fat fraction, FF vs T1 entropy, R2* vs T1 entropy in MI respectively. **A)** Scatter plots of relationship between R2* and fat fraction with linear regression, the fitted equations are shown in each plot with coefficient of determination and t-test results showing if the fitted slope is significantly different from 0. The results show strong correlation of fat fraction and iron deposition is shown in chronic MI. **B)** Scatter plots of relationship between fat fraction and T1 entropy, the correlation is established over time. **C)** Also scatter plots of relationship between R2* and T1 entropy is shown. Linear regression result shows that R2* is also a determinant factor of T1 entropy in MI.

3.3.4 T1 Entropy Categorized Based on R2* and Fat Fraction within MI in The Canine Model

T1 entropy, as an indicator of MI heterogeneity in native T1 mapping, was further studied by categorizing the fat fraction and R2* into four zones for putting all chronic (Month 6 and Year

1+) groups altogether, using the cutoff of R2* = 35 ms^{-1} and Fat Fraction (FF) = 4% (Figure 3.7A): Group 1: high FF and high R2* (N = 46); Group 2: low FF and high R2* (N = 27); Group 3: low FF and low R2* (N = 13); Group 4: high FF and low R2* (N = 0). Linear regression of FF and R2* for all zones showed strong correlation ($Y = 0.26X - 6.4$, $R^2 = 0.50$, $P < 0.001$). Each zone except Group 4 was further studied with linear regression of T1 entropy vs FF or R2*. For Group 1 (as shown in Figure 3.7B), strong correlation was found between all variables: R2* vs FF ($R^2 = 0.40$, $P < 0.001$), FF vs T1 entropy ($R^2 = 0.50$, $P < 0.001$), and R2* vs T1 entropy ($R^2 = 0.51$, $P < 0.001$), which indicates that for cases where both FF and R2* are high, they both contribute significantly to heterogeneity of T1 within MI region. For Group 2 (as shown in Figure 3.7C), no correlation is shown for R2* vs FF ($R^2 = 0.0050$, $P > 0.05$), and FF vs T1 entropy ($R^2 = 0.13$, $P > 0.05$), whereas weak correlation was found in R2* vs T1 entropy ($R^2 = 0.23$, $P < 0.05$), indicating that for cases where R2* is high but FF is low, only R2* is contributing significantly to T1 entropy. For Group 3 (as shown in Figure 3.7D), no correlation was found in R2* vs FF ($R^2 = 0.13$, $P > 0.05$), FF vs T1 entropy ($R^2 = 0.14$, $P > 0.05$), and R2* vs T1 entropy ($R^2 = 0.31$, $P = 0.050$). This indicates that for cases where both R2* and FF are low, neither FF nor R2* contributes to the heterogeneity of T1 within MI region. Notably, T1 entropy of Group 1, Group 2 and Group 3 are 3.04 ± 0.37, 2.57 ± 0.46 and 2.36 ± 0.63 respectively and its remote counterparts of T1 entropy are 1.44 ± 0.35, 1.49 ± 0.40, 1.39 ± 0.52 respectively (Figure 3.8). MI T1 entropy in Group 1 was significantly higher than Group 2 and Group 3 ($P < 0.001$ for both), and T1 entropy in Group 2 was significantly higher than Group 3 ($P < 0.05$). This indicates the effect from fat and/or iron deposition is playing a pivotal role in determining T1 entropy.

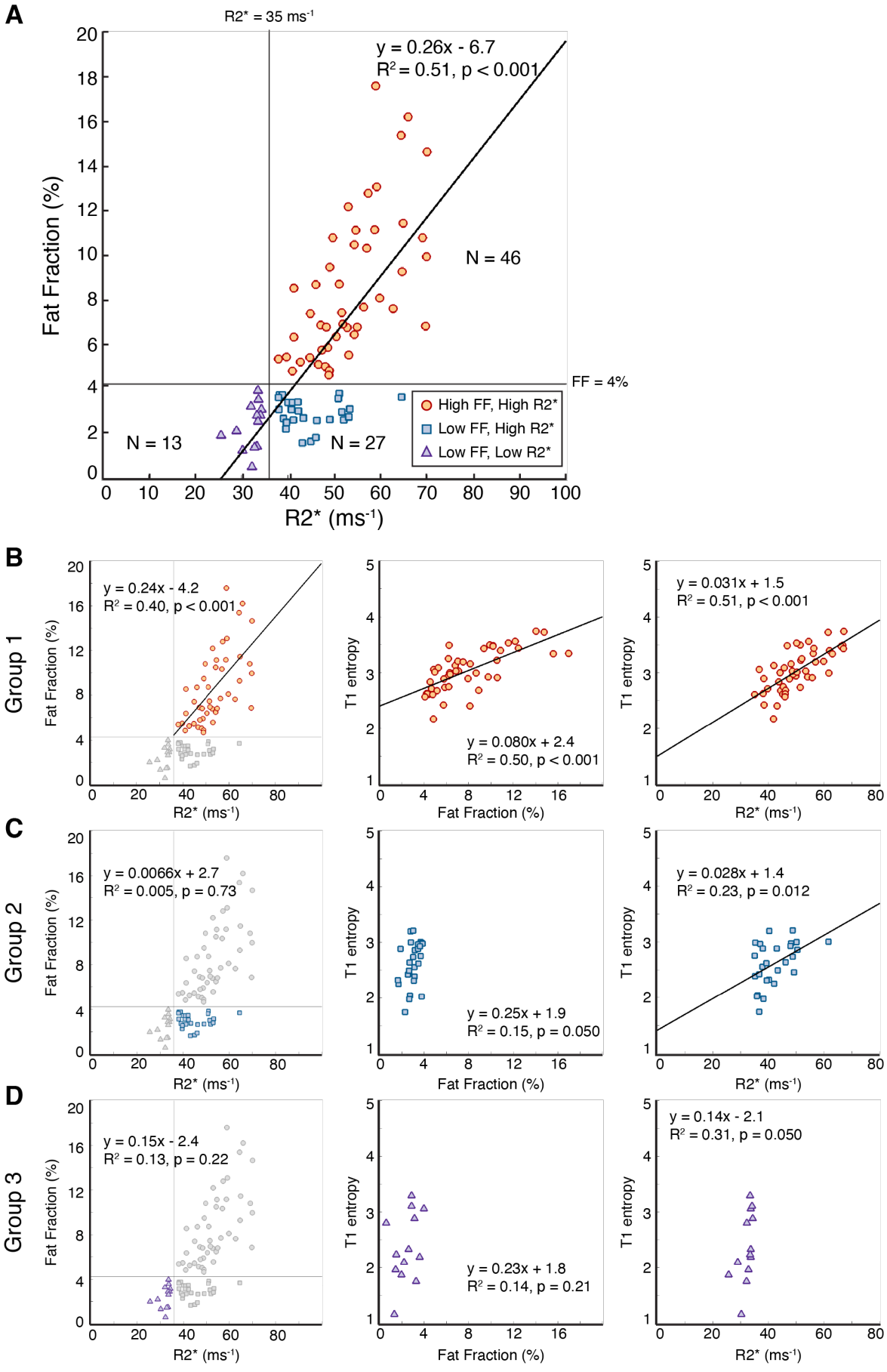

A
R2* = 35 ms-1
y = 0.26x - 6.7
R2 = 0.51, p < 0.001
N = 46
FF = 4%
N = 13
N = 27
High FF, High R2*
Low FF, High R2*
Low FF, Low R2*
Fat Fraction (%)
R2* (ms-1)
B
Group 1
y = 0.24x - 4.2
R2 = 0.40, p < 0.001
y = 0.080x + 2.4
R2 = 0.50, p < 0.001
y = 0.031x + 1.5
R2 = 0.51, p < 0.001
C
Group 2
y = 0.0066x + 2.7
R2 = 0.005, p = 0.73
y = 0.25x + 1.9
R2 = 0.15, p = 0.050
y = 0.028x + 1.4
R2 = 0.23, p = 0.012
D
Group 3
y = 0.15x - 2.4
R2 = 0.13, p = 0.22
y = 0.23x + 1.8
R2 = 0.14, p = 0.21
y = 0.14x - 2.1
R2 = 0.31, p = 0.050
T1 entropy
Fat Fraction (%)
R2* (ms-1)

Figure 3.7 Linear regressions of fat fraction and R2* for timepoints > 6 months can be divided into 3 sub-groups. **A)** Linear regression of FF vs. R2* are shown and categorized into 3 groups. Group 1: high fat fraction, high R2* group (R2* > 35 ms^{-1}, FF > 4%, red circle, N = 46), Group 2: low fat fraction, high R2* group (R2* > 35 ms^{-1}, FF < 4%, blue square, N = 27) and Group 3: low fat fraction and low R2* (R2* < 35 ms^{-1}, FF < 4%, red purple triangle, N = 13). Equation of linear regression is shown on top of the plot. The curves of linear regression fitting are shown only if the fitted slope is significantly different from 0 (P<0.05). Linear regression plots are shown in each group for R2* and fat fraction, fat fraction and T1 entropy, and R2* and T1 entropy respectively for 3 sub-groups in **B)**, **C)** and **D)**.

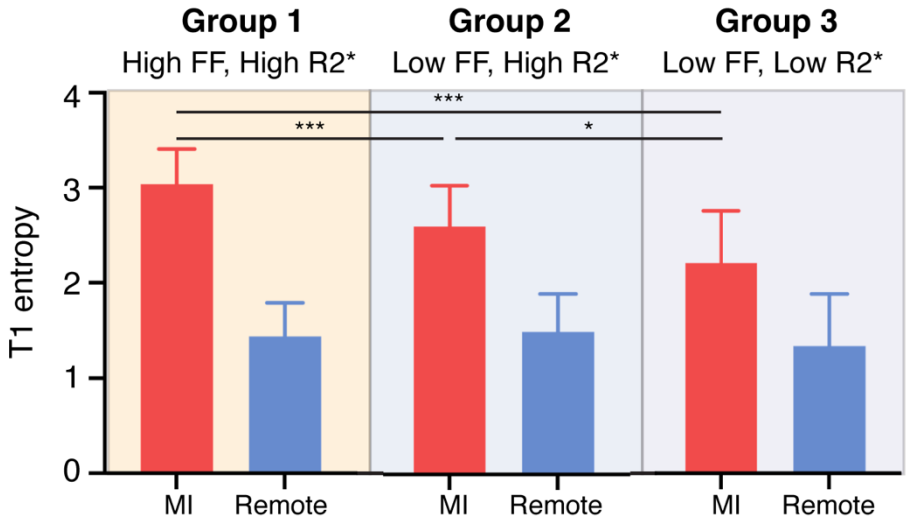


Figure 3.8 T1 entropy comparison in chronic MI (> 6 months) from three categories. Bar plot of T1 entropy in three categorized groups based on fat fraction and R2*. MI is encoded in red, and remote myocardium is encoded in blue. ns denotes P > 0.05 and *** P < 0.001.

Representative subjects for Group 1 (Subject 1), Group 2 (Subject 13) and Group 3 (Subject 14) are shown in Figure 3.9 respectively, where native T1 map, T1 histogram, FF map, R2* and LGE images from acute, sub-chronic and chronic time points are shown. Closest slices were matched according to LV and RV insertion points between different time points. For subject 1 (High R2*, high FF), T1 entropy goes from 3.00 to 3.00 to 3.72 from acute to chronic, while FF and R2* goes from 2.50%, 3.63%, 14.78%, and 58.73 ms^{-1}, 64.25 ms^{-1}, 61.44 ms^{-1} respectively (Figure 3.9A). For subject 2 (High R2*, low FF), T1 entropy goes from 2.14 to 2.87 to 2.93,

while FF and R2* goes from 1.22% to 1.30% to 3.62%, and 45.23 ms^{-1} to 61.95 ms^{-1} to 47.87 ms^{-1} respectively (Figure 3.9B). For subject 3 (Low R2*, low FF), T1 entropy goes from 1.93 to 2.22 to 1.16, while FF and R2* goes from 0.93% to 1.13% to 1.30%, and 18.12 ms^{-1}, 29.70 ms^{-1}, 30.30 ms^{-1} respectively (Figure 3.9C).

Histopathology from three representative subjects (same as Figure 3.9) with chronic MI are shown in Figure 3.10, where EMT staining was used to depict fibrotic and fat infiltration regions, and Prussian Blue sections were used to identify iron deposition. For subject 1 of high FF and R2*, fibrotic tissue, fat nodules, iron spots and necrotic tissue are colocalized within the MI region, validating that high heterogeneity in the MI tissue is the sources of T1 heterogeneity (Figure 3.10A). For subject 2 of low FF and high R2*, fibrotic tissue and iron spots co-localized within MI region, with few fat depositions, which is consistent with its MRI findings in the chronic phase (Figure 3.10B). Similar validations were found for subject 3, where few iron and fat depositions are shown in its pathohistological findings, validating its MRI findings for low FF, low R2* group (Figure 3.10C).

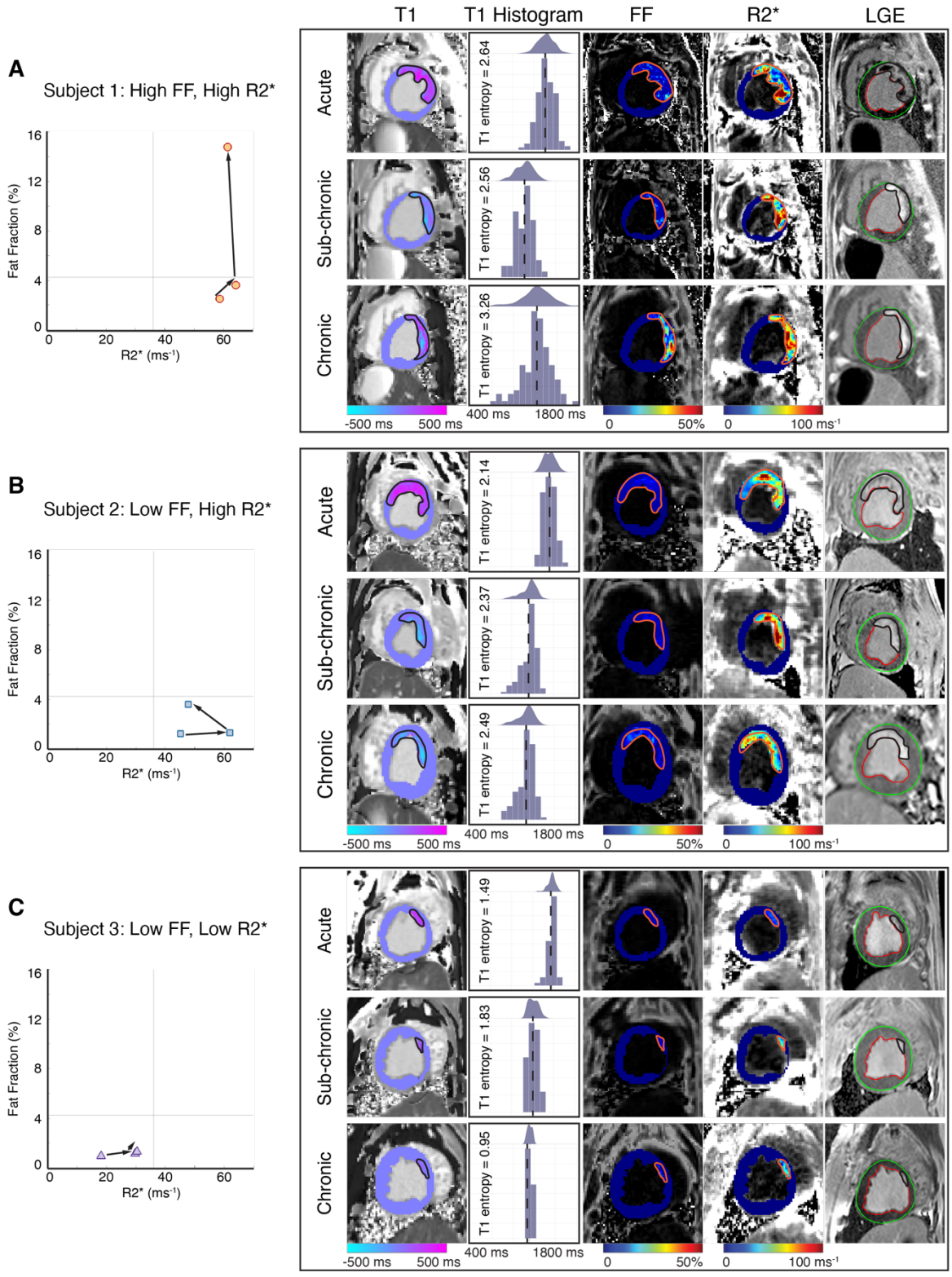


Figure 3.9 Representative cases for three subjects in each category depending on its fat fraction and R2* in MI region. One representative case for each zone is shown. On left: Scatter plot of R2* vs FF for each subject is shown at each time points, with arrows pointing from acute to sub-chronic to chronic phase. On right: Each subject contains native T1 map, histogram of T1 values within MI region, FF map,

R2* map and LGE images at acute, sub-chronic and chronic phases. For T1 maps, the myocardium is overlapped with a purple mask, with delineation of black contours denoting MI masks. Within MI masks, a color map was applied from -500 ms to +500 ms variation from T1 values of average remote myocardium. For T1 histogram, 20 bins were applied from T1 from 750 ms to 1750 ms, smoothed density plots are shown above the histogram. The dash lines show mean T1 values of the ROI and T1 entropy values are displayed on top of each plot. Both FF map and R2* maps are shown overlapping with myocardium masks in dark blue, with orange contoured MI region. And similarly, within MI region, color maps of fat fraction and R2* are shown respectively. LGE images for each subject with corresponding slices are shown with epicardium contours in green, endocardium in red, and MI in black.

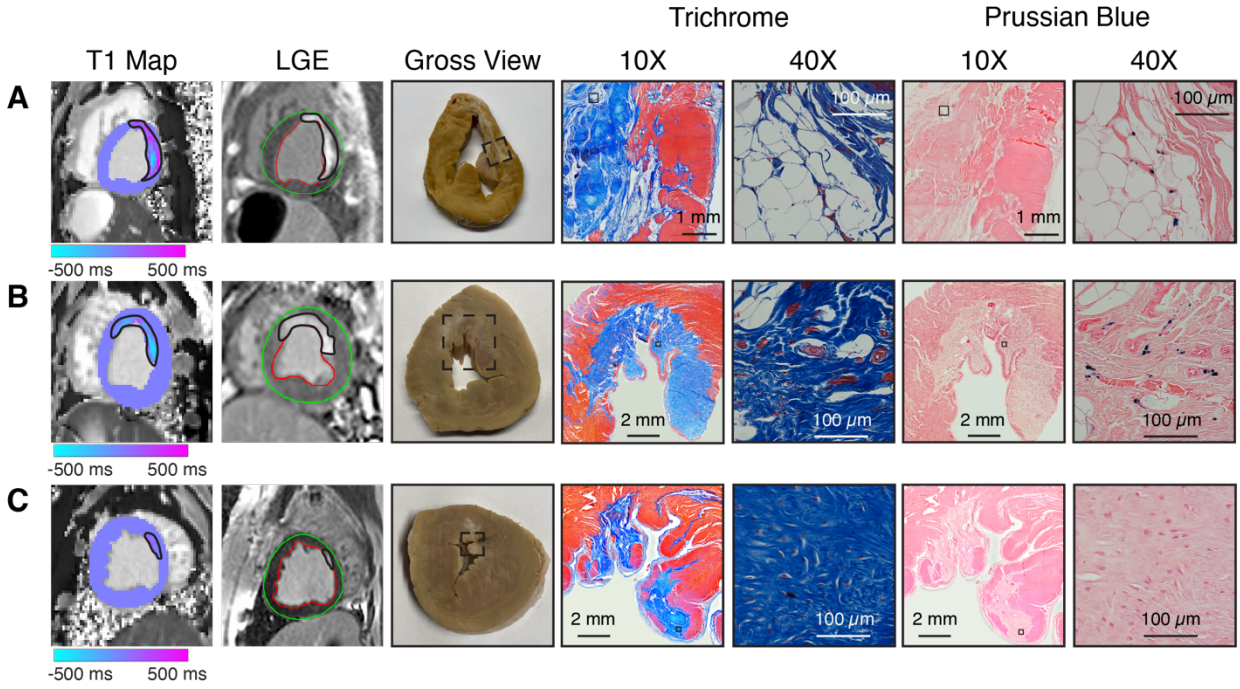


Figure 3.10 Histology validation of 3 Representative Subjects. Masson's Trichrome, Prussian Blue for three subjects: **A)** High fat fraction is shown as large nodules within fibrotic stains, blue spots were observed in Prussian blue staining with co-localization with fat nodules. **B)** Blue iron spots were found in Prussian blue staining while no high fat fraction area is seen**. C)** Small fibrotic region was found in Trichrome staining while no notable fat nodules or iron deposits were found in the infarcted region. Small rectangular arrows pointing to the 10× view images are magnified on the right with one remote region and one MI for each. Iron deposition is highlighted with triangular arrows.

3.3.5 T1 Entropy Validation in Patient Data

To further study the consistency of the tissue characters in ischemic MI and heterogeneity in T1 map within MI, patients subjects (N = 26) were studied on both acute (Day 7) and chronic (Month 6) phase. Patient characteristics along with CMR findings (LVEF, MI volume, IMH volume and MVO volume) are summarized in Table 3.3. T1 entropy and R2* were significant higher in MI than remote myocardium in both acute (T1 entropy: 2.97 $\pm$ 0.37 vs 1.90 $\pm$ 0.42, P < 0.001; R2*: 31.9 $\pm$ 12.7 ms^{-1} vs 28.5 $\pm$ 6.6 ms^{-1}, P < 0.001) and chronic MI (T1 entropy: 2.94 $\pm$ 0.37 vs 1.73 $\pm$ 0.50, P < 0.001; R2*: 34.1 $\pm$ 9.4 ms^{-1} vs 28.7 $\pm$ 6.2 ms^{-1}, P < 0.001, Figure 3.11A&E), while fat fraction was not significant different in acute phase between MI and remote myocardium (FF: 2.5 $\pm$ 1.1% vs 2.3 $\pm$ 1.3%, P > 0.05) while elevated in chronic MI (FF: 4.0 $\pm$ 2.5% vs 2.4 $\pm$ 1.3%, P < 0.001, Figure 3.11C). These findings are consistent with our animal study in canine subjects (Figure 3.5). For MI region specifically, T1 entropy and R2* were not significant different between two time points (Figure 3.11B&F), while fat fraction was significantly elevated in Month 6 (Figure 3.11D). Moderate relationship was found between R2* and fat fraction (Figure 3.12A, $R^2 = 0.45$, P < 0.001), fat fraction and T1 entropy (Figure 3.12B, $R^2 = 0.13$, P < 0.001), and R2* and T1 entropy (Figure 3.12C, $R^2 = 0.12$, P < 0.01). Similar results were found in canine data between Day 7 and Month 6, except R2* in MI at Day 7 and Month 6 were not significantly different (Figure 3.5F), and weaker relationships between R2*, Fat fraction and T1 entropy was found in patient studies (Figure 3.12).

Table 3.3 Characteristics of Patient Study Cohort

	Acute Phase (n = 26)	Chronic Phase (n = 26)
Age	55 ± 10	
Male sex, n (%)	24 (92)	
Body mass index (kg/m^2)	24.2 ± 2.4	
Cardiovascular risk factors, n (%)		
Hypertension	15 (58)	
Diabetes	8 (31)	
Hyperlipidemia	17 (65)	
Smoking	18 (69)	
Heart rate (bpm)	78 ± 11	
Infarct-related artery, n (%)		
Left anterior descending	21 (81)	
Left circumflex	(11)	
Right coronary artery	2 (8)	
Medication during admission, n (%)		
Antiplatelet therapy	26 (100%)	
Beta blocker	26 (100%)	
ACEI	23 (88%)	
ARB	5 (19%)	
CCB	2 (8%)	
Diuretic	8 (31%)	
Statin	26 (100%)	
Amiodarone	3 (12%)	
Nitrate	25 (96%)	
Cardiovascular magnetic resonance findings		
LV ejection fraction (%)	46.8 ± 6.2	49.3 ± 6.8
LV end-diastolic volume index (ml/m^2)	86.2 ± 14.7	84.7 ± 16.4
LV end-systolic volume index (ml/m^2)	46.1 ± 11.0	43.6 ± 13.1
MI volume (%LV)	33.7 ± 13.1	21.4 ± 8.6
IMH volume (%LV)	4.3 ± 4.9	3.3 ± 3.8
Late MVO volume (%LV)	3.6 ± 4.8	-

Data are reported as mean ± SD, median (IQR), or n (%) as appropriate.

None of the patients received thrombolysis

ACEI angiotensin converting enzyme inhibitor, ARB angiotensin receptor blocker, CCB calcium channel blocker, LV left ventricle, MI myocardial infarction, IMH intramyocardial hemorrhage, MVO microvascular obstruction

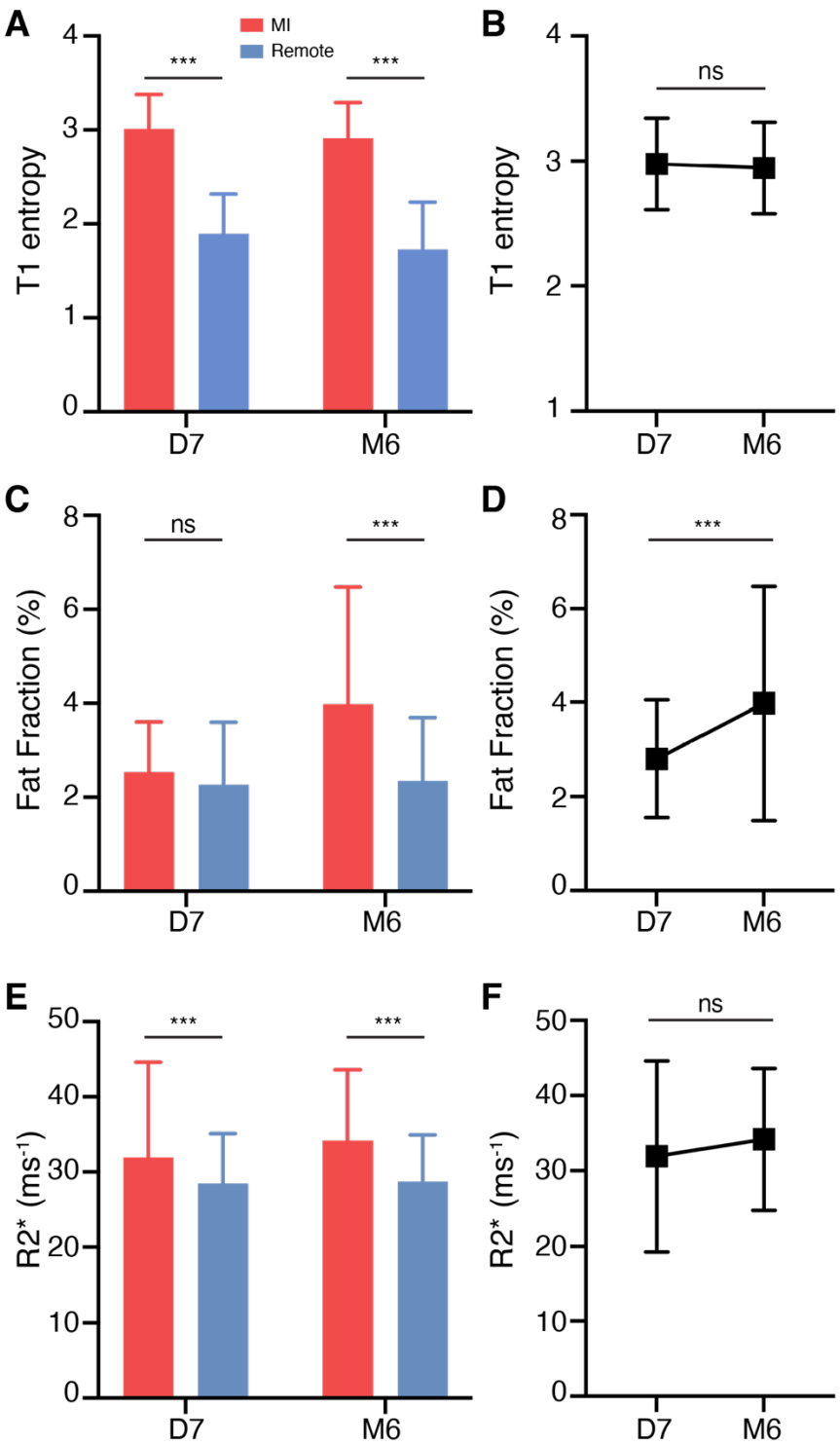


Figure 3.11 Time evolution of T1 entropy, fat fraction and R2* comparing between MI and remote myocardium in Day 7 (D7) and Month 6 (M6) respectively. Bar plot of **A)** T1 entropy, **C)** FF, **E)** R2* and at Day 7 and Month 6 (denoted as D7 and M6 respectively). Red bar denotes as MI while blue bar denotes as remote myocardium. All the columns are presented as mean values (column) plus standard deviations (whiskers). Line charts of **B)** T1 entropy, **D)** fat fraction (FF) and **F)** R2* within MI at D7 and M6 are shown on the left column. ns denotes $P > 0.05$, and *** denotes $P < 0.001$.

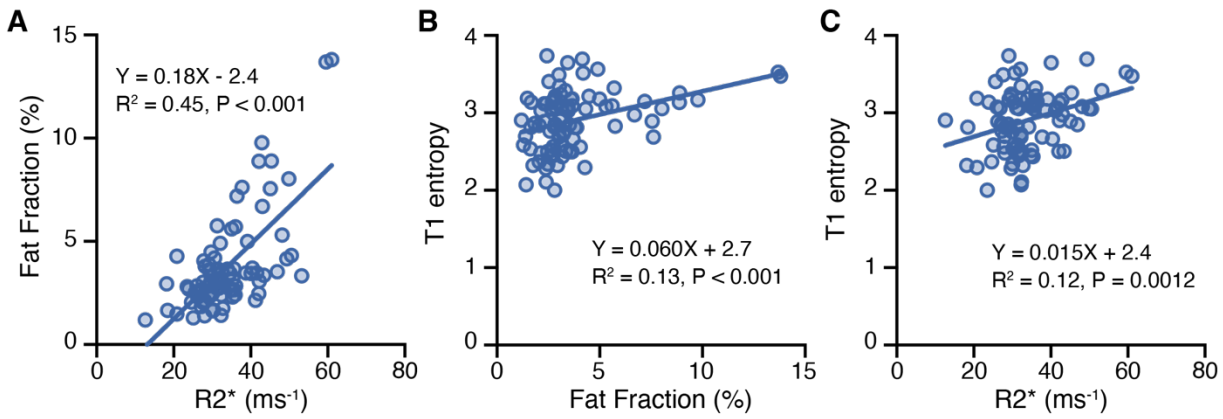


Figure 3.12 Linear regression between T1 entropy, fat fraction (FF) and R2* within MI region respectively at Month 6. Scatter plots of relationship between **A)** R2* and FF, **B)** FF and T1 entropy and **C)** R2* and T1 entropy within MI region with linear regression, and the fitted equations are shown in each plot with coefficient of determination and t-test results showing if the fitted slope is significantly different from 0. The results show strong correlation of fat fraction and iron deposition is shown in chronic MI.

By performing the same categorization on the human subjects, it is clear that there was more non-hemorrhagic slices in the dataset (Figure 3.13A, 60% in human subject vs. 15% in canine subject). With slices only from Group 1 (High FF, High R2*), the correlation between T1 entropy and fat fraction ($R^2 = 0.33$, $P < 0.05$), and T1 entropy and R2* ($R^2 = 0.26$, $P = 0.05$) are much stronger than the rest of the groups (Figure 3.13B). No significant differences were found in linear regression from Group 2 and Group 3. T1 entropies within MI of Group 1, Group 2 and Group 3 are 3.12 ± 0.28, 2.94 ± 0.33 and 2.78 ± 0.39 respectively and the remote counterparts are 1.53 ± 0.53, 1.77 ± 0.57, 1.78 ± 0.48 respectively (Figure 3.13C). Significant difference in Group 1 is found and Group 2 ($P < 0.05$) or Group 3 ($P < 0.001$). Our patient study validates the animal study and the theory we put forward about T1 heterogeneity and the severity of MI (Figure 3.1).

Representative images of one hemorrhagic (Group 1) and non-hemorrhagic MI (Group 3) patients are shown in Figure 3.14. The non-hemorrhagic MI subject shows no evident change in

T1 entropy along with fat fraction and R2* while the hemorrhagic MI subject shows increase in T1 entropy from iron and fat deposition.

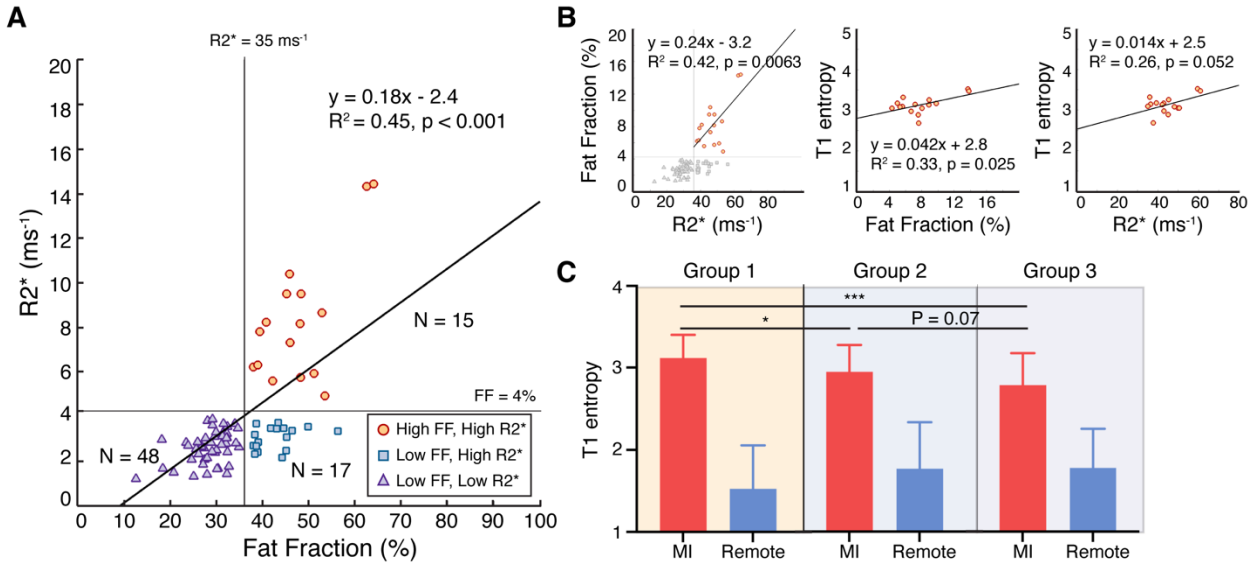


Figure 3.13 Categorization due to fat fraction (FF) and R2* on patient data. **A)** Linear regression of FF vs. R2* are shown and categorized into 3 groups same as canine data. Group 1: high FF, high R2* group (red circle, N = 15), Group 2: low FF, high R2* group (blue square, N = 17) and Group 3: low FF and low R2* (red purple triangle, N = 48). **B)** Scatter plot of R2* and fat fraction, fat fraction and T1 entropy, and R2* and T1 entropy respectively with linear regression is shown for Group 1. C) Bar plot of T1 entropy for each categorized group. T-test results are shown for each T1 entropy within MI among the three groups. *** denotes $P < 0.001$ and * denotes $P < 0.05$.

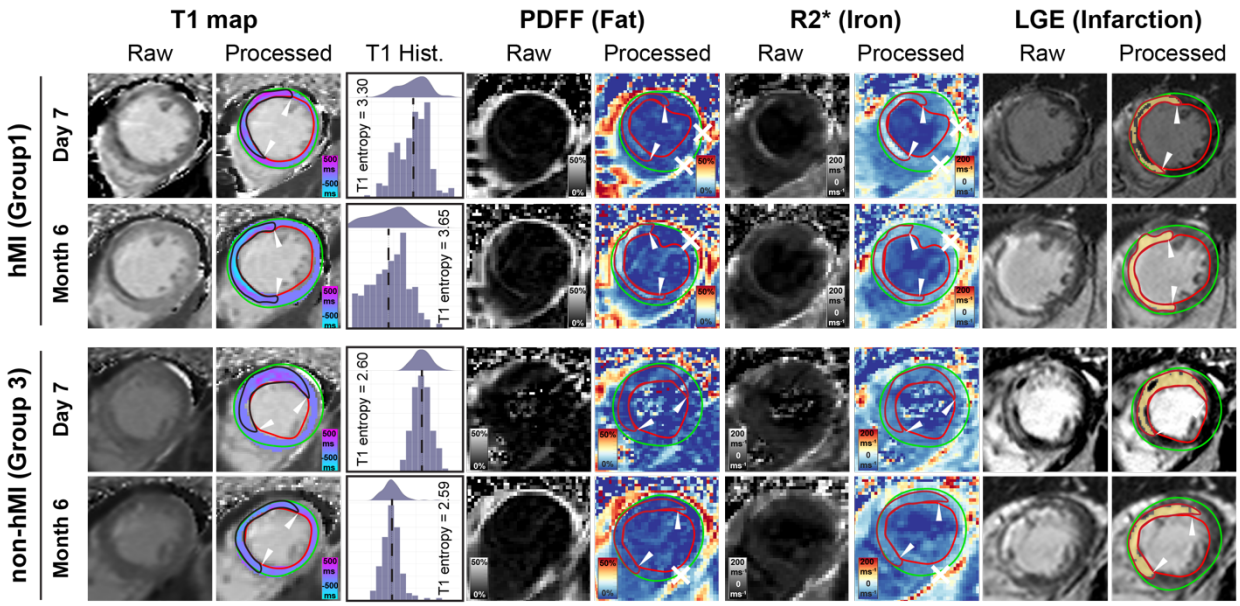


Figure 3.14 Representative images of two patients for hemorrhagic MI (hMI) and non-hemorrhagic MI (non-hMI). The subject of hMI is from Group 1 while non-hMI from Group 3. Each subject contains Native T1 map, histogram of T1 values within MI region, fat fraction map, R2* map and LGE images at Day 7 (acute) and Month 6 (chronic). For T1 maps, the myocardium overlapped with a purple mask, with delineation of black contours denoting MI masks. Within MI masks, a color map was applied from -500 ms to +500 ms variation from T1 values of average remote myocardium. For T1 histogram, 20 bins were applied from T1 from 6000 ms to 1600 ms, smoothed density plots are shown above the histogram. The dash lines show mean T1 values of the ROI and T1 entropy values are displayed on top of each plot. Both FF map and R2* maps are shown overlapping with myocardium masks in dark blue, with orange contoured MI region. Similarly, within the MI region, color maps of fat fraction and R2* are shown respectively. Heart-lung interface artifact from T2*w images were delineated in both maps as while crosses. LGE images for each subject with corresponding slices are shown with epicardium contours in green, endocardium in red, and MI in dark red. The extent of MI is also pointed out by white arrows.

3.4 Discussion

In this chapter, we demonstrated that native T1 entropy is capable of distinguishing MI from remote myocardium from acute to chronic phase. Due to its complex post-MI progression, the T1 entropy of MI was significantly elevated after 1 year for the canine model. By categorizing status of fat fraction and R2* (iron content) into four quadruples from chronic MI, we found T1 entropy of MI is strongly associated with both fat fraction and iron content in the high fat

fraction and high R2* group; T1 entropy is moderately associated with iron content in low fat fraction and high R2* group; and T1 entropy is not associated with iron content or fat fraction in low fat fraction and low R2* group. The difference in T1 entropy within MI between these three groups as well as remote myocardium lays the foundation for characterizing tissue substrates such as fibrosis, iron and fat deposition (Figure 3.1). Patient data with 6-month follow-up validates the findings from the canine model, albeit with slightly lower level of correlation. We conclude that T1 entropy is a predictor for heterogeneity of MI and a reliable biomarker for analysis of severity of chronic MI.

We also showed that over the progression of MI remodeling process toward chronic phase, fat fraction is significantly increased in after 6 month and R2* peaks during the subacute phase of MI (Figure 3.5), which are in line with the previous findings [45] where iron concentration increases until 6 months appears to be slight decrease between 6 months to 1 year. However, the effect of iron on fat metaplasia-inducing process is not reversible. In our study, a strong correlation between iron content and fat fraction within MI is established in Month 6 (Figure 3.6).

T1 entropy within MI, has shown to increase from acute to chronic phase after 1 year the canine study. Both canine and patient studies did not show significant changes in T1 entropy at 6 months, but fat fraction increased significantly, possibly due to large variation in the process of fat deposition for the 6-month MI. By dividing subjects into 4 quadrants based on fat fraction and R2*, we found three sub-groups in regarding to the iron and fat status of the tissue - Group 1: high fat fraction, high iron content; Group 2: low fat fraction, high iron content; Group 3: low fat fraction, low iron content. Significantly higher T1 entropy was discovered on the Group 1 than Group 2 and Group 3, indicating that fat is playing major effect in determining T1 entropy

for chronic MI, due to the fact that 1) the co-existence of fat and iron within MI: T1 increases as fat fraction increases under 20% while and T1 decreases as iron content increases; 2) non-monotonic response on T1 MOLLI map as a result of fat as illustrated in our phantom study for fat fraction from 20% to 40%.

The theory of T1 response to fat was initially put forth by Kellman et al. [245]. It was theorized in 1.5T based on the Bloch simulation of bSSFP sequence with conventional T1 MOLLI imaging parameters. The results were majorly validated in patient showcases under 1.5T field strength. In this study, we validated the T1 MOLLI response of varying water and fat mixture in our 3T system using Bloch simulation and ex-vivo fat phantoms we constructed. The trend of the T1 estimation from our simulation and ex-vivo phantom are comparable to previous reported study at 1.5T [245]. Generally, the estimated T1 values go through 3 phases as fat fraction increases from 0%. Phase 1: In low fat fraction (FF < 20%), T1 value increases almost linearly to fat fraction. Phase 2: In fat fraction from 20% to 50%, the estimated T1 value is extremely poorly fitted, where the estimated T1 can be undefined in this range. Phase 3: In fat fraction > 50%, fat signal starts to dominate and T1 values steadily increase to T1 value of fat. In our case, due to the fat fraction of our interest in lower than 50%, our phantom spans from 0% to 40% of fat. However, our studied showed that it is sufficient to prove that T1 increase over fat fraction 0-20% and decrease after that, laying the foundation for our heterogeneity analysis on large animals and patients.

Other than iron and fat deposition, T1 entropy in MI is also affected by edema or fibrosis. However, those were not directly addressed in this study. We know that edema peaks around 5-7 days after MI and resolves toward chronic phase. We found out that the entropy in acute MI (Day 7) when the edema is prominent, is significantly lower than that of chronic MI (Figure

3.4B), which indicates T1 entropy can also be a promising biomarker to distinguish acute vs chronic MI. For fibrosis, as it is hard to separate the effect of edema in acute to sub-chronic phase of MI, we found that MI T1 entropy from all subgroups are significantly higher than that of remote myocardium (Figure 3.8, $P < 0.001$). In addition, it is worth noting that for MI T1 entropy from Group 3 (low fat, low iron group) vs. that from remote showed in cases of low-fat fraction and low R2*, T1 entropy was significantly higher than that of remote myocardium (Figure 3.8), which indicates contribution of fibrotic tissue widespread in the MI region.

Despite the thoroughness of our work, it has its limitations. First, our work is limited to chronic MI. We were able to show acute MI with elevated MI T1 entropy, but it was not possible to validate edema. However, acute MI is studied extensively and existence of edema in acute phase is unquestionable. Therefore, it is reasonable to attribute T1 entropy elevation from acute MI primarily to edema. Second, the patient validation is not followed up longer than 1 year, where we found the most significant results in the canine model. However, using a sub-group of Month 6 patient data we were also able to show strong correlation between T1 entropy in MI and fat fraction and iron content.

3.5 Conclusion

In this chapter, we demonstrated native T1 entropy is elevated in chronic MI, which is strongly associated with iron and fat deposition. We conclude that the proposed native T1 entropy analysis offers a novel way to characterize chronic MI for risk stratification.

CHAPTER 4: INFLUENCE OF SPATIAL RESOLUTION AND SNR IN T2* MAPPING FOR DETECTION OF IRON DEPOSITS IN CHRONIC MI

4.1 Introduction

As discussed in Chapter 1, IMH and subsequent iron deposition are associated with the most severe form of reperfusion injury, which has emerged as the most prominent predictor of adverse clinical outcomes in MI [30,185,334,335]. Studies have shown that IMH is associated with larger MI size [25,208,336,337], adverse LV remodeling [43,338–340], poor clinical outcomes [26,341], and can serve as a substrate for lethal arrhythmias [48,49,293]. Further, several studies have also shown that IMH can result in persistent iron deposition and promote delayed infarct healing within the MI zone and cascading inflammation [46,155,211,294], which is a well-known factor associated with adverse remodeling. This iron-rich deposits in the scale of 10^{-1} mm^2 would cause much larger inflammatory area [46]. Thus, accurate detection and characterization of iron deposition within MI in sub-millimeter scale is crucial for investigating the mechanisms contributing to the adverse outcomes and development of novel therapies in MI patients with IMH. T2* CMR is the current clinical standard for detecting global and regional alterations in iron content in the heart [49,152,342]. However, current T2* CMR acquisitions are typically optimized for global myocardial iron deposition conditions (e.g., thalassemia) but not for regional iron deposition within chronic MI regions, including the spatial distribution and underlying myocardial tissue composition changes in IMH lesions.

Notably, the iron deposition in IMH in the myocardium can appear as a narrow band in chronic MI since there is about 20% of subjects suffered from wall thinning to < 6 mm [288]. While several studies point out that spatial resolution plays an important role in in diagnosis in small

focal lesions [289,290], current studies in attempting to use T2* CMR to characterize IMH often overlook its importance (Table 1.2). This leads to potential misses of small lesions of iron deposition. Being able to detect thin IMH in a small infarct is indispensable since existence of IMH results in multifold of MACE than the infarct without IMH [17]. Therefore, in order to detect and characterize the iron deposits within MI, however large the MI size is, spatial resolution and its influence needs to be studied to facilitate MI patients risk stratification and the following treatment plan.

As we know that from Equation 1.12, spatial resolution also proportionally affects SNR of the acquired MRI image. The latter is another key determinant for detection of iron deposits in T2* images. To define the SNR of images as an indicator for image quality can be subjective. Ideally, there is no downside of increasing SNR. From ISO industry standards, SNR thresholds of 40 is considered "excellent" image quality and 10 considered "acceptable" image quality [343]. In the field of medical imaging, it is widely accepted that an SNR of at least 5 is needed to be able to distinguish image features with certainty by Rose criterion [344,345]. A similar conclusion was found from a CT study that SNR is required for approximately 5 to be able to detect a circular 6-mm lesion [346]. Thus, as much as we would like to reach a finer resolution to reduce partial volume effect on one hand, we need to keep SNR high enough for the detection on the other hand. In this chapter we will systematically study this influence of spatial resolution on the detection and characterization of iron deposition in chronic MI. We hypothesized that the accuracy of detecting iron remnants from IMH in the chronic phase of MI may be compromised due to strong partial volume effects or low SNR at the typical spatial resolutions used with T2* CMR. We investigated our hypothesis using digital simulation phantom and a pig model of hemorrhagic MI to examine the effect of partial volume limitations in a rapidly thinning infarcted myocardium in the chronic phase following reperfusion. Subsequently, to remove other

confounding effects associated with cardiac and respiratory motion, blood flow, and off-resonance artifacts that are present in-vivo, we used freshly excised pig hearts with chronic MI. We then tested our studies with conventional T2* CMR with the same resolution sets in vivo. The endpoint of this study is to establish whether there is a limitation in identifying residual iron deposits in chronic hemorrhagic MI and, if so, to suggest a direction for improving the capability of detection based on T2* CMR.

4.2 Methods

4.2.1 Numerical Simulations

4.2.1.1 Ventricular Modeling

To investigate the relationship between spatial resolution, SNR on a thinned iron-rich (iron+) band on T2* maps of LV, a digital phantom was simulated in MATLAB 2022a (MathWorks, Natick, Massachusetts). The LV of a heart was simulated with a 3D ellipsoidal model. The model consists of a hollow truncated ellipsoid (see Figure 4.1) and the wall of the inner ventricle surface represents the endocardium and outer ventricle represents epicardium. The semi-axes in x, y, z directions are denoted as b_i, b_i (assuming circle shape in short-axis view), and a_i respectively and satisfies the equation [347]:

$$\frac{x^2}{b_i^2} + \frac{y^2}{b_i^2} + \frac{z^2}{a_i^2} = 1, \tag{4.1}$$

and is truncated at the intersection with the planes z = 0 and z = ka_O, where the k is a constant for truncation of slices of interest to display the ventricle from base to apex, where the usual location of MIs from LAD occlusion-reperfusion damage occurs. To reduce the computational expense, on x and y dimension, the simulated entity was truncated so that only second quadrant was left. Thus, the LV is displayed as a truncated quarter ellipsoid.

Previous CMR studies have shown that iron deposits within the chronic MIs begin at the sub-endocardium but do not extend beyond the mid-wall [293]. Thus, we simulated the iron+ band at the sub-endocardial region with semi-axis $b_{i1} = 1.2b_O$. To simulate a thinned iron+ band, the width of the iron+ band was approximately 1.0 mm so that it is simulated in transmurality of 2.5% on the truncated quarter ellipsoid (Figure 4.1B).

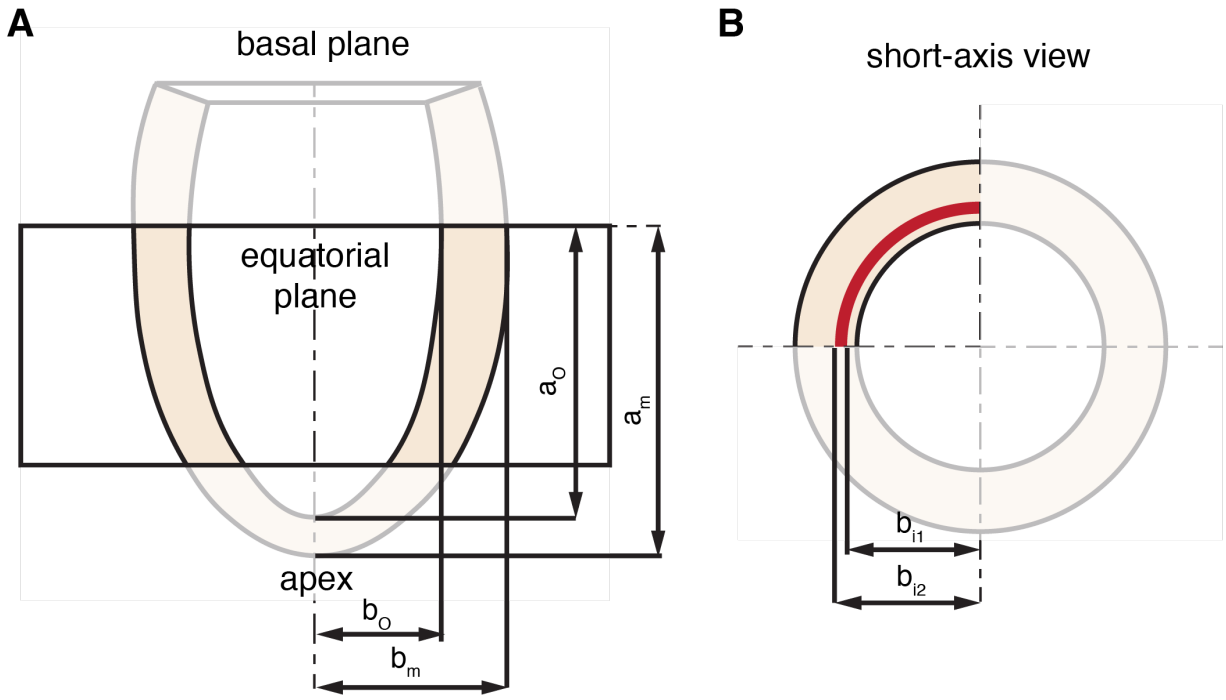


Figure 4.1 Side view and top view of the simulated ellipsoid for LV myocardium. The LV was simulated based on the ellipsoid modeling *[347]*, **A)** where $a_m = 5.0$ cm, $a_m = 4.0$ cm, $b_m = 4.0$ cm, $b_O = 2.4$ cm, the heart was truncated in long-axis dimension, where k = 0.6. **B)** In the short-axis view, the ellipsoid was truncated with the second quadrant. The iron-rich (iron+) band is simulated with parameters $b_{i1} = 1.2b_O$ and $b_{i2} = 1.2b_O + 0.025(b_m - b_O)$, such that the iron+ band is 1.0 mm wide at subendocardium.

4.2.1.2 Imaging Simulation

T2* is an empirical value under certain condition, as is briefly introduced in Equation 1.6. The field inhomogeneities is introduced when the spins diffuse through spatially varying static magnetic fields. When a spin diffuses through the spatially varying magnetic field, it experiences random magnetic field variations, and thereby loses phase coherence with neighboring spins. This mechanism particularly accelerates the decay of transverse magnetization and thereby reduces T2. The diffusion effect would dominate if the magnetic variability inducing particles are within radius of 10 μm [348]. In our case, the iron band is generally assumed as a homogeneous band range from 10^{-1} to 10^{0} mm which greatly surpasses 10 μm. Thus, it is reasonable to consider that the signal loss is independent of iron-band size because intravoxel dephasing is dominant. And this intravoxel dephasing can be approximated as T2* values.

Therefore, we used Bloch equation [133] to simulate T2* contrast in iron-rich region (T2* = 9.4 ms and T1 = 800 ms) and remote myocardium based on the existing literature (T2* = 40.1 ms and T1 = 1125 ms) [349,350]. The magnetization within the canvas was then simulated to derive the GRE signal at 5 different TEs based on the imaging parameter we would use for the ex-vivo scans (Table 4.1A). We employed the Bloch equation for spoiled GRE readouts [351]:

$$\frac{d\vec{M}(\vec{r},t)}{dt} = \gamma\vec{M}(\vec{r},t) \times \vec{B}(\vec{r},t) + \begin{bmatrix} -\frac{1}{T_2^*(\vec{r})} & 0 & 0 \\ 0 & -\frac{1}{T_2^*(\vec{r})} & 0 \\ 0 & 0 & -\frac{1}{T_1(\vec{r})} \end{bmatrix} + \begin{bmatrix} 0 \\ 0 \\ \frac{M_0(\vec{r})}{T_1(\vec{r})} \end{bmatrix}, \qquad (4.2)$$

where $\vec{M}(\vec{r},t)$ is the net magnetization, $\vec{B}(\vec{r},t)$ is magnetic field and $M_0(\vec{r},t)$ is the equilibrium magnetization. $T_1(\vec{r})$ is the longitudinal (M_Z) relaxation time constant, while $T_2(\vec{r})$ is the transverse relaxation time constant (M_{XY}). We assume perfect RF pulse excitation, thus the solution to Equation 4.2 can be simplified to:

$$M_{XY}(t) = M_{XY}(0)e^{-t/T_2^*}, \quad (4.3)$$

$$M_Z(t) = M_Z(0)e^{-t/T_1} + M_0\left(1 - e^{-t/T_1}\right), \quad (4.4)$$

here the shorthand complex notation is used: $M_{XY}(\vec{r}, t) = M_X(\vec{r}, t) + iM_Y(\vec{r}, t)$.

Each echo was added with different levels of Gaussian noise on both magnitude and phase dimension. The signal for the canvas was then averaged in a sliding window fashion based on different practical voxel sizes (in-plane resolution 0.4 - 2.0 mm^2 isotropic, and through-plane resolution 2 - 8 mm) to simulate the real imaging voxels at three different locations (illustrated in Figure 4.2A), where the through-plane resolution imposes stronger partial voluming effect towards apex. 5 different T2* weighted images were fitted using a 2-parameter fit to a mono-exponential model to generate T2* maps (Figure 4.2B). To assess the image quality, SNR the fitted of T2* map was computed using Equation 4.5 (Figure 4.2C):

$$SNR = \frac{mean(remote)}{\sigma(remote)}, \quad (4.5)$$

where $\sigma(remote)$ denotes SD of the remote myocardium. This will be used for determining if the noise level of the simulated images. The area under the curve (AUC) of Receiver operating characteristic (ROC) was performed to evaluate the performance of hemorrhage detection (Figure 4.2C). In total, 28 different spatial resolution, 3 noise levels, and at 3 different locations were simulated for the further analysis.

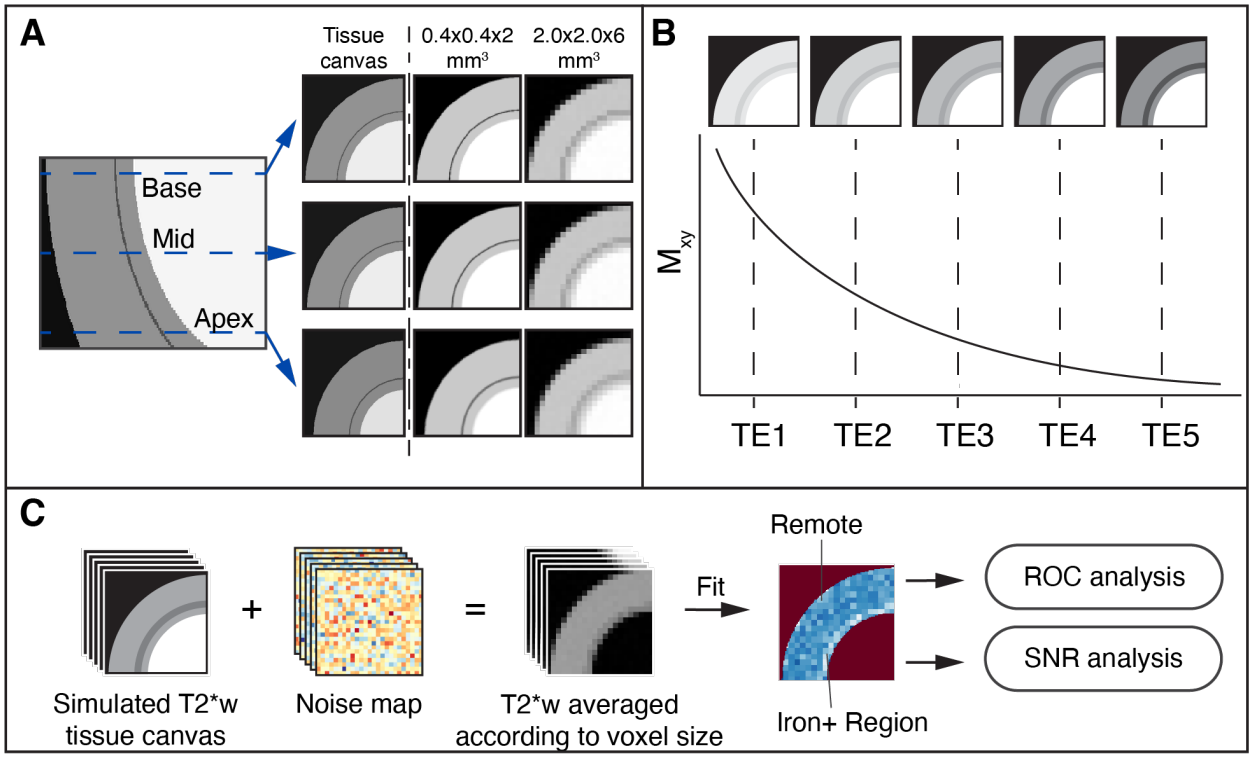


Figure 4.2 Numerical Phantom Simulation of iron deposits in the heart as T2* maps in various spatial resolution. **A)** Tissue canvas with $0.04 \times 0.04 \times 0.5$ mm^3 of matrix size $1024 \times 1024 \times 48$, the images are shown in T2* weighting. Three slices were imaged as basal, mid-ventricle and apical locations of the LV myocardium. Imaging voxels were simulated in a sliding window fashion. Here the sliding windows are $0.4 \times 0.4 \times 2$ mm^3 and $2.0 \times 2.0 \times 6$ mm^3 for illustration. **B)** Illustration of five, T2*-weighted (T2*w) images were simulated with TE1 to TE5 = 2.55, 5.80, 9.90, 15.56, 21.22 ms. This set of TEs was also used in ex-vivo imaging parameters (see Table 4.1). **C)** Illustration of different noise level adding to the weighted images, averaged to different resolution windows, and then fitted to T2* map. SNR analysis and ROC analysis were then computed to probe the image quality and capability of iron-rich (iron+) region detection.

4.2.2 Animal Studies

Pigs (N = 10, 20-25 kg at baseline) were sedated, intubated and anesthetized and subsequently underwent complete occlusion of the LAD with a balloon and reperfused after 90 min. Animals were euthanized at 8 weeks post-MI and the hearts were excised, rinsed, and preserved in 10% neutral buffered formalin (Sigma-Aldrich, MO, USA).

4.2.3 CMR Acquisitions

4.2.3.1 Ex-vivo Acquisition

CMR was performed on a 3T whole-body MRI system (Siemens MAGNETOM Verio, Erlangen, Germany) using a 20-channel head coil of while the hearts were suspended in formalin. Prior to measurements, B_0-shimming was applied using the scanner-integrated 3D-shimming algorithm covering the whole heart volume. Hearts were localized and imaged with a 3D mGRE sequence. Subsequently, a representative short-axis slice was identified and imaged with 2D mGRE sequence, with varying in-plane and through-plane spatial resolutions (for scan parameters see Table 4.1). Notably, an ECG signal was simulated at 60 bpm to imitate actual conventional CMR acquisition, in this way, the finest in-plane resolution is limited to 0.8×0.8 mm^2 at field of view (FOV) = 200×200 mm^2 for ex-vivo ECG gated acquisition. The in-plane resolution parameter set was from 0.8×0.8 mm^2 to 2.1×2.1 mm^2 while through-plane resolution ranges from 2 to 8 mm with total of 20 acquisitions per subject for ECG-gated ex-vivo scans (denoted as *Ex-vivo CMR* group). In order to isolate the effect of partial volume from SNR in iron+ band detection, a set of images were acquired acquire with 16 averages without ECG gating. Thus, the finest in-plane resolution achievable from the MRI scanner (0.3×0.3 mm^2) could be acquired to depict anatomical structure of the LV myocardium. A total of 28 in-plane (from 0.3×0.3 to 2.1×2.1 mm^2, see Table 4.1B) and through-plane resolution (2 to 8 mm, see Table 4.1A) parameters in this group were acquired (denoted as *Ex-vivo 16 Avgs* group). For both groups, the TEs and TR were minimized due to the number of readouts required for one phase encoding and flip angle were chosen according to the Ernst angle [352] to maximize MR signal. The total acquisition time for the ex-vivo protocols was approximately 22 hours.

Table 4.1 Imaging Parameters. **A)** Ex-vivo scan parameters for *Ex-vivo 16 Avgs* group, *Ex-vivo CMR* group and *In-vivo* group respectively. **B)** In-plane resolution between Ex-vivo 16 Avgs group (0.3 × 0.3 mm^2 - 2.1 × 2.1 mm^2), *Ex-vivo CMR* group (0.8 × 0.8 - 2.1 × 2.1 mm^2) and *In-vivo* group (1.6 × 1.6 mm^2).

A

	Ex-vivo 16 Avgs	***Ex-vivo CMR***	***In-vivo***
TR (ms)	788	80	83.51
TEs (ms)	4.95, 13.70, 22.45,	2.55, 5.80, 9.90, 15.56,	1.41, 2.64, 3.87, 5.10,
Flip Angle (º)	60	18	12
Bandwidth (Hz/pixel)	250	780	1185
Average number	16	1	
iPAT factor	NA	2	
Partial Fourier	NA	6/8	
ECG-gated	No	Yes	
Slice thickness (mm)	2, 4, 6, 8		6
Gradient polarity	Bipolar		

B

	In-plane Resolution (mm^2)						
Ex-vivo 16 Avgs	0.3×0.3	0.6×0.6	0.8×0.8	1.0×1.0	1.3×1.3	1.6×1.6	2.1×2.1
Ex-vivo CMR	NA		0.8×0.8	1.0×1.0	1.3×1.3	1.6×1.6	2.1×2.1
In-vivo						1.6×1.6	

4.2.3.2 In-vivo Acquisition

CMR was performed on a 3T whole-body MRI system (Siemens MAGNETOM Verio, Erlangen, Germany) using 18-channel body coil on post-MI pigs in 8 weeks. Full-stack 2D short-axis slice with T2* CMR was acquired using realistic conventional CMR imaging parameters with ECG gating at diastolic phase (denoted as *In-vivo* group, for scan parameters see Table 4.1).

4.2.4 Image Analysis

All postprocessing was performed on DICOM images created using the vendor's reconstruction pipeline and MATLAB, if not indicated otherwise. Endo- and epi-cardial contours were used to delineate the myocardial region. Remote myocardium and MI zone were drawn on the $0.3 \times 0.3 \times 2$ mm^3 T2* maps from the *Ex-vivo 16 Avgs* group and its contour coordinates were scaled according to the ratio of matrix size of target images compared to itself and then copied to the rest of the acquisitions in both ex-vivo groups to generate ROI binary masks. Subsequently, to assess image quality of the images, T2* weighted images were fit a 2-parameter mono-exponential decay model through an open-source MATLAB package qMRLab (http://qmrlab.org/) to derive T2* maps. To assess quality of T2* fits, the goodness of fit of T2* maps was elucidated as the coefficient of determination (R^2) within myocardial masks for all parameter sets. At the same time, SNR analysis was performed on the remote myocardium on T2* maps as the direct assessment of image quality.

To evaluate the detection accuracy on each acquisition, ROC analysis was performed subsequently: The data from the *Ex-vivo 16 Avgs of* $0.3 \times 0.3 \times 2$ mm^3 served as the reference standard while the rest of the datasets serving as variables (Figure 4.3). We employed 50 even segments on myocardium which is normally used for transmurality analysis in CMR to compare between different spatial resolution [117]. The 50 segments were further mapped to the MI region to avoid potential off-resonance artifacts from T2* maps. Subsequently, a mean-2SD criterion was used to delineate the iron+ MI zone [153,210]. The percentage of MI zone with iron+ territory was calculated for each segment and was converted to binary arrays as iron-rich and iron-absent zones with a cutoff of 1%. For this purpose, a segment with an iron+ size percentage > 1% by volume was consider positive for iron+, whereas a segment with an iron+ size < 1% by volume was considered negative. A 1% cutoff was used to eliminate segments with

spurious hypointense pixels from being considered as iron+ on T2* map. ROC analysis was performed to calculate the AUC by using the segmental iron+ size on T2* maps as the continuous variable and the presence or absence of iron+ using the 1% cutoff on the reference standard ($0.3 \times 0.3 \times 2$ mm^3 in *Ex-vivo 16 Avgs* group) as the status variable.

The transmural extent of MI has been proven to be an index of severe myocardial damage and of adverse LV remodeling [98,353]. We adopted the concept of transmurality as a more precise measure of the extent of iron+ distribution than global iron+ volume measure. Besides, to directly relate to spatial resolution, we also measured the width of the iron+ band in short axis view. Therefore, both the mean transmurality and the mean width of the iron+ territory within the MI zone were computed on the *Ex-vivo* reference standard images as demographic variables for later analysis.

Due to the intricacy of 50-segment analysis and the systolic arrest of explanted hearts, it is difficult to well align ex-vivo and in-vivo scans at different anatomical states. Instead, the percentage of iron volume were computed by summing up the iron+ region and normalized by the LV myocardium volume, which was sought to compare the difference of iron deposition between in-vivo images and ex-vivo reference standard, along with bias between the two groups (Figure 4.3).

To further study the contrast between iron+ region and remote myocardium, we first used iron+ mask identified from reference standard and down-sampled it to all ex-vivo images according to their spatial resolution, and then employed contrast-to-ratio (CNR) analysis on the T2* maps:

$$CNR = \frac{mean(remote) - mean(iron+)}{\sigma(remote)}, \tag{4.6}$$

where $\sigma(remote)$ denotes SD of the remote myocardium. The number of subjects for each spatial resolution with CNR exceeds 1 (acceptable) and 2 (rule of thumb) were calculated. This enables deeper understanding of partial volume artifact and noise level (SNR) in IMH detection.

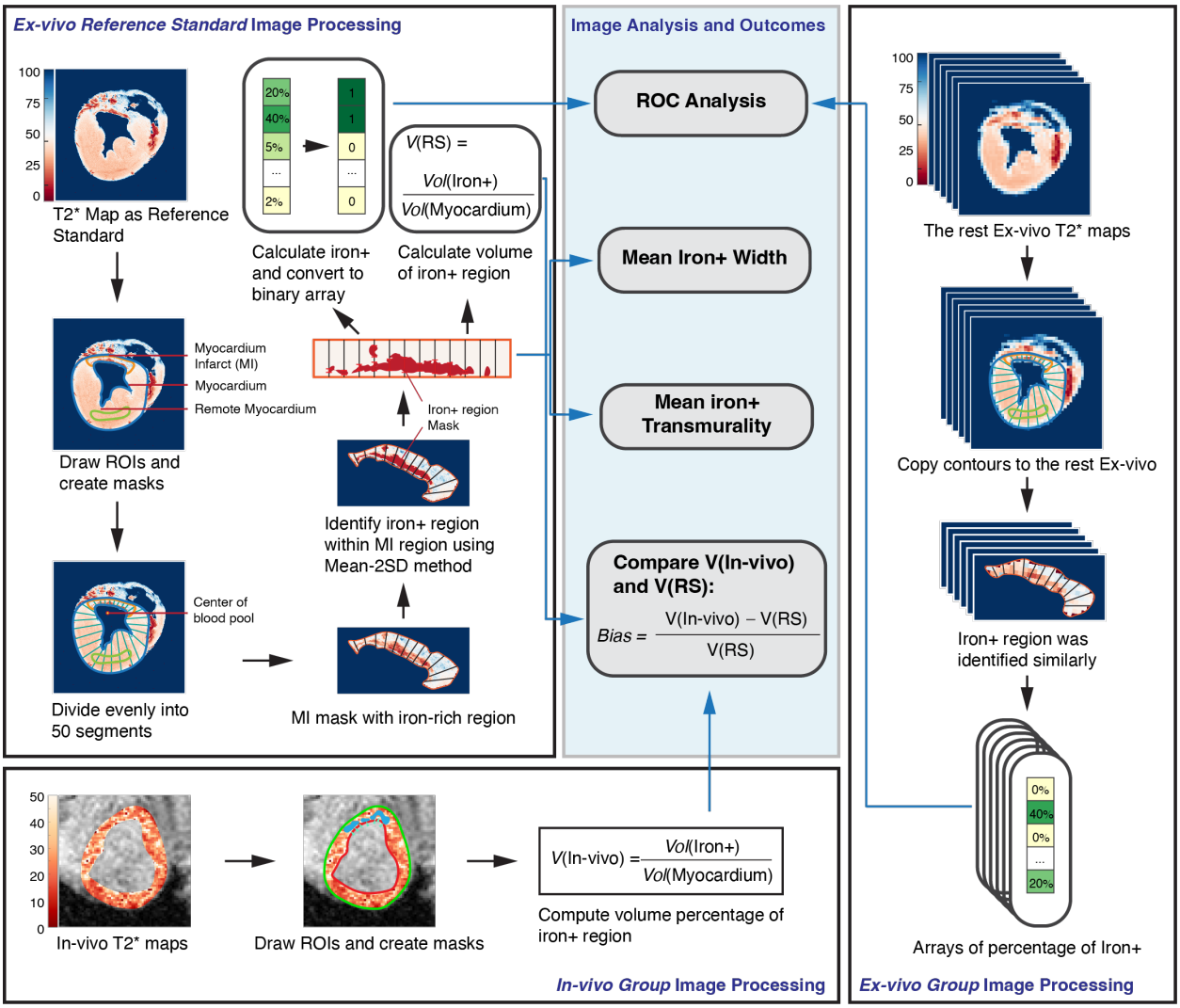


Figure 4.3 Image processing workflow to analyze detection capability of Ex-vivo and In-vivo T2* maps acquired with assigned spatial resolution. Ex-vivo Reference Standard Image Processing: The T2* map of spatial resolution 0.3×0.3×2 mm^3 with 16 averages was chosen as reference standard. Subsequently, contours (epi- and endo-cardium, MI, remote myocardium) were drawn and binary masks were created. The myocardium was then evenly divided into 50 segments and applied to MI mask. Iron deposits from hemorrhage (iron+) were identified within MI region using Mean-2SD method, converted to a segmental percentage of iron+. The mean iron+ transmurality, the width of the iron+ were then computed. Finally, the array of iron+ percentage was converted to binary array at 1% cutoff for as reference standard in ROC

analysis. The rest of ex-vivo group: The contours drawn from the reference standard were scaled accordingly to the remaining T2* images and binary ROI masks were generated. Similarly, each image was divided evenly into 50 segments for analysis, iron+ array with percentage was similarly generated as predictor group for ROC analysis as continuous variables. *In-vivo* group: The ROIs (epi- and endo-cardium, remote) were drawn from in-vivo T2* maps and iron+ masks were identified by Mean-2SD method. The iron+ volume normalized by total LV myocardium volume (represented as percentage of iron+ in the myocardium) for both in-vivo and reference standard (RS) is computed (as V(Invivo) and V(RS) respectively), and the bias of the volume percentage between in-vivo and ex-vivo Reference Standard was then computed as an indicator for the accuracy of iron+ detection for in-vivo data.

4.2.5 Sample Preparation & Validation Studies

The excised heart from each animal was sliced along the short-axis at 2-mm thickness. Two slices matched to CMR based on fiducial landmarks (long-axis ventricular dimension, hemorrhage appearance, papillary muscles, trabeculae, and right ventricle (RV) insertion point geometry) were identified. One slice was used for histopathology analysis and the other for Inductively Coupled Plasma – Mass Spectrometry (ICP-MS) analysis.

- Histopathology: For each slice, a region that includes the whole chronic hemorrhagic MI zone and partially remote myocardium were sectioned contiguously with 5 μm thickness and digitally imaged at 40-fold magnification. These sections were stained with Hematoxylin and Eosin (H&E) for tissue damage, EMT for fibrosis, and Prussian Blue for iron deposits. Tissue fiducial markers were used to correlate MR images with histology.
- ICP-MS Analysis: Each slice was sectioned further resulting in two remote and two chronic hemorrhagic MI sections. The total amount of iron within each of these sections was determined as [Fe] in micrograms per gram of tissue using ICP-MS (NexION 2000, PerkinElmer) without further purification or modification. Each sample was transferred to a clean Teflon vessel for acid digestion, which was carried out with a concentrated

HNO_3 (65-70%, Trace Metal Grade, Fisher Scientific) with a supplement of H_2O_2 (30%, Certified ACS, Fisher Scientific) at 190 °C for 20 min in a microwave digestion system (Titan MPS, PerkinElmer). Once the samples were cooled to room temperature, they were diluted to make a final volume of 50 mL by adding filtered deionized water for analysis. A calibration curve was established using a standard solution with the dwell time of 50 ms, thirty sweeps, and three replicates with background correction.

4.2.6 Statistical Analysis

All statistical testing was performed using MATLAB and Prism 9.2.0 (GraphPad, San Diego, California). Continuous variables are reported as mean ± SD. The normality test of continuous variables is reported by Kolmogorov-Smirnov test. The differences between remote and chronic iron+ MI zone were evaluated using Student's t-test and the difference in variation from *in-vivo* group was tested using F-test. Mann-Whitney U test was performed if any of the group data is non-Gaussian distributed. The goodness of fit (R^2) of T2* maps was averaged within myocardium and displayed as mean ± SD as well. Specifically, R^2 of each parameter set was tested using one-sample t-test to compare to 0.9 and 0.99. Association between continuous parameters was assessed using Pearson correlation coefficients and compared using linear regression. ROC analysis and its AUC were computed on simulation phantom and ex-vivo groups. Two-way ANOVA was performed on AUCs of all subjects across in-plane and through-plane dimensions. Results are shown as significant for $P < 0.05$ and indicated by *, $P < 0.01$ indicated by ** and $P < 0.001$ indicated by ***, or non-significance (NS) where $P > 0.05$, if not indicated otherwise.

4.3 Results

4.3.1 Numerical Simulations – SNR vs Spatial Resolution

Simulated T2* maps with in-plane resolution from 0.32 (0.4×0.4×2) mm^3 to 32 (2.0×2.0×8) mm^3 at 3 representative noise levels are shown in Figure 4.4A. Noise level 1 ranging from 1.2 ± 0.0 to 9.1 ± 1.0, which passes through SNR = 5 as voxel size increases and kept below 10 ("acceptable" image quality), represented as high noise level. Noise level 2 ranges from 2.3 ± 0.1 to 22.6 ± 3.2, which also passes through SNR = 5 as voxel size increases but reaches beyond "acceptable" level. Noise level 3 from 31.4 ± 0.4 to 317.5 ± 76.0 are in low noise level where SNRs are generally close to or beyond 40 ("excellent" image quality). Representative T2* maps at resolution 0.4×0.4×2, 0.4×0.4×8, 2.0×2.0×2 and 2.0×2.0×8 mm^3 from these three noise levels at basal, mid-ventricle and apical location in short axis are shown in Figure 4.4B. Intuitively, the visibility of iron+ band increases as SNR increases, across different spatial resolution or across noise levels. This indicates that the iron+ bands detection sensitivity is increased by increasing voxel size because of increased SNR. On the other hand, stronger partial volume effect can be seen from increasing voxel size in in-plane dimension (e.g. comparing images in 0.4×0.4×2 mm^3 to 2.0×2.0×2 mm^3 at noise level 3 in base location), or in through-plane dimension (e.g. comparing images in 0.4×0.4×2 mm^3 to 0.4×0.4×8 mm^3 at noise level 3 in apex location).

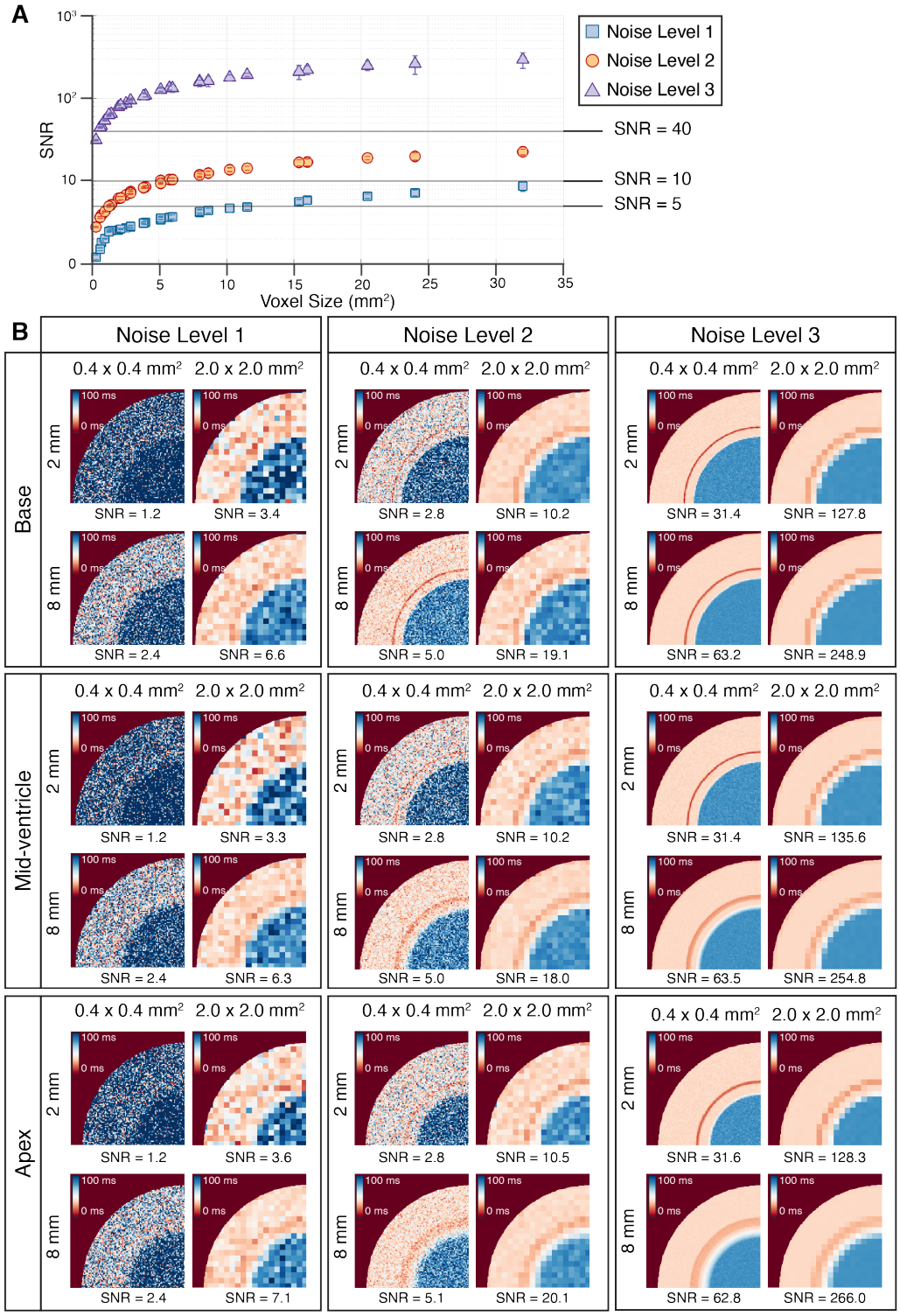


Figure 4.4 Representative T2* map images in various spatial resolution at 3 noise levels at basal, mid-ventricle and apex of simulated LV. **A)** Scatter plot of SNR with error bars at 3 noise levels with varying voxel size. SNR = 5 (from Rose Criterion), SNR = 10 ("acceptable") and SNR = 40 ("excellent") is plotted. Notably, Y-axis is log-scaled to make noise level 3 proportional in the plot. **B)** Representative T2* maps at resolution 0.4×0.4×2, 0.4×0.4×8, 2.0×2.0×2 and 2.0×2.0×8 mm^3 from these the noise levels

at basal, mid-ventricle and apical location with SNR in below to illustrate visibility of iron+ band from the influence of spatial resolution on SNR and partial volume effect.

AUC of ROC curves was performed to assess the accuracy of detection of iron+ region from hemorrhage of the simulation phantoms (Figure 4.5). AUC changes differently while voxel size increases according to different noise levels. In noise level 3, where image quality is “excellent”, there is a trend of decreasing AUC with increasing voxel size in in-plane dimension. A similar trend for through-plane dimension was also observed, which is more evident when the slice location moving towards apex. This indicates the effect of partial voluming alone playing a pivoting role in the iron+ band detection. If we inspect from same location across the three noise levels using 95% of highest AUC in each plot as an indicator, in increases from noise level 1 to noise level 3 (0.76 to 0.86 to 0.93) at base, (0.69 to 0.82 to 0.92) at mid-ventricle and (0.64 to 0.81 to 0.90) at apex, indicating the effect of noise alone is playing significant role in the iron+ band detection. Notably, in noise level 2, the spatial resolution that results in >95% of highest AUC in each location are neither finest or coarsest voxels (optimal AUC for voxel size from 0.96 to 11.52 mm^3 at base, 0.72 to 10.24 mm^3 at mid-ventricle and 0.72 to 10.24 mm^3 at apex). This lays the foundation for the notion that the compromise between partial volume effect and spatial resolution determined SNR would emerge in carefully choosing spatial resolution for maximizing detectability of the thin iron-rich band from the rest of the infarcted myocardium.

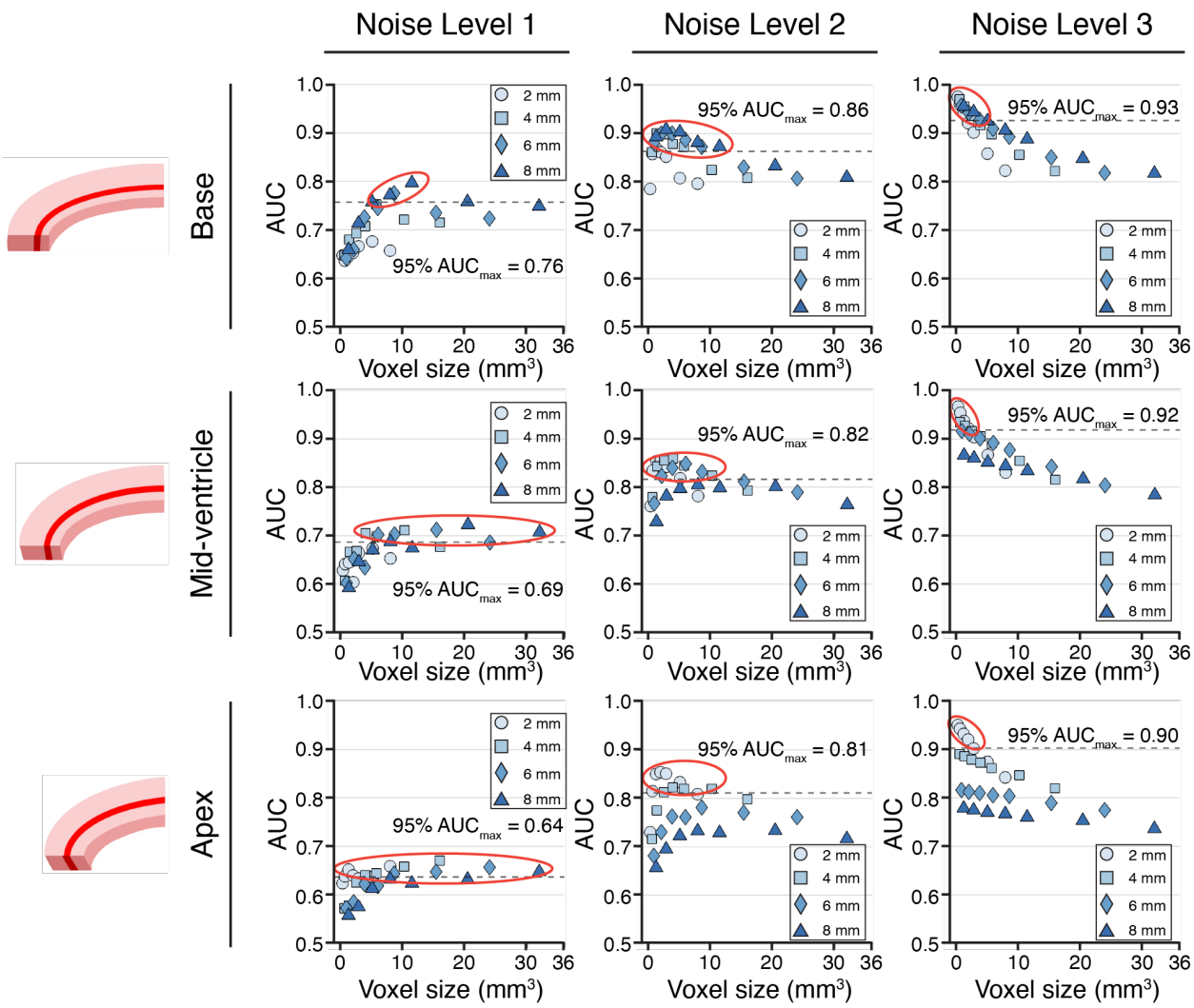


Figure 4.5 AUC of ROC curves as capability of iron+ detection from the simulated phantom at 3 noise levels and 3 locations. Three sketched simulated myocardium with iron deposits are illustrated on the left for each row (Base, Mid-ventricle and Apex). Nine scatter plots were shown: in horizontal direction from noise level 1 to 3, while in vertical direction from base to apex. In each scatter plots shows voxel size vs. AUC from ROC curves, where through-plane thickness 2, 4, 6, 8 mm is encoded in circle, square, diamond and triangle respectively. Optimal voxel size range is identified by a red circle encompassing the data points for its spatial resolution using 95% of maximum AUC (AUC_{max}) as cutoff (shown in dotted line in y-axis). The cutoff values are displayed in each plot as well.

4.3.2 Results from animal studies

4.3.2.1 IMH transmurality and width in Chronic MI

Two representative T2* images are shown; we observed that the iron-rich (iron+) region displays as a narrow band along to the thinned MI region close to endocardium. One with low iron+ band transmurality (5.5 %)/width (0.59 mm) (Swine 1) and the other with relatively high iron+ band transmurality (16.0 %)/width (2.40 mm) (Swine 2) respectively (Figure 4.6A). The hemorrhage transmurality and hemorrhage width for all animals are shown in Figure 4.6B and Figure 4.6C in a descending order. The transmurality ranged from 3.57 – 16.06 (%), and hemorrhage width ranged from 0.53 mm to 2.40 mm. This indicates only few pixels can be imaged for most of the subjects with currently available CMR imaging resolution: 1-2 pixels for 0.53 mm at and 3-4 pixels for 2.40 mm at 0.8×0.8 mm^2; 1-2 pixels for 0.53 mm and 2-3 pixels for 2.40 mm at 2.1×2.1 mm^2.

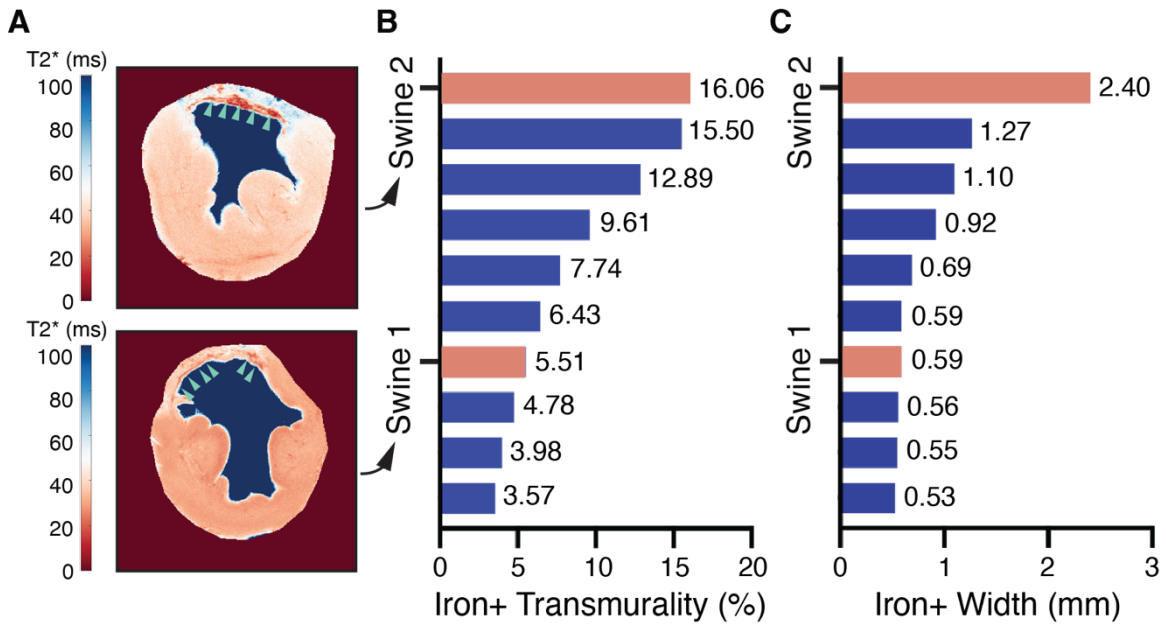


Figure 4.6 Iron+ widths and transmurality. **Panel A**: two representative cases are shown, one with extensive iron deposition (Swine 2) and the other with significantly lower iron deposition (Swine 1). B) and C) show the distribution of transmurality and iron+ width across all subjects studied, including the two representative cases highlighted.

4.3.2.2 Definition of Spatial Resolution Reference Standard for Detection of Iron Deposition

Based on our findings from numerical simulations (see Figure 4.5), spatial resolution is expected to play a critical role in detecting chronic iron deposits. However, since a decrease in voxel size is accompanied by a loss in SNR, it is possible that decreases in voxel size can limit the capability of detecting iron deposits based on T2* MRI. To address this practical challenge, we exploited our 3T MRI scanner with the highest reachable spatial resolution ($0.3 \times 0.3 \times 2$ mm^3) with 16 averages to provide the richest detail of myocardial tissue from as the reference standard for detecting chronic iron deposits. Since a key drawback of such a fine resolution is low SNR, we **1)** tested the goodness of fitting on from fitted T2* maps and **2)** directly computed SNR of T2* maps. Goodness of fit analysis was employed on T2* maps generated from the acquired T2*-weighted images to show that the R^2 of $0.3 \times 0.3 \times 2$ mm^3 in *Ex-vivo 16 Avgs* group is both significantly larger than 0.99 and 0.9 (Figure 4.7A). And SNR of the T2* map at remote myocardium is 19.7 ± 2.8 (Figure 4.7B). Those results confirm the $0.3 \times 0.3 \times 2$ mm^3 in *Ex-vivo 16 Avgs* group is in high image quality and thus can be cast as the reference standard for later AUC analysis.

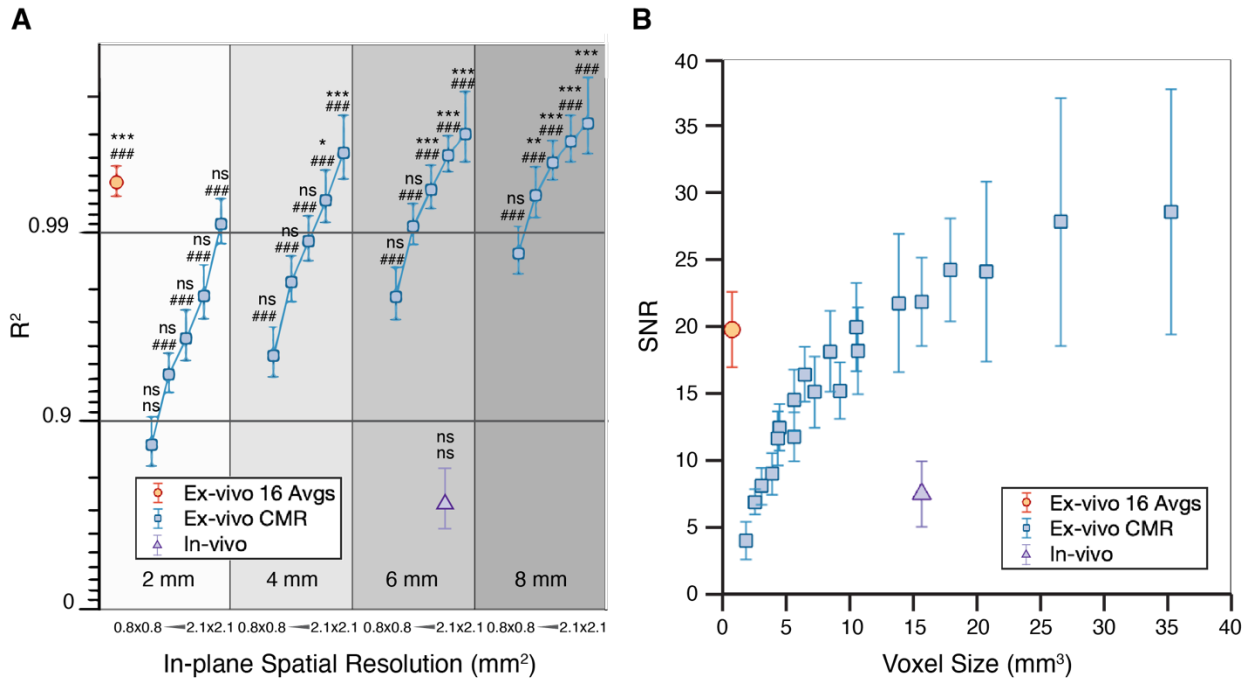
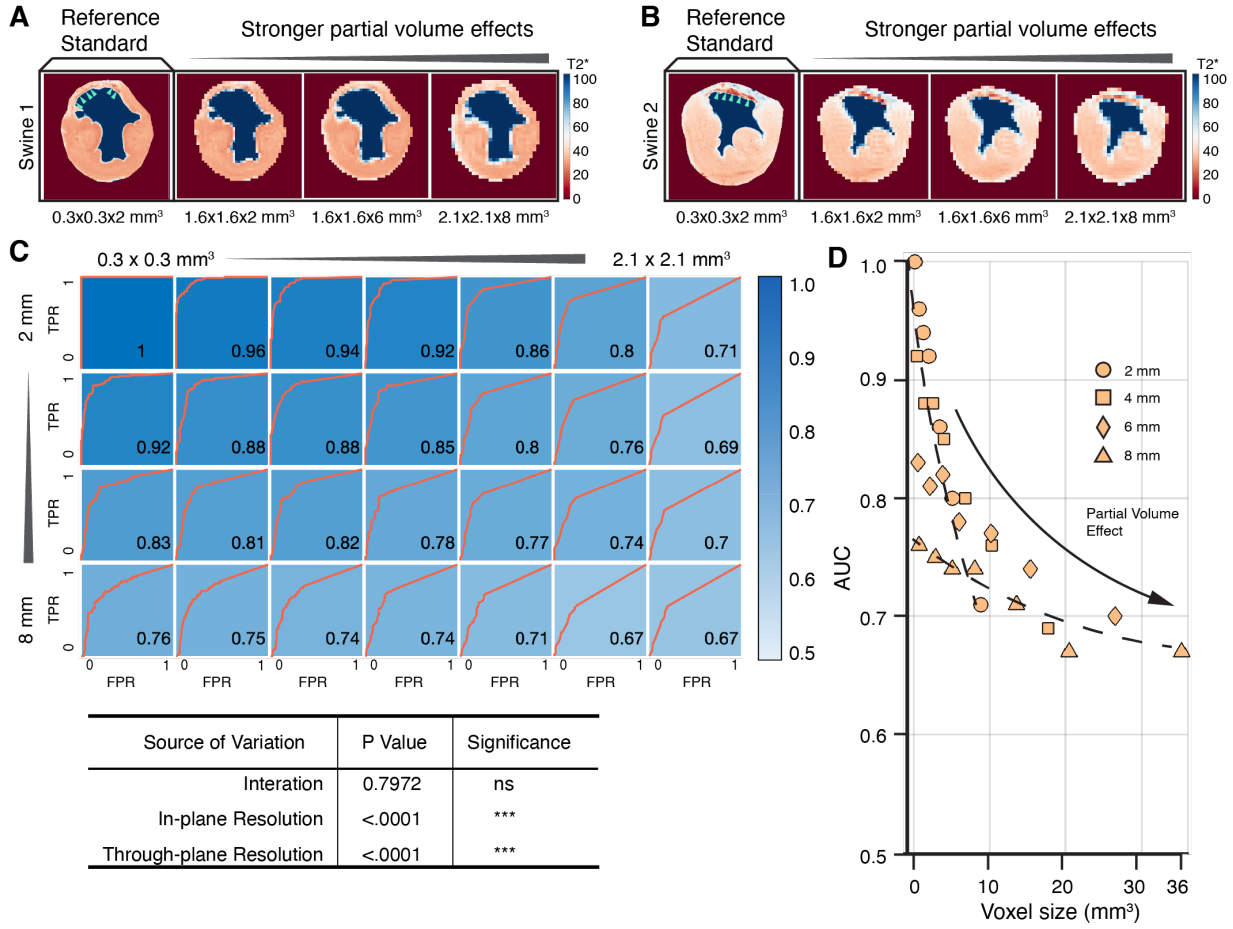


Figure 4.7 Goodness of fitting and SNR analysis T2* maps as indicators for image quality. **A)** Scatter plot with error bars in determination of correlation for imaging acquisition in all three groups ($0.3 \times 0.3 \times 2$ mm^3 *Ex-vivo 16 Avgs*, *Ex-vivo CMR* and *In-vivo* groups) is shown for goodness of fitting. Y-axis is log-scaled. ns indicates no significant difference ($P > 0.05$). * ($P < 0.05$), ** ($P < 0.01$), *** ($P < 0.001$) comparing to $R^2 = 0.99$, $^{\#}$ ($P < 0.05$), $^{\#\#}$ ($P < 0.01$), $^{\#\#\#}$ ($P < 0.001$) comparing to $R^2 = 0.9$. **B)** Scatter plot with error bars showing SNR of T2* maps as function of voxel size in the same groups as A).

4.3.2.3 Effect of Partial Volume Artifact

To isolate the effect of partial volume artifact, we employed a set of scans with 16 averages so that the SNR of those images are no longer the limitation. Representative images from two swine (swine 1 with narrow distribution of iron (Figure 4.8A); swine 2 with broader distribution of iron (Figure 4.8B)) in *Ex-vivo 16 Avgs* group are shown. Independent of spatial distribution of iron within chronic MI, it is evident that conspicuity of iron+ band on T2* maps decrease with decreasing spatial resolution. The AUC from ROC analysis is shown in Figure 4.8C, where AUC significantly decreases from in both in-plane and through-plane resolution independently (from two-way ANOVA analysis). A general decreasing trend of AUC from ROC curves as a function

of voxel size (Figure 4.8D) is observed. Notably, a steeper decrease is found as in-plane resolution going from 0.3×0.3 mm^2 to 2.1×2.1 mm^2 (1.00 to 0.71) for through-plane resolution = 2 mm than that of through-plane resolution = 8 mm (0.76 to. 0.67). This indicates partial volume effects are both prominent on in-plane and through-plane resolution.



Source of Variation	P Value	Significance
Interation	0.7972	ns
In-plane Resolution	<.0001	***
Through-plane Resolution	<.0001	***

Figure 4.8 ROC analysis with AUC in iron deposits detection accuracy for ex-vivo subjects to demonstrate partial volume effect. Two examples **A)** Swine 1 and **B)** Swine 2 of One reference standard and 3 ex-vivo acquisitions with 16 averages of T2* map: Left to right are 0.3×0.3×2, 1.6×1.6×2, 1.6×1.6×6 and 2.1×2.1×8 mm^3. The iron+ region is pointed out by triangle arrows. **C)** ROC curves and AUC at each spatial resolution is shown for *Ex-vivo 16 Avgs* group. Two-way ANOVA analysis of in-plane resolution and through-plane resolution showed significant difference respectively. AUC is shown on each of the ROC curve with its background color coded from 0.5 to 1.0. **D)** A scatter plot of different through-plane resolution (2, 4, 6, 8 mm) is encoded with different shapes (circle, square, diamond and triangle).

4.3.2.4 Effect of In-Plane vs. Through-Plane Resolution

Representative images from the same two swine (swine 1 with narrow distribution of iron (Figure 4.9A); swine 2 with broader distribution of iron (Figure 4.9B)) in *Ex-vivo CMR* group are shown. Similar to the *Ex-vivo 16 Avgs* group, the conspicuity of iron+ region on T2* maps decrease with increasing voxel size. However, at the same time, the noise level of T2* maps decrease as voxel size increases (Comparing between 1.6×1.6×2 and 1.6×1.6×6 mm^3 in Figure 4.9A&B), indicating that spatial resolution may influence detection of iron in both SNR and partial volume effect. ROC analysis performed using images acquired at the various spatial resolution parameter sets from the *Ex-vivo CMR* Group across all subjects showed that both in-plane and through-plane resolution play a significant role in identifying iron+ regions within chronic MI by two-way ANOVA analysis (see Figure 4.9C). This suggests that within practical limits, both in-plane and through-plane resolution is critical in detecting iron deposits within chronic MI. Further, in the *Ex-vivo CMR* Group, optimal AUC for each slice thickness group was observed at 1.6×1.6, 1.3×1.3, 1.0×1.0 and 0.8×0.8 mm^2 for slice thickness = 2, 4, 6, 8 mm respectively (AUC = 0.82, 0.8, 0.77, 0.71 respectively, see Figure 4.9C). The highest AUC decreases as slice thickness is thicker, indicating partial volume effect in through-plane resolution as well. Highest AUC (0.82) was found at 1.6×1.6×2 mm^3, and the optimal range of AUC was identified with the cut-off of 95% of the highest AUC (Figure 4.9D). Thus, the AUC peak was achieved for 1.6×1.6×2 mm^3 (0.82) and 1.3×1.3×4 mm^3 (0.8). This is also indicated in the simulation phantom at noise level 2 that optimal range of spatial resolution can be achieved given the opposite effect from spatial resolution in SNR and partial voluming (Figure 4.5).

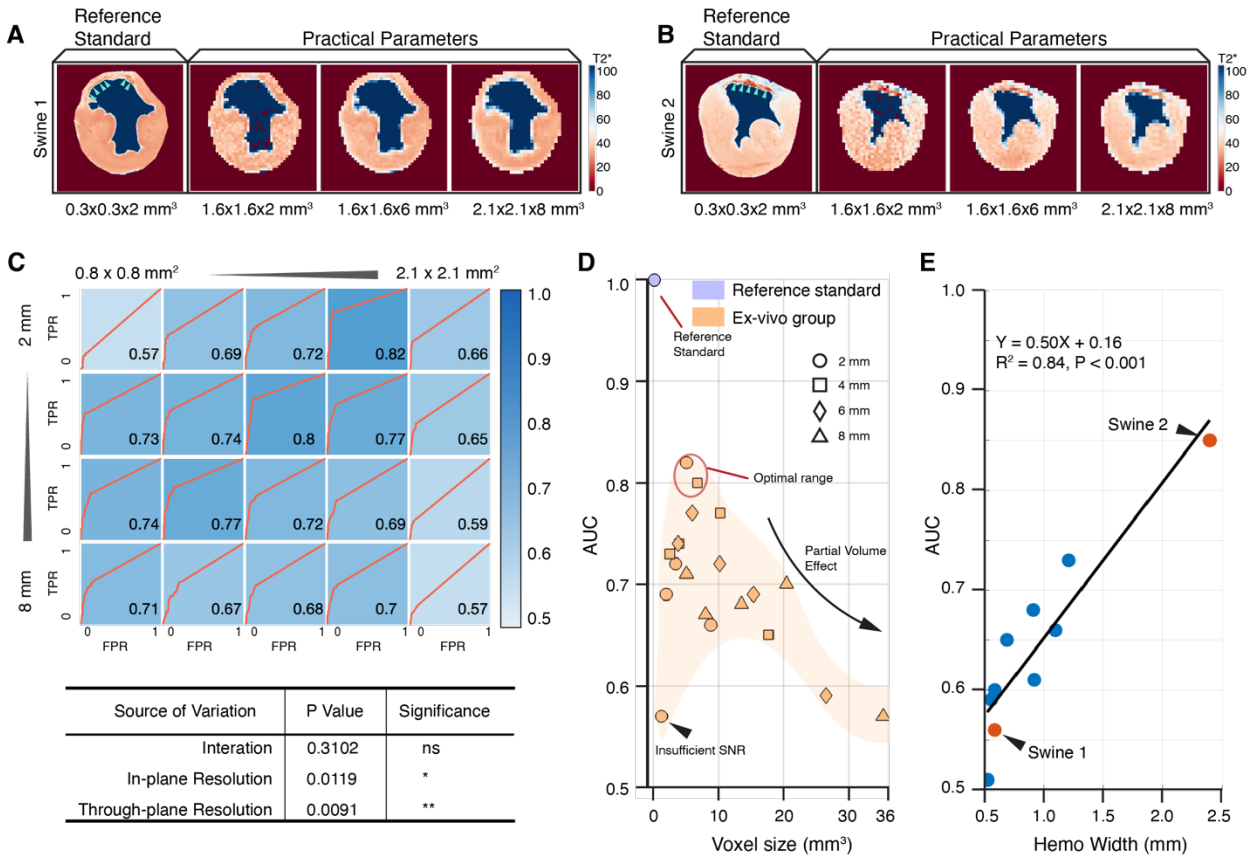


Figure 4.9 ROC analysis with AUC in iron deposits detection accuracy for Ex-vivo CMR subjects. Two examples **A)** Swine 1 and **B)** Swine 2 of one 0.3×0.3×2 mm^3 from *Ex-vivo 16 Avgs* group and 3 *Ex-vivo CMR* acquisitions of T2* map: Left to right are 1.6×1.6×2, 1.6×1.6×6 and 2.1×2.1×8 mm^3. Iron+ is pointed out by triangle arrows. **C)** ROC curves and AUC at each spatial resolution is shown for *Ex-vivo CMR group*. Two-way ANOVA analysis of in-plane resolution and through-plane resolution for is shown. AUC is shown on each of the ROC curve with its background color coded from 0.5 to 1.0. **D)** Optimal voxel size range for *Ex-vivo CMR group* is identified by a circle encompassing the data points for its spatial resolution: 1.6×1.6×2 and 1.3×1.3×4 mm^3 using 95% AUC as a cutoff, forth AUC ranging from 0.8 to 0.82. Different through-plane resolution (2, 4, 6, 8 mm) is encoded with different shapes (circle, square, diamond and triangle). E) Scatterplot of mean AUC vs iron+ width. A trend of higher AUC with higher iron+ width is observed (Y = 0.50X + 0.16, R^2=0.84, P<0.001). As highlighted AUC for Swine 1 is 0.56 while AUC for Swine 2 is 0.85.

4.3.2.5 Effect of Spatial Extent of Iron Distribution

We found that infarcts with thinner (less transmural) iron+ regions are less likely to be accurately detected with the CMR imaging settings (See Figure 4.9E, $R^2 = 0.84$). To further analyze the effect of spatial extent of iron distribution from thinned chronic MI, we divided the 10 subjects into two groups based on the rank of mean iron+ width. We put 5 highest widths into high iron+ group and the rest 5 subjects into low iron+ group (1.27 ± 0.66 mm and 0.57 ± 0.03 mm respectively, $P = 0.04$). Significant difference was found from optimal detection accuracy in varying spatial resolution: highest AUC was 0.90 ± 0.09 for high iron+ group while that for low iron+ group is 0.77 ± 0.09 ($P = 0.02$). The results are also consistent with observations made for swine 1 and 2 (as shown in Figure 4.9A and Figure 4.9B) where swine 1 with narrower band of iron deposits showed lower AUC than swine 2.

4.3.2.6 Limitation of Detection of Iron Deposition From CNR Analysis

Due to the benefit of no motion artifact for suspended ex-vivo heart scans, we were able to perform CNR analysis to illustrate the limitation in iron+ detection within MI. For extremely thinned IMH (iron+ width = 0.59 mm), CNR can be negative due to partial volume effect, which also results in low detection accuracy (Figure 4.10A). And the optimal resolution ($1.6\times1.6\times2$ mm^3) found from the previous session showed relatively higher AUC than the others. While for thicker IMH (iron+ width = 2.40 mm), spatial resolution at both $1.6\times1.6\times2$ mm^3 and $1.6\times1.6\times6$ mm^3 showed CNR >2 with excellent AUC for iron+ detection (Figure 4.10B, 0.91 and 0.92 respectively). We calculated number of subjects for all ex-vivo scans with in-plane resolution 0.8×0.8 to 2.1×2.1 mm^2 and through-plane resolution 2 to 8 mm that with CNR exceeds 2 (rule of thumb, Figure 4.10C) and 1 (acceptable contrast, Figure 4.10D). Similarly, highest number of CNR > 1 and CNR > 2 can be found in the same spatial resolution ($1.6\times1.6\times2$ mm^3). This

explains the optimal resolution in the *Ex-vivo CMR* group, as well as indicates the limitation in iron+ region detection for extremely thinned IMH.

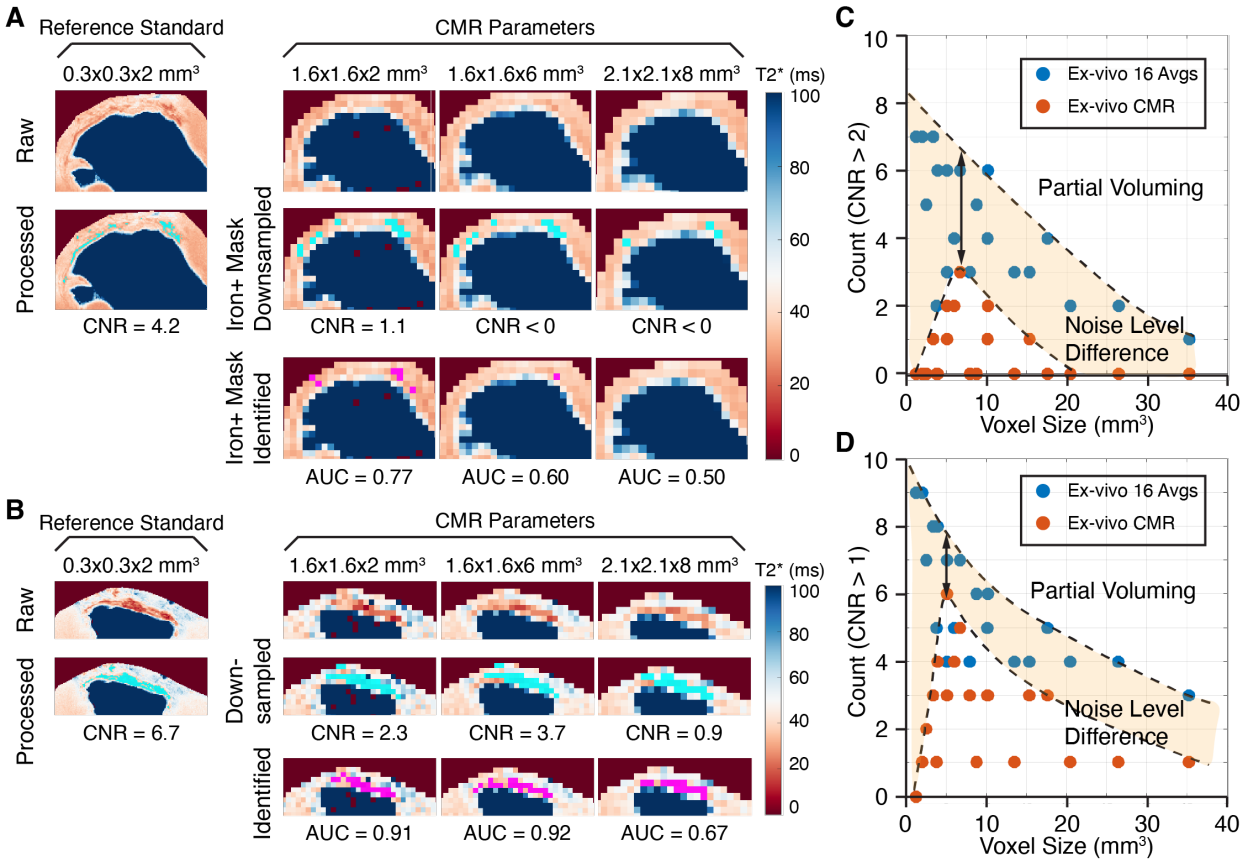


Figure 4.10 Effect of Spatial Resolution on CNR and Iron+ Detection. Representative images magnified around MI region in the two subjects are shown in **A)** and **B)**. Reference standard 0.3×0.3×2 mm^3 from *Ex-vivo 16 Avgs* group and 3 *Ex-vivo CMR* acquisitions: Left to right are 1.6×1.6×2, 1.6×1.6×6 and 2.1×2.1×8 mm^3. Iron+ region was identified by Mean-2SD method and down-sampled to the rest of the three sets of spatial resolution overlaid with cyan masks. For *Ex-vivo CMR* group, each iron-positive region from IMH was identified by Mean-2SD method overlaid with magenta masks. **C)** and **D)** are scatter plots of voxel size and number of subjects with CNR > 2 and CNR > 1 respectively. All ex-vivo scans are displayed on the plots, in both *Ex-vivo 16 Avgs* (Blue) and *Ex-vivo CMR* (Red) groups.

4.3.2.7 Histology and Mass Spectrometry Based Validation for Detecting Iron within Chronic MI

Histopathology from two representative animals (same as in Figure 4.9) with chronic MI are shown in Figure 4.11 (Swine 1: panels A-C; and Swine 2: D-F), where contiguous H&E sections

are used to identify tissue damage, Prussian Blue stained sections are used to identify iron, and EMT stained sections are used to depict fibrotic regions. A similar pattern of fibrosis and necrosis is seen between the two subjects. MIs are mostly stained as both necrotic and fibrotic tissue (Figure 4.11A&B and Figure 4.11D&E), with scattered iron deposition in the MI region. From inspection, more iron-stained regions were seen in Swine 2 than Swine 1 (Figure 4.11C and Figure 4.11F). The difference in the extent of iron deposition is consistent with the MRI findings between the two animals, where larger transmurality of iron deposition was observed in Swine 2 (comparing between Figure 4.9B and Figure 4.11F). Quantitative findings from ICP-MS of MI region and remote myocardium (n = 10) are shown in Figure 4.11G. Iron concentration within chronic MI regions (45.1 ± 9.3 μg/g) was significantly higher than the remote myocardium (35.3 ± 4.7 μg/g, $p < 0.01$), confirming the presence of iron deposition in the MI zone. The iron content with the MI region further correlates with hemorrhage width of iron deposits ($R^2 = 0.87$, $P < 0.001$, Figure 4.11H), indicating a strong association between iron concentration (i.e. T2*) and the extent of iron deposition.

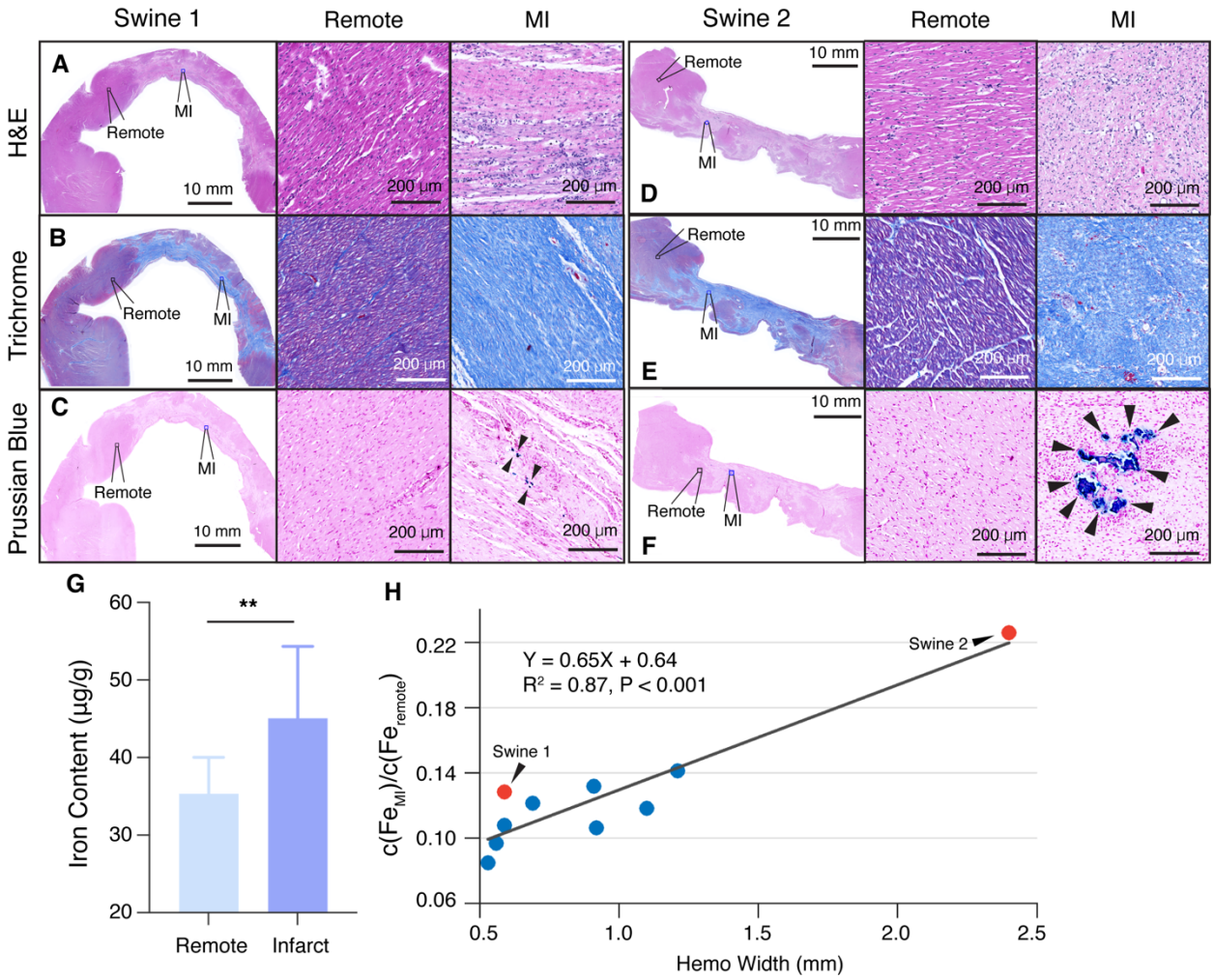


Figure 4.11 Histology Validation of Representative Subjects. **A)** and **D)** H&E and **B)** and **E)** Trichrome staining show infarct, fibrosis and nonviable myocytes, with low transmurality/width for Swine 1 and relatively high transmurality/width for Swine 2 (same as in Figure 4.9). Prussian blue staining of Swine 1 **C)** shows relatively low abundance inside the infarct, while Swine 2 **F)** shows abundant iron accumulation. Small rectangular arrows pointing to the 10× view images are magnified on the right with one remote region and one MI for each. Iron deposition is highlighted with triangular arrows. **G)** Bar plot of iron concentration in remote myocardium vs. MI zone. ** denotes in paired t-test $P < 0.01$. **H)** Linear regression of hemorrhage width vs the ratio of c(Fe) in MI vs c(Fe) in remote, showed good correlation ($Y = 0.65X + 0.64$, $R^2 = 0.87$).

4.3.2.8 Limitation of detection in *In-vivo* CMR

In-vivo CMR with 1.6×1.6×6 mm^3 was also analyzed and compared with the ground truth. We found iron+ volume bias was highest for narrow iron-rich band (low hemorrhage width) and

decreases as hemorrhage band gets broader (Figure 4.12A). Furthermore, there is significant difference in variance between the high iron+ group and low iron+ group (Figure 4.12B), which supports the notion that the accuracy of hemorrhage detection is strongly determined by hemorrhage width with conventional CMR imaging resolution. Three examples of over-, correct-, under-estimate of IMH is shown in Figure 4.12C. It also supports that with current CMR protocol, IMH may be detected in wide iron+ band but it is either over-estimated or under-estimated for narrower band for in-vivo scans.

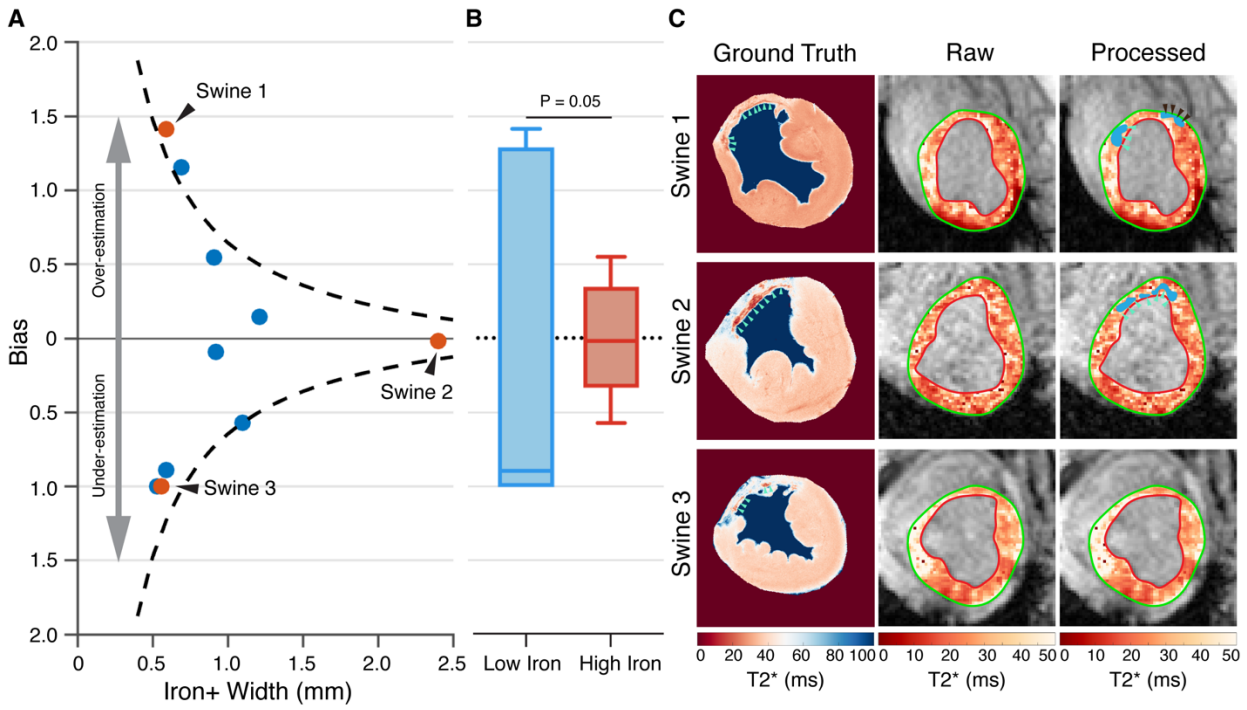


Figure 4.12 Iron Deposits Detection for in-vivo Subjects. A) Scatter plot of Normalized Iron volume bias vs. Iron+ width is shown. A trend of larger Iron+ band with lower bias is observed. Three representative examples with B) 10 subjects were divided into two groups by hemorrhage width: Low Iron (n=5) and High Iron (n=5). F-test was done to compare the variance (P=0.05) between two groups. C) Three representative examples with over-estimated of iron+ region in Swine 1, low-bias estimation of Swine 2 and under-estimation of iron+ region in Swine 3 (in this case, the iron+ is completely undetected) are shown.

4.4 Discussion

In this chapter, we systematically investigated the influence of the relationship between image resolution on T2*-based detection of iron deposits in IMH from chronic MI. We first showed that imaging resolution from both in-plane and through-plane are key determinants for accurate iron deposits detection by numeric simulation. We validated our findings in ex-vivo pig hearts with chronic hemorrhagic infarction and identified the optimal imaging resolution for detecting IMH. In particular, our studies demonstrate that finer through-plane resolution (2 - 4 mm) with relatively moderate in-plane resolution (1.3 - 1.6 mm^2) may be a favorable option for optimal detection of IMH in myocardial infarction for a balance between SNR and partial voluming effect that determined by spatial resolution. However, the accuracy of detection is also highly dependent on the non-spatial-resolution-determined noise level as well as the size of IMH. We also found from *in-vivo* dataset the limitation of detection capability with conventional spatial resolution for thinned IMH. By evaluating T2* maps over a range of spatial resolution and realistic CMR imaging parameters, we conclude that the accuracy of detecting IMH in T2* maps is strongly tied to spatial resolution, noise level, and size of IMH.

IMH, which can be noninvasively detected using T2*-based MRI, has emerged as one of the strongest predictors of adverse outcomes in post-MI patients. Cardiac T2* mapping has become the non-invasive standard for detecting and characterizing IMH, given that cardiac biopsy is challenging. Unlike acute MI, the thin myocardial wall in chronic MI can be between 1 to 5 mm [354], and when it comes to IMH in the MI region, we showed hemorrhage can be as thin as 0.5 mm (Figure 4.6C), which means that only 1-2 pixels are imaged with current T2* CMR in-plane resolution (0.8 - 2.1 mm); These T2* CMR studies in sub-chronic to chronic MI, when myocardial wall-thinning is prevalent, tend to have in-plane resolution within the range of this study, and coarse through-plane resolution (See Table 1.2). The sub-optimal and inconsistent

spatial resolution measurements could introduce strong biases and lower the sensitivity in detecting and characterizing hemorrhagic remnants in chronic MI. Thus, the optimal spatial resolution for accurate T2*-based characterization remains to be investigated.

To address this gap in knowledge, we first investigated in our simulation model on the influence of spatial resolution on partial volume effect and SNR on the T2* maps. With the knowledge of the simulation results, we then tested and validated the following: 1) how voxel size affects the SNR of the T2* map; 2) how partial volume effect affects the detection accuracy of iron deposits by tweaking the spatial resolution; 3) how the interplay of partial volume effect and SNR would result in an optimal range for choosing spatial resolution. More specifically, the reduced image resolution provides higher SNR and thus improving the lesion detection. From Rose's criteria, SNR of an object needs to be at least 5 to be visually detectable [346,355]. We found increasing voxel size of image acquisition, the SNR of T2* map will also increase. This is also validated in ex-vivo heart scans (Figure 4.7B) and in line with the MRI theory. On the other hand, lower resolution images can increase the partial volume effect and compromise the contrast between normal myocardium and hemorrhagic lesion with reduced T2* differences. Putting together the compromise between the two, we found an optimal range of feasible spatial resolution of the CMR protocol in the ex-vivo scans.

Our simulations were based on T2* values of remote myocardium and IMH that were determined from experimental measurements and are within T2* range (10 - 50 ms) as reported in the literature [153,292,356]. Due to the accessibility of voxel-wise analysis for the simulation phantom, we instead used ROC analysis on the simulated T2* maps after transformation. In this way, we were able to more accurately test the performance of iron+ region classification without applying specific segmentation methods that are usually applied to CMR T2* map analysis.

What's more to the 3 major findings previously addressed about the influence of spatial resolution on SNR and partial voluming is that the location of IMH. We employed the American Heart Association (AHA) segment along long axis of the heart. As more apical the IMH located, the partial volume effect from through-plane resolution is stronger (comparing between the AUC of 2 mm and 8 mm through-plane resolution at noise level 3), which will weaken the detection accuracy by increasing the through-plane thickness to accommodate for SNR requirements for image quality. We simplify the iron+ region in simulation phantom as a homogeneous source of iron as 1 mm based on reasonable deduction from the knowledge of thinned myocardium (1-5 mm). Plus, it is close to our heart data (the iron+ width is 0.95 ± 0.56 mm). Rather than homogeneous distribution of iron within MI from simulation, it is more likely in real data to be in a scattered form, where the partial volume effect will be even stronger. This indicates that how strong partial volume effect could be for iron remnants in the thinned MI region.

We carried out ex-vivo studies in explanted hearts with different voxel sizes and acquisition parameters to test our hypothesis and validate the knowledge from our simulation. Given the complications associated with direct comparison of iron-rich remnants from IMH to its MRI images (see Results on definition of spatial resolution of reference standard), we proposed the ground truth (reference standard) to be our $0.3\times0.3\times2$ mm^3 spatial resolution with 16 averages for ROC analysis. Based on this analysis, we found both the in-plane and through-plane resolutions to play a significant role in detection of iron deposits, where peak performance was achieved only when the spatial resolution is between $1.6\times1.6\times2$ and $1.3\times1.3\times4$ mm^3. Notably, under practical conditions, increasing slice thickness decreases the highest detection accuracy on the same through-plane resolution. This suggests that increasing through-plane thickness introduces strong partial voluming effect in iron deposits detection. Comparing to our simulation, this aligns with the tendency that the location of LAD occlusion induced MI are probable to

show in mid-ventricle to apex of LV myocardium. Further, our findings also support the notion that the lower the transmurality of IMH (i.e. thinner the IMH) the greater the importance spatial resolution plays in the detection of IMH, due to the high association of concentration of iron within the MI zone and iron+ width (Figure 4.11H).

Our *in-vivo* scans also support the notion that IMH size is strongly associated with accurate detection of IMH with current *in-vivo* CMR acquisition. However, as is shown in the goodness of fitting of the T2* maps (Figure 4.7A), the R^2 of fitting is around 0.7, which is significantly lower than a decent R^2 (0.9). The image quality of the *in-vivo* data along with low SNR (7.5 ± 2.1, Figure 4.7B) which is slightly above Rose's criteria, limits the detection capability.

We used Mean-2SD methods to identify the iron deposits in IMH for actual acquired T2* maps because this is one of the gold standard methods. Using absolute values (T2* < 20 ms) will lead to different results, however, this method overlooks the inter-subject variability of tissues, as well as studies has shown better performance of Mean-2SD over 20 ms thresholding method [153]. Other methods such as Full-Width at Half Maximum (FWHM) also depends on the relativity of T2* values on remote myocardium, however, it does not take noise level of the image into consideration, which falls into the same drawbacks of using 20 ms thresholding method.

We found strong limitation of IMH detection capability for our *in-vivo* scans compared to our *ex-vivo CMR* scans. Multiple differences between in-vivo and ex-vivo scans such as cardiac and respiratory motions, surroundings of the heart, imaging coil selection could introduce more artifactual and/or lower SNR image for in-vivo scans. We further discussed the spatial-resolution-determined SNR and non-spatial-resolution-determined SNR by plotting the

relationship between voxel size and SNR (Figure 4.13). With the same FOV, the relationship of SNR of MR signal and voxel size from Equation 1.12 can be rewritten as:

$$SNR \propto \frac{\sqrt{N_{acq}} \cdot \sqrt{\Delta x \Delta y \Delta z}}{\sqrt{BW_{read}}}, \tag{4.7}$$

which indicates SNR is proportional to the square root of voxel size. From our study, we have observed a non-linear relationship between imaging spatial resolution and SNR on T2* maps in both simulation phantom and *Ex-vivo CMR* dataset. By performing linear regression of the square root of the voxel size vs. SNR on T2* map, we found it aligns well with the linearity relationship from Equation 4.7 (Figure 4.13). Notably, the slope of the regression result is shown to be an indicator for accessing noise level outside the spatial-resolution-influenced SNR. The SNR for *in-vivo* scans is only slightly higher than that of simulation phantom at noise level 1 in the same spatial resolution (7.5 ± 2.1 vs. 5.6 ± 0.4, $P = 0.02$), while much lower than both ex-vivo CMR scans (7.5 ± 2.1 vs. 21.8 ± 3.1, $P < 0.001$) and simulation phantom at noise level 2 (7.5 ± 2.1 vs. 16.8 ± 1.4, $P < 0.001$). This indicates the SNR level of *in-vivo* data acquisition falls into scenario that a thinned iron-rich band is unlikely to be detected. As a result, it imposes the limitation of the detection of iron deposits from thinned myocardium.

We found great diagnostic performance (AUC > 0.8) from *ex-vivo CMR* that the optimal spatial resolution is 1.6×1.6×2 mm^3 and 1.3×1.3×4 mm^3. This aligns well with our simulation at noise level 2 on apex location, where the optimal through-plane resolution is 2 and 4 mm. Both results also indicate that the long-axis location of the heart is also needed to be taken into consideration, emphasizing the demand for high resolution 3D T2* mapping techniques. On the other hand, the SNR of T2* maps for 1.6×1.6×2 mm^3 and 1.3×1.3×4 mm^3 are 11.7 ± 1.8 and 15.0 ± 2.6 respectively, suggesting that minimal SNR for excellent iron deposits detection in thinned myocardium may need to be above 10. Our CNR analysis further validated the connection

between the optimal resolution and the contrast between iron-rich region and remote myocardium. This set of spatial resolution is most effective in extremely thinned IMH where the averaged iron+ width can be as low as 0.6 mm within MI region. However, even the optimal spatial resolution may still be limited due to the AUC from ROC analysis is still under 0.8 (see Figure 4.10A).

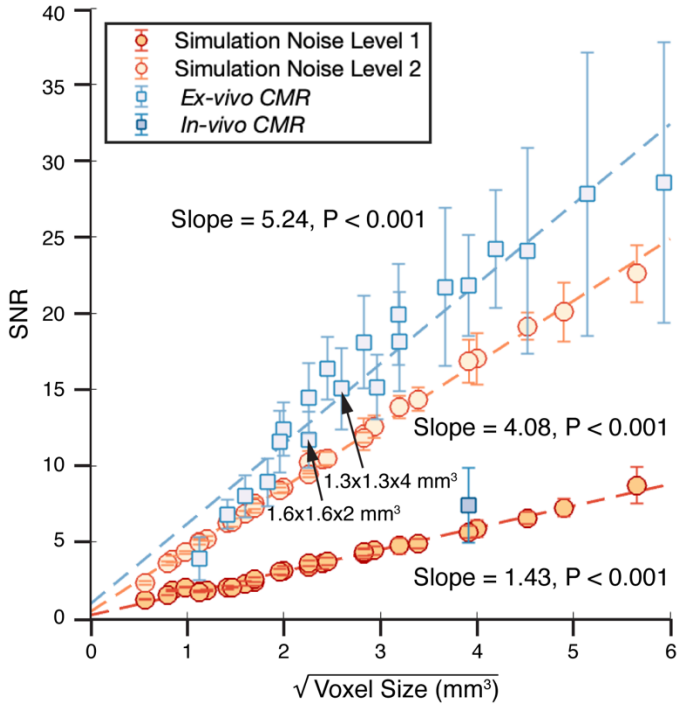


Figure 4.13 SNR analysis on simulated and CMR acquired T2* maps on remote myocardium. Scatter plot with error bars of square root of voxel size vs SNR of the remote myocardium on T2* maps (Simulation: circle, *Ex-vivo CMR*: square, and *In-vivo*: triangle) is shown. Linear regression was performed to the simulation and ex-vivo dataset. The slope of the linear regression for simulation noise level 1, 2, and *Ex-vivo CMR* are 1.43, 4.08 and 5.24 respectively.

The current *in-vivo* acquisition scheme may be limited in its accuracy for detection of thinned myocardium in iron deposits within IMH in cardiac patient because: 1) Its lower SNR compared to the *Ex-vivo CMR* group, due to limited hardware limitation. 2) Strong motion artifacts due to unsuccessful ECG-gating and breathing holding. 3) Possible vulnerability to low SNR in long

TEs from conventional 2-parameter fitting for T2* maps. To address the current issue of iron deposits detection in practice, an increase of the SNR level on the image is needed: 1) The current CMR protocol requires breath-holding of the patients which limits the sampled data points within one breath-hold. To achieve higher SNR, a free-breathing high resolution T2* mapping approaches is necessary. There are several studies developed such techniques with T2* CMR [275,357–359], but their availability to the thinned iron deposits needs to be further tested. 2) There are multiple ways to improve SNR in its hardware settings: for example, number of channels for the RF coil, using specific coil instead of general-purpose coil [360], optimizing receiving gain parameters [361], increasing field strength etc. 3) We can also improve the SNR of maps after acquisition. It is already widely studied that using a more sophisticated fitting strategy, e.g. offset exponential or bi-exponential [149], discarding long echoes where the SNR falls below 2.5 [362]. In addition, with the rapid adoption of machine learning in the field of MRI, deep learning based technique to enhance T2*-weighted image or maps could be a great potential in iron deposits within chronic MI [363].

4.5 Study Limitations

In spite rigor of this study, it is not without limitations. First, due to the retrospective nature of this study, all ex-vivo scans were performed in formalin-fixed hearts, which may affect the T2* values of the myocardium. However, based on previous publications, the T2* value of myocardium even after 50 days post-fixation has been shown to be not different from the T2* values of fresh hearts [364]. We, therefore, expect the T2* values reported in our study to be applicable to in-vivo scans. Second, the current study focused on investigating the image resolution and partial volume effect in IMH detection; however, other potential confounders, such as B_0 off-resonance, motion (respiratory, cardiac and blood flow) can also be important factors in-vivo IMH detection T2* CMR but these were not investigated in this study. Third, we

utilized a 20-channel head coil in ex-vivo scan settings. Since SNR can be dependent on coil selection, our findings remain to be validated against coil selections available for in-vivo CMR of the heart. Fourth, our study used LAD occlusion surgery for generating IMH heart model, resulting in the location of iron-rich region within MI concentrated at mid-ventricle to apex region of LV myocardium. Further study with more widely distributed iron deposits region can be exploited to validate partial voluming effect on different locations of hemorrhagic MI along long-axis.

4.6 Conclusions

In summary, in this chapter, we have conducted a rigorous investigation into the relationship between T2* CMR and spatial resolution of images on the detectability of IMH in the post MI setting using simulations, explanted hearts along with multiple ex-vivo and in-vivo validation. We found that spatial resolution is a critical parameter for detection of IMH, and that within the practical range of consideration, great sensitivity for detecting iron deposits from IMH can be reached by adjusting spatial resolution. Besides, the size of IMH also strongly affect the accuracy of detection. We proposed a SNR profile that would determine how spatial-resolution-determined SNR and non-spatial-resolution-determined SNR are playing a role in IMH detection. The spatial resolution thresholds for optimal detection of hemorrhagic remnants based on T2* CMR requires SNR of the T2* map to be at least at SNR = 10, within this standard, the imaging voxels needs to stay as small as possible to minimize the partial volume effect.

CHAPTER 5: SUMMARY AND FUTURE DIRECTIONS

5.1 Summary

IMH has emerged as an important predictor of adverse long-term outcomes in patients treated with reperfusion therapy for MI. Notably, studies have shown that hemorrhagic MI is associated with delayed infarct healing, larger MIs, presence of persistence MVO, higher LV volumes, fat infiltration, compromised LVEF and late arrhythmogenic risk [17]. This precipitated significant clinical interest in the management of MI patients with IMH and driven investigations focused on understanding the mechanisms contributing to the adverse outcomes.

For MRI-based characterization of MI to determine prognosis and therapeutic care of patients several major challenges need to be overcome: 1) inefficient CMR protocol limiting rapid characterization of MI, MVO, IMH, and cardiac function; 2) lack of multi-contrast definition to characterize chronic MI without exogenous contrast agents; and 3) limitations in spatial resolution to accurately characterize chronic iron remnants following IMH. This dissertation addressed these key challenges.

In Chapter 2, to shorten CMR exams for rapid characterization of necrotic tissue, IMH, MVO and cardiac function, as well as address the issue of motion artifacts due to unsuccessful breath-holding and ECG-gating in patient with both acute and chronic MI, a 3D fully ungated free-breathing motion-resolved cardiac T1, T2* imaging approach was developed based on an LRT framework. The proposed 3D LRT T1, T2* imaging was tested and validated on animal models. Accurate assessment of MI, MVO and IMH as well as cardiac function of the post-contrast myocardium is crucial for diagnosis and treatment planning in patients after reperfusion therapy.

While conventional Gd-enhanced imaging has been widely used in the clinical assessment of MI/MVO characterization, T2* imaging for IMH extent, CINE imaging for cardiac function, which often take nearly one hour to complete present multiple hurdles – limited scanner throughput, patient adherence to imaging protocol, and logistical hurdles in busy clinical settings. We demonstrated that the proposed LRT approach can provide equivalent LVEF, MI size, MI transmurality, MVO size and IMH size to 2D conventional method, with cardiac and respiratory motion-resolved imaging in both acute and chronic settings in a canine with a reduction in scan time from about 55 min to less than 15 min.

In Chapter 3, due to the complex response in MOLLI-based T1 mapping, a novel approach in distinguishing chronic MI substrates was investigated using entropy analysis. A confounder-corrected water-fat separation algorithm was used to separate signals from fat and iron. The fat phantom study was used as a demonstration for validation of the T1 entropy determined by different fat fractions. T1 entropy in MI was found to be higher than that of remote myocardium across acute to chronic time period. High fat fraction was observed in animals with high iron (R2*) content. We categorized the subjects into 3 groups: 1) high fat fraction, high R2*; 2) low fat fraction, high R2*; and 3) low fat fraction, low R2*. The native T1 entropy from MI regions showed different level of correlation in the presence and/or absence of fat and iron. The native T1 entropy was distinctive between groups and the highest T1 entropy was found when fat and iron were colocalized, indicating its potential use for MI patient risk stratification related to MI tissue characterization. A patient study was conducted to validate T1 entropy at both acute and chronic MI.

In Chapter 4, studies were performed to emphasize on the influence of spatial resolution on T2* images when quantifying iron overload in chronic hemorrhagic MIs, especially those with thin

(infarcted) myocardial walls. A numerical simulation was used to demonstrate that the detection of IMH can be limited by SNR, size of hemorrhage, and spatial resolution. The ex-vivo study to validate the numerical stimulation was performed with a practical imaging parameter set. An optimal range of in voxel size was found to detect IMH in thinned myocardium under specific SNR conditions. The ex-vivo study also showed that the accuracy of detecting iron remnants with T2* maps is strongly dependent on spatial resolution, SNR and size of iron-rich regions. In-vivo data was also analyzed, which showed that the commonly used T2* have insufficient in SNR for detection, especially when the width of the iron-rich regions is low. SNR profile was plotted to guide the further improvement of non-spatial-resolution-determined SNR in IMH detection for in-vivo CMR scans.

In summary, this dissertation has made significant contributions to advance our understanding, methods for diagnosing, and optimal detection of hemorrhagic MI. Deployment of these advances through further studies are expected to empower CMR based evaluation of myocardial infarction.

5.2 Future Directions

Since the development of LGE imaging in MI quantification about 2 decades ago, investigators were becoming to realize that the physical substrate within the infarction is more than a homogeneous focal scar in the myocardium, and that MVO, IMH, fat deposition are strongly associated with MACE in patients. The studies in this dissertation are expected to pave the way for more reliable characterization of MI with multiple CMR techniques and close the gap between research and clinical settings in the dimension of spatial information, acquisition time, and novel image contrast. With those advancements, we hope to facilitate substrate-targeted therapies for MI patients' long-term survival and quality of life. Hence, the future direction for

this study is to push the boundaries in these aspects of CMR as a clinical useful instrument to benefit the needed patients and improve patient outcomes.

5.2.1 Validation on Proposed LRT T1, T2* Patients with IMH

The newly developed fully ungated, free-breathing, 3D T1, T2* technique has been validated in animals with MI at both acute and chronic phase. Animal scans were performed with intubation and anesthesia which reduced unexpected motion. In human studies, large movement may affect the reconstruction efficiency for LRT techniques but this remains to be investigated in patients with MI under a range of health conditions.

5.2.2 Further Development of LRT T1, T2* Imaging Method

With the developed 3D free-breathing, non-ECG-gated T1, T2* LRT technique, MI, IMH, MVO and cardiac function can now be characterized in single acquisition. In Chapter 2, we were able to demonstrate superior temporal resolution and spatial coverage on MVO characterization, which also indicates the potential of its application in Gd perfusion and its enhancement dynamics and contrast wash-out kinetics. Future study can be performed to quantitatively assess myocardial viability using delayed-phase dynamic contrast-enhanced (dDCE) modeling with shortened scan time based on the proposed LRT approach. Besides, we noticed that 14 min continuous scan can be challenging for claustrophobic MI patients, we would like to further shorten the sequence with dDCE model to predict LGE images for MI characterization.

5.2.3 Post-contrast T1 entropy vs Pre-contrast T1 entropy

Post-contrast T1 based images (LGE, T1 mapping) has been broadly studied with texture analysis in establishing diagnosis, determining age of infarct or risk stratification [332]. Similar bSSFP readout performed in post-contrast T1 mapping could also show heterogeneity response

in T1 to fat deposition. Thus, we extend the T1 entropy analysis to post-contrast T1 mapping and our preliminary data is starting to show appreciable correlation between pre-contrast and post-contrast MI T1 mapping for MI beyond year one post MI (n=7). Additional studies would be needed to translate our findings in patients.

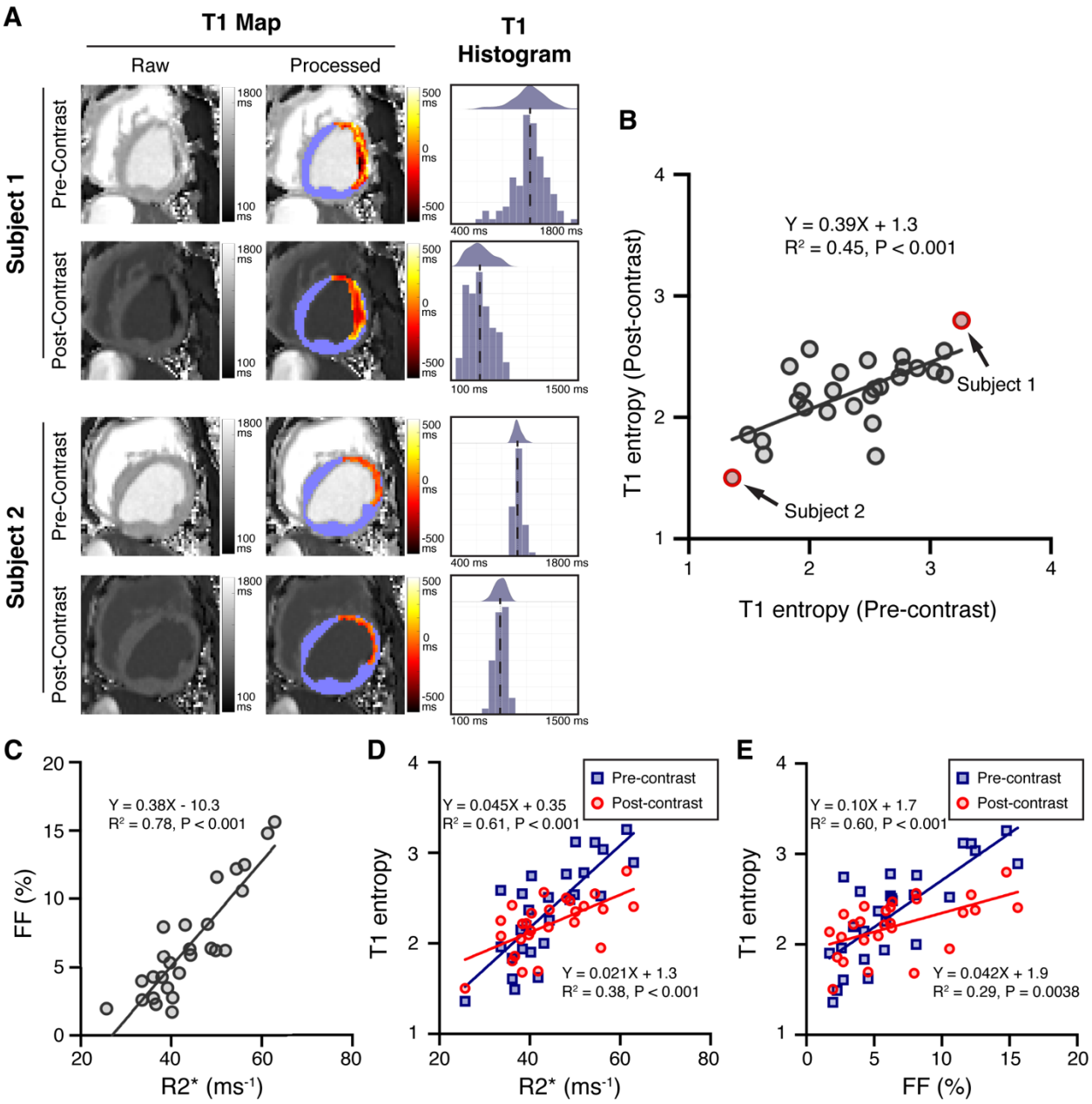


Figure 5.1 Entropy analysis on post-contrast T1 maps. A) Representative images of pre-contrast and post-contrast T1 maps. Processed MI masks is shown as ±500 ms of mean value within the MI region. T1 histograms are shown in the same range (1400 ms) for both pre- and post-contrast images, with pre-

contrast 400 ms to 1800 ms, while post-contrast 100 ms to 1500 ms. B) Scatter plot to compare Pre-contrast T1 entropy and post-contrast T1 entropy. Two representative subjects were highlighted as red data points. And linear regression shows moderate correlation between two entropies determined with pre- and post-contrast T1 maps ($R^2 = 0.45$, $P < 0.001$). C) Strong correlation of R2* and FF is shown in this subset of the chronic data ($R^2 = 0.78$, $P < 0.001$). D) and E) shows relationship of R2* vs T1 entropy, and FF vs T1 entropy in both pre- and post-contrast T1 maps. Notably, pre-contrast is shown in blue square while post-contrast is shown in red circle.

5.2.4 Improvement of spatial resolution on T2* CMR

We have demonstrated that spatial resolution in T2* CMR plays an indispensable role in detecting IMH in thinned myocardium mostly from ex-vivo study. However, from our in-vivo T2* CMR study, SNR profile has been shown to be the bottleneck of the capability of IMH detection. With the free-breathing nature of our proposed LRT framework, we may be able to improve the SNR for optimal IMH detection.

REFERENCES

1. Martin SS, Aday AW, Almarzooq ZI, et al. 2024 Heart Disease and Stroke Statistics: A Report of US and Global Data From the American Heart Association. *Circulation*. 2024;149(8):e347-e913. doi:10.1161/CIR.0000000000001209
2. Cardiovascular diseases - Level 2 cause | Institute for Health Metrics and Evaluation. Accessed August 21, 2024. https://www.healthdata.org/research-analysis/diseases-injuries-risks/factsheets/2021-cardiovascular-diseases-level-2-disease
3. Reimer KA, Jennings RB, Tatum AH. Pathobiology of acute myocardial ischemia: metabolic, functional and ultrastructural studies. *Am J Cardiol*. 1983;52(2):72A-81A. doi:10.1016/0002-9149(83)90180-7
4. Kligfield P. Heart Disease: A textbook of Cardiovascular Medicine, 5/E, edited by Eugene Braunwald, W.B. Saunders, Philadelphia (1997) 2143 pages, illustrated, $125.00 ISBN: 9-7216-5666-8. *Clin Cardiol*. 2009;21(2):147-148. doi:10.1002/clc.4960210223
5. Thygesen K, Alpert JS, White HD, et al. Universal Definition of Myocardial Infarction. *Circulation*. 2007;116(22):2634-2653. doi:10.1161/CIRCULATIONAHA.107.187397
6. Reimer KA, Jennings RB. The "wavefront phenomenon" of myocardial ischemic cell death. II. Transmural progression of necrosis within the framework of ischemic bed size (myocardium at risk) and collateral flow. *Lab Investig J Tech Methods Pathol*. 1979;40(6):633-644.
7. Effectiveness of intravenous thrombolytic treatment in acute myocardial infarction. Gruppo Italiano per lo Studio della Streptochinasi nell'Infarto Miocardico (GISSI). *Lancet Lond Engl*. 1986;1(8478):397-402.
8. Randomised trial of intravenous streptokinase, oral aspirin, both, or neither among 17,187 cases of suspected acute myocardial infarction: ISIS-2. ISIS-2 (Second International Study of Infarct Survival) Collaborative Group. *Lancet Lond Engl*. 1988;2(8607):349-360.

9. The GUSTO Investigators. An International Randomized Trial Comparing Four Thrombolytic Strategies for Acute Myocardial Infarction. *N Engl J Med*. 1993;329(10):673-682. doi:10.1056/NEJM199309023291001
10. Fibrinolytic Therapy Trialists' (FTT) Collaborative Group. Indications for fibrinolytic therapy in suspected acute myocardial infarction: collaborative overview of early mortality and major morbidity results from all randomised trials of more than 1000 patients. *The Lancet*. 1994;343(8893):311-322. doi:10.1016/S0140-6736(94)91161-4
11. Berger PB, Ellis SG, Holmes DR, et al. Relationship between delay in performing direct coronary angioplasty and early clinical outcome in patients with acute myocardial infarction: results from the global use of strategies to open occluded arteries in Acute Coronary Syndromes (GUSTO-IIb) trial. *Circulation*. 1999;100(1):14-20. doi:10.1161/01.cir.100.1.14
12. Weaver WD, Cerqueira M, Hallstrom AP, et al. Prehospital-initiated vs hospital-initiated thrombolytic therapy. The Myocardial Infarction Triage and Intervention Trial. *JAMA*. 1993;270(10):1211-1216.
13. Eitel I, Desch S, Fuernau G, et al. Prognostic significance and determinants of myocardial salvage assessed by cardiovascular magnetic resonance in acute reperfused myocardial infarction. *J Am Coll Cardiol*. 2010;55(22):2470-2479. doi:10.1016/j.jacc.2010.01.049
14. Larose E, Rodés-Cabau J, Pibarot P, et al. Predicting late myocardial recovery and outcomes in the early hours of ST-segment elevation myocardial infarction traditional measures compared with microvascular obstruction, salvaged myocardium, and necrosis characteristics by cardiovascular magnetic resonance. *J Am Coll Cardiol*. 2010;55(22):2459-2469. doi:10.1016/j.jacc.2010.02.033

15. Milavetz JJ, Giebel DW, Christian TF, Schwartz RS, Holmes DR, Gibbons RJ. Time to therapy and salvage in myocardial infarction. *J Am Coll Cardiol*. 1998;31(6):1246-1251. doi:10.1016/s0735-1097(98)00088-6

16. Yellon DM, Hausenloy DJ. Myocardial reperfusion injury. *N Engl J Med*. 2007;357(11):1121-1135. doi:10.1056/NEJMra071667

17. Kumar A, Connelly K, Vora K, et al. The Canadian Cardiovascular Society Classification of Acute Atherothrombotic Myocardial Infarction Based on Stages of Tissue Injury Severity: An Expert Consensus Statement. *Can J Cardiol*. 2024;40(1):1-14. doi:10.1016/j.cjca.2023.09.020

18. Willerson JT, Scales F, Mukherjee A, et al. Abnormal myocardial fluid retention as an early manifestation of ischemic injury. *Am J Pathol*. 1977;87(1):159-188.

19. Kloner RA, Ganote CE, Jennings RB. The "no-reflow" phenomenon after temporary coronary occlusion in the dog. *J Clin Invest*. 1974;54(6):1496-1508. doi:10.1172/JCI107898

20. Bresnahan GF, Roberts R, Shell WE, Ross J, Sobel BE. Deleterious effects due to hemorrhage after myocardial reperfusion. *Am J Cardiol*. 1974;33(1):82-86. doi:10.1016/0002-9149(74)90742-5

21. Lie JT, Lawrie GM, Morris GC, Winters WL. Hemorrhagic myocardial infarction associated with aortocoronary bypass revascularization. *Am Heart J*. 1978;96(3):295-302. doi:10.1016/0002-8703(78)90039-x

22. Fishbein MC, Y-Rit J, Lando U, Kanmatsuse K, Mercier JC, Ganz W. The relationship of vascular injury and myocardial hemorrhage to necrosis after reperfusion. *Circulation*. 1980;62(6):1274-1279. doi:10.1161/01.cir.62.6.1274

23. Reffelmann T, Kloner RA. The "no-reflow" phenomenon: basic science and clinical correlates. *Heart*. 2002;87(2):162-168. doi:10.1136/heart.87.2.162

24. Reffelmann T, Kloner RA. The no-reflow phenomenon: A basic mechanism of myocardial ischemia and reperfusion. *Basic Res Cardiol*. 2006;101(5):359-372. doi:10.1007/s00395-006-0615-2

25. Garcia-Dorado D, Théroux P, Solares J, et al. Determinants of hemorrhagic infarcts. Histologic observations from experiments involving coronary occlusion, coronary reperfusion, and reocclusion. *Am J Pathol*. 1990;137(2):301-311.

26. Eitel I, Kubusch K, Strohm O, et al. Prognostic value and determinants of a hypointense infarct core in T2-weighted cardiac magnetic resonance in acute reperfused ST-elevation-myocardial infarction. *Circ Cardiovasc Imaging*. 2011;4(4):354-362. doi:10.1161/CIRCIMAGING.110.960500

27. Vyas R, Changal KH, Bhuta S, et al. Impact of Intramyocardial Hemorrhage on Clinical Outcomes in ST-Elevation Myocardial Infarction: A Systematic Review and Meta-analysis. *J Soc Cardiovasc Angiogr Interv*. 2022;1(6). doi:10.1016/j.jscai.2022.100444

28. Ndrepepa G, Tiroch K, Fusaro M, et al. 5-year prognostic value of no-reflow phenomenon after percutaneous coronary intervention in patients with acute myocardial infarction. *J Am Coll Cardiol*. 2010;55(21):2383-2389. doi:10.1016/j.jacc.2009.12.054

29. Hamirani YS, Wong A, Kramer CM, Salerno M. Effect of Microvascular Obstruction and Intramyocardial Hemorrhage by CMR on LV Remodeling and Outcomes After Myocardial Infarction. *JACC Cardiovasc Imaging*. 2014;7(9):940-952. doi:10.1016/j.jcmg.2014.06.012

30. Reinstadler SJ, Stiermaier T, Reindl M, et al. Intramyocardial haemorrhage and prognosis after ST-elevation myocardial infarction. *Eur Heart J - Cardiovasc Imaging*. 2019;20(2):138-146. doi:10.1093/ehjci/jey101

31. Carrick D, Haig C, Ahmed N, et al. Myocardial Hemorrhage After Acute Reperfused ST-Segment-Elevation Myocardial Infarction: Relation to Microvascular Obstruction and

Prognostic Significance. *Circ Cardiovasc Imaging*. 2016;9(1):e004148. doi:10.1161/CIRCIMAGING.115.004148

32. Lombardo A, Niccoli G, Natale L, et al. Impact of microvascular obstruction and infarct size on left ventricular remodeling in reperfused myocardial infarction: a contrast-enhanced cardiac magnetic resonance imaging study. *Int J Cardiovasc Imaging*. 2012;28(4):835-842. doi:10.1007/s10554-011-9901-7
33. Weir RAP, Murphy CA, Petrie CJ, et al. Microvascular obstruction remains a portent of adverse remodeling in optimally treated patients with left ventricular systolic dysfunction after acute myocardial infarction. *Circ Cardiovasc Imaging*. 2010;3(4):360-367. doi:10.1161/CIRCIMAGING.109.897439
34. de Waha S, Desch S, Eitel I, et al. Relationship and prognostic value of microvascular obstruction and infarct size in ST-elevation myocardial infarction as visualized by magnetic resonance imaging. *Clin Res Cardiol Off J Ger Card Soc*. 2012;101(6):487-495. doi:10.1007/s00392-012-0419-3
35. Marc MC, Iancu AC, Ober CD, et al. Pre-revascularization coronary wedge pressure as marker of adverse long-term left ventricular remodelling in patients with acute ST-segment elevation myocardial infarction. *Sci Rep*. 2018;8(1):1897. doi:10.1038/s41598-018-20276-6
36. Kloner RA. Does reperfusion injury exist in humans? *J Am Coll Cardiol*. 1993;21(2):537-545. doi:10.1016/0735-1097(93)90700-B
37. Olafsson B, Forman MB, Puett DW, et al. Reduction of reperfusion injury in the canine preparation by intracoronary adenosine: importance of the endothelium and the no-reflow phenomenon. *Circulation*. 1987;76(5):1135-1145. doi:10.1161/01.cir.76.5.1135
38. Betgem RP, de Waard GA, Nijveldt R, Beek AM, Escaned J, van Royen N. Intramyocardial haemorrhage after acute myocardial infarction. *Nat Rev Cardiol*. 2015;12(3):156-167. doi:10.1038/nrcardio.2014.188

39. Roberts CS, Schoen FJ, Kloner RA. Effect of coronary reperfusion on myocardial hemorrhage and infarct healing. *Am J Cardiol*. 1983;52(5):610-614. doi:10.1016/0002-9149(83)90036-X

40. Reffelmann T, Kloner RA. Microvascular reperfusion injury: rapid expansion of anatomic no reflow during reperfusion in the rabbit. *Am J Physiol-Heart Circ Physiol*. 2002;283(3):H1099-H1107. doi:10.1152/ajpheart.00270.2002

41. Marc MC, Iancu AC, Bălănescu Ş, Dregoesc MI. Microvascular obstruction in acute myocardial infarction: an old and unsolved mystery. *Med Pharm Rep*. 2019;92(3):216-219. doi:10.15386/mpr-1261

42. Mather AN, Fairbairn TA, Artis NJ, Greenwood JP, Plein S. Relationship of cardiac biomarkers and reversible and irreversible myocardial injury following acute myocardial infarction as determined by cardiovascular magnetic resonance. *Int J Cardiol*. 2013;166(2):458-464. doi:10.1016/j.ijcard.2011.11.004

43. Bekkers SCAM, Smulders MW, Passos VL, et al. Clinical implications of microvascular obstruction and intramyocardial haemorrhage in acute myocardial infarction using cardiovascular magnetic resonance imaging. *Eur Radiol*. 2010;20(11):2572-2578. doi:10.1007/s00330-010-1849-9

44. Mayr A, Klug G, Reindl M, et al. Evolution of Myocardial Tissue Injury: A CMR Study Over a Decade After STEMI. *JACC Cardiovasc Imaging*. 2022;15(6):1030-1042. doi:10.1016/j.jcmg.2022.02.010

45. Cokic I, Chan SF, Guan X, et al. Intramyocardial hemorrhage drives fatty degeneration of infarcted myocardium. *Nat Commun*. 2022;13(1):6394. doi:10.1038/s41467-022-33776-x

46. Kali A, Cokic I, Tang R, et al. Persistent Microvascular Obstruction After Myocardial Infarction Culminates in the Confluence of Ferric Iron Oxide Crystals, Proinflammatory

Burden, and Adverse Remodeling. *Circ Cardiovasc Imaging*. 2016;9(11):e004996. doi:10.1161/CIRCIMAGING.115.004996

47. Ghugre NR, Pop M, Thomas R, et al. Hemorrhage promotes inflammation and myocardial damage following acute myocardial infarction: insights from a novel preclinical model and cardiovascular magnetic resonance. *J Cardiovasc Magn Reson*. 2017;19(1):50. doi:10.1186/s12968-017-0361-7
48. Cokic I, Kali A, Yang HJ, et al. Iron-Sensitive Cardiac Magnetic Resonance Imaging for Prediction of Ventricular Arrhythmia Risk in Patients With Chronic Myocardial Infarction. *Circ Cardiovasc Imaging*. 2015;8(8):e003642. doi:10.1161/CIRCIMAGING.115.003642
49. Mather AN, Fairbairn TA, Ball SG, Greenwood JP, Plein S. Reperfusion haemorrhage as determined by cardiovascular MRI is a predictor of adverse left ventricular remodelling and markers of late arrhythmic risk. *Heart*. 2011;97(6):453-459. doi:10.1136/hrt.2010.202028
50. Sung E, Prakosa A, Zhou S, et al. Fat infiltration in the infarcted heart as a paradigm for ventricular arrhythmias. *Nat Cardiovasc Res*. 2022;1(10):933-945. doi:10.1038/s44161-022-00133-6
51. Wang Q, Ji J, Hao S, Zhang M, Li K, Qiao T. Iron Together with Lipid Downregulates Protein Levels of Ceruloplasmin in Macrophages Associated with Rapid Foam Cell Formation. *J Atheroscler Thromb*. 2016;23(10):1201-1211. doi:10.5551/jat.32292
52. Ramakrishna G, Rooke TW, Cooper LT. Iron and peripheral arterial disease: revisiting the iron hypothesis in a different light. *Vasc Med*. 2003;8(3):203-210. doi:10.1191/1358863x03vm493ra
53. Goldfarb JW, Roth M, Han J. Myocardial Fat Deposition after Left Ventricular Myocardial Infarction: Assessment by Using MR Water-Fat Separation Imaging. *Radiology*. 2009;253(1):65-73. doi:10.1148/radiol.2532082290

54. Cheniti G, Sridi S, Sacher F, et al. Post-Myocardial Infarction Scar With Fat Deposition Shows Specific Electrophysiological Properties and Worse Outcome After Ventricular Tachycardia Ablation. *J Am Heart Assoc*. 2019;8(15):e012482. doi:10.1161/JAHA.119.012482

55. Su L, Siegel JE, Fishbein MC. Adipose tissue in myocardial infarction. *Cardiovasc Pathol*. 2004;13(2):98-102. doi:10.1016/S1054-8807(03)00134-0

56. Goldfarb JW, Arnold S, Han J. Recent Myocardial Infarction: Assessment with Unenhanced T1-weighted MR Imaging1. *Radiology*. Published online October 1, 2007. doi:10.1148/radiol.2451061590

57. Mordi I, Radjenovic A, Stanton T, et al. Prevalence and Prognostic Significance of Lipomatous Metaplasia in Patients With Prior Myocardial Infarction. *JACC Cardiovasc Imaging*. 2015;8(9):1111-1112. doi:10.1016/j.jcmg.2014.07.024

58. Krug A, Du Mesnil de Rochemont null, Korb G. Blood supply of the myocardium after temporary coronary occlusion. *Circ Res*. 1966;19(1):57-62. doi:10.1161/01.res.19.1.57

59. Bradley WG. MR appearance of hemorrhage in the brain. *Radiology*. 1993;189(1):15-26. doi:10.1148/radiology.189.1.8372185

60. Ertl G, Frantz S. Healing after myocardial infarction. *Cardiovasc Res*. 2005;66(1):22-32. doi:10.1016/j.cardiores.2005.01.011

61. Frangogiannis NG, Smith CW, Entman ML. The inflammatory response in myocardial infarction. *Cardiovasc Res*. 2002;53(1):31-47. doi:10.1016/s0008-6363(01)00434-5

62. Gomori JM, Grossman RI, Goldberg HI, Zimmerman RA, Bilaniuk LT. Intracranial hematomas: imaging by high-field MR. *Radiology*. 1985;157(1):87-93. doi:10.1148/radiology.157.1.4034983

63. Baroldi G, Silver MD, De Maria R, Parodi O, Pellegrini A. Lipomatous metaplasia in left ventricular scar. *Can J Cardiol*. 1997;13(1):65-71.

64. Pouliopoulos J, Chik WWB, Kanthan A, et al. Intramyocardial Adiposity After Myocardial Infarction. *Circulation*. 2013;128(21):2296-2308. doi:10.1161/CIRCULATIONAHA.113.002238

65. Sasaki T, Calkins H, Miller CF, et al. New Insight into Scar-related Ventricular Tachycardia Circuits in Ischemic Cardiomyopathy: Fat Deposition after Myocardial Infarction on Computed Tomography: A Pilot Study. *Heart Rhythm Off J Heart Rhythm Soc*. 2015;12(7):1508-1518. doi:10.1016/j.hrthm.2015.03.041

66. Roberts WC, Siegel RJ, McManus BM. Idiopathic dilated cardiomyopathy: analysis of 152 necropsy patients. *Am J Cardiol*. 1987;60(16):1340-1355. doi:10.1016/0002-9149(87)90618-7

67. de Leeuw N, Ruiter DJ, Balk AH, de Jonge N, Melchers WJ, Galama JM. Histopathologic findings in explanted heart tissue from patients with end-stage idiopathic dilated cardiomyopathy. *Transpl Int Off J Eur Soc Organ Transplant*. 2001;14(5):299-306. doi:10.1007/s001470100339

68. Brooks A, Schinde V, Bateman AC, Gallagher PJ. Interstitial fibrosis in the dilated non-ischaemic myocardium. *Heart*. 2003;89(10):1255-1256.

69. Querejeta R, López B, González A, et al. Increased collagen type I synthesis in patients with heart failure of hypertensive origin: relation to myocardial fibrosis. *Circulation*. 2004;110(10):1263-1268. doi:10.1161/01.CIR.0000140973.60992.9A

70. Whittaker P, Boughner DR, Kloner RA. Analysis of healing after myocardial infarction using polarized light microscopy. *Am J Pathol*. 1989;134(4):879-893.

71. Schwarz F, Mall G, Zebe H, et al. Quantitative morphologic findings of the myocardium in idiopathic dilated cardiomyopathy. *Am J Cardiol*. 1983;51(3):501-506. doi:10.1016/s0002-9149(83)80088-5

72. Schalla S, Bekkers SC, Dennert R, et al. Replacement and reactive myocardial fibrosis in idiopathic dilated cardiomyopathy: comparison of magnetic resonance imaging with right ventricular biopsy. *Eur J Heart Fail*. 2010;12(3):227-231. doi:10.1093/eurjhf/hfq004

73. Abraham TP, Dimaano VL, Liang HY. Role of Tissue Doppler and Strain Echocardiography in Current Clinical Practice. *Circulation*. 2007;116(22):2597-2609. doi:10.1161/CIRCULATIONAHA.106.647172

74. Dandel M, Lehmkuhl H, Knosalla C, Suramelashvili N, Hetzer R. Strain and Strain Rate Imaging by Echocardiography – Basic Concepts and Clinical Applicability. *Curr Cardiol Rev*. 2009;5(2):133-148. doi:10.2174/157340309788166642

75. Stewart GA, Foster J, Cowan M, et al. Echocardiography overestimates left ventricular mass in hemodialysis patients relative to magnetic resonance imaging. *Kidney Int*. 1999;56(6):2248-2253. doi:10.1046/j.1523-1755.1999.00786.x

76. Hunold P, Vogt FM, Heemann UW, Zimmermann U, Barkhausen J. Myocardial mass and volume measurement of hypertrophic left ventricles by MRI--study in dialysis patients examined before and after dialysis. *J Cardiovasc Magn Reson Off J Soc Cardiovasc Magn Reson*. 2003;5(4):553-561. doi:10.1081/jcmr-120025230

77. Thornhill RE, Prato FS, Wisenberg G. The assessment of myocardial viability: a review of current diagnostic imaging approaches. *J Cardiovasc Magn Reson Off J Soc Cardiovasc Magn Reson*. 2002;4(3):381-410. doi:10.1081/jcmr-120013301

78. Vanoverschelde JL, Gerber B, Pasquet A, Melin JA. Nuclear and echocardiographic imaging for prediction of reversible left ventricular ischemic dysfunction after coronary revascularization: current status and future directions. *J Cardiovasc Pharmacol*. 1996;28 Suppl 1:S27-36. doi:10.1097/00005344-199600003-00005

79. Clark AN, Beller GA. The present role of nuclear cardiology in clinical practice. *Q J Nucl Med Mol Imaging Off Publ Ital Assoc Nucl Med AIMN Int Assoc Radiopharmacol IAR Sect Soc Of*. 2005;49(1):43-58.

80. Thompson RC, Cullom SJ. Issues regarding radiation dosage of cardiac nuclear and radiography procedures. *J Nucl Cardiol Off Publ Am Soc Nucl Cardiol*. 2006;13(1):19-23. doi:10.1016/j.nuclcard.2005.11.004

81. Meijboom WB, Meijs MFL, Schuijf JD, et al. Diagnostic accuracy of 64-slice computed tomography coronary angiography: a prospective, multicenter, multivendor study. *J Am Coll Cardiol*. 2008;52(25):2135-2144. doi:10.1016/j.jacc.2008.08.058

82. Lardo AC, Cordeiro MAS, Silva C, et al. Contrast-Enhanced Multidetector Computed Tomography Viability Imaging After Myocardial Infarction: Characterization of Myocyte Death, Microvascular Obstruction, and Chronic Scar. *Circulation*. 2006;113(3):394-404. doi:10.1161/CIRCULATIONAHA.105.521450

83. Hoffmann U, Millea R, Enzweiler C, et al. Acute Myocardial Infarction: Contrast-enhanced Multi–Detector Row CT in a Porcine Model. *Radiology*. 2004;231(3):697-701. doi:10.1148/radiol.2313030132

84. Gerber BL, Belge B, Legros GJ, et al. Characterization of acute and chronic myocardial infarcts by multidetector computed tomography: comparison with contrast-enhanced magnetic resonance. *Circulation*. 2006;113(6):823-833. doi:10.1161/CIRCULATIONAHA.104.529511

85. Mahnken AH, Koos R, Katoh M, et al. Assessment of myocardial viability in reperfused acute myocardial infarction using 16-slice computed tomography in comparison to magnetic resonance imaging. *J Am Coll Cardiol*. 2005;45(12):2042-2047. doi:10.1016/j.jacc.2005.03.035

86. Choe YH, Choo KS, Jeon ES, Gwon HC, Choi JH, Park JE. Comparison of MDCT and MRI in the detection and sizing of acute and chronic myocardial infarcts. *Eur J Radiol*. 2008;66(2):292-299. doi:10.1016/j.ejrad.2007.06.010

87. Oda S, Emoto T, Nakaura T, et al. Myocardial Late Iodine Enhancement and Extracellular Volume Quantification with Dual-Layer Spectral Detector Dual-Energy Cardiac CT. *Radiol Cardiothorac Imaging*. 2019;1(1):e180003. doi:10.1148/ryct.2019180003

88. Saeed M, Van TA, Krug R, Hetts SW, Wilson MW. Cardiac MR imaging: current status and future direction. *Cardiovasc Diagn Ther*. 2015;5(4):290-310. doi:10.3978/j.issn.2223-3652.2015.06.07

89. Einstein AJ, Berman DS, Min JK, et al. Patient-centered imaging: shared decision making for cardiac imaging procedures with exposure to ionizing radiation. *J Am Coll Cardiol*. 2014;63(15):1480-1489. doi:10.1016/j.jacc.2013.10.092

90. Kallianos K, Moraes GL, Ordovas KG. Prognostic role of MR imaging in nonischemic myocardial disease. *Magn Reson Imaging Clin N Am*. 2015;23(1):89-94. doi:10.1016/j.mric.2014.09.004

91. Kathiria NN, Higgins CB, Ordovas KG. Advances in MR imaging assessment of adults with congenital heart disease. *Magn Reson Imaging Clin N Am*. 2015;23(1):35-40. doi:10.1016/j.mric.2014.09.005

92. Kohi MP, Ordovas KG, Naeger DM, Meadows AK, Foster E, Higgins CB. CMR assessment of right ventricular function in patients with combined pulmonary stenosis and insufficiency after correction of tetralogy of Fallot. *Acta Radiol Stockh Swed 1987*. 2013;54(10):1132-1137. doi:10.1177/0284185113491565

93. Naeger DM, Higgins C, De Marco T, Muzzarelli S, Ordovas KG. Low-intensity late gadolinium enhancement predominates in hypertrophic cardiomyopathy. *Clin Imaging*. 2015;39(3):432-436. doi:10.1016/j.clinimag.2015.01.001

94. Mazaheri Y, Akin O, Hricak H. Dynamic contrast-enhanced magnetic resonance imaging of prostate cancer: A review of current methods and applications. *World J Radiol*. 2017;9(12):416-425. doi:10.4329/wjr.v9.i12.416

95. Karamitsos TD, Francis JM, Myerson S, Selvanayagam JB, Neubauer S. The role of cardiovascular magnetic resonance imaging in heart failure. *J Am Coll Cardiol*. 2009;54(15):1407-1424. doi:10.1016/j.jacc.2009.04.094

96. Mahrholdt H, Wagner A, Judd RM, Sechtem U, Kim RJ. Delayed enhancement cardiovascular magnetic resonance assessment of non-ischaemic cardiomyopathies. *Eur Heart J*. 2005;26(15):1461-1474. doi:10.1093/eurheartj/ehi258

97. McCrohon JA, Moon JCC, Prasad SK, et al. Differentiation of heart failure related to dilated cardiomyopathy and coronary artery disease using gadolinium-enhanced cardiovascular magnetic resonance. *Circulation*. 2003;108(1):54-59. doi:10.1161/01.CIR.0000078641.19365.4C

98. Kim RJ, Wu E, Rafael A, et al. The Use of Contrast-Enhanced Magnetic Resonance Imaging to Identify Reversible Myocardial Dysfunction. *N Engl J Med*. 2000;343(20):1445-1453. doi:10.1056/NEJM200011163432003

99. Orn S, Manhenke C, Anand IS, et al. Effect of left ventricular scar size, location, and transmurality on left ventricular remodeling with healed myocardial infarction. *Am J Cardiol*. 2007;99(8):1109-1114. doi:10.1016/j.amjcard.2006.11.059

100. Assomull RG, Prasad SK, Lyne J, et al. Cardiovascular magnetic resonance, fibrosis, and prognosis in dilated cardiomyopathy. *J Am Coll Cardiol*. 2006;48(10):1977-1985. doi:10.1016/j.jacc.2006.07.049

101. Bello D, Shah DJ, Farah GM, et al. Gadolinium cardiovascular magnetic resonance predicts reversible myocardial dysfunction and remodeling in patients with heart failure undergoing beta-blocker therapy. *Circulation*. 2003;108(16):1945-1953. doi:10.1161/01.CIR.0000095029.57483.60

102. Kwong RY, Chan AK, Brown KA, et al. Impact of unrecognized myocardial scar detected by cardiac magnetic resonance imaging on event-free survival in patients presenting with signs or symptoms of coronary artery disease. *Circulation*. 2006;113(23):2733-2743. doi:10.1161/CIRCULATIONAHA.105.570648

103. Bello D, Fieno DS, Kim RJ, et al. Infarct morphology identifies patients with substrate for sustained ventricular tachycardia. *J Am Coll Cardiol*. 2005;45(7):1104-1108. doi:10.1016/j.jacc.2004.12.057

104. Rubinshtein R, Glockner JF, Ommen SR, et al. Characteristics and clinical significance of late gadolinium enhancement by contrast-enhanced magnetic resonance imaging in patients with hypertrophic cardiomyopathy. *Circ Heart Fail*. 2010;3(1):51-58. doi:10.1161/CIRCHEARTFAILURE.109.854026

105. Kwon DH, Smedira NG, Rodriguez ER, et al. Cardiac magnetic resonance detection of myocardial scarring in hypertrophic cardiomyopathy: correlation with histopathology and prevalence of ventricular tachycardia. *J Am Coll Cardiol*. 2009;54(3):242-249. doi:10.1016/j.jacc.2009.04.026

106. Austin BA, Tang WHW, Rodriguez ER, et al. Delayed hyper-enhancement magnetic resonance imaging provides incremental diagnostic and prognostic utility in suspected cardiac amyloidosis. *JACC Cardiovasc Imaging*. 2009;2(12):1369-1377. doi:10.1016/j.jcmg.2009.08.008

107. Judd RM, Lugo-Olivieri CH, Arai M, et al. Physiological basis of myocardial contrast enhancement in fast magnetic resonance images of 2-day-old reperfused canine infarcts. *Circulation*. 1995;92(7):1902-1910. doi:10.1161/01.cir.92.7.1902

108. Lima JA, Judd RM, Bazille A, Schulman SP, Atalar E, Zerhouni EA. Regional heterogeneity of human myocardial infarcts demonstrated by contrast-enhanced MRI. Potential mechanisms. *Circulation*. 1995;92(5):1117-1125. doi:10.1161/01.cir.92.5.1117

109. Kim RJ, Fieno DS, Parrish TB, et al. Relationship of MRI delayed contrast enhancement to irreversible injury, infarct age, and contractile function. *Circulation*. 1999;100(19):1992-2002. doi:10.1161/01.cir.100.19.1992

110. Mahrholdt H, Wagner A, Holly TA, et al. Reproducibility of chronic infarct size measurement by contrast-enhanced magnetic resonance imaging. *Circulation*. 2002;106(18):2322-2327. doi:10.1161/01.cir.0000036368.63317.1c

111. Ricciardi MJ, Wu E, Davidson CJ, et al. Visualization of Discrete Microinfarction After Percutaneous Coronary Intervention Associated With Mild Creatine Kinase-MB Elevation. *Circulation*. 2001;103(23):2780-2783. doi:10.1161/hc2301.092121

112. Wu E, Judd RM, Vargas JD, Klocke FJ, Bonow RO, Kim RJ. Visualisation of presence, location, and transmural extent of healed Q-wave and non-Q-wave myocardial infarction. *Lancet Lond Engl*. 2001;357(9249):21-28. doi:10.1016/S0140-6736(00)03567-4

113. Schmidt A, Azevedo CF, Cheng A, et al. Infarct Tissue Heterogeneity by Magnetic Resonance Imaging Identifies Enhanced Cardiac Arrhythmia Susceptibility in Patients With Left Ventricular Dysfunction. *Circulation*. 2007;115(15):2006-2014. doi:10.1161/CIRCULATIONAHA.106.653568

114. Yan AT, Shayne AJ, Brown KA, et al. Characterization of the peri-infarct zone by contrast-enhanced cardiac magnetic resonance imaging is a powerful predictor of post-myocardial

infarction mortality. *Circulation*. 2006;114(1):32-39. doi:10.1161/CIRCULATIONAHA.106.613414

115. Watanabe E, Abbasi SA, Heydari B, et al. Infarct tissue heterogeneity by contrast-enhanced magnetic resonance imaging is a novel predictor of mortality in patients with chronic coronary artery disease and left ventricular dysfunction. *Circ Cardiovasc Imaging*. 2014;7(6):887-894. doi:10.1161/CIRCIMAGING.113.001293
116. Nathan M, Ying LC, Pierre C, David B, João L. Assessment of Myocardial Fibrosis with Cardiac Magnetic Resonance. *J Am Coll Cardiol*. 2011;57(8):891-903. doi:10.1016/j.jacc.2010.11.013
117. Kali A, Choi EY, Sharif B, et al. Native T 1 Mapping by 3-T CMR Imaging for Characterization of Chronic Myocardial Infarctions. *JACC Cardiovasc Imaging*. 2015;8(9):1019-1030. doi:10.1016/j.jcmg.2015.04.018
118. Kali A, Cokic I, Tang RLQ, et al. Determination of Location, Size, and Transmurality of Chronic Myocardial Infarction Without Exogenous Contrast Media by Using Cardiac Magnetic Resonance Imaging at 3 T. *Circ Cardiovasc Imaging*. 2014;7(3):471-481. doi:10.1161/CIRCIMAGING.113.001541
119. Messroghli DR, Walters K, Plein S, et al. Myocardial T1 mapping: application to patients with acute and chronic myocardial infarction. *Magn Reson Med*. 2007;58(1):34-40. doi:10.1002/mrm.21272
120. Dall'Armellina E, Piechnik SK, Ferreira VM, et al. Cardiovascular magnetic resonance by non contrast T1-mapping allows assessment of severity of injury in acute myocardial infarction. *J Cardiovasc Magn Reson Off J Soc Cardiovasc Magn Reson*. 2012;14(1):15. doi:10.1186/1532-429X-14-15

121. Puntmann VO, Peker E, Chandrashekhar Y, Nagel E. T1 Mapping in Characterizing Myocardial Disease. *Circ Res*. 2016;119(2):277-299. doi:10.1161/CIRCRESAHA.116.307974

122. Messroghli DR, Radjenovic A, Kozerke S, Higgins DM, Sivananthan MU, Ridgway JP. Modified Look-Locker inversion recovery (MOLLI) for high-resolution T1 mapping of the heart. *Magn Reson Med*. 2004;52(1):141-146. doi:10.1002/mrm.20110

123. Messroghli DR, Greiser A, Fröhlich M, Dietz R, Schulz-Menger J. Optimization and validation of a fully-integrated pulse sequence for modified look-locker inversion-recovery (MOLLI) T1 mapping of the heart. *J Magn Reson Imaging JMRI*. 2007;26(4):1081-1086. doi:10.1002/jmri.21119

124. Messroghli DR, Niendorf T, Schulz-Menger J, Dietz R, Friedrich MG. T1 mapping in patients with acute myocardial infarction. *J Cardiovasc Magn Reson Off J Soc Cardiovasc Magn Reson*. 2003;5(2):353-359. doi:10.1081/jcmr-120019418

125. Messroghli DR, Plein S, Higgins DM, et al. Human Myocardium: Single-Breath-hold MR T1 Mapping with High Spatial Resolution—Reproducibility Study. *Radiology*. 2006;238(3):1004-1012. doi:10.1148/radiol.2382041903

126. Seno A, Antiochos P, Lichtenfeld H, et al. Prognostic Value of T1 Mapping and Feature Tracking by Cardiac Magnetic Resonance in Patients With Signs and Symptoms Suspecting Heart Failure and No Clinical Evidence of Coronary Artery Disease. *J Am Heart Assoc*. 2022;11(2):e020981. doi:10.1161/JAHA.121.020981

127. Aquaro GD, Monastero S, Todiere G, et al. Diagnostic Role of Native T1 Mapping Compared to Conventional Magnetic Resonance Techniques in Cardiac Disease in a Real-Life Cohort. *Diagnostics*. 2023;13(14):2461. doi:10.3390/diagnostics13142461

128. Dall 'Armellina Erica, Ferreira VM, Kharbanda RK, et al. Diagnostic Value of Pre-Contrast T1 Mapping in Acute and Chronic Myocardial Infarction. *JACC Cardiovasc Imaging*. 2013;6(6):739-742. doi:10.1016/j.jcmg.2012.11.020

129. Liu D, Borlotti A, Viliani D, et al. CMR Native T1 Mapping Allows Differentiation of Reversible Versus Irreversible Myocardial Damage in ST-Segment–Elevation Myocardial Infarction. *Circ Cardiovasc Imaging*. 2017;10(8):e005986. doi:10.1161/CIRCIMAGING.116.005986

130. Rommel KP, Lücke C, Lurz P. Diagnostic and Prognostic Value of CMR T1-Mapping in Patients With Heart Failure and Preserved Ejection Fraction. *Rev Esp Cardiol Engl Ed*. 2017;70(10):848-855. doi:10.1016/j.rec.2017.02.018

131. Dastidar AG, Harries I, Pontecorboli G, et al. Native T1 mapping to detect extent of acute and chronic myocardial infarction: comparison with late gadolinium enhancement technique. *Int J Cardiovasc Imaging*. 2019;35(3):517-527. doi:10.1007/s10554-018-1467-1

132. Jia Z, Wang L, Jia Y, et al. Detection of acute myocarditis using T1 and T2 mapping cardiovascular magnetic resonance: A systematic review and meta-analysis. *J Appl Clin Med Phys*. 2021;22(10):239-248. doi:10.1002/acm2.13365

133. Bloch F. Nuclear Induction. *Phys Rev*. 1946;70(7-8):460-474. doi:10.1103/PhysRev.70.460

134. McNamara MT, Higgins CB, Schechtmann N, et al. Detection and characterization of acute myocardial infarction in man with use of gated magnetic resonance. *Circulation*. 1985;71(4):717-724. doi:10.1161/01.CIR.71.4.717

135. Giri S, Chung YC, Merchant A, et al. T2 quantification for improved detection of myocardial edema. *J Cardiovasc Magn Reson Off J Soc Cardiovasc Magn Reson*. 2009;11(1):56. doi:10.1186/1532-429X-11-56

136. Foltz WD, Al-Kwifi O, Sussman MS, Stainsby JA, Wright GA. Optimized spiral imaging for measurement of myocardial T2 relaxation. *Magn Reson Med*. 2003;49(6):1089-1097. doi:10.1002/mrm.10467

137. Huang TY, Liu YJ, Stemmer A, Poncelet BP. T2 measurement of the human myocardium using a T2-prepared transient-state TrueFISP sequence. *Magn Reson Med*. 2007;57(5):960-966. doi:10.1002/mrm.21208

138. van Heeswijk RB, Feliciano H, Bongard C, et al. Free-breathing 3 T magnetic resonance T2-mapping of the heart. *JACC Cardiovasc Imaging*. 2012;5(12):1231-1239. doi:10.1016/j.jcmg.2012.06.010

139. Fernández-Jiménez R, Sánchez-González J, Aguero J, et al. Fast T2 gradient-spin-echo (T2-GraSE) mapping for myocardial edema quantification: first in vivo validation in a porcine model of ischemia/reperfusion. *J Cardiovasc Magn Reson*. 2015;17:92. doi:10.1186/s12968-015-0199-9

140. Galán-Arriola C, Lobo M, Vílchez-Tschischke JP, et al. Serial Magnetic Resonance Imaging to Identify Early Stages of Anthracycline-Induced Cardiotoxicity. *J Am Coll Cardiol*. 2019;73(7):779-791. doi:10.1016/j.jacc.2018.11.046

141. Baeßler B, Schaarschmidt F, Stehning C, Schnackenburg B, Maintz D, Bunck AC. Cardiac T2-mapping using a fast gradient echo spin echo sequence - first in vitro and in vivo experience. *J Cardiovasc Magn Reson*. 2015;17(1):67. doi:10.1186/s12968-015-0177-2

142. Simonetti OP, Finn JP, White RD, Laub G, Henry DA. "Black blood" T2-weighted inversion-recovery MR imaging of the heart. *Radiology*. 1996;199(1):49-57. doi:10.1148/radiology.199.1.8633172

143. Messroghli DR, Moon JC, Ferreira VM, et al. Clinical recommendations for cardiovascular magnetic resonance mapping of T1, T2, T2* and extracellular volume: A consensus statement by the Society for Cardiovascular Magnetic Resonance (SCMR) endorsed by the

European Association for Cardiovascular Imaging (EACVI). *J Cardiovasc Magn Reson*. 2017;19(1):75. doi:10.1186/s12968-017-0389-8

144. Zia MI, Ghugre NR, Connelly KA, et al. Characterizing myocardial edema and hemorrhage using quantitative T2 and T2* mapping at multiple time intervals post ST-segment elevation myocardial infarction. *Circ Cardiovasc Imaging*. 2012;5(5):566-572. doi:10.1161/CIRCIMAGING.112.973222
145. Payne AR, Berry C, Kellman P, et al. Bright-blood T(2)-weighted MRI has high diagnostic accuracy for myocardial hemorrhage in myocardial infarction: a preclinical validation study in swine. *Circ Cardiovasc Imaging*. 2011;4(6):738-745. doi:10.1161/CIRCIMAGING.111.965095
146. Kali A, Tang RLQ, Kumar A, Min JK, Dharmakumar R. Detection of Acute Reperfusion Myocardial Hemorrhage with Cardiac MR Imaging: T2 versus T2*. *Card IMAGING*. 2013;269(2):9.
147. Carpenter JP, He T, Kirk P, et al. On T2* Magnetic Resonance and Cardiac Iron. *Circulation*. 2011;123(14):1519-1528. doi:10.1161/CIRCULATIONAHA.110.007641
148. Ghugre NR, Enriquez CM, Gonzalez I, Nelson MD, Coates TD, Wood JC. MRI Detects Myocardial Iron in the Human Heart. *Magn Reson Med Off J Soc Magn Reson Med Soc Magn Reson Med*. 2006;56(3):681-686. doi:10.1002/mrm.20981
149. He T, Gatehouse PD, Smith GC, Mohiaddin RH, Pennell DJ, Firmin DN. Myocardial T2* Measurements in Iron Overloaded Thalassemia. *Magn Reson Med Off J Soc Magn Reson Med Soc Magn Reson Med*. 2008;60(5):1082-1089. doi:10.1002/mrm.21744
150. House MJ, Fleming AJ, de Jonge MD, et al. Mapping iron in human heart tissue with synchrotron x-ray fluorescence microscopy and cardiovascular magnetic resonance. *J Cardiovasc Magn Reson*. 2014;16(1):80. doi:10.1186/s12968-014-0080-2

151. Kirk P, Sheppard M, Carpenter JP, et al. Post-mortem study of the association between cardiac iron and fibrosis in transfusion dependent anaemia. *J Cardiovasc Magn Reson Off J Soc Cardiovasc Magn Reson*. 2017;19(1):36. doi:10.1186/s12968-017-0349-3

152. Anderson L. Cardiovascular T2-star (T2*) magnetic resonance for the early diagnosis of myocardial iron overload. *Eur Heart J*. 2001;22(23):2171-2179. doi:10.1053/euhj.2001.2822

153. Chen Y, Ren D, Guan X, et al. Quantification of myocardial hemorrhage using T2* cardiovascular magnetic resonance at 1.5T with ex-vivo validation. *J Cardiovasc Magn Reson*. 2021;23(1):104. doi:10.1186/s12968-021-00779-4

154. Guan X, Chen Y, Yang HJ, et al. Assessment of intramyocardial hemorrhage with dark-blood T2*-weighted cardiovascular magnetic resonance. *J Cardiovasc Magn Reson*. 2021;23(1):88. doi:10.1186/s12968-021-00787-4

155. Carberry J, Carrick D, Haig C, et al. Persistent Iron Within the Infarct Core After ST-Segment Elevation Myocardial Infarction. *JACC Cardiovasc Imaging*. 2018;11(9):1248-1256. doi:10.1016/j.jcmg.2017.08.027

156. Musthafa HSN, Dragneva G, Lottonen L, et al. Longitudinal rotating frame relaxation time measurements in infarcted mouse myocardium in vivo. *Magn Reson Med*. 2013;69(5):1389-1395. doi:10.1002/mrm.24382

157. Berisha S, Han J, Shahid M, Han Y, Witschey WRT. Measurement of Myocardial T1ρ with a Motion Corrected, Parametric Mapping Sequence in Humans. *PLOS ONE*. 2016;11(3):e0151144. doi:10.1371/journal.pone.0151144

158. Witschey WR, Pilla JJ, Ferrari G, et al. Rotating Frame Spin Lattice Relaxation in a Swine Model of Chronic, Left Ventricular Myocardial Infarction. *Magn Reson Med Off J Soc Magn Reson Med Soc Magn Reson Med*. 2010;64(5):1453-1460. doi:10.1002/mrm.22543

159. Witschey WR, Zsido GA, Koomalsingh K, et al. In vivo chronic myocardial infarction characterization by spin locked cardiovascular magnetic resonance. *J Cardiovasc Magn Reson*. 2012;14(1):37. doi:10.1186/1532-429X-14-37

160. de Jong S, Zwanenburg JJ, Visser F, et al. Direct detection of myocardial fibrosis by MRI. *J Mol Cell Cardiol*. 2011;51(6):974-979. doi:10.1016/j.yjmcc.2011.08.024

161. Zhou Z, Nguyen C, Chen Y, et al. Optimized CEST cardiovascular magnetic resonance for assessment of metabolic activity in the heart. *J Cardiovasc Magn Reson Off J Soc Cardiovasc Magn Reson*. 2017;19(1). doi:10.1186/s12968-017-0411-1

162. Sanbe A, Tanonaka K, Hanaoka Y, Katoh T, Takeo S. Regional energy metabolism of failing hearts following myocardial infarction. *J Mol Cell Cardiol*. 1993;25(9). doi:10.1006/jmcc.1993.1113

163. Nguyen C, Fan Z, Xie Y, et al. In vivo contrast free chronic myocardial infarction characterization using diffusion-weighted cardiovascular magnetic resonance. *J Cardiovasc Magn Reson*. 2014;16(1):68. doi:10.1186/s12968-014-0068-y

164. Pop M, Ghugre NR, Ramanan V, et al. Quantification of fibrosis in infarcted swine hearts by ex vivo late gadolinium-enhancement and diffusion-weighted MRI methods. *Phys Med Biol*. 2013;58(15):5009-5028. doi:10.1088/0031-9155/58/15/5009

165. Abdullah OM, Drakos SG, Diakos NA, et al. Characterization of Diffuse Fibrosis in the Failing Human Heart via Diffusion Tensor Imaging and Quantitative Histological Validation. *NMR Biomed*. 2014;27(11):1378-1386. doi:10.1002/nbm.3200

166. Scholz TD, Hoyt RF, DeLeonardis JR, Ceckler TL, Balaban RS. Water-macromolecular proton magnetization transfer in infarcted myocardium: a method to enhance magnetic resonance image contrast. *Magn Reson Med*. 1995;33(2):178-184. doi:10.1002/mrm.1910330206

167. Germain P, El Ghannudi S, Labani A, et al. A dual flip angle 3D bSSFP magnetization transfer-like method to differentiate between recent and old myocardial infarction. *J Magn Reson Imaging JMRI*. 2018;47(3):798-808. doi:10.1002/jmri.25821

168. Bieri O, Scheffler K. On the origin of apparent low tissue signals in balanced SSFP. *Magn Reson Med*. 2006;56(5):1067-1074. doi:10.1002/mrm.21056

169. Bieri O, Scheffler K. Optimized balanced steady-state free precession magnetization transfer imaging. *Magn Reson Med*. 2007;58(3):511-518. doi:10.1002/mrm.21326

170. Stromp TA, Leung SW, Andres KN, et al. Gadolinium free cardiovascular magnetic resonance with 2-point Cine balanced steady state free precession. *J Cardiovasc Magn Reson*. 2015;17(1):90. doi:10.1186/s12968-015-0194-1

171. van Oorschot JWM, Visser F, Eikendal ALM, et al. Single Breath-Hold T1ρ-Mapping of the Heart for Endogenous Assessment of Myocardial Fibrosis. *Invest Radiol*. 2016;51(8):505-512. doi:10.1097/RLI.0000000000000261

172. van Oorschot JW, El Aidi H, Jansen of Lorkeers SJ, et al. Endogenous assessment of chronic myocardial infarction with T1ρ-mapping in patients. *J Cardiovasc Magn Reson*. 2014;16(1):104. doi:10.1186/s12968-014-0104-y

173. Schuijf JD, Ambale-Venkatesh B, Kassai Y, et al. Cardiovascular ultrashort echo time to map fibrosis—promises and challenges. *Br J Radiol*. 2019;92(1103):20190465. doi:10.1259/bjr.20190465

174. Diao KY, Yang ZG, Guo YK, et al. P1072Myocardial creatine metabolism evaluation in patients with acute myocardial infarction with chemical exchange saturation transfer (CEST). *Eur Heart J*. 2017;38(suppl_1):ehx502.P1072. doi:10.1093/eurheartj/ehx502.P1072

175. Fan ZY, Lin YW, Shi RY, et al. Creatine chemical exchange saturation transfer (CEST) CMR imaging reveals myocardial early involvement in idiopathic inflammatory myopathy

at 3T: feasibility and initial experience. *Eur Radiol*. 2023;33(6):3897-3907. doi:10.1007/s00330-022-09363-5

176. Wu MT, Su MYM, Huang YL, et al. Sequential Changes of Myocardial Microstructure in Patients Postmyocardial Infarction by Diffusion-Tensor Cardiac MR. *Circ Cardiovasc Imaging*. 2009;2(1):32-40. doi:10.1161/CIRCIMAGING.108.778902
177. Mazur W, Urbańczyk-Zawadzka M, Czyż Ł, et al. Diffusion-tensor magnetic resonance imaging of the human heart in health and in acute myocardial infarction using diffusion-weighted echo-planar imaging technique with spin-echo signals. *Postępy W Kardiologii Interwencyjnej Adv Interv Cardiol*. 2022;18(4):416-422. doi:10.5114/aic.2022.121344
178. Mekkaoui C, Jackowski MP, Kostis WJ, et al. Myocardial Scar Delineation Using Diffusion Tensor Magnetic Resonance Tractography. *J Am Heart Assoc*. 7(3):e007834. doi:10.1161/JAHA.117.007834
179. López K, Neji R, Bustin A, et al. Quantitative magnetization transfer imaging for non-contrast enhanced detection of myocardial fibrosis. *Magn Reson Med*. 2021;85(4):2069-2083. doi:10.1002/mrm.28577
180. López K, Neji R, Mukherjee RK, et al. Contrast-free high-resolution 3D magnetization transfer imaging for simultaneous myocardial scar and cardiac vein visualization. *Magma N Y N*. 2020;33(5):627-640. doi:10.1007/s10334-020-00833-9
181. Carrick D, Haig C, Ahmed N, et al. Temporal Evolution of Myocardial Hemorrhage and Edema in Patients After Acute ST-Segment Elevation Myocardial Infarction: Pathophysiological Insights and Clinical Implications. *J Am Heart Assoc*. 2016;5(2):e002834. doi:10.1161/JAHA.115.002834
182. Jugdutt BI. Ventricular Remodeling After Infarction and the Extracellular Collagen Matrix. *Circulation*. 2003;108(11):1395-1403. doi:10.1161/01.CIR.0000085658.98621.49

183. Chan SF, Vora K, Dharmakumar R. Chronic heart failure following hemorrhagic myocardial infarction: mechanism, treatment and outlook. *Cell Stress*. 7(2):7-11. doi:10.15698/cst2023.02.276

184. Garg P, Broadbent DA, Swoboda PP, et al. Extra-cellular expansion in the normal, non-infarcted myocardium is associated with worsening of regional myocardial function after acute myocardial infarction. *J Cardiovasc Magn Reson Off J Soc Cardiovasc Magn Reson*. 2017;19(1):73. doi:10.1186/s12968-017-0384-0

185. Ibanez B, Aletras AH, Arai AE, et al. Cardiac MRI Endpoints in Myocardial Infarction Experimental and Clinical Trials. *J Am Coll Cardiol*. 2019;74(2):238-256. doi:10.1016/j.jacc.2019.05.024

186. Karamitsos TD, Piechnik SK, Banypersad SM, et al. Noncontrast T1 mapping for the diagnosis of cardiac amyloidosis. *JACC Cardiovasc Imaging*. 2013;6(4):488-497. doi:10.1016/j.jcmg.2012.11.013

187. Fontana M, Banypersad SM, Treibel TA, et al. Native T1 mapping in transthyretin amyloidosis. *JACC Cardiovasc Imaging*. 2014;7(2):157-165. doi:10.1016/j.jcmg.2013.10.008

188. Sado DM, White SK, Piechnik SK, et al. Identification and assessment of Anderson-Fabry disease by cardiovascular magnetic resonance noncontrast myocardial T1 mapping. *Circ Cardiovasc Imaging*. 2013;6(3):392-398. doi:10.1161/CIRCIMAGING.112.000070

189. Bull S, White SK, Piechnik SK, et al. Human non-contrast T1 values and correlation with histology in diffuse fibrosis. *Heart Br Card Soc*. 2013;99(13):932-937. doi:10.1136/heartjnl-2012-303052

190. Sparrow P, Messroghli DR, Reid S, Ridgway JP, Bainbridge G, Sivananthan MU. Myocardial T1 mapping for detection of left ventricular myocardial fibrosis in chronic

aortic regurgitation: pilot study. *AJR Am J Roentgenol*. 2006;187(6):W630-635. doi:10.2214/AJR.05.1264

191. Dass S, Suttie JJ, Piechnik SK, et al. Myocardial Tissue Characterization Using Magnetic Resonance Noncontrast T1 Mapping in Hypertrophic and Dilated Cardiomyopathy. *Circ Cardiovasc Imaging*. 2012;5(6):726-733. doi:10.1161/CIRCIMAGING.112.976738
192. Puntmann VO, Voigt T, Chen Z, et al. Native T1 mapping in differentiation of normal myocardium from diffuse disease in hypertrophic and dilated cardiomyopathy. *JACC Cardiovasc Imaging*. 2013;6(4):475-484. doi:10.1016/j.jcmg.2012.08.019
193. Wong TC. Cardiovascular Magnetic Resonance Imaging of Myocardial Interstitial Expansion in Hypertrophic Cardiomyopathy. *Curr Cardiovasc Imaging Rep*. 2014;7(5):9267. doi:10.1007/s12410-014-9267-z
194. Wang G, Lee SE, Yang Q, et al. Multicenter Study on the Diagnostic Performance of Native-T1 Cardiac Magnetic Resonance of Chronic Myocardial Infarctions at 3T. *Circ Cardiovasc Imaging*. 2020;13(6):e009894. doi:10.1161/CIRCIMAGING.119.009894
195. Kaolawanich Y, Azevedo CF, Kim HW, et al. Native T1 Mapping for the Diagnosis of Myocardial Fibrosis in Patients With Chronic Myocardial Infarction. *JACC Cardiovasc Imaging*. 2022;15(12):2069-2079. doi:10.1016/j.jcmg.2022.09.011
196. Azarisman SM, Carbone A, Shirazi M, et al. Characterisation of Myocardial Injury via T1 Mapping in Early Reperfused Myocardial Infarction and its Relationship with Global and Regional Diastolic Dysfunction. *Heart Lung Circ*. 2016;25(11):1094-1106. doi:10.1016/j.hlc.2016.03.011
197. Shin JM, Choi EY, Park CH, Han K, Kim TH. Quantitative T1 Mapping for Detecting Microvascular Obstruction in Reperfused Acute Myocardial Infarction: Comparison with Late Gadolinium Enhancement Imaging. *Korean J Radiol*. 2020;21(8):978-986. doi:10.3348/kjr.2019.0736

198. Cameron D, Siddiqi N, Neil CJ, et al. T_1 mapping for assessment of myocardial injury and microvascular obstruction at one week post myocardial infarction. *Eur J Radiol*. 2016;85(1):279-285. doi:10.1016/j.ejrad.2015.10.008

199. Abbas A, Matthews GH, Brown IW, Shambrook JS, Peebles CR, Harden SP. Cardiac MR assessment of microvascular obstruction. *Br J Radiol*. 2015;88(1047):20140470. doi:10.1259/bjr.20140470

200. Bodi V, Sanchis J, Nunez J, et al. Prognostic value of a comprehensive cardiac magnetic resonance assessment soon after a first ST-segment elevation myocardial infarction. *JACC Cardiovasc Imaging*. 2009;2(7):835-842. doi:10.1016/j.jcmg.2009.03.011

201. Bruder O, Breuckmann F, Jensen C, et al. Prognostic impact of contrast-enhanced CMR early after acute ST segment elevation myocardial infarction (STEMI) in a regional STEMI network: results of the "Herzinfarktverbund Essen." *Herz*. 2008;33(2):136-142. doi:10.1007/s00059-008-3102-8

202. Cochet AA, Lorgis L, Lalande A, et al. Major prognostic impact of persistent microvascular obstruction as assessed by contrast-enhanced cardiac magnetic resonance in reperfused acute myocardial infarction. *Eur Radiol*. 2009;19(9):2117-2126. doi:10.1007/s00330-009-1395-5

203. Hombach V, Grebe O, Merkle N, et al. Sequelae of acute myocardial infarction regarding cardiac structure and function and their prognostic significance as assessed by magnetic resonance imaging. *Eur Heart J*. 2005;26(6):549-557. doi:10.1093/eurheartj/ehi147

204. Nijveldt R, Beek AM, Hirsch A, et al. Functional recovery after acute myocardial infarction: comparison between angiography, electrocardiography, and cardiovascular magnetic resonance measures of microvascular injury. *J Am Coll Cardiol*. 2008;52(3):181-189. doi:10.1016/j.jacc.2008.04.006

205. Ørn S, Manhenke C, Greve OJ, et al. Microvascular obstruction is a major determinant of infarct healing and subsequent left ventricular remodelling following primary percutaneous coronary intervention. *Eur Heart J*. 2009;30(16):1978-1985. doi:10.1093/eurheartj/ehp219

206. Wong DTL, Leung MCH, Richardson JD, et al. Cardiac magnetic resonance derived late microvascular obstruction assessment post ST-segment elevation myocardial infarction is the best predictor of left ventricular function: a comparison of angiographic and cardiac magnetic resonance derived measurements. *Int J Cardiovasc Imaging*. 2012;28(8):1971-1981. doi:10.1007/s10554-012-0021-9

207. Limalanathan S, Eritsland J, Andersen GØ, Kløw NE, Abdelnoor M, Hoffmann P. Myocardial Salvage is Reduced in Primary PCI-Treated STEMI Patients with Microvascular Obstruction, Demonstrated by Early and Late CMR. *PLoS ONE*. 2013;8(8):e71780. doi:10.1371/journal.pone.0071780

208. Asanuma T, Tanabe K, Ochiai K, et al. Relationship Between Progressive Microvascular Damage and Intramyocardial Hemorrhage in Patients With Reperfused Anterior Myocardial Infarction. *Circulation*. 1997;96(2):448-453. doi:10.1161/01.CIR.96.2.448

209. Ochiai K, Shimada T, Murakami Y, et al. Hemorrhagic myocardial infarction after coronary reperfusion detected in vivo by magnetic resonance imaging in humans: prevalence and clinical implications. *J Cardiovasc Magn Reson Off J Soc Cardiovasc Magn Reson*. 1999;1(3):247-256. doi:10.3109/10976649909088337

210. Kumar A, Green JD, Sykes JM, et al. Detection and Quantification of Myocardial Reperfusion Hemorrhage Using T2*-Weighted CMR. *JACC Cardiovasc Imaging*. 2011;4(12):1274-1283. doi:10.1016/j.jcmg.2011.08.016

211. Kali A, Kumar A, Cokic I, et al. Chronic manifestation of postreperfusion intramyocardial hemorrhage as regional iron deposition: a cardiovascular magnetic resonance study with ex

vivo validation. *Circ Cardiovasc Imaging*. 2013;6(2):218-228. doi:10.1161/CIRCIMAGING.112.000133

212. Lotan CS, Miller SK, Cranney GB, Pohost GM, Elgavish GA. The effect of postinfarction intramyocardial hemorrhage on transverse relaxation time. *Magn Reson Med*. 1992;23(2):346-355. doi:10.1002/mrm.1910230214
213. O'Brien AT, Gil KE, Varghese J, Simonetti OP, Zareba KM. T2 mapping in myocardial disease: a comprehensive review. *J Cardiovasc Magn Reson*. 2022;24(1):33. doi:10.1186/s12968-022-00866-0
214. Wang G, Yang HJ, Kali A, et al. Influence of Myocardial Hemorrhage on Staging of Reperfused Myocardial Infarctions With T2 Cardiac Magnetic Resonance Imaging. *JACC Cardiovasc Imaging*. 2019;12(4):693-703. doi:10.1016/j.jcmg.2018.01.018
215. Bilheimer DW, Buja LM, Parkey RW, Bonte FJ, Willerson JT. Fatty acid accumulation and abnormal lipid deposition in peripheral and border zones of experimental myocardial infarcts. *J Nucl Med Off Publ Soc Nucl Med*. 1978;19(3):276-283.
216. Pantanowitz L. Fat infiltration in the heart. *Heart*. 2001;85(3):253. doi:10.1136/heart.85.3.253
217. Roberts WC, Roberts JD. The floating heart or the heart too fat to sink: analysis of 55 necropsy patients. *Am J Cardiol*. 1983;52(10):1286-1289. doi:10.1016/0002-9149(83)90589-1
218. Crocker DW. Lipomatous infiltrates of the heart. *Arch Pathol Lab Med*. 1978;102(2):69-72.
219. Dixon WT. Simple proton spectroscopic imaging. *Radiology*. 1984;153(1):189-194. doi:10.1148/radiology.153.1.6089263
220. Goldfarb JW, Arnold S, Roth M, Han J. T1-weighted magnetic resonance imaging shows fatty deposition after myocardial infarction. *Magn Reson Med*. 2007;57(5):828-834. doi:10.1002/mrm.21207

221. Molinari G, Sardanelli F, Zandrino F, et al. Adipose replacement and wall motion abnormalities in right ventricle arrhythmias: evaluation by MR imaging. Retrospective evaluation on 124 patients. *Int J Card Imaging*. 2000;16(2):105-115. doi:10.1023/a:1006304626233

222. Vignaux O, Lazarus A, Varin J, et al. Right ventricular MR abnormalities in myotonic dystrophy and relationship with intracardiac electrophysiologic test findings: initial results. *Radiology*. 2002;224(1):231-235. doi:10.1148/radiol.2241010986

223. Burke AP, Farb A, Tashko G, Virmani R. Arrhythmogenic right ventricular cardiomyopathy and fatty replacement of the right ventricular myocardium: are they different diseases? *Circulation*. 1998;97(16):1571-1580. doi:10.1161/01.cir.97.16.1571

224. Eggers H, Börnert P. Chemical shift encoding-based water–fat separation methods. *J Magn Reson Imaging*. 2014;40(2):251-268. doi:10.1002/jmri.24568

225. Babcock EE, Brateman L, Weinreb JC, Horner SD, Nunnally RL. Edge artifacts in MR images: chemical shift effect. *J Comput Assist Tomogr*. 1985;9(2):252-257. doi:10.1097/00004728-198503000-00004

226. Dwyer AJ, Knop RH, Hoult DI. Frequency shift artifacts in MR imaging. *J Comput Assist Tomogr*. 1985;9(1):16-18. doi:10.1097/00004728-198501000-00003

227. Bley TA, Wieben O, François CJ, Brittain JH, Reeder SB. Fat and water magnetic resonance imaging. *J Magn Reson Imaging JMRI*. 2010;31(1):4-18. doi:10.1002/jmri.21895

228. Rieke V, Pauly KB. MR Thermometry. *J Magn Reson Imaging JMRI*. 2008;27(2):376-390. doi:10.1002/jmri.21265

229. Haase A, Frahm J, Hänicke W, Matthaei D. 1H NMR chemical shift selective (CHESS) imaging. *Phys Med Biol*. 1985;30(4):341-344. doi:10.1088/0031-9155/30/4/008

230. Meyer CH, Pauly JM, Macovski A, Nishimura DG. Simultaneous spatial and spectral selective excitation. *Magn Reson Med*. 1990;15(2):287-304. doi:10.1002/mrm.1910150211

231. Bydder GM, Pennock JM, Steiner RE, Khenia S, Payne JA, Young IR. The short TI inversion recovery sequence--an approach to MR imaging of the abdomen. *Magn Reson Imaging*. 1985;3(3):251-254. doi:10.1016/0730-725x(85)90354-6

232. Reeder SB, Wen Z, Yu H, et al. Multicoil Dixon chemical species separation with an iterative least-squares estimation method. *Magn Reson Med*. 2004;51(1):35-45. doi:10.1002/mrm.10675

233. Hargreaves BA, Bangerter NK, Shimakawa A, Vasanawala SS, Brittain JH, Nishimura DG. Dual-acquisition phase-sensitive fat-water separation using balanced steady-state free precession. *Magn Reson Imaging*. 2006;24(2):113-122. doi:10.1016/j.mri.2005.10.013

234. Glover GH, Schneider E. Three-point Dixon technique for true water/fat decomposition with B0 inhomogeneity correction. *Magn Reson Med*. 1991;18(2):371-383. doi:10.1002/mrm.1910180211

235. Szumowski J, Coshow WR, Li F, Quinn SF. Phase unwrapping in the three-point Dixon method for fat suppression MR imaging. *Radiology*. 1994;192(2):555-561. doi:10.1148/radiology.192.2.8029431

236. Kovanlikaya A, Guclu C, Desai C, Becerra R, Gilsanz V. Fat quantification using three-point dixon technique: in vitro validation. *Acad Radiol*. 2005;12(5):636-639. doi:10.1016/j.acra.2005.01.019

237. Berglund J, Johansson L, Ahlström H, Kullberg J. Three-point Dixon method enables whole-body water and fat imaging of obese subjects. *Magn Reson Med*. 2010;63(6):1659-1668. doi:10.1002/mrm.22385

238. Hardy PA, Hinks RS, Tkach JA. Separation of fat and water in fast spin-echo MR imaging with the three-point Dixon technique. *J Magn Reson Imaging JMRI*. 1995;5(2):181-185. doi:10.1002/jmri.1880050213

239. Wang Y, Li D, Haacke EM, Brown JJ. A three-point Dixon method for water and fat separation using 2D and 3D gradient-echo techniques. *J Magn Reson Imaging JMRI*. 1998;8(3):703-710. doi:10.1002/jmri.1880080329

240. Schneider E, Chan TW. Selective MR imaging of silicone with the three-point Dixon technique. *Radiology*. 1993;187(1):89-93. doi:10.1148/radiology.187.1.8451442

241. Reeder SB, Pineda AR, Wen Z, et al. Iterative decomposition of water and fat with echo asymmetry and least-squares estimation (IDEAL): application with fast spin-echo imaging. *Magn Reson Med*. 2005;54(3):636-644. doi:10.1002/mrm.20624

242. Szczepaniak LS, Babcock EE, Schick F, et al. Measurement of intracellular triglyceride stores by H spectroscopy: validation in vivo. *Am J Physiol*. 1999;276(5):E977-989. doi:10.1152/ajpendo.1999.276.5.E977

243. Yu H, Shimakawa A, McKenzie CA, Brodsky E, Brittain JH, Reeder SB. Multiecho water-fat separation and simultaneous R estimation with multifrequency fat spectrum modeling. *Magn Reson Med*. 2008;60(5):1122-1134. doi:10.1002/mrm.21737

244. Henze Bancroft LC, Strigel RM, Hernando D, et al. Utilization of a Balanced SSFP Signal Model for Improved Fat/Water Decomposition. *Magn Reson Med*. 2016;75(3):1269-1277. doi:10.1002/mrm.25728

245. Kellman P, Bandettini WP, Mancini C, Hammer-Hansen S, Hansen MS, Arai AE. Characterization of myocardial T1-mapping bias caused by intramyocardial fat in inversion recovery and saturation recovery techniques. *J Cardiovasc Magn Reson*. 2015;17(1):33. doi:10.1186/s12968-015-0136-y

246. García-Dorado D, Oliveras J, Gili J, et al. Analysis of myocardial oedema by magnetic resonance imaging early after coronary artery occlusion with or without reperfusion. *Cardiovasc Res*. 1993;27(8):1462-1469. doi:10.1093/cvr/27.8.1462

247. Aletras AH, Tilak GS, Natanzon A, et al. Retrospective determination of the area at risk for reperfused acute myocardial infarction with T2-weighted cardiac magnetic resonance imaging: histopathological and displacement encoding with stimulated echoes (DENSE) functional validations. *Circulation*. 2006;113(15):1865-1870. doi:10.1161/CIRCULATIONAHA.105.576025

248. Friedrich MG, Abdel-Aty H, Taylor A, Schulz-Menger J, Messroghli D, Dietz R. The salvaged area at risk in reperfused acute myocardial infarction as visualized by cardiovascular magnetic resonance. *J Am Coll Cardiol*. 2008;51(16):1581-1587. doi:10.1016/j.jacc.2008.01.019

249. Berry C, Kellman P, Mancini C, et al. Magnetic resonance imaging delineates the ischemic area at risk and myocardial salvage in patients with acute myocardial infarction. *Circ Cardiovasc Imaging*. 2010;3(5):527-535. doi:10.1161/CIRCIMAGING.109.900761

250. Abdel-Aty H, Zagrosek A, Schulz-Menger J, et al. Delayed enhancement and T2-weighted cardiovascular magnetic resonance imaging differentiate acute from chronic myocardial infarction. *Circulation*. 2004;109(20):2411-2416. doi:10.1161/01.CIR.0000127428.10985.C6

251. Francone M, Bucciarelli-Ducci C, Carbone I, et al. Impact of primary coronary angioplasty delay on myocardial salvage, infarct size, and microvascular damage in patients with ST-segment elevation myocardial infarction: insight from cardiovascular magnetic resonance. *J Am Coll Cardiol*. 2009;54(23):2145-2153. doi:10.1016/j.jacc.2009.08.024

252. Kim HW, Van Assche L, Jennings RB, et al. Relationship of T2-Weighted MRI Myocardial Hyperintensity and the Ischemic Area-At-Risk. *Circ Res*. 2015;117(3):254-265. doi:10.1161/CIRCRESAHA.117.305771

253. Fernández-Jiménez R, Barreiro-Pérez M, Martin-García A, et al. Dynamic Edematous Response of the Human Heart to Myocardial Infarction: Implications for Assessing

Myocardial Area at Risk and Salvage. *Circulation*. 2017;136(14):1288-1300. doi:10.1161/CIRCULATIONAHA.116.025582

254. Andrés-Villarreal M, Barba I, Poncelas M, et al. Measuring Water Distribution in the Heart: Preventing Edema Reduces Ischemia–Reperfusion Injury. *J Am Heart Assoc Cardiovasc Cerebrovasc Dis*. 2016;5(12):e003843. doi:10.1161/JAHA.116.003843
255. Friedrich MG. Myocardial edema—a new clinical entity? *Nat Rev Cardiol*. 2010;7(5):292-296. doi:10.1038/nrcardio.2010.28
256. Cury RC, Shash K, Nagurney JT, et al. Cardiac magnetic resonance with T2-weighted imaging improves detection of patients with acute coronary syndrome in the emergency department. *Circulation*. 2008;118(8):837-844. doi:10.1161/CIRCULATIONAHA.107.740597
257. Smulders MW, Bekkers SCAM, Kim HW, Van Assche LMR, Parker MA, Kim RJ. Performance of CMR Methods for Differentiating Acute From Chronic MI. *JACC Cardiovasc Imaging*. 2015;8(6):669-679. doi:10.1016/j.jcmg.2014.12.030
258. McAlindon EJ, Pufulete M, Harris JM, et al. Measurement of myocardium at risk with cardiovascular MR: comparison of techniques for edema imaging. *Radiology*. 2015;275(1):61-70. doi:10.1148/radiol.14131980
259. Higgins CB, Herfkens R, Lipton MJ, et al. Nuclear magnetic resonance imaging of acute myocardial infarction in dogs: alterations in magnetic relaxation times. *Am J Cardiol*. 1983;52(1):184-188. doi:10.1016/0002-9149(83)90093-0
260. Williams ES, Kaplan JI, Thatcher F, Zimmerman G, Knoebel SB. Prolongation of proton spin lattice relaxation times in regionally ischemic tissue from dog hearts. *J Nucl Med Off Publ Soc Nucl Med*. 1980;21(5):449-453.
261. Brown JJ, Peck WW, Gerber KH, Higgins CB, Strich G, Slutsky RA. Nuclear magnetic resonance analysis of acute and chronic myocardial infarction in dogs: Alterations in spin-

lattice relaxation times. *Am Heart J*. 1984;108(5):1292-1297. doi:10.1016/0002-8703(84)90756-7

262. Buda AJ, Aisen AM, Juni JE, Gallagher KP, Zotz RJ. Detection and sizing of myocardial ischemia and infarction by nuclear magnetic resonance imaging in the canine heart. *Am Heart J*. 1985;110(6):1284-1290. doi:10.1016/0002-8703(85)90025-0
263. Ferreira VM, Piechnik SK, Dall'Armellina E, et al. Non-contrast T1-mapping detects acute myocardial edema with high diagnostic accuracy: a comparison to T2-weighted cardiovascular magnetic resonance. *J Cardiovasc Magn Reson Off J Soc Cardiovasc Magn Reson*. 2012;14(1):42. doi:10.1186/1532-429X-14-42
264. Ugander M, Bagi PS, Oki AJ, et al. Myocardial edema as detected by pre-contrast T1 and T2 CMR delineates area at risk associated with acute myocardial infarction. *JACC Cardiovasc Imaging*. 2012;5(6):596-603. doi:10.1016/j.jcmg.2012.01.016
265. Bulluck H, White SK, Rosmini S, et al. T1 mapping and T2 mapping at 3T for quantifying the area-at-risk in reperfused STEMI patients. *J Cardiovasc Magn Reson*. 2015;17(1):73. doi:10.1186/s12968-015-0173-6
266. Shaw JL, Yang Q, Zhou Z, et al. Free-breathing, non-ECG, continuous myocardial T1 mapping with cardiovascular magnetic resonance multitasking. *Magn Reson Med*. 2019;81(4):2450-2463. doi:10.1002/mrm.27574
267. Christodoulou AG, Shaw JL, Nguyen C, et al. Magnetic resonance multitasking for motion-resolved quantitative cardiovascular imaging. *Nat Biomed Eng*. 2018;2(4):215-226. doi:10.1038/s41551-018-0217-y
268. Ma S, Nguyen CT, Christodoulou AG, et al. Accelerated Cardiac Diffusion Tensor Imaging Using Joint Low-Rank and Sparsity Constraints. *IEEE Trans Biomed Eng*. 2018;65(10):2219-2230. doi:10.1109/TBME.2017.2787111

269. Wang N, Christodoulou AG, Xie Y, et al. Quantitative 3D dynamic contrast-enhanced (DCE) MR imaging of carotid vessel wall by fast T1 mapping using Multitasking. *Magn Reson Med*. 2019;81(4):2302-2314. doi:10.1002/mrm.27553

270. Hu Z, Christodoulou AG, Wang N, et al. Magnetic resonance multitasking for multidimensional assessment of cardiovascular system: Development and feasibility study on the thoracic aorta. *Magn Reson Med*. 2020;84(5):2376-2388. doi:10.1002/mrm.28275

271. Han P, Zhang R, Wagner S, et al. Electrocardiogram-less, free-breathing myocardial extracellular volume fraction mapping in small animals at high heart rates using motion-resolved cardiovascular magnetic reesonance multitasking: a feasibility study in a heart failure with preserved ejection fraction rat model. *J Cardiovasc Magn Reson Off J Soc Cardiovasc Magn Reson*. 2021;23(1):8. doi:10.1186/s12968-020-00699-9

272. Tucker LR. Some mathematical notes on three-mode factor analysis. *Psychometrika*. 1966;31(3):279-311. doi:10.1007/BF02289464

273. Tensor Completion for Estimating Missing Values in Visual Data | IEEE Journals & Magazine | IEEE Xplore. Accessed May 18, 2024. https://ieeexplore.ieee.org/document/6138863

274. De Lathauwer L, De Moor B, Vandewalle J. A Multilinear Singular Value Decomposition. *SIAM J Matrix Anal Appl*. 2000;21(4):1253-1278. doi:10.1137/S0895479896305696

275. Cao T, Wang N, Kwan AC, et al. Free-breathing, non-ECG, simultaneous myocardial T1 , T2 , T2 *, and fat-fraction mapping with motion-resolved cardiovascular MR multitasking. *Magn Reson Med*. Published online June 17, 2022. doi:10.1002/mrm.29351

276. Hu Z, Xiao J, Mao X, et al. MR Multitasking-based multi-dimensional assessment of cardiovascular system (MT-MACS) with extended spatial coverage and water-fat separation. *Magn Reson Med*. 2023;89(4):1496-1505. doi:10.1002/mrm.29522

277. Mao X, Lee HL, Hu Z, et al. Simultaneous Multi-Slice Cardiac MR Multitasking for Motion-Resolved, Non-ECG, Free-Breathing T1–T2 Mapping. *Front Cardiovasc Med*. 2022;9. Accessed May 14, 2022. https://www.frontiersin.org/article/10.3389/fcvm.2022.833257

278. Baessler B, Mannil M, Oebel S, Maintz D, Alkadhi H, Manka R. Subacute and Chronic Left Ventricular Myocardial Scar: Accuracy of Texture Analysis on Nonenhanced Cine MR Images. *Radiology*. 2018;286(1):103-112. doi:10.1148/radiol.2017170213

279. Larroza A, Materka A, López-Lereu MP, Monmeneu JV, Bodí V, Moratal D. Differentiation between acute and chronic myocardial infarction by means of texture analysis of late gadolinium enhancement and cine cardiac magnetic resonance imaging. *Eur J Radiol*. 2017;92:78-83. doi:10.1016/j.ejrad.2017.04.024

280. Chen BH, An DA, He J, et al. Myocardial extracellular volume fraction radiomics analysis for differentiation of reversible versus irreversible myocardial damage and prediction of left ventricular adverse remodeling after ST-elevation myocardial infarction. *Eur Radiol*. 2021;31(1):504-514. doi:10.1007/s00330-020-07117-9

281. Larroza A, López-Lereu MP, Monmeneu JV, et al. Texture analysis of cardiac cine magnetic resonance imaging to detect nonviable segments in patients with chronic myocardial infarction. *Med Phys*. 2018;45(4):1471-1480. doi:10.1002/mp.12783

282. Ma Q, Ma Y, Yu T, Sun Z, Hou Y. Radiomics of Non-Contrast-Enhanced T1 Mapping: Diagnostic and Predictive Performance for Myocardial Injury in Acute ST-Segment-Elevation Myocardial Infarction. *Korean J Radiol*. 2021;22(4):535-546. doi:10.3348/kjr.2019.0969

283. Kotu LP, Engan K, Skretting K, Ørn S, Woie L, Eftestøl T. Segmentation of Scarred Myocardium in Cardiac Magnetic Resonance Images. *Int Sch Res Not*. 2013;2013:e504594. doi:10.1155/2013/504594

284. Kotu LP, Engan K, Skretting K, et al. Probability mapping of scarred myocardium using texture and intensity features in CMR images. *Biomed Eng Online*. 2013;12:91. doi:10.1186/1475-925X-12-91

285. Engan K, Eftestol T, Orn S, Kvaloy JT, Woie L. Exploratory data analysis of image texture and statistical features on myocardium and infarction areas in cardiac magnetic resonance images. *Annu Int Conf IEEE Eng Med Biol Soc IEEE Eng Med Biol Soc Annu Int Conf*. 2010;2010:5728-5731. doi:10.1109/IEMBS.2010.5627866

286. Antiochos P, Ge Y, van der Geest RJ, et al. Entropy as a Measure of Myocardial Tissue Heterogeneity in Patients With Ventricular Arrhythmias. *JACC Cardiovasc Imaging*. 2022;15(5):783-792. doi:10.1016/j.jcmg.2021.12.003

287. Akins EW, Hill JA, Sievers KW, Conti CR. Assessment of left ventricular wall thickness in healed myocardial infarction by magnetic resonance imaging. *Am J Cardiol*. 1987;59(1):24-28. doi:10.1016/s0002-9149(87)80063-2

288. Shah DJ, Kim HW, James O, et al. Prevalence of Regional Myocardial Thinning and Relationship With Myocardial Scarring in Patients With Coronary Artery Disease. *JAMA*. 2013;309(9):909. doi:10.1001/jama.2013.1381

289. Bitar R, Moody AR, Leung G, et al. In vivo 3D high-spatial-resolution MR imaging of intraplaque hemorrhage. *Radiology*. 2008;249(1):259-267. doi:10.1148/radiol.2491071517

290. Link TM, Majumdar S, Peterfy C, et al. High resolution MRI of small joints: impact of spatial resolution on diagnostic performance and SNR. *Magn Reson Imaging*. 1998;16(2):147-155. doi:10.1016/s0730-725x(97)00244-0

291. Ghugre NR, Ramanan V, Pop M, et al. Quantitative tracking of edema, hemorrhage, and microvascular obstruction in subacute myocardial infarction in a porcine model by MRI. *Magn Reson Med*. 2011;66(4):1129-1141. doi:10.1002/mrm.22855

292. Moon BF, Iyer SK, Hwuang E, et al. Iron imaging in myocardial infarction reperfusion injury. *Nat Commun*. 2020;11(1):3273. doi:10.1038/s41467-020-16923-0

293. Cokic I, Kali A, Wang X, et al. Iron Deposition following Chronic Myocardial Infarction as a Substrate for Cardiac Electrical Anomalies: Initial Findings in a Canine Model. Sovari AA, ed. *PLoS ONE*. 2013;8(9):e73193. doi:10.1371/journal.pone.0073193

294. Bulluck H, Rosmini S, Abdel-Gadir A, et al. Residual Myocardial Iron Following Intramyocardial Hemorrhage During the Convalescent Phase of Reperfused ST-Segment-Elevation Myocardial Infarction and Adverse Left Ventricular Remodeling. *Circ Cardiovasc Imaging*. 2016;9(10):e004940. doi:10.1161/CIRCIMAGING.116.004940

295. Signal, Contrast, and Noise. In: *Magnetic Resonance Imaging: Physical Principles and Sequence Design*. John Wiley & Sons, Ltd; 2014:325-373. doi:10.1002/9781118633953.ch15

296. Ibáñez B, Heusch G, Ovize M, Van de Werf F. Evolving therapies for myocardial ischemia/reperfusion injury. *J Am Coll Cardiol*. 2015;65(14):1454-1471. doi:10.1016/j.jacc.2015.02.032

297. Husser O, Bodi V, Sanchis J, et al. Predictors of cardiovascular magnetic resonance-derived microvascular obstruction on patient admission in STEMI. *Int J Cardiol*. 2013;166(1):77-84. doi:10.1016/j.ijcard.2011.09.083

298. Piper HM, García-Dorado D, Ovize M. A fresh look at reperfusion injury. *Cardiovasc Res*. 1998;38(2):291-300. doi:10.1016/s0008-6363(98)00033-9

299. Hendel RC, Patel MR, Kramer CM, et al. ACCF/ACR/SCCT/SCMR/ASNC/NASCI/SCAI/SIR 2006 appropriateness criteria for cardiac computed tomography and cardiac magnetic resonance imaging: a report of the American College of Cardiology Foundation Quality Strategic Directions Committee Appropriateness Criteria Working Group, American College of Radiology, Society of

Cardiovascular Computed Tomography, Society for Cardiovascular Magnetic Resonance, American Society of Nuclear Cardiology, North American Society for Cardiac Imaging, Society for Cardiovascular Angiography and Interventions, and Society of Interventional Radiology. *J Am Coll Cardiol*. 2006;48(7):1475-1497. doi:10.1016/j.jacc.2006.07.003

300. Wagner A, Mahrholdt H, Holly TA, et al. Contrast-enhanced MRI and routine single photon emission computed tomography (SPECT) perfusion imaging for detection of subendocardial myocardial infarcts: an imaging study. *Lancet Lond Engl*. 2003;361(9355):374-379. doi:10.1016/S0140-6736(03)12389-6
301. Simonetti OP, Kim RJ, Fieno DS, et al. An improved MR imaging technique for the visualization of myocardial infarction. *Radiology*. 2001;218(1):215-223. doi:10.1148/radiology.218.1.r01ja50215
302. Choudhury L, Mahrholdt H, Wagner A, et al. Myocardial scarring in asymptomatic or mildly symptomatic patients with hypertrophic cardiomyopathy. *J Am Coll Cardiol*. 2002;40(12):2156-2164. doi:10.1016/s0735-1097(02)02602-5
303. Keller DI, Osswald S, Bremerich J, et al. Arrhythmogenic right ventricular cardiomyopathy: diagnostic and prognostic value of the cardiac MRI in relation to arrhythmia-free survival. *Int J Cardiovasc Imaging*. 2003;19(6):537-543; discussion 545-547. doi:10.1023/b:caim.0000004351.40409.ee
304. Moon JCC, McKenna WJ, McCrohon JA, Elliott PM, Smith GC, Pennell DJ. Toward clinical risk assessment in hypertrophic cardiomyopathy with gadolinium cardiovascular magnetic resonance. *J Am Coll Cardiol*. 2003;41(9):1561-1567. doi:10.1016/s0735-1097(03)00189-x
305. Adabag AS, Maron BJ, Appelbaum E, et al. Occurrence and frequency of arrhythmias in hypertrophic cardiomyopathy in relation to delayed enhancement on cardiovascular

magnetic resonance. *J Am Coll Cardiol*. 2008;51(14):1369-1374. doi:10.1016/j.jacc.2007.11.071

306. Flett AS, Westwood MA, Davies LC, Mathur A, Moon JC. The Prognostic Implications of Cardiovascular Magnetic Resonance. *Circ Cardiovasc Imaging*. 2009;2(3):243-250. doi:10.1161/CIRCIMAGING.108.840975
307. Kramer CM. The expanding prognostic role of late gadolinium enhanced cardiac magnetic resonance. *J Am Coll Cardiol*. 2006;48(10):1986-1987. doi:10.1016/j.jacc.2006.08.018
308. Nijveldt R, Hofman MBM, Hirsch A, et al. Assessment of microvascular obstruction and prediction of short-term remodeling after acute myocardial infarction: cardiac MR imaging study. *Radiology*. 2009;250(2):363-370. doi:10.1148/radiol.2502080739
309. García-Prieto J, Villena-Gutiérrez R, Gómez M, et al. Neutrophil stunning by metoprolol reduces infarct size. *Nat Commun*. 2017;8(1):14780. doi:10.1038/ncomms14780
310. Wu KC. CMR of microvascular obstruction and hemorrhage in myocardial infarction. *J Cardiovasc Magn Reson*. 2012;14(1):68. doi:10.1186/1532-429X-14-68
311. Bekkers SCAM, Backes WH, Kim RJ, et al. Detection and characteristics of microvascular obstruction in reperfused acute myocardial infarction using an optimized protocol for contrast-enhanced cardiovascular magnetic resonance imaging. *Eur Radiol*. 2009;19(12):2904-2912. doi:10.1007/s00330-009-1489-0
312. Mayr A, Klug G, Schocke M, et al. Late microvascular obstruction after acute myocardial infarction: relation with cardiac and inflammatory markers. *Int J Cardiol*. 2012;157(3):391-396. doi:10.1016/j.ijcard.2010.12.090
313. Kandler D, Lücke C, Grothoff M, et al. The relation between hypointense core, microvascular obstruction and intramyocardial haemorrhage in acute reperfused myocardial infarction assessed by cardiac magnetic resonance imaging. *Eur Radiol*. 2014;24(12):3277-3288. doi:10.1007/s00330-014-3318-3

314. Mao X, Bari S, Love DJ, Rispoli JV. Global and peak local specific absorption rate control on parallel transmit systems using k-means SAR compression model. *Magn Reson Med*. 2021;85(2):1093-1103. doi:10.1002/mrm.28456

315. Reeder SB, Faranesh AZ, Boxerman JL, McVeigh ER. In vivo measurement of T*2 and field inhomogeneity maps in the human heart at 1.5 T. *Magn Reson Med*. 1998;39(6):988-998. doi:10.1002/mrm.1910390617

316. Triadyaksa P, Oudkerk M, Sijens PE. Cardiac T2* mapping: Techniques and clinical applications. *J Magn Reson Imaging*. 2020;52(5):1340-1351. doi:10.1002/jmri.27023

317. Atalay MK, Poncelet BP, Kantor HL, Brady TJ, Weisskoff RM. Cardiac susceptibility artifacts arising from the heart-lung interface. *Magn Reson Med*. 2001;45(2):341-345. doi:10.1002/1522-2594(200102)45:2<341::aid-mrm1043>3.0.co;2-q

318. Guan X, Yang HJ, Zhang X, et al. Non-electrocardiogram-gated, free-breathing, off-resonance reduced, high-resolution, whole-heart myocardial T2* mapping at 3 T within 5 min. *Magn Reson Med*. 2024;91(5):1936-1950. doi:10.1002/mrm.29968

319. Yan AT, Gibson CM, Larose E, et al. Characterization of microvascular dysfunction after acute myocardial infarction by cardiovascular magnetic resonance first-pass perfusion and late gadolinium enhancement imaging. *J Cardiovasc Magn Reson Off J Soc Cardiovasc Magn Reson*. 2006;8(6):831-837. doi:10.1080/10976640600778049

320. Lund GK, Stork A, Saeed M, et al. Acute myocardial infarction: evaluation with first-pass enhancement and delayed enhancement MR imaging compared with 201Tl SPECT imaging. *Radiology*. 2004;232(1):49-57. doi:10.1148/radiol.2321031127

321. de Waha S, Desch S, Eitel I, et al. Impact of early vs. late microvascular obstruction assessed by magnetic resonance imaging on long-term outcome after ST-elevation myocardial infarction: a comparison with traditional prognostic markers. *Eur Heart J*. 2010;31(21):2660-2668. doi:10.1093/eurheartj/ehq247

322. Gerber BL, Rochitte CE, Melin JA, et al. Microvascular Obstruction and Left Ventricular Remodeling Early After Acute Myocardial Infarction. *Circulation*. 2000;101(23):2734-2741. doi:10.1161/01.CIR.101.23.2734

323. Elster AD, Sobol WT, Hinson WH. Pseudolayering of Gd-DTPA in the urinary bladder. *Radiology*. 1990;174(2):379-381. doi:10.1148/radiology.174.2.2296649

324. Benjamin EJ, Muntner P, Alonso A, et al. Heart Disease and Stroke Statistics-2019 Update: A Report From the American Heart Association. *Circulation*. 2019;139(10):e56-e528. doi:10.1161/CIR.0000000000000659

325. Levy D, Kenchaiah S, Larson MG, et al. Long-term trends in the incidence of and survival with heart failure. *N Engl J Med*. 2002;347(18):1397-1402. doi:10.1056/NEJMoa020265

326. Baessler B, Luecke C, Lurz J, et al. Cardiac MRI Texture Analysis of T1 and T2 Maps in Patients with Infarctlike Acute Myocarditis. *Radiology*. 2018;289(2):357-365. doi:10.1148/radiol.2018180411

327. Hassani C, Saremi F, Varghese BA, Duddalwar V. Myocardial Radiomics in Cardiac MRI. *Am J Roentgenol*. 2020;214(3):536-545. doi:10.2214/AJR.19.21986

328. Gillies RJ, Kinahan PE, Hricak H. Radiomics: Images Are More than Pictures, They Are Data. *Radiology*. 2016;278(2):563-577. doi:10.1148/radiol.2015151169

329. Neisius U, El-Rewaidy H, Nakamori S, Rodriguez J, Manning WJ, Nezafat R. Radiomic Analysis of Myocardial Native T1 Imaging discriminates between Hypertensive Heart Disease and Hypertrophic Cardiomyopathy. *JACC Cardiovasc Imaging*. 2019;12(10):1946-1954. doi:10.1016/j.jcmg.2018.11.024

330. Cai JH, He Y, Zhong XL, et al. Magnetic Resonance Texture Analysis in Alzheimer's disease. *Acad Radiol*. 2020;27(12):1774-1783. doi:10.1016/j.acra.2020.01.006

331. Castellano G, Bonilha L, Li LM, Cendes F. Texture analysis of medical images. *Clin Radiol*. 2004;59(12):1061-1069. doi:10.1016/j.crad.2004.07.008

332. Peng F, Zheng T, Tang X, et al. Magnetic Resonance Texture Analysis in Myocardial Infarction. *Front Cardiovasc Med*. 2021;8:724271. doi:10.3389/fcvm.2021.724271

333. Hines CDG, Yu H, Shimakawa A, McKenzie CA, Brittain JH, Reeder SB. T1 independent, T2* corrected MRI with accurate spectral modeling for quantification of fat: validation in a fat-water-SPIO phantom. *J Magn Reson Imaging JMRI*. 2009;30(5):1215-1222. doi:10.1002/jmri.21957

334. Carrick D, Haig C, Ahmed N, et al. Myocardial Hemorrhage After Acute Reperfused ST-Segment–Elevation Myocardial Infarction: Relation to Microvascular Obstruction and Prognostic Significance. *Circ Cardiovasc Imaging*. 2016;9(1). doi:10.1161/CIRCIMAGING.115.004148

335. de Waha S, Patel MR, Granger CB, et al. Relationship between microvascular obstruction and adverse events following primary percutaneous coronary intervention for ST-segment elevation myocardial infarction: an individual patient data pooled analysis from seven randomized trials. *Eur Heart J*. 2017;38(47):3502-3510. doi:10.1093/eurheartj/ehx414

336. Higginson LA, Beanlands DS, Nair RC, Temple V, Sheldrick K. The time course and characterization of myocardial hemorrhage after coronary reperfusion in the anesthetized dog. *Circulation*. 1983;67(5):1024-1031. doi:10.1161/01.CIR.67.5.1024

337. Pislaru SV, Barrios L, Stassen T, Jun L, Pislaru C, Van de Werf F. Infarct size, myocardial hemorrhage, and recovery of function after mechanical versus pharmacological reperfusion: effects of lytic state and occlusion time. *Circulation*. 1997;96(2):659-666. doi:10.1161/01.cir.96.2.659

338. Ganame J, Messalli G, Dymarkowski S, et al. Impact of myocardial haemorrhage on left ventricular function and remodelling in patients with reperfused acute myocardial infarction. *Eur Heart J*. 2009;30(12):1440-1449. doi:10.1093/eurheartj/ehp093

339. Beek AM, Nijveldt R, van Rossum AC. Intramyocardial hemorrhage and microvascular obstruction after primary percutaneous coronary intervention. *Int J Cardiovasc Imaging*. 2010;26(1):49-55. doi:10.1007/s10554-009-9499-1

340. Husser O, Monmeneu JV, Sanchis J, et al. Cardiovascular magnetic resonance-derived intramyocardial hemorrhage after STEMI: Influence on long-term prognosis, adverse left ventricular remodeling and relationship with microvascular obstruction. *Int J Cardiol*. 2013;167(5):2047-2054. doi:10.1016/j.ijcard.2012.05.055

341. Liu T, Howarth AG, Chen Y, et al. Intramyocardial Hemorrhage and the "Wave Front" of Reperfusion Injury Compromising Myocardial Salvage. *J Am Coll Cardiol*. 2022;79(1):35-48. doi:10.1016/j.jacc.2021.10.034

342. O'Regan DP, Ahmed R, Karunanithy N, et al. Reperfusion hemorrhage following acute myocardial infarction: assessment with T2* mapping and effect on measuring the area at risk. *Radiology*. 2009;250(3):916-922. doi:10.1148/radiol.2503081154

343. 14:00-17:00. ISO 15739:2017. ISO. Accessed June 18, 2024. https://www.iso.org/standard/72361.html

344. Mahesh M. The Essential Physics of Medical Imaging, Third Edition. *Med Phys*. 2013;40(7). doi:10.1118/1.4811156

345. Rose A. *Vision: Human and Electronic*. Springer US; 1974.

346. Hsieh SS, Leng S, Yu L, Huber NR, McCollough CH. A minimum SNR criterion for computed tomography object detection in the projection domain. *Med Phys*. 2022;49(8):4988-4998. doi:10.1002/mp.15832

347. van den Broek JHJM, van den Broek MHLM. Application of an ellipsoidal heart model in studying left ventricular contractions. *J Biomech*. 1980;13(6):493-503. doi:10.1016/0021-9290(80)90342-5

348. Weisskoff RM, Zuo CS, Boxerman JL, Rosen BR. Microscopic susceptibility variation and transverse relaxation: theory and experiment. *Magn Reson Med*. 1994;31(6):601-610. doi:10.1002/mrm.1910310605

349. Moon BF, Iyer SK, Josselyn NJ, et al. Magnetic susceptibility and R2* of myocardial reperfusion injury at 3T and 7T. *Magn Reson Med*. 2022;87(1):323-336. doi:10.1002/mrm.28955

350. Tribuna L, Oliveira PB, Iruela A, Marques J, Santos P, Teixeira T. Reference Values of Native T1 at 3T Cardiac Magnetic Resonance—Standardization Considerations between Different Vendors. *Diagnostics*. 2021;11(12):2334. doi:10.3390/diagnostics11122334

351. Hargreaves BA. Rapid gradient-echo imaging. *J Magn Reson Imaging JMRI*. 2012;36(6):1300-1313. doi:10.1002/jmri.23742

352. Ernst RR, Anderson WA. Application of Fourier Transform Spectroscopy to Magnetic Resonance. *Rev Sci Instrum*. 1966;37(1):93-102. doi:10.1063/1.1719961

353. Choi KM, Kim RJ, Gubernikoff G, Vargas JD, Parker M, Judd RM. Transmural Extent of Acute Myocardial Infarction Predicts Long-Term Improvement in Contractile Function. *Circulation*. 2001;104(10):1101-1107. doi:10.1161/hc3501.096798

354. Takigawa M, Martin R, Cheniti G, et al. Detailed comparison between the wall thickness and voltages in chronic myocardial infarction. *J Cardiovasc Electrophysiol*. 2019;30(2):195-204. doi:10.1111/jce.13767

355. Rose A. The Sensitivity Performance of the Human Eye on an Absolute Scale*. *JOSA*. 1948;38(2):196-208. doi:10.1364/JOSA.38.000196

356. Stirrat CG, Alam SR, MacGillivray TJ, et al. Ferumoxytol-enhanced magnetic resonance imaging methodology and normal values at 1.5 and 3T. *J Cardiovasc Magn Reson*. 2016;18(1):46. doi:10.1186/s12968-016-0261-2

357. Jin N, da Silveira JS, Jolly MP, et al. Free-breathing myocardial T2* mapping using GRE-EPI and automatic non-rigid motion correction. *J Cardiovasc Magn Reson Off J Soc Cardiovasc Magn Reson*. 2015;17:113. doi:10.1186/s12968-015-0216-z

358. Kellman P, Xue H, Spottiswoode BS, et al. Free-breathing T2* mapping using respiratory motion corrected averaging. *J Cardiovasc Magn Reson*. 2015;17(1):3. doi:10.1186/s12968-014-0106-9

359. Lima da Cruz GJ, Velasco C, Lavin B, Jaubert O, Botnar RM, Prieto C. Myocardial T1, T2, T2*, and fat fraction quantification via low-rank motion-corrected cardiac MR fingerprinting. *Magn Reson Med*. 2022;87(6):2757-2774. doi:10.1002/mrm.29171

360. Hadley R, Parker D, Minalga E. Improving signal-to-noise ratio in transcranial magnetic resonance guided focused ultrasound. *J Ther Ultrasound*. 2015;3(Suppl 1):O36. doi:10.1186/2050-5736-3-S1-O36

361. Wu L, Zhang S, Zhang T. MRI-Based Image Signal-to-Noise Ratio Enhancement with Different Receiving Gains in K-Space. *Sensors*. 2021;21(16):5296. doi:10.3390/s21165296

362. Sandino CM, Kellman P, Arai AE, Hansen MS, Xue H. Myocardial T2* mapping: influence of noise on accuracy and precision. *J Cardiovasc Magn Reson*. 2015;17(1):7. doi:10.1186/s12968-015-0115-3

363. Genc O, Morrison MA, Villanueva-Meyer JE, et al. DeepSWI: Using Deep Learning to Enhance Susceptibility Contrast on T2*-Weighted MRI. *J Magn Reson Imaging JMRI*. 2023;58(4):1200-1210. doi:10.1002/jmri.28622

364. Lohr D, Terekhov M, Veit F, Schreiber LM. Longitudinal assessment of tissue properties and cardiac diffusion metrics of the ex vivo porcine heart at 7 T: Impact of continuous tissue fixation using formalin. *NMR Biomed*. 2020;33(7):e4298. doi:10.1002/nbm.4298